The Preparation and Characterisation of Intercalation Compounds

Maria-Laura S. Kosidowski

A Thesis submitted for the Degree
of
Doctor of Philosophy

Heriot-Watt University
Department of Chemistry
September 1999

For my parents.

Table of Contents

Chapter One: Introduction

Chapter Two: Experimental Techniques

Chapter Three: Intercalation of Naphthalene into MoS_2

Chapter Four: Organic Intercalation Compounds of MoS_2

Chapter Five: Electron Volt Spectroscopy

Chapter Six: Discussion

Chapter Seven: Conclusions

List of Figures

List of Tables

Acknowledgements

I would like to thank my supervisor for his encouragement, support and continual good humour throughout the PhD; the PGD impressions were very good.

Dr. Jerry Mayers of the ISIS facility for his insight into the physics of eVS,
Dr. Winnie Kagunya of the ISIS facility for her assistance on TFXA.
Dr. Richard Strange of the Daresbury laboratory for the EXAFS.

Also, thanks go to,

Paz for bringing order to the lab, even with five of us in there (or just Sean).

The second floor posse, for the solvents and the good nights out.

Paul, Alan and Bill for having "magic hands" before ISIS trips.

My family for all their support.

Jim, for being there or not, when needed, for four years.

Heriot-Watt University
Edinburgh

Abstract of Thesis Form

(Form to be completed in block letters)

Surname KOSIDOWSKI	**Forename(s)** MARIA-LAURA S.	**Matriculation Number** 9511710031738

Postgraduate Study (tick)	**PhD**	✓	**MPhil**	☐	**MSc**	☐

Thesis Title

THE PREPARATION AND CHARACTERISATION OF INTERCALATION COMPOUNDS.

Signature: M·L· Kosidowski **Date:** 6th October 1999

Abstract

A series of hybrid organic-inorganic materials, (guest)$_x$MoS$_2$, were prepared by the method of exfoliation-reflocculation. Guest species, which include naphthalene, biphenyl and benzofuran, possess extended π-electron networks and were selected to examine the effects of the number of rings, heteroatom functionality and the size of the incorporated molecules on the physical properties of the host. The poorly crystalline products exhibit an increase in interlayer spacing of up to 5.8Å, the magnitude of this increase may be correlated with the orientation of the intercalated species. Inelastic neutron scattering of the naphthalene intercalate indicates that the majority of naphthalene vibrations have been suppressed. EXAFS data for a sub-set of these materials reveal changes in the local co-ordination of the molybdenum atom, resulting in a range of Mo-Mo distances. Electrical transport and magnetic properties were investigated by four-probe conductivity and SQUID magnetometry respectively. All products are semi-conducting but exhibit anomalies in $\sigma(T)$ for $50 \leq T/K \leq 100$. Intercalates of naphthalene, 2-methylnaphthalene and biphenyl are paramagnetic.

The applicability of the technique of neutron Compton scattering to the study of the dynamical properties of guest species was investigated. Measurements were made of the kinetic energy of hydrogen in H_xMoO_3(x=0.3, 1.57) and lithium in $LiTiS_2$, $Li_{0.45}MoO_3$ and LiV_2O_5, in the temperature range 5-300K. The more complex motion of the ammonium ion in a pyrochlore host was studied in NH_4TaWO_6. These investigations led to the establishment of criteria for the successful application of this technique to the study of guest species in complex chemical environments.

See reverse side for notes

Chapter One

Introduction

1.1 INTERCALATION

In the intercalation process, mobile guest species are inserted into a solid host structure that provides an interconnected system of vacant lattice sites. The reaction can be generalised by Equation 1.1 given below.

$$x(\text{Guest}) + \square_x[\text{Host}] = (\text{Guest})_x\,[\text{Host}] \qquad (1.1)$$

Since the intercalation reaction is carried out at or close to ambient temperature, there is minimal structural rearrangement of the host lattice and the process may be described as topotactic. One consequence of the fact that guest species may be inserted or removed without destroying the host structure is that such reactions are reversible. Significantly, the intercalation reaction is generally accompanied by a redox process which usually involves electron transfer from guest to host.

However, graphite is also capable of acting as host to electron acceptors such as halides, halogens and oxides[1]. True molecular insertion reactions with no accompanying redox process are very uncommon. Nonetheless, there are a few examples for which substantial empirical evidence exists for a simple molecular insertion mechanism. One such example is the ammoniate of ZrS_2, which has been demonstrated to be a molecular intercalation compound unlike the intercalates of TiS_2, 2H-TaS_2 and NbS_2, in which co-intercalation of NH_3 and NH_4^+ occurs with an accompanying redox reaction.

Intercalation is accompanied by a large negative free energy change and can result in changes to the physical properties (e.g. colour, electrical conductivity, magnetism) of the host. These features lead to a variety of applications including electrochromic display devices[2], batteries[3] and catalysts[4]. The existence of one or more stable or metastable intercalation phases over a range of composition, creates the possibility of subtly controlling properties by varying the degree of intercalation, x. Hence the interest in intercalation chemistry arises from both the ambient temperature synthetic route, which allows access to compounds not previously obtainable using other methods and also the potential for synthesising materials whose physical properties may be tailored to specific applications.

1.2 TECHNOLOGICAL APPLICATIONS

Solids which undergo reversible topotactic redox reactions have a number of technological applications. Insertion reactions are a route to energy storage in the form of chemical and electrochemical energy[64]. The origin of the energy can be electrical, thermal or photonic energy, the latter being feasible with semi-conducting insertion compounds. Thus insertion reactions find use in high-energy density batteries as reversible cathode materials, solar energy storage, photo-induced pumping of ions through membranes and optical information storage. Other areas of technology which exploit these materials include their use as electrochromic devices, optical sensors and as catalysts.

1.2.1 Electrochemical Insertion Batteries.

The application of solid state ionic materials to battery technology has been extensive. The application of intercalation compounds originated from using solid state ionic compounds as cathodes in which the diffusing cation dissolved to form an insertion compound in the form of a solid solution electrode. For this application, the host should ideally have high values of both ionic and electronic conductivity.

Secondary batteries that can be recharged by de-intercalation of the cathode require reversible intercalation reactions. Basic requirements for the cathode materials with topotactic reactivity are:-

- a wide range of x, since the energy density of the battery is determined by the maximum degree of insertion achieved.
- little change in free energy over the composition range, to produce a constant cell voltage.
- minor structural changes so that the reaction is reversible.
- high mobility of the guest ions in the solid phase.
- quantitative reversibility of the reaction.
- high electronic conductivity of the insertion compound.
- no solubility in the electrolyte and no co-insertion of the electrolyte.

Lithium and sodium are favoured as battery anodes on account of their high electrode potentials and their low atomic masses, a combination which optimises battery specific energy. Table 1.1 shows some lithium rechargeable batteries which have been developed or commercialised.

Table 1.1: Lithium batteries commercialised

Positive Electrode	**Performance (W h dm^{-3})**	**Company**
MnO_2	220	Sony
V_2O_5	220	Matsushita
MoS_2	60	Moli Energy
Mo_6S_8	100	Moli Energy
TiS_2	180	Eveready
$NbSe_3$	200	AT&T

Lithium prematurely reduces the life cycle of lithium batteries compared with Ni-Cd cells, because of its high chemical reactivity. In addition, production is made complicated and expensive because of the need for dry conditions when handling Li metal.

Owing to problems regarding the production and longevity of lithium batteries, an innovative secondary cell system has been developed that uses another intercalation compound as the negative electrode. Carbon is often used as the host for the anode. These are called "rocking chair" batteries and they offer advantages owing to the absence of lithium metal. Some examples of such batteries which have been developed are listed in Table 1.2.

Table 1.2: "Rocking chair" batteries compared with Ni-Cd cell.

Type	**Voltage**	**Energy (W h kg^{-1})**	**Company**
$LiCoO_2$-C	3.6	78	Sony
$LiMnO_2$-C	3.7	91	Asahi/Toshiba
$LiNiO_2$-C	3.2	80	EIC Labs. Inc.
Ni-Cd	1.2	30	Various

There is currently only one rechargeable battery of this type that has been commercialised which is not a coin cell. This is the "Lithium-Ion Cell" produced by Sony. It is at present used in cellular phones, video tape recorders and notebook computers.

1.2.2 Electrochromic Devices

Electrochromic displays utilise an applied external voltage to insert small atoms such as lithium or hydrogen into host electrodes e.g. WO_3, MoO_3[62], $Ir(OH)_x$[63]. Usually the host material is white and colouration occurs with insertion. However, in the case of $Ir(OH)_x$, the material is bleached upon insertion as it is reduced and colour is restored when it is oxidised. The change in colour is caused by the insertion of guest species; at low levels of insertion, new electronic energy levels within the band gap region of the semi-conducting host are produced. Electronic excitation from these levels provides additional optical absorption in a spectral region where previously the host material was transparent. At higher levels of insertion, the Fermi level is shifted sufficiently close to the conduction band that the new levels created can donate electrons into the conduction band at room temperature. This increases the free carrier absorption and produces colouration. The minimum electrochemical energy required in the colouration process corresponds to this shift in the Fermi level of the host electrode.

The most well known electrochromic system employing intercalation chemistry is WO_3 into which hydrogen or lithium are inserted. With the former guest, the pale green tungsten trioxide turns dark blue, the maximum degree of insertion being 10%. Response times are typically 0.5 sec. for lithium insertion and 0.1 sec. for hydrogen insertion. This is a key factor in uses of such devices as is the charge consumption for the required change in optical density required and the durability of the device i.e. its reversibility.

1.2.3 Chemical Sensors

Chemical sensors work on the principle of measuring the change in the electrochemical potential or the conductivity of the host material resulting from intercalation of the chemical species which is being detected. The most successful application of chemical sensors has been the measurement of oxygen concentration using zirconia solid electrolytes. The electrochemical reaction concerned is strongly temperature dependent and can be written as

$$O_2 + 4e^- \rightarrow 2O_2^-$$

The oxygen ions are formed within the zirconium oxide layers adjacent to the metal contact providing the electrons. It has been discovered that by applying an external electric field, the motion of the ions can be favourably influenced such that the reaction of oxygen atoms at the interface with the host can be enhanced, thereby increasing the sensitivity at lower temperatures.

1.3 HOST STRUCTURES

The host structure must possess certain properties for intercalation to be favourable. Primarily, a strong iono/covalently bonded network of atoms to ensure retention of structural integrity upon insertion is required. In combination with this, there must be a network of unoccupied lattice sites which allow easy diffusion of guest species through the host structure. In addition, if the reaction is accompanied by electron transfer from guest to host, low lying vacant orbitals are required, necessitating a metal in a high oxidation state.

Host structures may be divided into three general classes, according to their structural characteristics. Three dimensional systems or framework hosts either contain an interconnected or isolated network of channels, as shown in Figure 1.1. These tend to prevent ready movement of the guest species through the lattice and as a consequence, impose the greatest steric restrictions on the guest species. The dimensions of any guest species must be below a critical radius that is determined by the dimensions of the channels within the host structure for intercalation to occur.

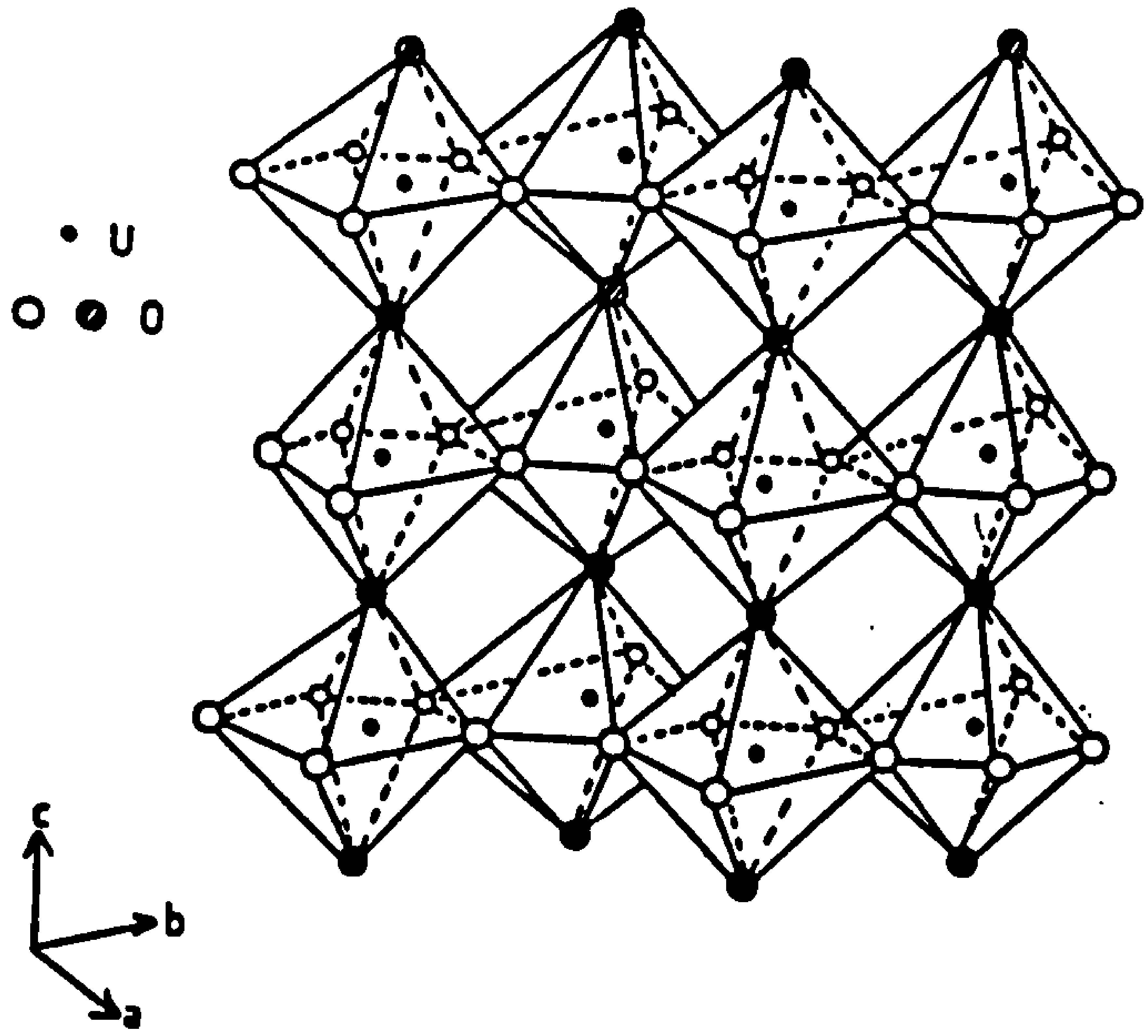

Figure 1.1: *Framework host structure of α-U_3O_8.*

The two-dimensional or lamellar host is the most widely studied (Figure 1.2). Such a host possesses a connected network of lattice sites in the interlayer space. They provide structural flexibility, manifested by their ability to adapt to the geometry of the guest species by simple expansion of the interlayer distance. They also possess structural stability, since the covalently bonded host layers can be separated by large distances to accommodate the guest in the van der Waals gap. Two-dimensional hosts are therefore able to incorporate a wide variety of guest species.

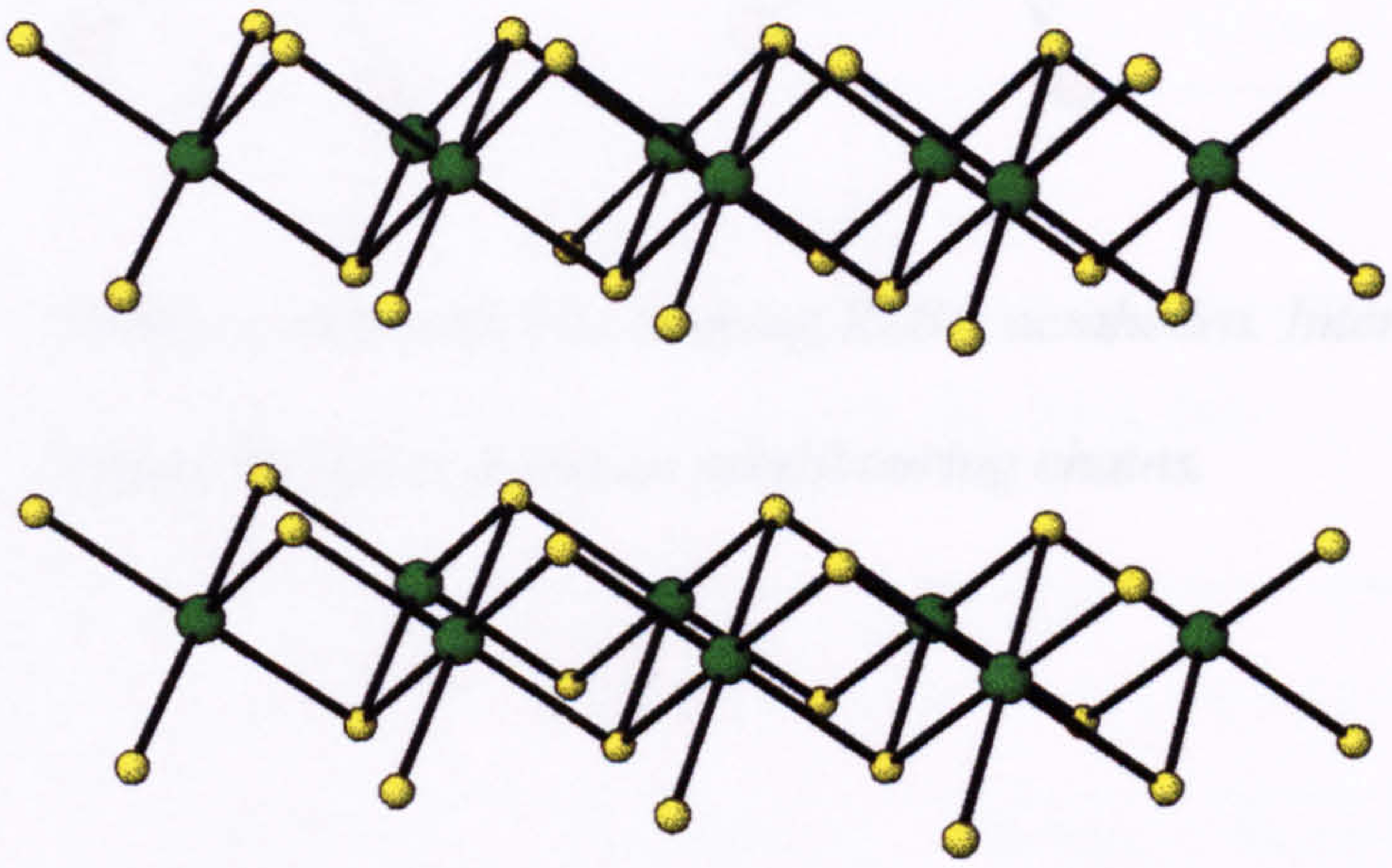

Figure 1.2: *TiS_2 layered transiton metal dichalcogenide host.*

The final class is the one-dimensional host which consists of chain type units separated by van der Waals gaps, providing neighbouring empty lattice sites; an example is shown in Figure 1.3. They have a structural flexibility that allows them potentially to intercalate the widest variety of guest species. However in general, these materials have low structural stability and they are also susceptible to lattice defects and to irreversible modification by chemical attack.

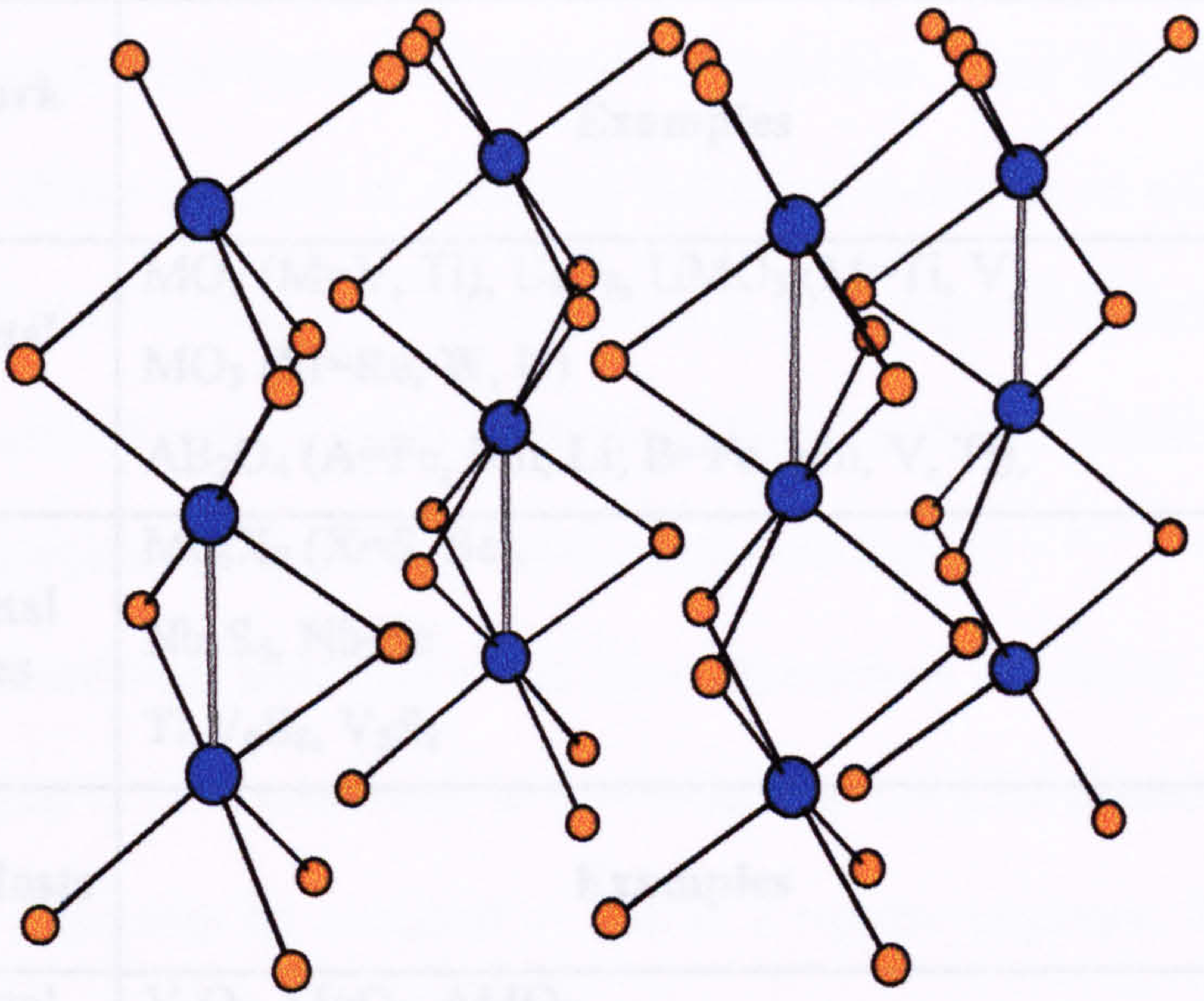

Figure 1.3: *$(RuBr_3)_\infty$ chains of face-sharing $RuBr_6$ octahedra. Intercalated cations occupy the space between neighbouring chains.*

Table 1.3: Host structures

3-D Framework Hosts	**Examples**	**Ref.**
Transition metal oxides	MO_2 (M=V, Ti), U_3O_8, UMO_5 (M=Ti, V) MO_3 (M=Re, W, U) AB_2O_4 (A=Fe, Mn, Li; B=Fe, Mn, V, Ti),	4,5
Transition metal chalcogenides	Mo_6X_8 (X=S, Se), Nb_3S_4, Nb_2Se $Tl_xV_6S_8$, V_5S_8	6
2-D Layered Hosts	**Examples**	**Ref.**
Transition metal oxides	V_2O_5, MoO_3, AMO_2 (A=alkali metals, M=Fe, Co, Ni)	7,8,9
Transition metal dichalcogenides	MX_2 (M=Mo, Ti, Zr, Hf, W, Sn; X=S, Se)	10,3
Transition metal oxyhalides	MOX (M= Ti, V, Cr, Fe; X=Cl, Br)	11
Phosphate Materials	$Zr(RPO_3)_2$, $Zr(ROPO_3)_2$ [R=Me, Et, Ph, CH_2COOH]	12
Metal halides	α-$RuCl_3$, β-ZrNCl	13,14
Clays and Silicates	Kaolinites ($Al_4Si_4O_{10}(OH)_8$) Montmorillonite $[Ca_{0.35}[Mg_{0.7}Al_{3.3}](Si_8)O_{20}(OH)_4]$	15, 16
1-D Chain Hosts	**Examples**	**Refs**
Transition metal trichalcogenides	MX_3 (M=Ti, Zr, Hf, Ta, Nb, Mo; X=S, Se)	17
Ternary molybdenum chalcogenides	AMo_3X_3 (A=alkali metal, In, Tl; X=S, Se)	18
Transition metal halides	$RuBr_3$	67

1.4 GUEST SPECIES

There are a large variety of atomic or molecular guest species which can be intercalated by direct insertion or exchange reactions, examples of which are listed in Table 1.4. This can be either as neutral units (e.g. polar organic molecules) or as ionic species (e.g. metal cations, H^+, metal complex cations, organic protonated or quaternary ions) depending upon the type and structure of the host lattice.

Specific ordering phenomena and phase transitions are found for layered host materials. Staging is the occurrence, at low stoichiometries, of phases where alternate van der Waals gaps may be occupied or not, in a regular sequence. The order of the staging is given by the number of layers between filled or partially filled layers as shown in Figure 1.4.

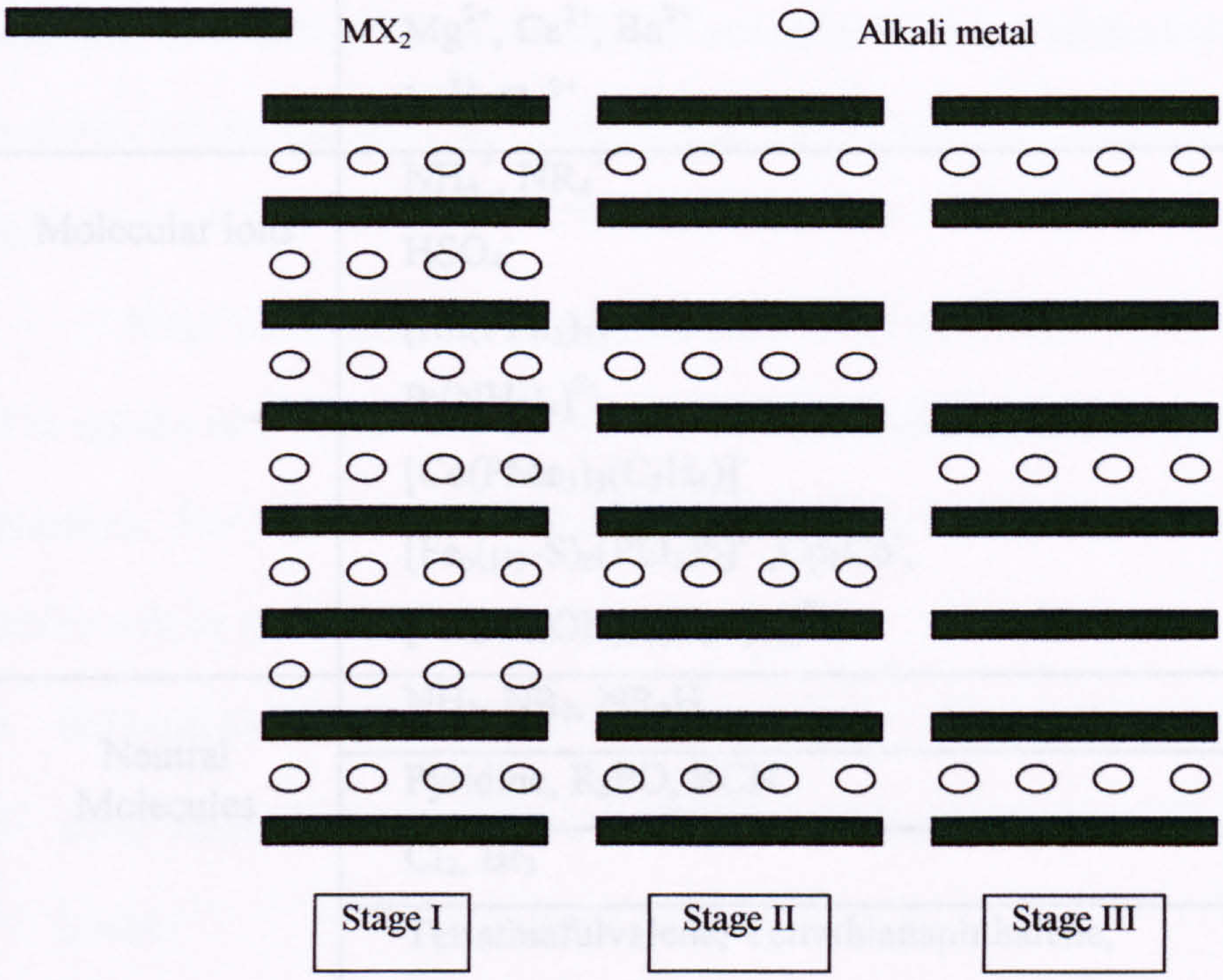

Figure 1.4: Schematic representation of staging phenomena.

The mechanism of easy conversion from one stage to another is not certain. A thermodynamic explanation of this phenomenon, first observed for graphite but subsequently observed for other layered hosts, described it as a gain in lattice energy if the guest species are concentrated in a restricted number[75] of van der Waals gaps rather than distributed evenly throughout all available gaps.

A domain model by Daumas and Herold, based on elastic forces, has been proposed which involves all the van der Waals gaps, but with local concentrations of the guest species across the basal plane in certain regions[19]. This has been supported by electron microscopy work by Thomas et al[20].

Table 1.4: Guest species

Guest type	Examples	Ref.
Atomic ions	H^+	21,22
	Li^+, Na^+, K^+, Cs^+	23, 24
	Mg^{2+}, Ca^{2+}, Ba^{2+}	25
	La^{3+}, Ce^{2+}	14
Molecular ions	NH_4^+, NR_4^+	26
	HSO_4^-	1
	$[Rh(PPh_3)_3]^+$	27
	$Pt(NH_3)_4]^{2-}$	28
	$[Co(PMe_3)_3(C_2H_4)]^-$	29
	$[Fe_6(\mu_3\text{-}S)_8(PEt_3)6]^{2+}$,$Cp_2Co^-$, $[Al_{13}O_4(OH)_{24}(H_2O)_{12}]^{7+}$	30
Neutral Molecules	NH_3, NR_3, NR_2H	31
	Pyridine, R_3PO, RCN	32
	Cl_2, Br_2	1
	Tetrathiafulvalene, Tetrathianaphthalene, Tetrathiatetracene	33
	$SnMe_3Cl$, $SnCl_4$	34

1.5 REDOX CHEMISTRY

With respect to the redox chemistry of intercalation compounds, there are two types of host; firstly, insulating host lattices such as zeolites, pyrochlores, layered aluminosilicates or metal phosphates where the basic physical properties of the lattice are not affected by intercalation. They have strongly localised charges and wide band gaps. Hence, their behaviour is characterised predominantly by acid/base and ion exchange properties.

The second type includes host lattices that have low-lying electronic states in which electrons can be accommodated. These may undergo redox reactions by electron/ion transfer processes, resulting in a strong perturbation of the physical properties of the host structure. Interest arises therefore, because from their potential to be useful functional materials for electrodes in secondary batteries, electrochromic systems, electrocatalysis etc. Numerous examples of redox intercalation reactions exist and only a brief summary will be presented here in an effort to illustrate the diversity of systems.

Small electropositive cations are usually the most readily inserted guest species. The uptake of a metal M is carried out as a simultaneous uptake of an ion M^{x+} and x electrons. For insertion of metal ions, the maximum uptake of guest ions into the host lattice will be governed by:-

- the band structure of the solid
- steric limitations, lattice strain effects and mutual Coulomb repulsion of guest cations

Quantitative charge transfer to the host lattice is favoured by:-

- high electron affinity E_A of the host lattice (as an electron acceptor)
- low ionization energy E_I of the guest species (as an electron donor)
- low guest metal content

As well as simple metal ions, a wide range of neutral molecular species with Lewis base character (e.g. NH_3, amines, pyridine, acid amides) can be intercalated into layered host lattices with neutral layer units which then become electronically conducting. Investigations have revealed that the intercalation process is associated with a partial irreversible transformation of the guest species yielding electrons that are transferred to the host lattice[13]; consequently ionic guest species develop from charge transfer. For many MS_2 hosts (M=Nb, Ti, Ta), when exposed to liquid ammonia alone, the intercalation compounds were formulated $(NH_3)_xMX_2$. However, ^1H NMR measurements established that the NH_3 is located in the interlayer space with its C_3 axis parallel to the layer planes[107]. This orientation does not favour direct charge transfer from the nitrogen lone pair to the layers of the host and further detailed characterisation by NMR[216], neutron diffraction[217] and inelastic neutron scattering measurements[218] have revealed that it is more correctly formulated as $(NH_3)_y(NH_4)_xMS_2$.

Investigations have been carried out into the intercalation of metallocenes into transition metal dichalcogenides, metal thiophosphates and oxides such as MoO_3, V_2O_5, xerogels[36], misfit layer chalcogenides[37]. The interaction between the host and the guest appears to be a balance between the electron affinity (E_A) of the host and that of the guest, and is of interest with respect to the orientation of the arene rings within the layers.

Graphite is the only host lattice known to be able to undergo intercalation reactions by electron transfer to the guest as well as vice versa. This amphoteric behaviour is due to the nature of the band structure that allows uptake of excess electrons into the conduction band as well as the formation of holes in the valence band upon oxidation. Facile intercalation of the alkali metals is accomplished, in particular with the heavier alkali metals K, Rb and Cs, which all have ionisation energies lower than the electron affinity of graphite (4.2eV). The increase in interlayer spacing is shown in Table 1.5.

When intercalating the alkali metals, electron transfer from guest to host is demonstrated by the change in the host from diamagnetic to Pauli paramagnetic behaviour and the coloured nature of the alkali metal intercalates. Solvated alkali metal intercalation compounds e.g. $Li(NH_3)_2C_{24}$ or $K(DMSO)_yC_{19}$ behave like the related solvated phases of layered hosts and can be described by quantitative charge transfer[38]. However, for the 1st stage phases LiC_6 and AC_8 (A=K, Rb, Cs), recent NMR studies support the idea of fractional ionisation of the intercalated guest metal atoms. The fractional ionic character for K, Rb and Cs amounts to 60%. The Li NMR data for LiC_6 suggest that the lithium guest atoms exhibit partial covalent bonding to the graphite. Knight shift measurements show low metallic character for lithium[66].

Table 1.5: Interlayer increases for alkali metal insertion in graphite.

Cation	Li^+	Na^+	K^+	Rb^+	Cs^+
Δc/Å	0.38	1.15	2.0	2.3	2.6

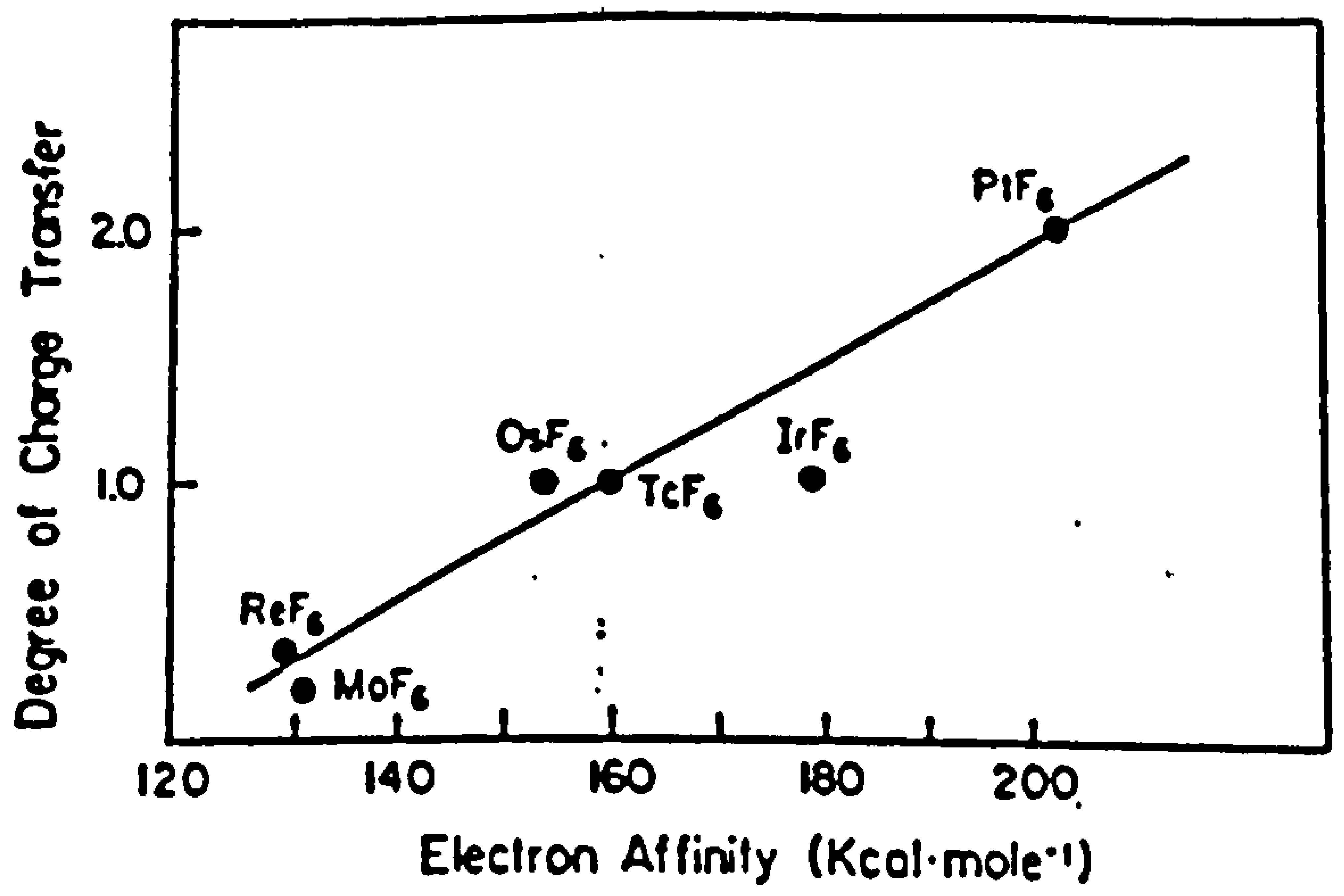

Figure 1.5: Estimated degree of charge transfer (x) as a function of estimated electron affinity for the metal hexafluorides intercalated into graphite. (From Ref 40)

Electron acceptors that have been inserted into graphite include HSO_4, NO_3, CrO_2Cl_2, CrO_3, MoO_3, Br_2 and metal halides such as $FeCl_2$ and MoF_6[39]. The direction of electron transfer can be established from Hall effect measurements which show the presence of p-type carriers. These graphite salts are good conductors in the *ab* plane. For the MF_6 inclusion compounds, the electron affinity of MF_6 has been found to be of prime importance to the stability of the intercalate and a linear relationship (Figure 1.5) has been established between the electron affinity and the host-to-guest charge transfer[40].

Although, most redox intercalation reactions are based upon metal cation reactions producing mixed cation valence states, intercalation processes based on anion redox reactions and mixed anion valence states are known. These concern mainly chalcogenide systems e.g. copper chromium spinels $CuCr_2S_4$[41] and KCu_4S_3[42]. These correspond to chalcogen mixed valence states X^{2-}/X^- of the host lattice anions and a formal redox process of the type

$$X^{2-} \Leftrightarrow X^- + e^- \qquad (1.2)$$

with constant valency of the metal ion.

In recent years, considerable interest has focused upon the synthesis of multilayer composites of macromolecules inserted into layered host lattices. Such a constrained environment is believed to lead to a higher degree of polymer ordering. Intercalation of conducting polymers has introduced novel properties to insulating host lattices. One technique involves the intercalation of monomers with subsequent chemical, thermal or photoinduced *in situ* polymerisation. Iron oxychloride has been shown to be a suitable host for the oxidative polymerisation of aniline to produce $(\text{aniline})_{0.28}FeOCl$. The polymer intercalate behaves as a p-type semiconductor with a conductivity measured on a single crystal of 1.5×10^2 S/cm[43].

1.6 PREPARATIVE ROUTES TO INTERCALATION COMPOUNDS

There are a variety of preparative routes to intercalation compounds. The main approaches are summarised in Table 1.6.

Table 1.6: Examples of Synthetic Approaches in Intercalation Chemistry

Method	**Example**	**Ref**
Direct reaction	$0.5C_5H_5N + TaS_2 \rightarrow TaS_2(C_5H_5N)_{0.5}$	45
	$KNbWO_6 + K(NH_3(l)) \rightarrow K_2NbWO_6$	46
	$OsF_6 + C\text{ (graphite)} \rightarrow C_8(OsF_6)$	40
Chemical Reagents	$LiAlH_4 + WO_3 \rightarrow Li_{0.33}WO_3$	47
	$0.2NaI + \alpha\text{-}UO_3 \rightarrow \alpha\text{-}Na_{0.2}UO_3 + 0.1I_2$	48
	$(C_5H_5)_2Zn + 10TiS_2 \rightarrow 10Zn_{0.1}TiS_2 + C_4H_{10}$	49
Ion Exchange	$Mn_{0.8}PS_3(K)_{0.4}(H_2O)_y + (TTF)_3(BF_4)_2 \rightarrow Mn_{0.8}PS_3(TTF)_{0.42}(K)_{0.1}(H_2O)_{0.4}$	50
	$Na_{0.3}(H_2O)_yTaS_2 + [(\eta\text{-}C_6H_6)_2Cr]I \rightarrow [(\eta\text{-}C_6H_6)_2Cr]_{0.13}TaS_2$	51
Electro-intercalation	$xCu^+ + TiS_2 \rightarrow Cu_xTiS_2\ (x \leq 0.9)$	52

1.6.1 Direct Reaction

This is the most straightforward method for preparing large amounts of an intercalation compound. Direct reaction was first used to prepare the alkali metal intercalates of the transition metal dichalcogenides, by exposing the host lattice to the alkali metal vapour at 600-800°C. Drawbacks were found for the intercalation of the most reactive alkali metals in the form of side reactions of the alkali metal with the reaction vessel and over-reaction. Direct reaction can lead to impurity phases, as for that between europium and NbS_2 where EuS is formed[35]. This method has been found to be most suitable for guest species such as the post transition elements.

1.6.2 Chemical Reagents

One of the earliest chemical reagents to be used was an alkali metal in liquid ammonia. This enabled intercalation to occur at ambient temperature and was applied initially to alkali metal intercalation of the transition metal chalcogenides[53], and has subsequently been used for alkali metal insertion in the transition metal oxides. Complications arise as it is often accompanied by co-intercalation of ammonia, and when heated under vacuum, unwanted side products appear. Organometallic reagents provide a more convenient chemical route. The most common of these is n-butyllithium, the reaction for which is shown in Equation 1.3. Typically, the n-butyllithium is dissolved in hexane and added to a suspension of the host lattice. The reaction time depends on the host, taking from a few minutes at ambient temperature to several days at reflux[54].

$$LiBu^n + MX_n \rightarrow Li_xMX_n + x/_2\, C_8H_{18} \qquad (1.3)$$

Other organometallic reagents in use include a variety of alkali metal aluminohydrides and borohydrides (M=Na, Li)[55], Na or K naphthalides or benzophenone[56]. For the preparation of magnesium insertion compounds, dibutylmagnesium in ether or a number of Grignard reagents (RMgBr) in diethylether such as magnesium bis(2,6,-di-tert-butylphenoxide) have been used[57].

Murphy and Christian[58] carried out a comparative study of the redox potentials of a variety of intercalation reagents; these are shown in Figure 1.6. It has been found that by careful choice of a reagent just on the reducing side of the host, the extent of reduction can be controlled. Hence, the reaction of V_2O_5 with reactive n-BuLi leads to amorphisation[54] but with LiI, the reaction product is polycrystalline $Li_xV_2O_5$ ($0 \leq x \leq 1$)[59].

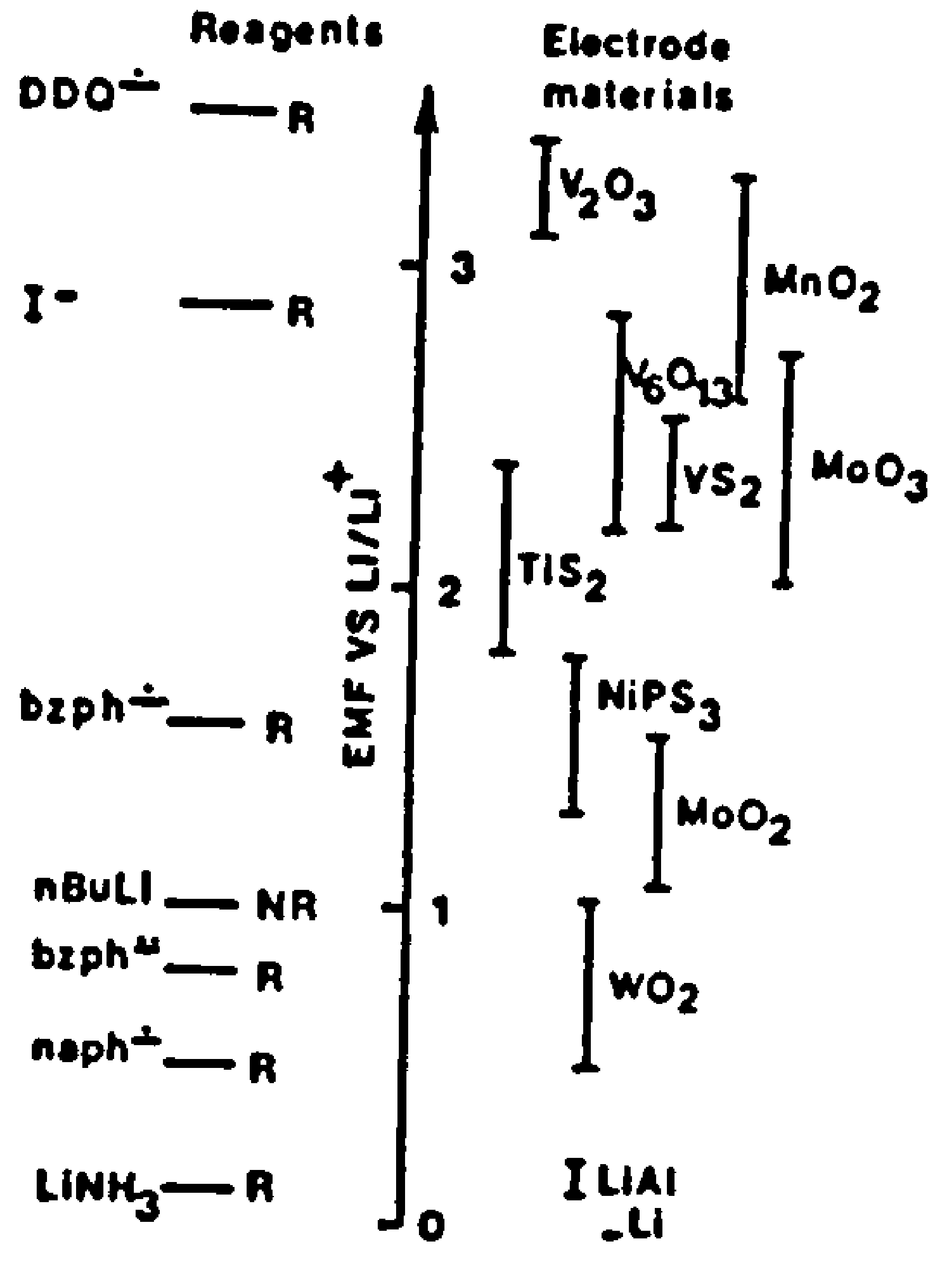

Figure 1.6: Redox scale of various electrode materials and reagents vs. Li/Li$^+$ couple. [after Ref. 58]

1.6.3 Ion Exchange

A guest species, introduced by one of the above routes, may often be wholly or partially replaced by another. This is achieved by use of a solution containing an excess of a second ion and is a useful strategy for carrying out intercalation of a large guest ion that will not intercalate by direct reaction. This method was used by Clement[60] to intercalate many species including tris(2,2'-bipyridyl)ruthenium di-cations into $MnPS_3$. This is also the route to most intercalation products of zeolites, pyrochlores, silicates and clays.

1.6.4 Electrointercalation

In this method the host material serves as the cathode in an electrochemical cell. The alkali metal or any other electropositive metal acts as the anode and, using a non-aqueous medium as the electrolyte, the reaction occurs by discharging a cell of the form $A(s) | A^+ | MO_n(s)$. The advantages of this method include the control of the redox potential and hence the rate and degree of intercalation. The shape of the discharge curve provides information on the thermodynamics and phase behaviour of the system i.e the range of existence of two-phase systems and solid solution regions. The disadvantages of this method are that it cannot be used to intercalate insulating hosts or for the insertion of neutral guest species into a host. Neither can it be used for the preparation of bulk samples and production of a pure sample is often not possible, since frequently a binder such as PTFE or a conduction improver such as graphite is required.

1.7 MEASUREMENT OF DYNAMICAL PROPERTIES

Of central importance to many of the applications of Section 1.2, is the mobility and dynamical properties of inserted guests. The techniques used to study the dynamical motion of ions and molecules within hosts are varied and each provides a specific type of information.

With ionic conductors, a.c. methods are used to measure the conductivity of the material and so give information on the mobility of the ions within the solid. For electronic conductors, similar d.c. measurements provide information on the charge carriers and activation energies. Determination of the sign of the Seebeck coefficient can be used to identify the charge of the dominant carriers and using Hall effect measurements combined with conductivity data, information about the density of carriers, the nature of the charge carriers and their mobility can be disentangled.

Optical vibrational spectra directly provide information on the vibrational motion of molecular species within the solid. Such modes can be classified as external or internal modes of vibration. External modes encompass rigid body motion, the motion of molecular groups as a whole, translational motion involving translation of the molecular groups and rotational or librational modes involving rotation of the molecular groups about their centres of gravity. Internal modes involve non-rigid molecular motion and allow for coupling between different groups and crystal periodicity. The torsional motions of guest molecules give rise to bands appearing in the far-infrared region. The torsional frequencies of a guest molecule can be compared to those of the free molecule. Empirically, if the guest molecule frequencies are closer to those in the liquid phase than those in the gaseous phase, this indicates a degree of host-guest interaction, restricting the internal rotations of the molecule. Equally, evidence for host-guest interactions can be obtained by comparing the frequency of vibration of a guest molecule with that of the free gaseous molecule. For example, the Raman spectra of TaS_2 and $TaSe_2$ intercalated with 1,2-diaminoethane are superpositions of the spectra of the individual components, indicative of weak host-guest interactions.

If optical methods are unsuitable, owing to the metallic nature of the solid, then the technique of incoherent inelastic neutron spectroscopy (INS) is potentially applicable. Neutrons interacting with atomic nuclei are not subject to the selection rules which govern IR and Raman activity of vibrations. Thermal neutrons have kinetic energies of the same order as the energy of lattice vibrations. INS spectra are dominated by modes involving large amplitudes of vibration of light atoms with large incoherent scattering cross-sections. Hence, this is a particularly powerful technique for looking at hydrogenous species. Using the method of normal co-ordinate analysis to analyse a high resolution spectrum, information can be obtained on specific vibrational motions of a species and on interatomic forces.

Solid state NMR produces broad spectra which can usually only be used in specific cases e.g. aluminosilicates. However, atomic migration processes can also be studied. Nuclear spin systems can come into thermal equilibrium more quickly via relaxation processes in solids; various types of motion including hindered rotation of molecules, torsional oscillations and translational diffusion, motion of conduction electrons or the presence of paramagnetic impurities cause a narrowing of the resonance lines.

Measurement of the spin-spin and spin-lattice relaxation times with temperature can provide information on the activation energies of the translational motion of intercalated species within a solid[139, 140, 141]. The line broadening is determined by the dipole-dipole interactions, and is sensitive to the distance separating interacting spins. If the nuclei reorient in the solid in some way, then this modulates the internuclear interaction and its magnitude is reduced. The peak widths may be measured as a function of temperature and from this, the activation energy for conduction can be calculated.

Each of these techniques provide some information on the dynamics of guest species in intercalation compounds but, as has been described, there are restrictions with each technique which limits their use to specific systems. The timescale of these techniques can limit the information obtained by the technique. If the material under examination is non-rigid under the timescale characteristic of the technique employed, then the information obtained will refer to an average motion.

1.8 FRAMEWORK OXIDES

The range of framework host oxides that undergo intercalation reactions is extensive, as shown in Table 1.3. These contain transition metal ions in high oxidation states, and have open iono-covalent structures and are able to incorporate a range of alkali metal and other electropositive metals under mild conditions. For framework hosts containing a network of interconnecting vacant channels, severe restrictions on the size of guest may be imposed by the host structure. Even though a suitable site may exist for the guest, the larger species may not be able to diffuse effectively through the lattice owing to the presence of size-limiting features such as metal-oxygen windows. Thus, kinetic rather than thermodynamic factors are of greater importance for ambient temperature insertion reactions. However, the size limiting window does have the advantage that intercalation can be selective such that transition metal ions can be reversibly inserted from an aqueous electrolyte without danger of co-intercalating the solvation shell. The range of intercalation chemistry demonstrated by three-dimensional oxide hosts can be classified by structure type and some of the more important examples are discussed below.

1.8.1 The ReO_3 Structure

The ReO_3 structure consists of vertex linked octahedra of ReO_6 in which each rhenium atom is connected to six others via connecting oxygen atoms. Hence an infinite three-dimensional network of interconnecting tunnels with overall cubic symmetry is formed. Complete occupation of the central cavity produces the AMO_3 perovskite structure. Reaction of ReO_3 with lithium iodide[68] results in the formation of a phase $Li_{0.2}ReO_3$ which has been shown to be isostructural with the high temperature lithium tungsten bronze. Reaction of ReO_3 with a more powerful lithiating reagent, n-BuLi, produces a single-phase material with stoichiometry Li_2ReO_3[69]. De-lithiation of this phase results in two further phases; $Li_{1.0}ReO_3$ and $Li_{0.35}ReO_3$. The powder X-ray diffraction data of these latter two indicate that they are of rhombohedral symmetry, suggesting that a distortion of the host framework has occurred. Powder neutron diffraction studies on $Li_{1.0}ReO_3$ and $Li_{2.0}ReO_3$ showed that the basic structure consists of chains of face-shared MO_6 octahedra with neighbouring chains sharing corners[70].

The flexibility of the O-M-O linkage already touched upon, allows various twists and tilts of the octahedra to form structures of lower symmetry than that of ReO_3. WO_3 can form one such configuration. At ambient temperature, it adopts a monoclinically distorted form that changes to the cubic structure at high temperatures. The intercalation compounds prepared at ambient temperature do have some properties in common with the high temperature bronzes; they are often intensely coloured, good electronic conductors and are generally non-stoichiometric. However, they differ from their high temperature counterparts in that the latter achieve a thermodynamically stable condition in their formation, only by substantial structural rearrangement and the process is not readily reversible.

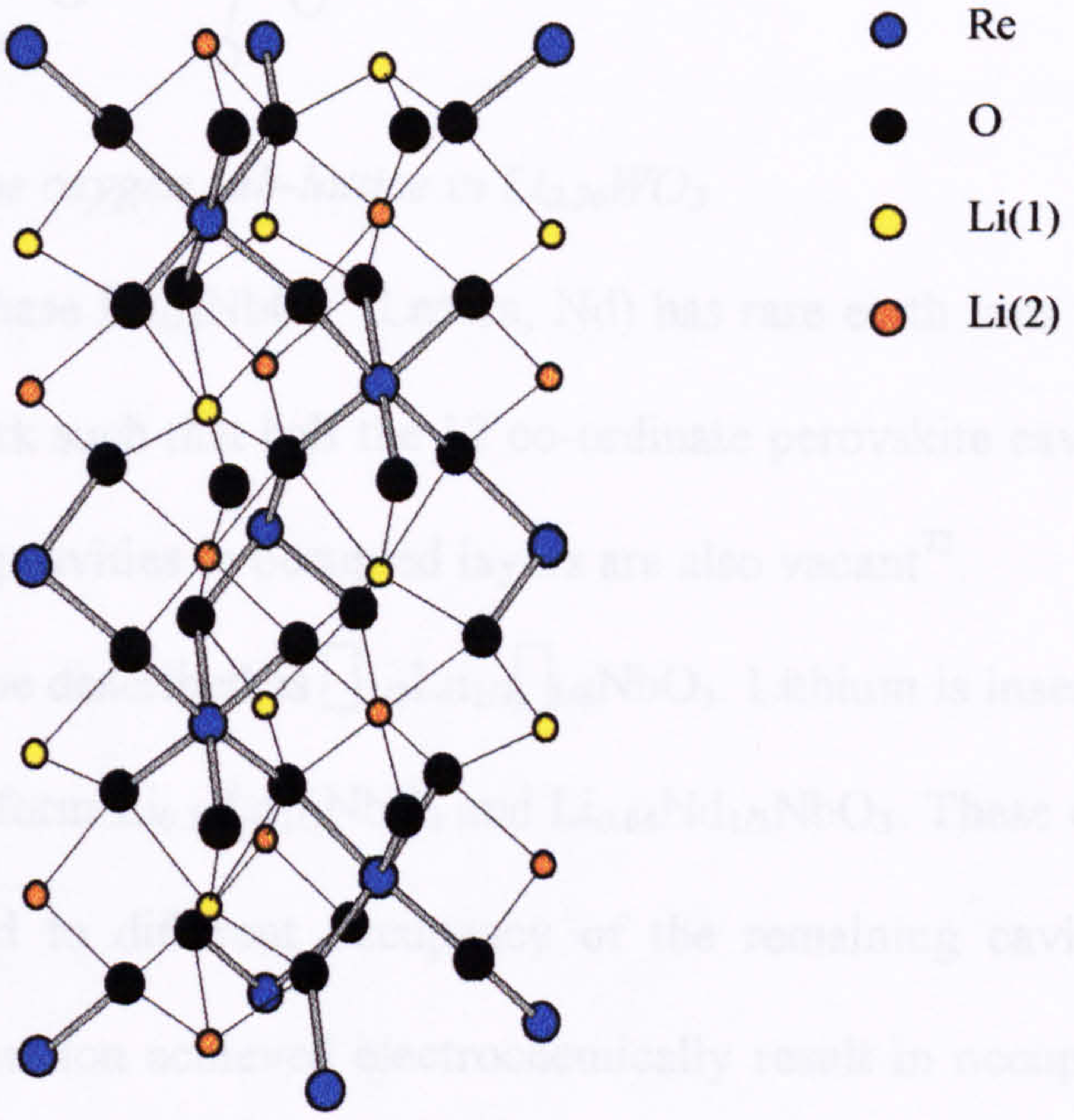

Figure 1.7: *Li_2ReO_3, The MO_6 octahedra are occupied in the sequence Re-Li(1)-Li(2)-Re-Li(1)...*

Cava et al prepared an ambient temperature phase[68] $Li_{0.36}WO_3$, the analogue of the tungsten bronze $Li_{0.36}WO_3$ prepared by Dickens and Wiseman[72]. Analysis of powder neutron diffraction data revealed that these are isostructural; both materials have a distorted perovskite structure where the oxygen sub-lattice is distorted such that four oxygen atoms are displaced towards the centre of the cavity. This results in two distinct cavity sites, one having a rectangular environment of four oxygen atoms and the other is an expanded twelve co-ordinate site. Although the occupancy of these sites was not determined, structure refinement suggests that thermodynamic control does not seem to differentiate between the ambient and high temperature preparations of this mixed oxide.

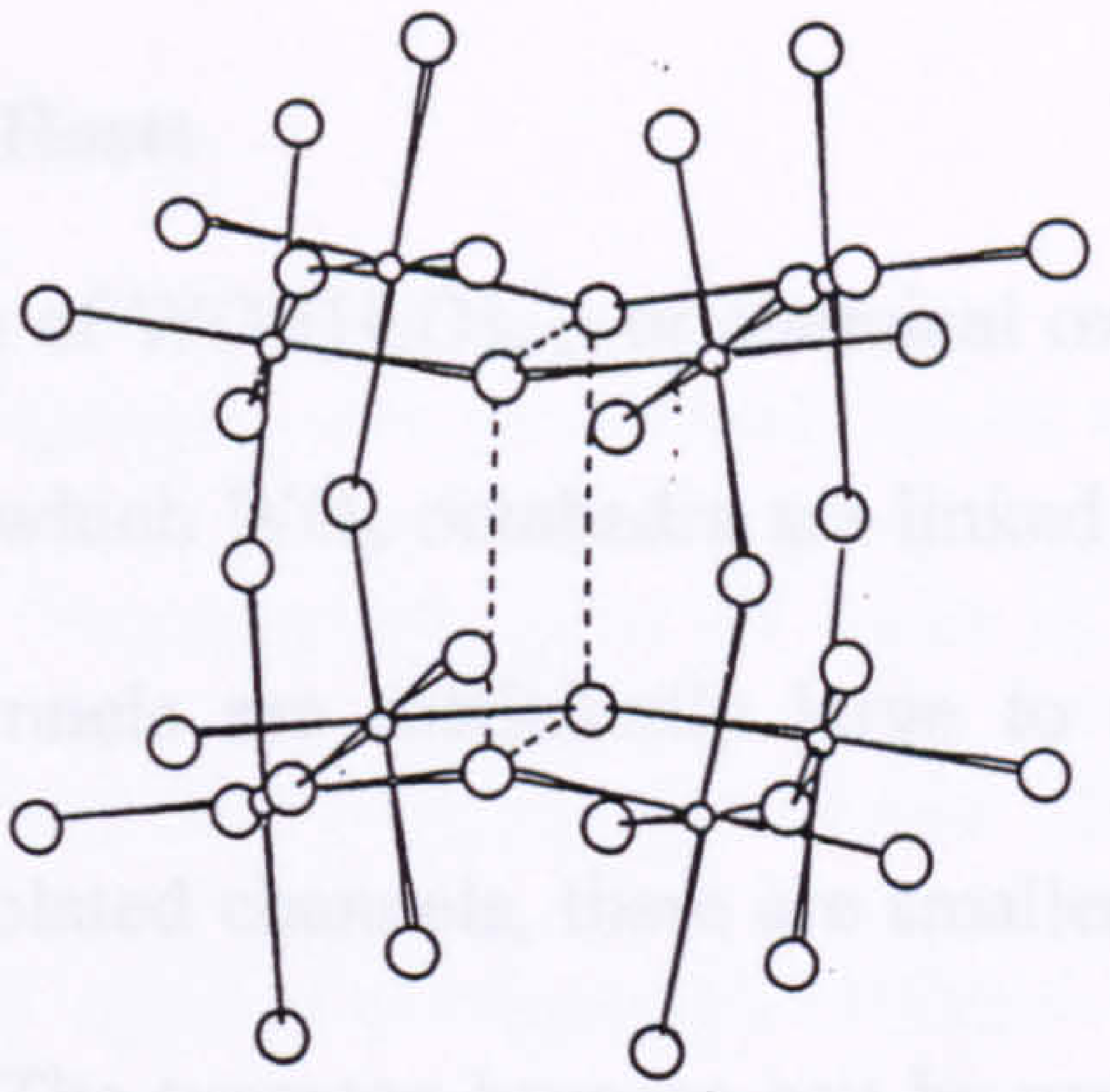

Figure 1.8: Distortion of the oxygen sub-lattice in $Li_{0.36}WO_3$

The perovskite type phase $Ln_{1/3}NbO_3$ (Ln=La, Nd) has rare earth ions partially ordered in the NbO_3 framework such that half the 12 co-ordinate perovskite cavities are empty and $^{1}/_{3}$ of the remaining cavities in occupied layers are also vacant[73].

The formulations can be described as $\square_{1/2}Ln_{1/3}\square_{1/6}NbO_3$. Lithium is inserted into these phases using n-BuLi to form $Li_{0.53}La_{1/3}NbO_3$ and $Li_{0.64}Nd_{1/3}NbO_3$. These different degrees of uptake correspond to different occupancy of the remaining cavity sites. Higher degrees of lithium insertion achieved electrochemically result in occupation of additional sites by lithium which are thought to be the bottlenecks between the cavities[74].

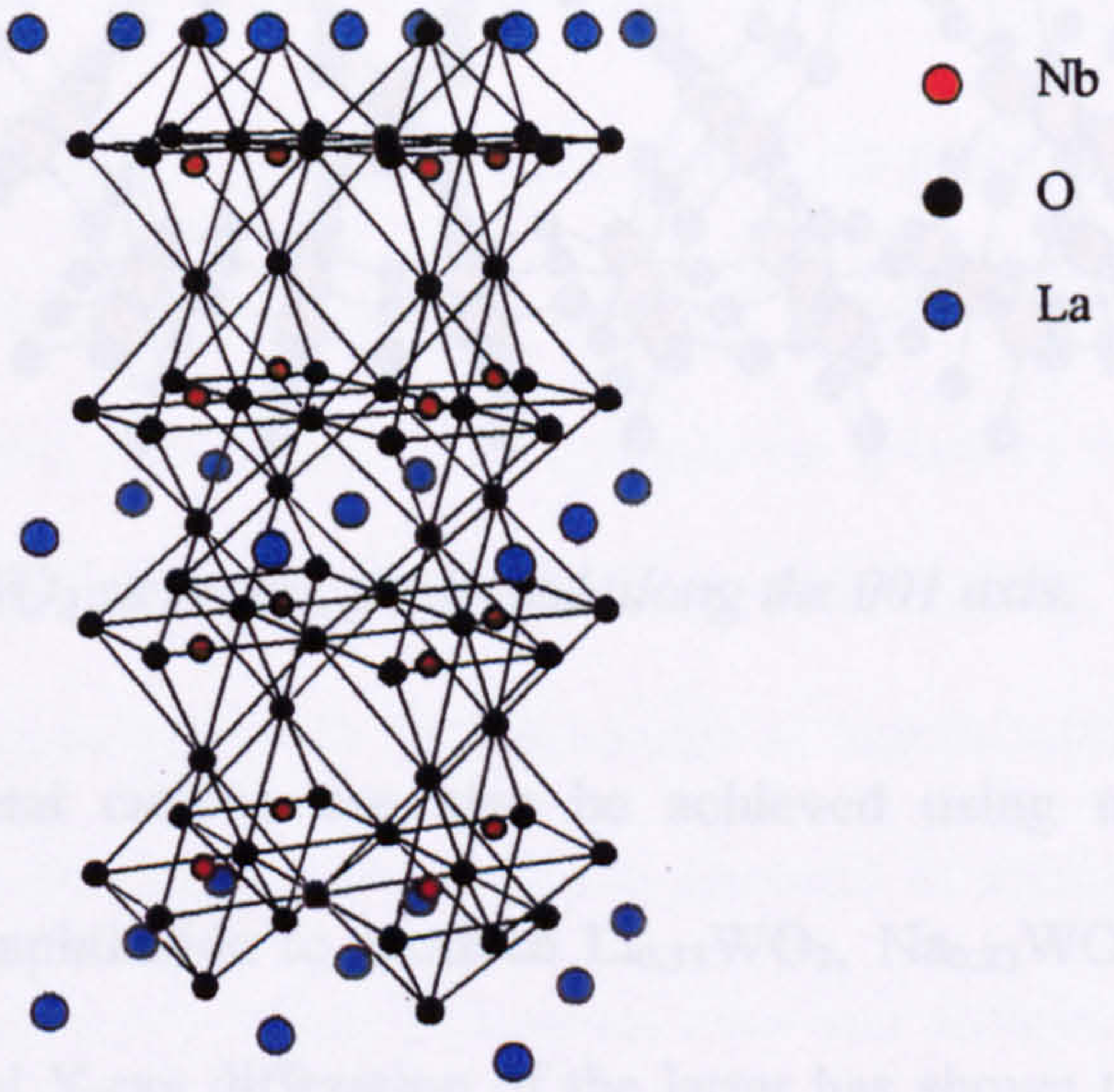

Figure 1.9: Parent structure of $La_{1/3}NbO_3$

1.8.2 Hexagonal Hosts

Dehydration of $WO_3(H_2O)_{0.33}$ or chemical oxidation of $(NH_4)_xWO_3$ can produce hexagonal WO_3 in which WO_6 octahedra are linked by their vertices to form hexagonal tunnels[77]. These tunnels are sufficiently large to undergo intercalation reactions. In addition to these isolated channels, there are smaller triangular tunnels running parallel to the larger ones. The tungsten bronzes can be prepared by reduction of this form of WO_3 with Zn/HCl or by electrochemical reduction in 0.1M H_2SO_4. The composition range obtained is $0<x<0.6$; the protons are found to have high mobility and their motion is strongly one-dimensional.

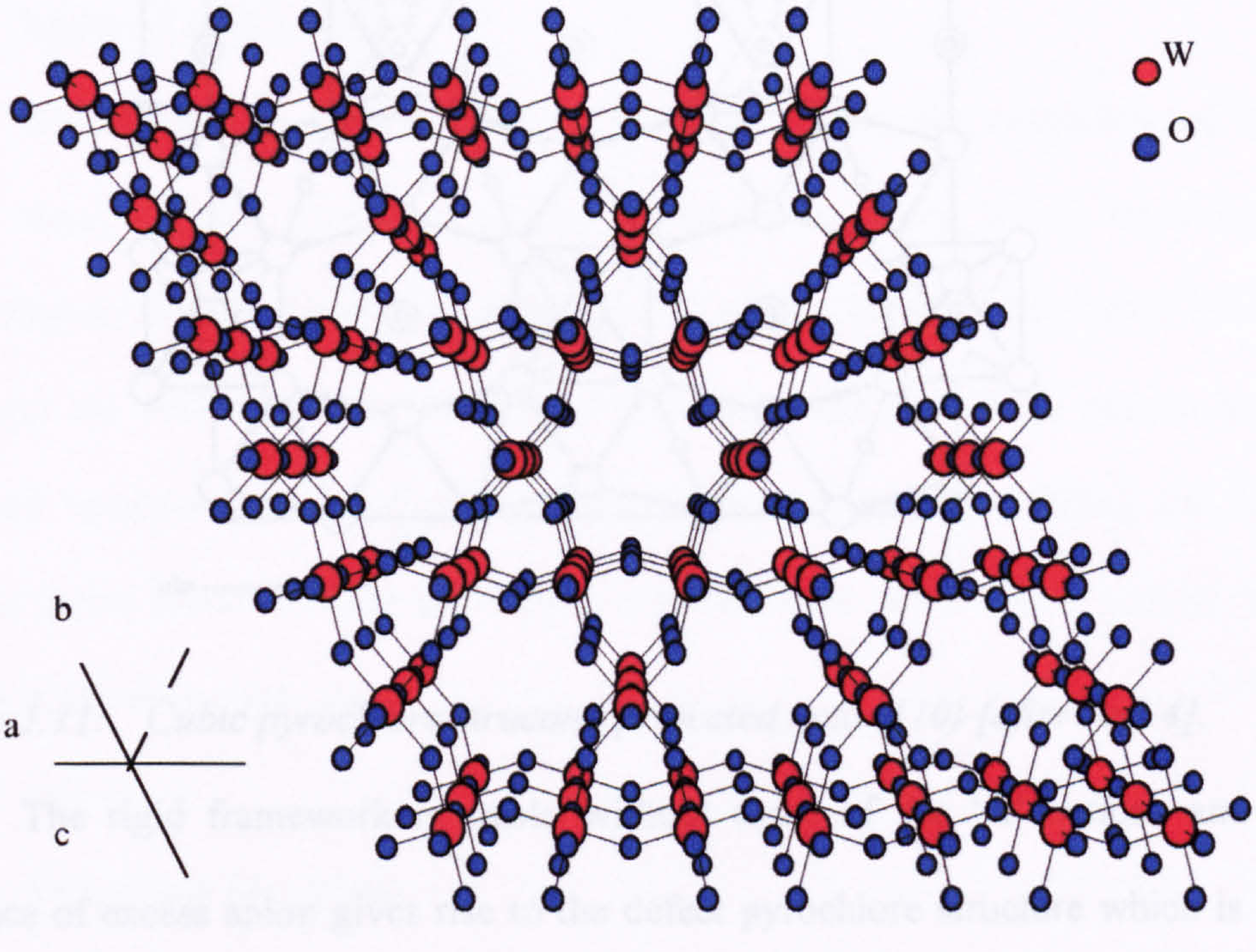

Figure 1.10: Hexagonal WO_3 structure, projected along the 001 axis.

Insertion of the alkali metal cations can also be achieved using n-BuLi, sodium naphthalide or potassium naphthalide to produce $Li_{0.33}WO_3$, $Na_{0.23}WO_3$ and $K_{0.3}WO_3$ respectively[78]. Single crystal X-ray diffraction of the latter has shown that the K^+ ions reside in the larger hexagonal tunnels.

1.8.3 Pyrochlores

The general formula of a pyrochlore can be written as $A_2B_2O_6O'$. There are four crystallographically inequivalent types of atom in the unit cell which contains eight formula units. The structure is composed of two different types of cation co-ordination polyhedron. The 'A' cations are eight co-ordinate and located within distorted cubes; six of the oxygen atoms are at a slightly shorter distance from the central cation. The smaller 'B' cation is located within a trigonal antiprism with all six anions equidistant. These polyhedra are vertex linked as shown in Figure 1.11 to create a framework containing large cavities linked by channels.

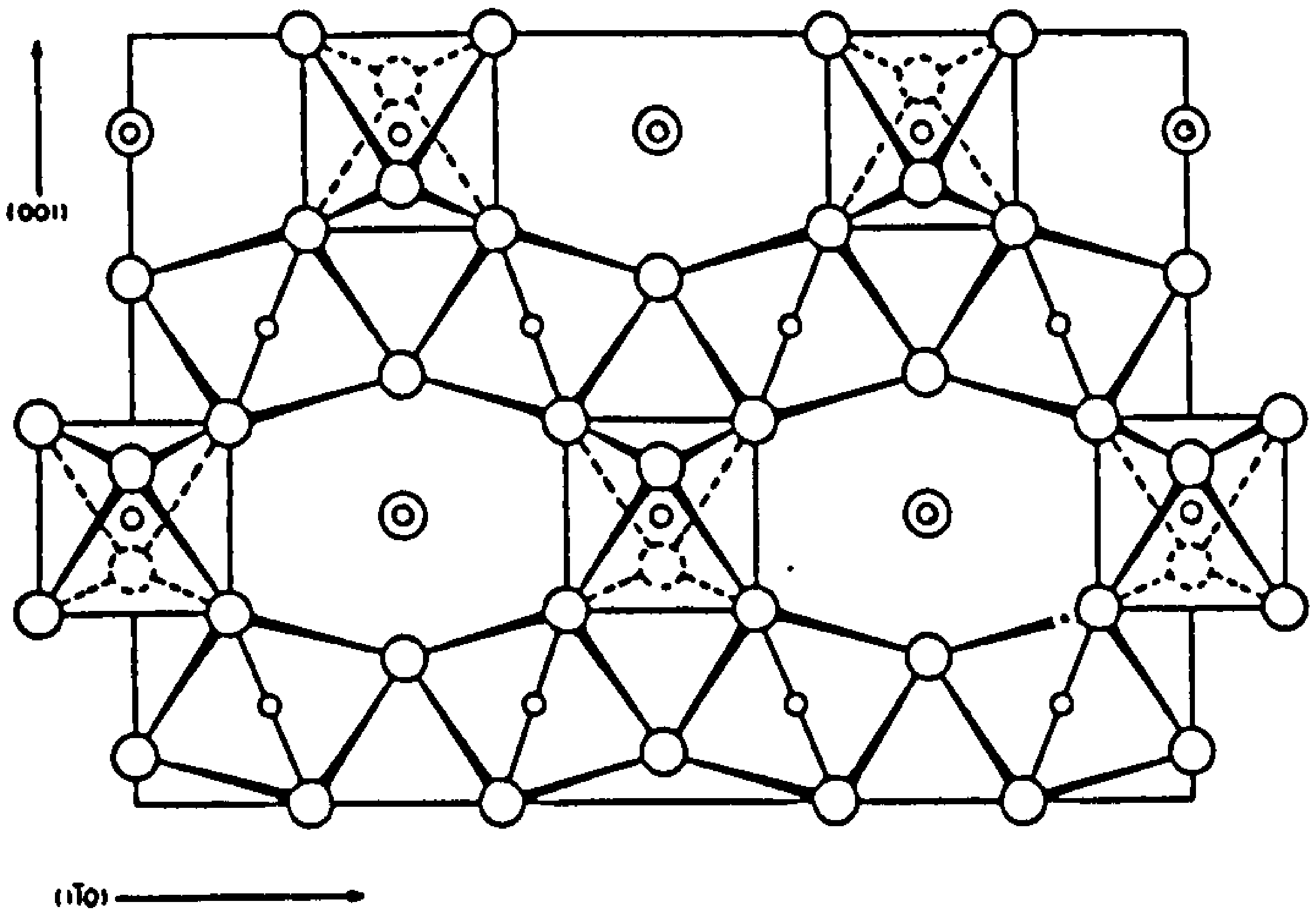

Figure 1.11: Cubic pyrochlore structure projected onto (110) [after Ref. 4].

The rigid framework is stable without some of the 'A' cations and anions. Absence of excess anion gives rise to the defect pyrochlore structure which is adopted by mixed metal oxides of the form $AMM'O_6$ (A=alkali metal or NH_4, M and M'= W, Nb, Ta). These have been investigated for their potential as intercalation hosts. Murphy et al have studied $ANbWO_6$ (A=Na, K, Rb) that give products of formula A_2NbWO_6[79]. A powder neutron diffraction study of the potassium insertion compound showed that the $NbWO_6$ framework is invariant upon insertion. However, the potassium ions occupy different sites in $KNbWO_6$ and $K_{1.88}NbWO_6$.

1.9 LAYERED OXIDES

A number of oxide materials possess layered structures; when transition metal cations are in a high oxidation state. As such, these cations are able to form strong multiple bonds to oxygen which are shorter than the average single metal-oxide bond. This overcomes the destabilisation experienced from electrostatic repulsions between layers of negatively charged oxide ions which are not counterbalanced with sufficiently strong van der Waals forces. Layered transition metal oxides may be stabilised when the electrostatic repulsions have been reduced by the presence of interlayer cations or hydrogen bonding.

1.9.1 Layered AMO_2 oxides

These comprise alternating layers of edge-sharing MO_6 octahedra and layers of alkali metal cations. They are similar in structure to the alkali transition metal dichalcogenides in that their structure depends on the alkali metal cation content and size, and the ionicity of the M-O bond. However, the pure MO_2 phases cannot be prepared because some alkali metal presence is required to stabilise the structure, staging is not found because each layer requires some alkali metal content to offset repulsion between oxide layers.

1.9.2 Vanadium Phosphate

The α form of $VOPO_4$ is a layered compound. The structure is composed of MO_6 octahedra and XO_4 tetrahedra, linked by their vertices (Figure 1.12). The layers are joined along the c axis by shared oxygen atoms. The presence of the phosphate groups reduces the number of V=O...V interactions per unit area relative to that of V_2O_5 which results in the interlayer interactions being much weaker and so $VOPO_4$ behaves as a two-dimensional system. $VOPO_4$ readily forms hydrated phases; the dihydrate being an intercalate with one water molecule co-ordinated to the vanadium and the second located in the interlayer space. Species such as pyridine, bipyridines, ethanol can also be incorporated[85].

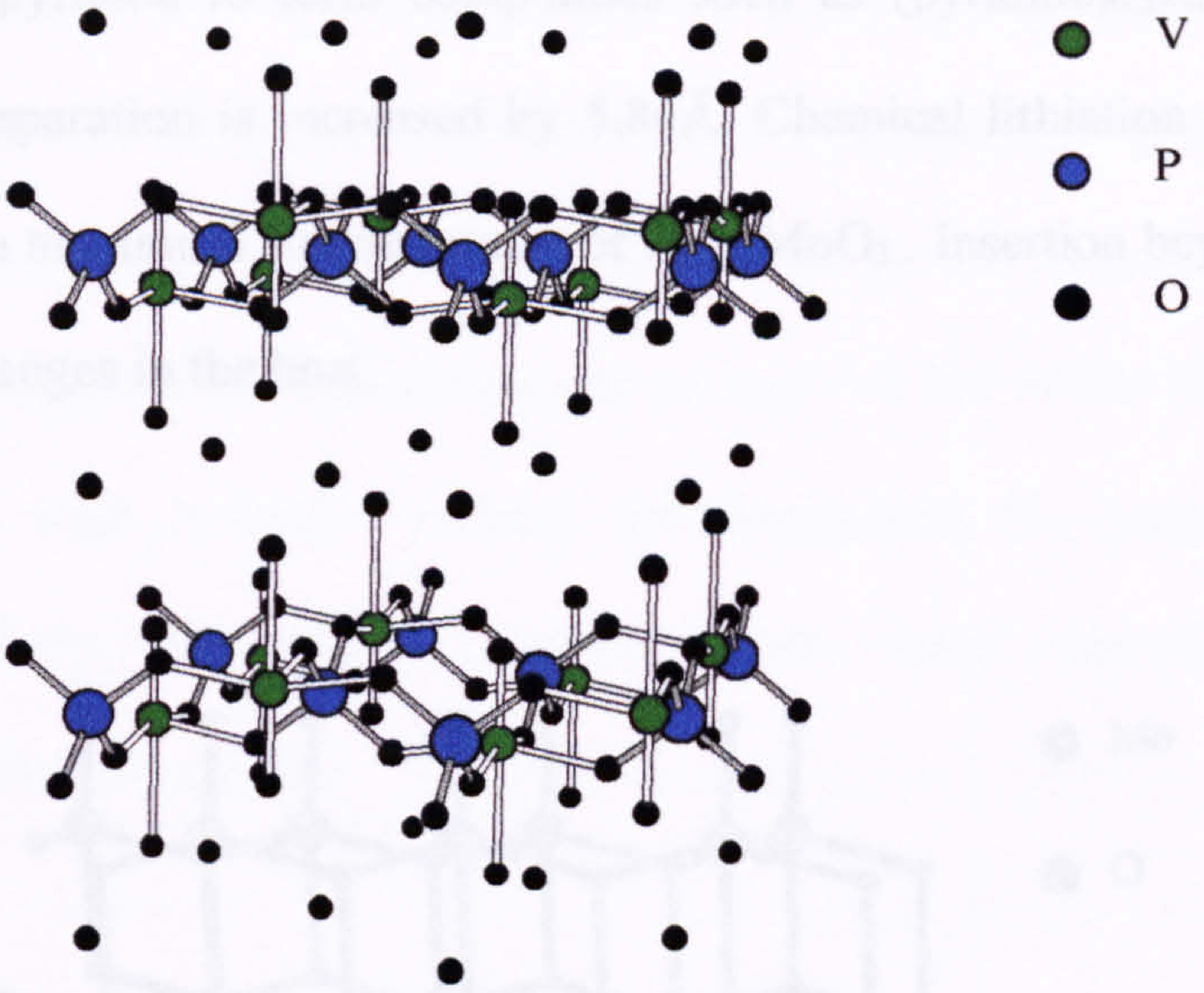

Fig 1.12: *$VOPO_4.2H_2O$. One oxygen from water is co-ordinated to vanadium, the second is located in the interlayer space.*

1.9.3 MoO_3

This oxide has a unique structure consisting of double layers of edge sharing and corner sharing MoO_6. The transition metal ion is in a grossly distorted octahedral environment, with one shorter multiple bond to oxygen. Individual layers are separated by a van der Waals gap and consequently the oxide shows similar topotactic redox chemistry to that exhibited by the transition metal dichalcogenides.

Hydrogen can be inserted via reduction in acid solution or reaction with hydrogen and a noble metal catalyst. Four separate phases have been identified by Glemser and co-workers[65]. All these H_xMoO_3 phases show metallic conductivity and weak temperature independent paramagnetism. These insertion compounds react with Lewis bases such as pyridine to form compounds such as $(pyridine)_{0.3}H_{0.5}MoO_3$ in which the interlayer separation is increased by 5.84Å. Chemical lithiation at ambient temperature produces a maximum stoichiometry of $Li_{1.55}MoO_3$.. Insertion beyond x~1.5 leads to irreversible changes in the host.

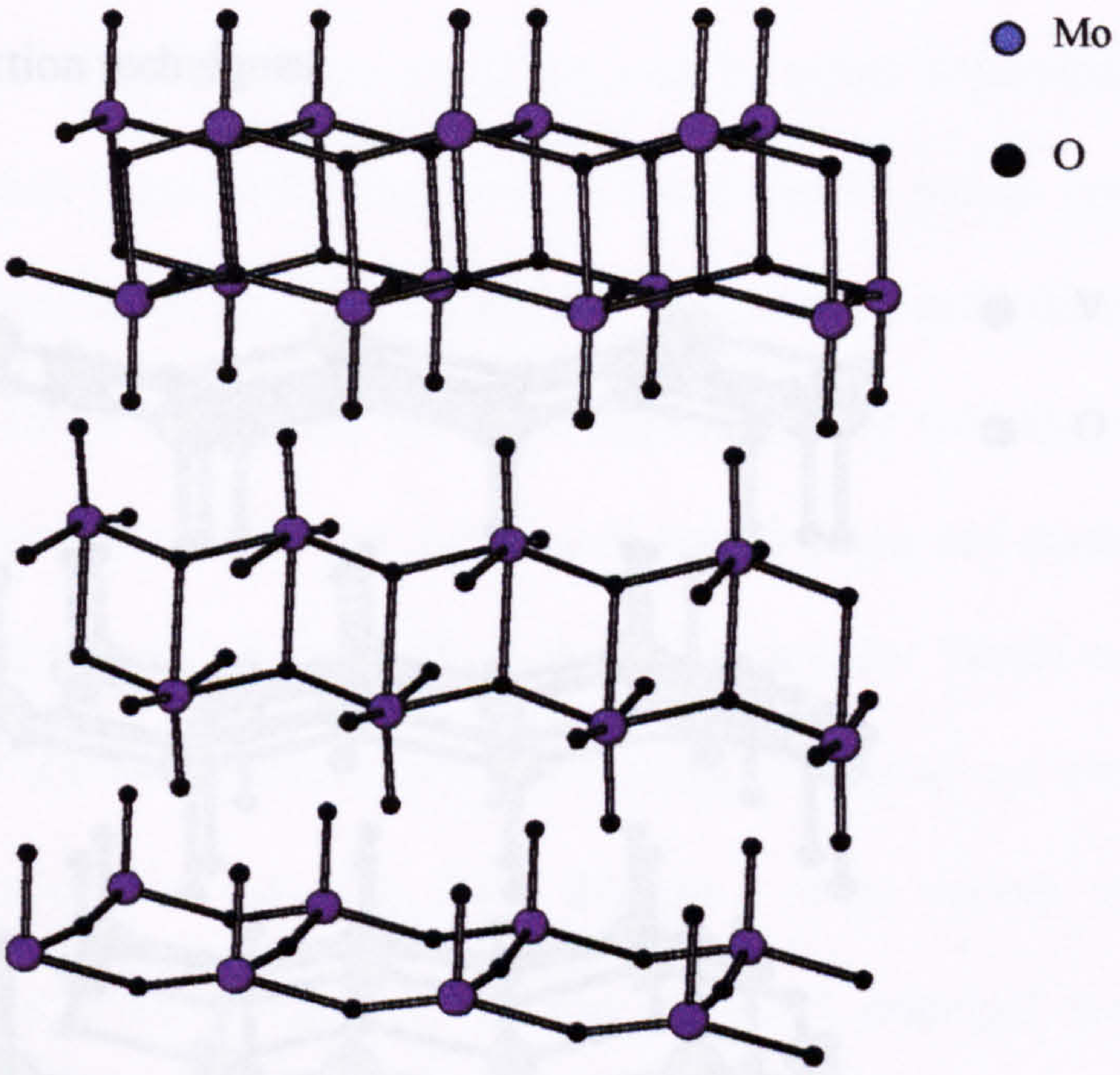

Figure 1.13: MoO_3

1.9.4 V_2O_5

V_2O_5 has a pseudo-layered structure; it is made up of V_2O_5 ribbons, formed by shearing two ReO_3 chains. Vanadium cations are in a highly distorted octahedral environment in which the shortest metal-oxygen bond is perpendicular to the layers.

The interlayer interactions are sufficiently strong that V_2O_5 behaves in most respects like a three-dimensional structure rather than a layered compound. Hence, intercalation of large cations is unsuccessful; only the smaller cations such as lithium[88] and magnesium[57] can be inserted into the framework. The former can be intercalated using lithium iodide in acetonitrile to form ternary phases $0 \leq x \leq 2.0$. Three regions in which there are crystalline phases have been identified, lattice constants of which indicate topochemical insertion.

Hydrogen intercalation can be achieved for up to $x \approx 3.8$ but unlike H_xMoO_3, the $H_xV_2O_5$ phases with high hydrogen content are amorphous to X-rays and are semiconducting[90]. Three single-phase regions have been identified using electrochemical insertion techniques.

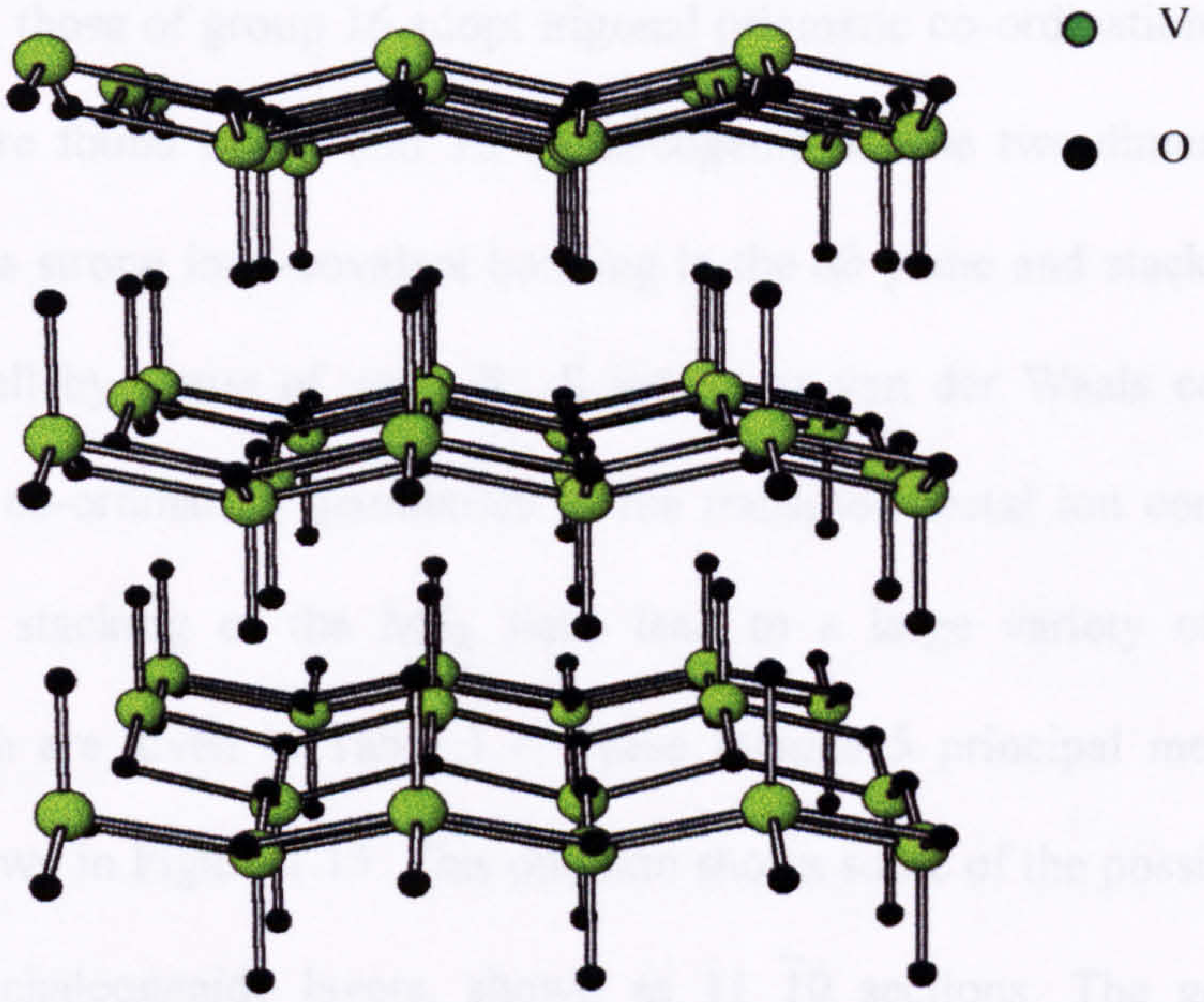

Figure 1.14: *V_2O_5*

1.10 STRUCTURE OF DICHALCOGENIDES

As a consequence of the high electronegativity and low polarisability of oxygen, metal/oxygen bonds have more ionic character than metal/sulphur bonds. The structures of oxides and sulphides are frequently therefore quite different. The increased covalent nature of the chalcogenides over the oxides favours the involvement of metal d orbitals in covalent bonding. The higher polarisability of the chalcogenide anion X^{2-} allows the adoption of structures where the environment of the X^{2-} ion is highly asymmetric. As a consequence of these differences, the chalcogenides frequently adopt a large number of structure types of lower dimensionality than the corresponding oxides. These structures are in turn able to incorporate a wide variety of guest species, their intercalation chemistry is extensive therefore and has been much studied.

The basic building block of the layered transition metal dichalcogenides consists of two close packed layers of chalcogens between which is situated the transition metal ion. The co-ordination of the transition metal ion may be either octahedral or trigonal prismatic. The transition metal dichalcogenides of the group 14 metals contain cations in octahedral sites; those of group 16 adopt trigonal prismatic co-ordination. Both types of co-ordination are found in Nb and Ta dichalcogenides. The two-dimensional MS_2 compounds possess strong iono-covalent bonding in the *ab* plane and stack along the c axis of the unit cell by virtue of weak S...S interlayer van der Waals contacts. The possibility of two co-ordination geometries of the transition metal ion combined with different ways of stacking of the MS_2 slabs lead to a large variety of polytypes, examples of which are given in Table 1.7. These include 5 principal metal sulphide structure types shown in Figure 1.15. This diagram shows some of the possible stacking sequences of the chalcogenide layers, shown as $11\bar{1}0$ sections. The generic layer sequence along the c axis is SMS-SMS-SMS where S-S represents the van der Waals gap. These structures can be conveniently described by the Ramsdell notation where the letters A, B, C are used to denote respectively sites at 0,0; 1/3, 2/3; 2/3, 1/3 in a two dimensional hexagonal lattice (Figure 1.16). The 1T structure, where the anions are hexagonally close packed, is adopted by all the group 14 and vanadium compounds together with one phase of TaS_2.

Table 1.7: Examples of polytypes adopted by transition metal dichalcogenides.

Symbol	Space Group	Examples	Metal co-ordination
1T	$P\bar{3}m1$	MX_2 (M=Ti, Zr, Hf; X=S, Se, Te)	Distorted O_h
$2H_a$	$P6_3/mmc$	MX_2 (M=Nb, Ta; X=S, Se)	Trigonal prismatic
$2H_b$	$P\bar{6}m2$	MSe_2 (M=Nb, Ta)	Trigonal prismatic
$2H_c$	$P6_3/mmc$	MX_2 (M=Mo, W; X=S, Se)	Trigonal prismatic
3R	$R\bar{3}m$	MX_2 (M=Nb, Ta; X=S, Se), WS_2	Trigonal prismatic
$4H_b$	$P6_3/mmc$	TaX_2 (X=S, Se)	Trigonal prismatic, distorted O_h
6R	$R\bar{3}m$	TaX_2 (X=S, Se)	Trigonal prismatic, distorted O_h

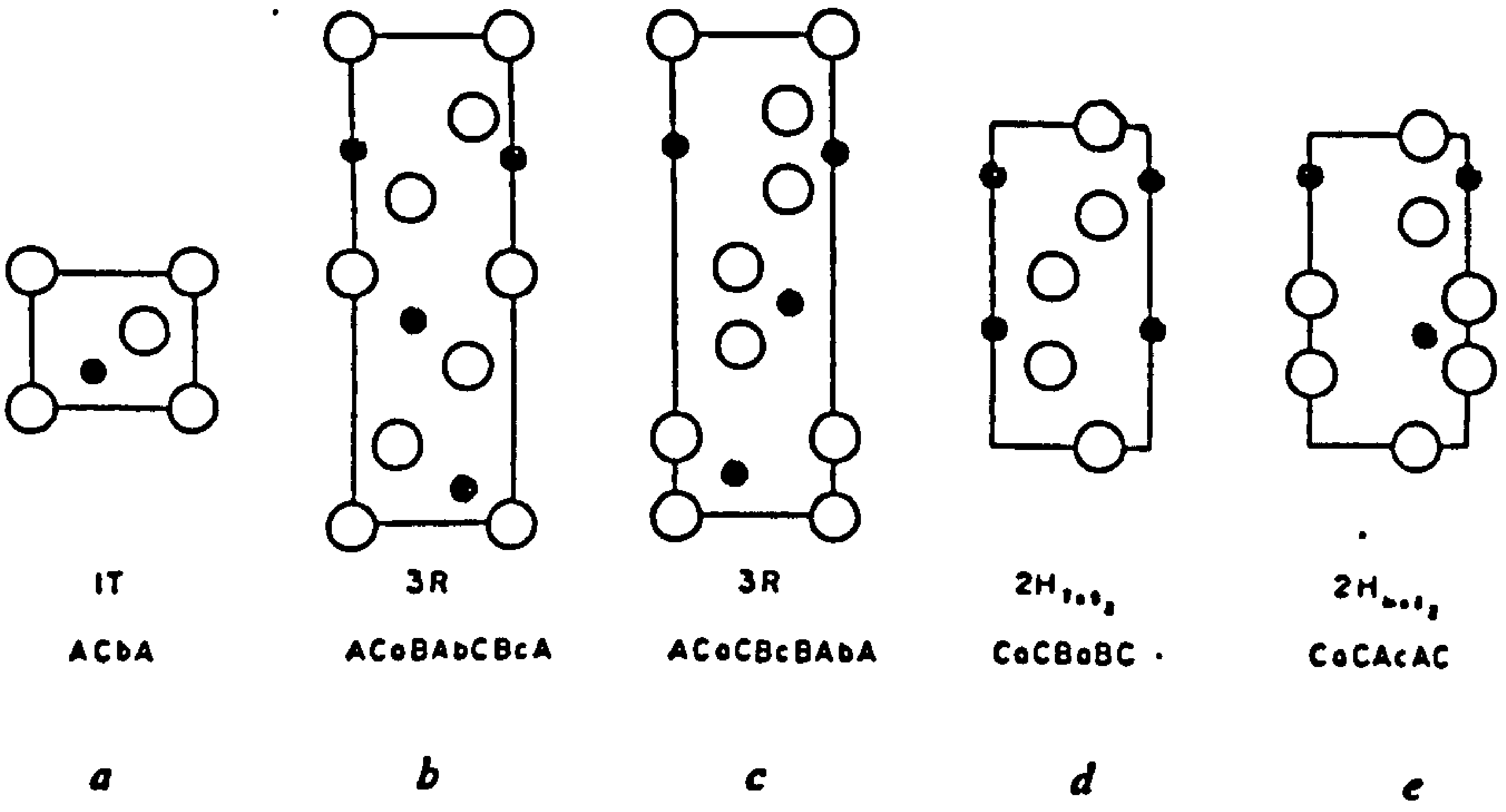

Figure 1.15: The five principal MX_2 structure types with their ABC notations. The black and white circles represent metal and sulphur atoms respectively. The upper-case letters denote S atoms and the lower-case letters denote the transition metal atoms [after Ref. 3].

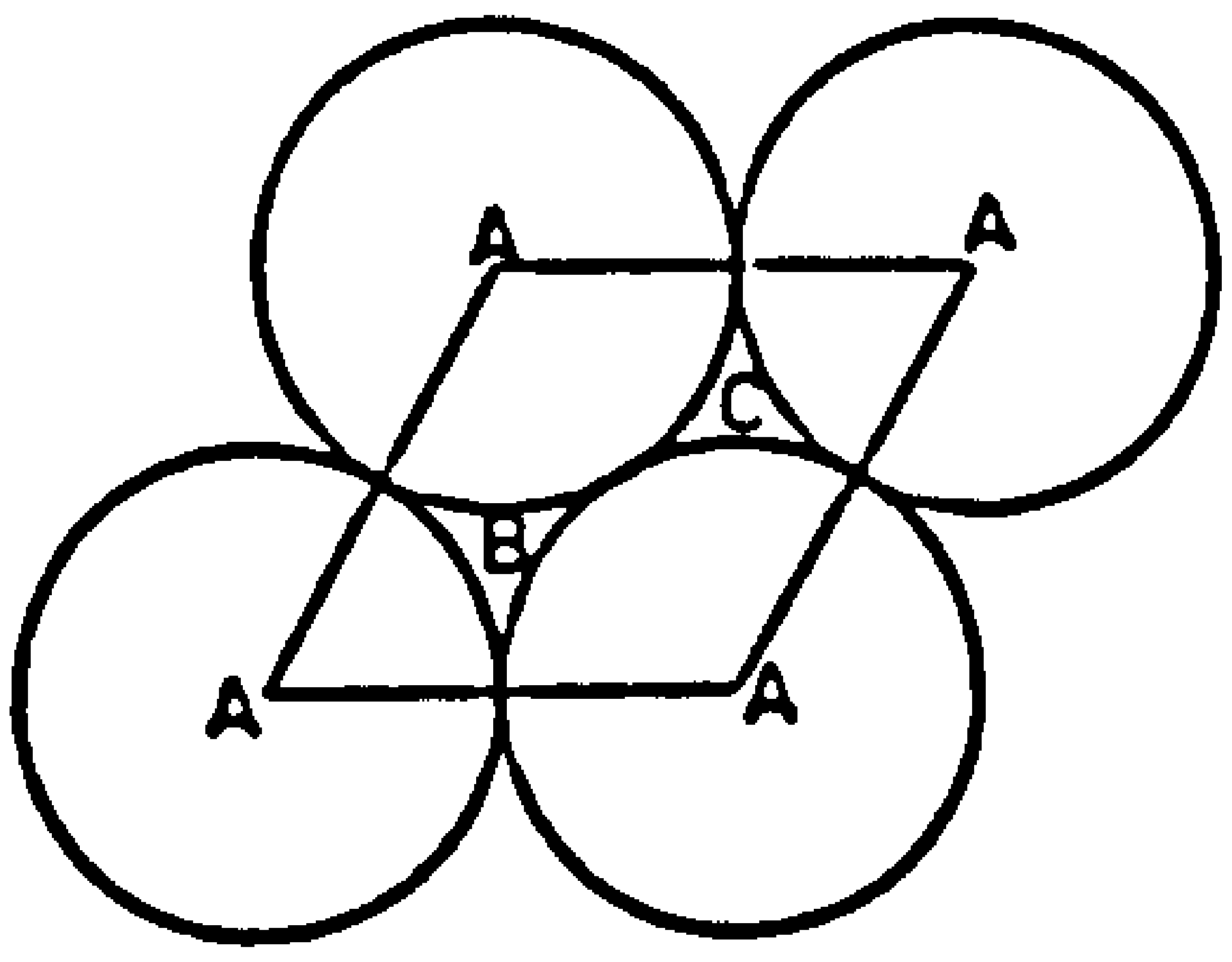

Figure 1.16: The different sites in closest packed MX_2 lattice.

The 1T structure is also the stable one for chalcogenides of Ta and Nb, but only at high temperature. At low temperature, trigonal prismatic co-ordination is adopted. In the 2H form of the group 15 metals, the metal atoms are directly above each other in the form denoted $2H_a$. Such subscripts a, b, c are used to identify differences in the relative displacements of adjacent MX_2 layers. Thus $2H_b$ and $2H_c$ are polytypes where the metal atoms are staggered. Polymorphs containing a large number of MX_2 layers in the unit cell also exist; the 3R polymorph has a stacking sequence of aC | AbA | BcB | Ca. There are also several mixed co-ordination polymorphs which have both octahedral and trigonal prismatic co-ordinated metal atoms. It has been suggested that charge transfer between octahedral to trigonal prismatic units stabilises these structures[92].

The weak cohesive forces permit ready intercalation of a variety of guest species that can be accommodated by a simple expansion perpendicular to the layers. The particular stacking sequence of the layers can also be altered by intercalation. Frequently, the change in inter-layer spacing upon insertion of an atom/molecule between the layers does not correspond to that expected from purely geometric considerations. Although the Δc observed is predominantly geometric in origin, there is also an electronic contribution; as the d band is filled, there may be changes in the dimensions of the MX_2 sandwich itself.

Madelung energies favour occupation of the octahedral interstitial sites over trigonal prismatic[93] sites by 20%. Consequently, the group 14 structures contain transition metal ions with this co-ordination geometry exclusively. However, as electrons are added to the d band, an extra stabilisation arises from adoption of a trigonal prismatic geometry as the dz^2 band is lowered in energy (Figure 1.17).

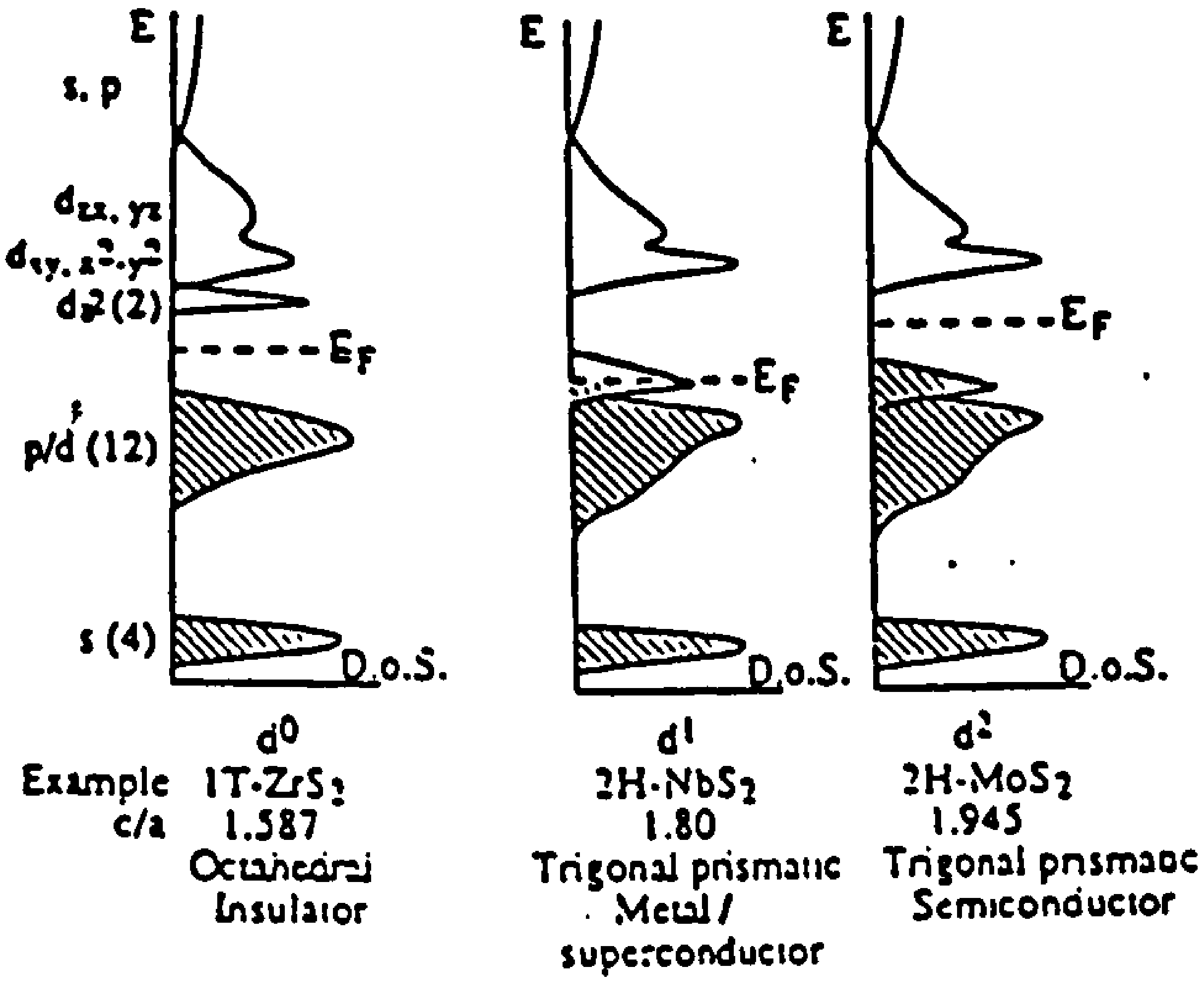

Figure 1.17: Schematic of the band models for Groups 14, 15 and 16 transition metal dichalcogenides.(From Ref 114)

Hence, in the group 15 dichalcogenides, geometries of both types exist, as the Madelung and electronic energies are finely balanced. On moving to group 16 chalcogenides, the trigonal prismatic co-ordination geometry is favoured. Calculated density of states curves support these trends[94].

1.10.1 Structure of MoS_2

MoS_2 exists in several polytypes. The most common is the $2H_c$-MoS_2 in which the metal atoms are trigonally prismatically co-ordinated and staggered along the c axis. The structure of this polytype is shown in Figure 1.18. The band structure of MoS_2 is shown in Figure 1.17. As expected from this band structure, hexagonal MoS_2 is a semiconductor; its conductivity has been interpreted as intrinsic and predominantly n-type[95]. The dz^2 band is filled which results in diamagnetic behaviour. A 3R structure for MoS_2 is also known, in which the molybdenum atoms are octahedrally co-ordinated. Rhombohedral MoS_2 has been prepared by bromine vapour transport[71].

A metastable phase with a distorted layer structure and octahedral co-ordination of the metal atoms has also been reported. The structure has been proposed to be trigonal TiS_2 type with octahedral M^{4+} ions and has been termed 1T-MoS_2[97]. It may be prepared by the oxidation of $K_x(H_2O)_yMoS_2$ ($x=0.3$). It exhibits metallic conductivity and demonstrates an exothermic transition at 90-100°C, as it reverts to the more stable 2H form. The relationship between the unit cells of this polytype and 2H-MoS_2 is $a \approx a_{2H}\sqrt{3}$ and $c \approx ½c_{2H}$.

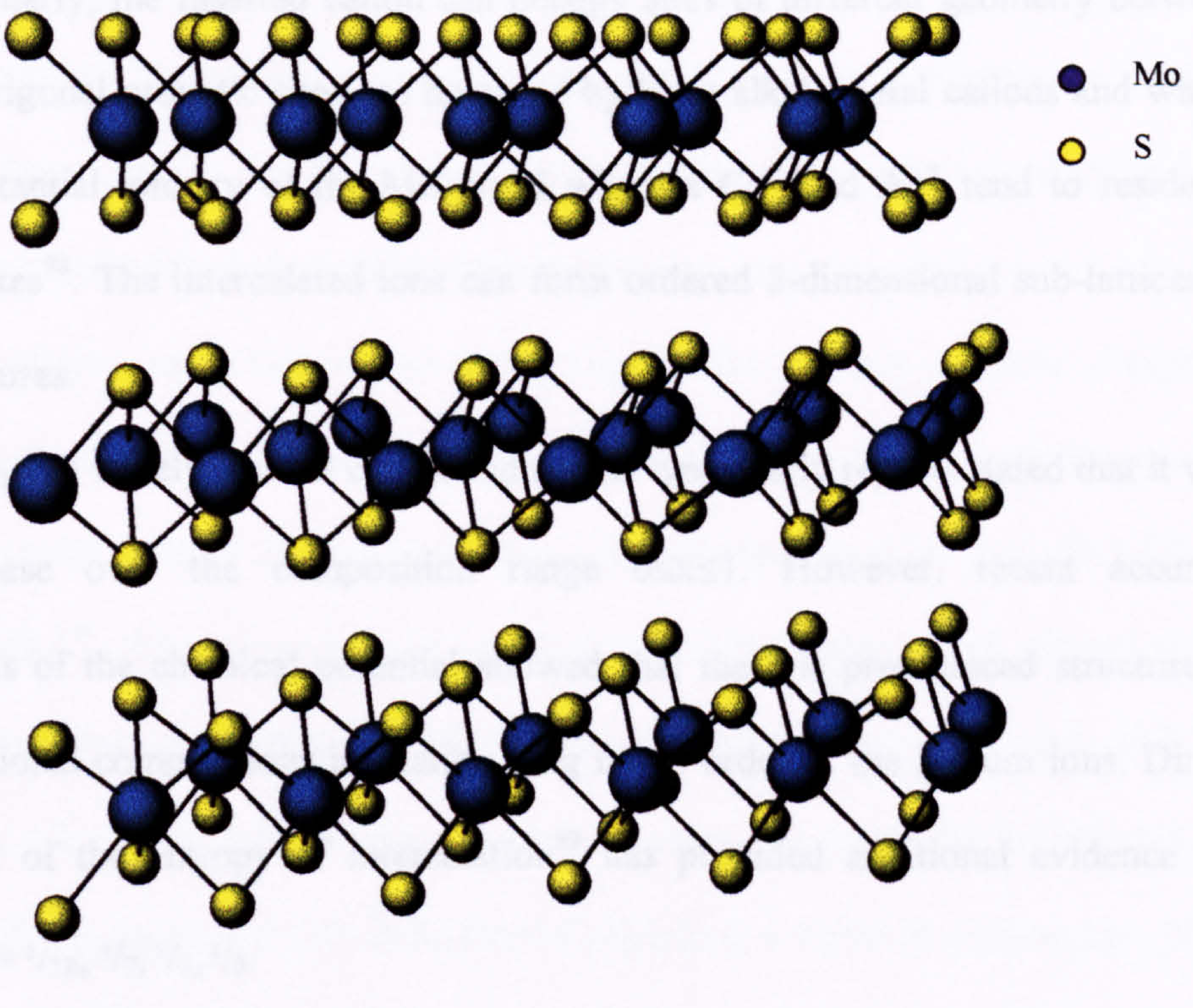

Figure 1.18: 2H-MoS_2

1.11 INTERCALATION COMPOUNDS OF DICHALCOGENIDES

The intercalation compounds of transition metal dichalcogenides can be divided into three classes:-

- Compounds containing metal cations or molecular cations.
- Compounds containing Lewis base type molecules.
- Compounds containing both cations and neutral molecules.

1.11.1 Cation Intercalation

Monovalent cation intercalation compounds AMX_2 (M= Group 14 or 15; X=S,Se) are important as possible electrode materials in solid state batteries. Just as the transition metal ion can adopt a variety of co-ordination geometries within the host structure similarly, the inserted cation can occupy sites of different geometry between the layers. Trigonal primatic sites are favoured by large alkali metal cations and where there is substantial ionicity of the MX bond whereas Cu^+ and Ag^+ tend to reside in tetrahedral sites[98]. The intercalated ions can form ordered 2-dimensional sub-lattices at low temperatures.

$LiTiS_2$ is a widely studied compound of this type. Early reports stated that it was a single phase over the composition range $0 \leq x \leq 1$. However, recent accurate measurements of the chemical potential showed that there is pronounced structure at specific fractional compositions indicating long range order of the lithium ions. Direct measurement of the entropy of intercalation[99] has provided additional evidence for ordering at $x = {}^1/_{12}, {}^1/_7, {}^1/_4, {}^1/_3$.

Interestingly, it has been found that there is not necessarily complete charge transfer between guest and host. With $LiTiS_2$, measurements of the Knight shift and electric quadrupole coupling constant have indicated that quantitative charge transfer does not occur for high values of x. For $LiTiS_2$ itself, only 85% charge transfer is observed[86].

1.11.2 Organometallic Intercalation

A variety of organometallic sandwich compounds undergo intercalation into transition metal dichalcogenides. There is a correlation between the reducing power of the organometallic guest, measured by its first ionisation potential (I.P.) and its ability to intercalate into specific host lattices[100]. For example, $Co(\eta\text{-}C_5H_5)_2$ with an I.P. of 5.56eV will intercalate into both TaS_2 and FeOCl but ferrocene (I.P.=6.88eV) will only intercalate into the more oxidising host FeOCl. However, there are systems which meet the I.P. criterion and yet do not intercalate, for example $(C_6H_6)_2V$ (I.P.=5.2eV) and $(\eta\text{-}C_5H_5)_2MoH_2$, which do not form stable cations. Steric effects may also inhibit intercalation either kinetically or by reducing guest-host or guest-guest π electron interactions, depending on whether the molecular planes of the sandwich compound are parallel or perpendicular to the host layers respectively.

Intercalation may involve electron transfer from guest to host. Magnetic susceptibility measurements[102] have shown this to be quantitative in the cobaltocene and chromocene intercalates of 2H-TaS_2, which can be described as $(CoCp_2)^{+}{}_{1/4}TaS_2{}^{1/4-}$ and $(CrCp_2)^{+}{}_{1/4}TaS_2{}^{1/4-}$. The orientation of unsubstituted metallocenes with respect to the host layers has been the subject of debate. The observed lattice expansion of 5.31Å observed for all simple metallocene intercalates does not immediately indicate the orientation of the guest. For 2H-$TaS_2[Co(\eta\text{-}C_5H_5)_2]_{0.25}$, a variable temperature NMR study strongly indicated that both parallel and perpendicular orientations exist in dynamic equilibrium[101].

A great deal of research activity has been dedicated to these sandwich intercalates since the discovery of their superconducting properties. However, it is now believed that the superconducting behaviour is restricted to the 2-dimensional MX_2 sheets, since there has been a failure to observe an increase in T_c with variation of guest. Two experimental observations have confirmed that interlayer coupling via Josephson coupling between the layers is not involved. Firstly, an increase in Δc of up to 60Å in TaS_2 does not affect T_c. The second stemmed from the isostructural cobaltocene and chromocene intercalates whose lattice expansions are identical. The cobaltocene intercalate is diamagnetic whereas the chromocene intercalate is paramagnetic. Despite the presence of localised magnetic moments on the latter, the intercalates demonstrate virtually identical superconducting properties showing that Josephson coupling is not essential in the superconducting mechanism.

1.11.3 Organic Intercalates

The transition metal dichalcogenides that are capable of acting as hosts to organic Lewis-base molecules are the disulphides and diselenides. The ditellurides form unstable intercalates. N-alkylamines ($C_nH_{2n+1}NH_2$) have been inserted into 2H-TaS_2 for n=1 to 18 by direct reaction[104]. For n up to 4, the c axis expansion is small and constant at ~3.0Å which implies that the hydrocarbon chains are lying parallel to the sulphide layers. For larger values of n, a stoichiometric phase is obtained, $A_{2/3}TaS_2$ where the c axis expansion increases linearly with carbon chain length. For n=4 to n=9, a bilayer structure is present but the alkylamine molecules are tilted at 56° to the c direction. For other values of n, the bilayer is virtually perpendicular to the sulphide layers (Figure 1.19). N-alkylammonium compounds can be prepared for Group 16 via ion exchange reactions with hydrated sodium intercalates e.g $Na_{0.1}(H_2O)_{0.6}MoS_2$. These intercalates also show lattice expansions related to the alkyl chain length, very similar to the behaviour of the n-alkylamine–MX_2 systems.

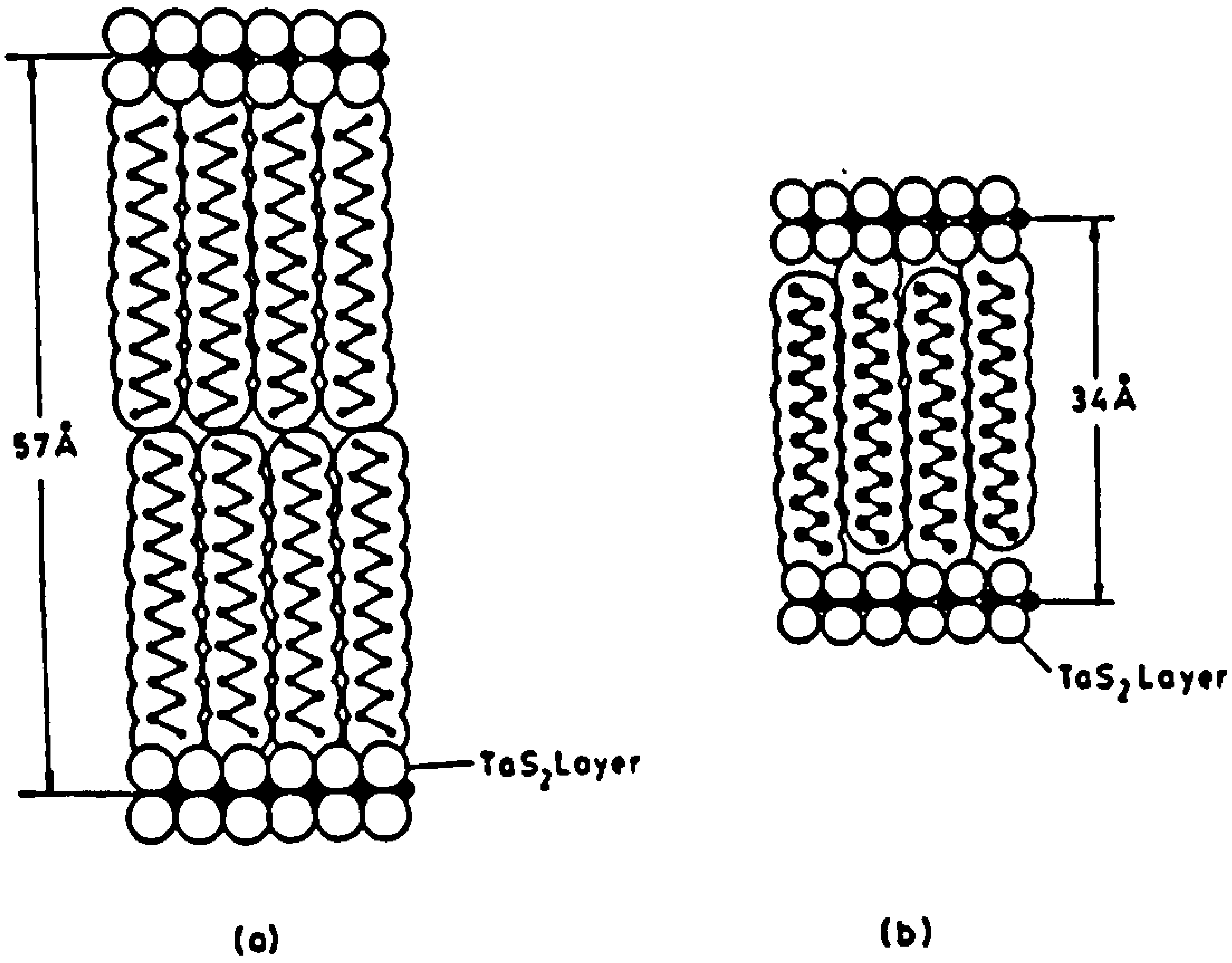

Figure 1.19: Orientation of n-alkylamines in TaS_2 for n>9.

With pyridine as a guest, the limiting composition is $(pyridine)_{0.5}MX_2$ for Ti, Ta and Nb chalcogenides[105]. Of the three orientations available for the pyridine molecule, the one where the long C-N bond is parallel to the dichalcogenide layer is favoured. Pyridine in both $(pyridine)_{0.5}NbS_2$ and $(pyridine)_{0.5}TaS_2$ seems to be ordered in 2-dimensions to give a rectangular superlattice with $2\sqrt{3}a \times 13a$ (a=a of TaS_2). The volume of the supercell indicates that there is one pyridine molecule for every $2\frac{1}{6}$ TaS_2 units. This corresponds to a stoichiometry of $(pyridine)_{0.46}TaS_2$.

Initially, it was thought that the intercalation of these Lewis bases was a simple molecular insertion mechanism; any charge transfer was assumed to be covalent in nature and resulting from either direct or indirect guest-host orbital overlap[106] with retention of the structural integrity of the guest species. This was supported by the observation that a large number of neutral molecules with Lewis base character (e.g. NH_3, aliphatic and aromatic amines and amides, nitrogen heterocycles) could be intercalated thermally into neutral vacant layered dichalcogenides with electronic conductivity. However, ^1H-NMR measurements on $(NH_3)_{1.0}TaS_2$ and $(NH_3)_{1.0}TiS_2$ established the position of NH_3 in the interlayer space with the C_3 axis oriented parallel to the layers[107]. This orientation of the guest molecule does not permit direct overlap of the σ lone pairs of the Lewis base and the orbitals of the host. The INS spectrum is also inconsistent with direct lone pair σ donation.

It has subsequently been proposed[108] that there is some redox chemistry associated with the insertion of these Lewis bases and that a combination of neutral and ionic guest species are incorporated into the host structure; the former interacting with the guest ions via ion/dipole forces. Charge is transferred from the organic molecule to the empty Ti, Hf, Zr or half filled Nb, Ta dz^2 band of the dichalcogenide. Evidence for this comes from measurement of the electric field gradient at Nb in the Nb NMR of $(\text{pyridine})_{0.5}\text{NbS}_2$. This indicates a transfer of 0.2 electrons to the Nb conduction band. Shifts in the nitrogen 1s level from XPS also qualitatively suggest charge transfer to the host. Subsequent studies by Schöllhorn were able to show that a fraction of the guest molecules undergo redox reactions resulting in products cointercalated neutral molecules which interact with the guest ions via ion/dipole interactions[142, 143]. Schöllhorn went on to propose a molecular disproportionation reaction of a fraction of the guest molecules leading to the formation of bipyridine:-

$$x\ \text{pyridine} \rightarrow x/2\ \text{bipyridine} + xH^+ + xe^-$$

$$x\ \text{pyridine} + xH^+ \rightarrow x[\text{py}H^+]$$

$$xe^- + \text{TaS}_2 \rightarrow \text{TaS}_2^{x-}$$

The final product of this scheme is $(\text{py}H^+)_x(\text{py})_{0.5-2x}(\text{bipyridine})_{x/2}[\text{TaS}_2]^{x-}$

A similar reaction shown for the intercalation of ammonia was proposed:-

$$2NH_3 \rightarrow N_2 + 6H^+ + 6e^-$$

$$xe^- + \text{TaS}_2 \rightarrow \text{TaS}_2^{x-}$$

$$H + NH_3 \rightarrow NH_4^+$$

The final product being $(NH_4^+)_x(NH_3)_{1-x}[\text{TaS}_2]^{x-}$

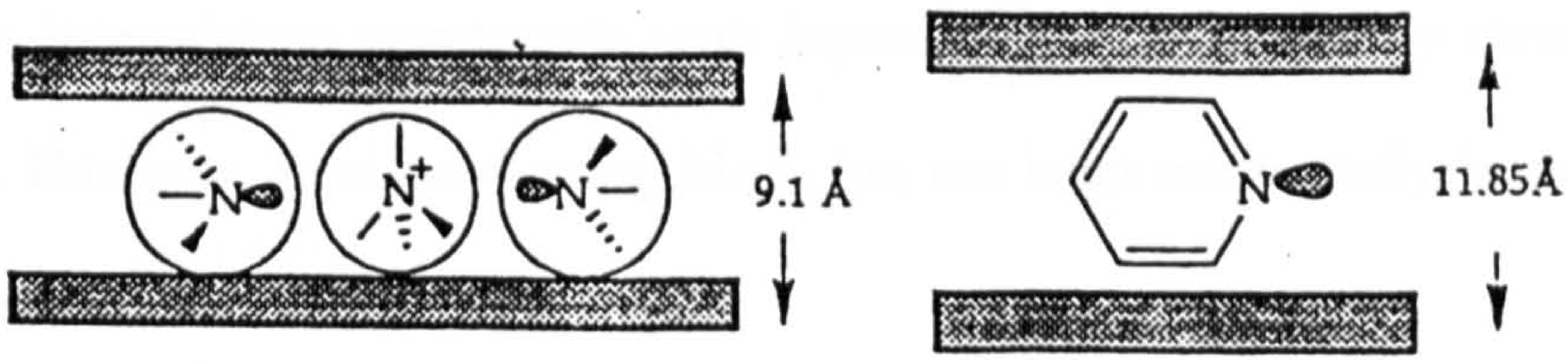

Figure 1.20: Schematic of the orientation of (a) ammonia and (b) pyridine, when intercalated into TaS_2 [after Ref. 5].

Where Lewis bases have low ionisation potentials and are able to form stable radical cations, a less complicated reaction mechanism can be expected. Indirect evidence for this in the case of phenylenediamine has been reported[109].

The most definitive evidence for a simple molecular insertion mechanism into transition metal dichalcogenides has been reported for the ammonia insertion into ZrS_2. This intercalate is single phase[110], of the 3R structure and is formed by exposing the sulphide to anhydrous liquid ammonia. No N_2 or H_2 is released on the intercalation or deintercalation reaction (as measured by evolved gas analysis). This has always been characteristic feature of the ammonia insertion compounds of Ti, Ta and Nb disulphides. Upon deintercalation, stoichiometric NH_3 is released and there is complete regeneration of the original ZrS_2.

1.12 INTERCALATION VIA EXFOLIATION

As has been described in Section 1.6.1, guest molecules have been intercalated into metallic transition metal disulphides, such as NbS_2 and TaS_2, by direct insertion reactions. The intercalation into the semiconducting disulphides is more difficult. The insertion of such reactive species such as the alkali metals results in intercalation compounds that are highly susceptible to decomposition upon exposure to air or moisture. A large variety of inorganic and organic neutral molecular species with Lewis base character (NH_3, hydrazines, amines, heterocycles, N-oxides) are able to form Lewis base intercalation compounds with layered dichalcogenides by direct thermal reaction[111]. However, semi-conducting MoS_2 has not been successfully intercalated by such species via direct reaction.

It has long been known that smectite clays can spontaneously exfoliate in water (separate into individual layers) to form sols or gels depending on the concentration of colloidal particles. Studies of such dispersions have shown them to contain significant concentrations of single layers or isolated chains and it is these entities which can be used in the synthesis of new intercalation compounds, particularly for the insertion of large guest species such as metal chelates[112]. They can also be used for the formation of high surface area materials for applications in catalysis and for the formation of thin film materials.

Application of this procedure has now been extended to a wide range of layered and chain compounds. Table 1.8 shows examples of the range of materials for which the formation of stable colloidal dispersions has been achieved. The layer charge is related to the ease of synthesis; higher layer charges requiring additional modifications to achieve stable dispersions. Stable colloidal dispersions of several classes of compound with layered or chain structures can be prepared by the manipulation of the interlayer or interchain interactions. Although these dispersions are unstable with respect to flocculation (aggregation of the layers or chains), they can be stabilised by the appropriate choice of cation/solvent combination.

Table 1.8: Materials for which exfoliation has been achieved.

Compound	Area Å^2/Charge	Ref
Smectites	40-120	133
Vermiculites	27-40	133
Kaolinites	Neutral	133
Mica	24	133
$M_{1/4}MoO_3$	117	117
$HCa_2Nb_3O_{10}$	28	135
$MFeS_2$	40-60	136
$M_2Mo_6Se_6$	40	137
MoS_2	Neutral	138

There are three general techniques for the formation of these dispersions; chemical exfoliation, mechanical exfoliation and pre-intercalation.

1.12.1 Chemical Exfoliation

Spontaneous exfoliation can occur at low layer charges and with the appropriate interlayer cation and solvent. Montmorillonites consist of stacks of negatively charged aluminosilicate sheets separated by interlayer cations. Hydration of the interlayer region forces the aluminosilicate layers apart and causes the clay to swell. This happens spontaneously in the presence of water. For some clays, the interlayer separation is simply dependent on the electrolyte concentration. For other materials, such as the hydrated alkali metal intercalation compounds of the dichalcogenides, which also form single layer dispersions, solvation in water produces discrete hydrate phases with no further tendency to disperse[113].

Some of the earliest work for the extension of this phenomenon beyond clays, was carried out by Lerf and Schöllhorn on transition metal dichalcogenides. They found that solvated alkali metal dichalcogenides $A^+_x(solv)[MS_2]^{x-}$ exfoliated to form colloidal suspensions under the application of weak shear forces when the solvents had high dielectric constants e.g. N-methyl formamide. Studies of $Na^{+}_{x}(DMF)_{y}[TiS_2]^{x-}$ showed that these dispersions contained negatively charged dichalcogenide layers which could be flocculated by the addition of a trivalent cation. Nazar and Jacobson extended this work to the exfoliation of TaS_2[115]. Initially they formed the intermediate phase $Na_{1/3}TaS_2(solv)_y$ by reducing TaS_2 in a 50/50 mixture of NMF and water, using sodium dithionite. When the solid was placed in NMF and then water (or vice versa), there was immediate swelling and stable dispersions were obtained by sonication of the mixtures, having concentrations between 0.01% to 0.5% weight. Murphy and Hull[116] studied $HTaS_2$, obtained by the electrolysis of 2H-TaS_2 in 1M H_2SO_4. Addition of the hydrogen intercalate to de-ionised water produced a swelling due to the intercalation of water molecules which was found to be reversible as a function of pH. Similar behaviour has been observed for some oxides. For example, $Li_{0.25}MoO_3(H_2O)_y$ exfoliates in water to give a very stable dispersion of reduced MoO_3 layers[117]. The sodium analogue swells in water but does not disperse.

1.12.2 Mechanical Techniques

High intensity ultrasound is known to assist the rate of intercalation. Examples of its effect are given in Table 1.9 below.

Table 1.9: Reduced reaction lengths using sonication methods.

$(Guest)_x$Host	**Reaction Conditions**	
	Thermal	Sonochemical
$(Cp_2Co)_{0.25}ZrS_2$	50h/20°C	2h/20°C
$(RNH_2)_xTaS_2$	50h/20°C	15min/20°C
$(pyridine)_xMoO_3$	30 days/180°C	3 days/80°C

Suslick and Green[118] have reported the effects of ultrasound on the intercalation of guest molecules into layered inorganic hosts. They found that the use of sonication reduced the reaction length to hours rather than days. The actual mechanism by which sonication can cause an increase in the rate of a reaction is not fully understood. It is known that the phenomenon of transient cavitation, the violent collapse of small bubbles during a compression cycle of a sound wave, is necessary. Various effects of this cavitation have been suggested, including direct mechanical cleavage of the bonds, generation of an electric field causing an electrochemical reaction, hot-spot pyrolysis and enhanced solvation of the transition state.

When the reaction between n-hexylamine and TaS_2 was studied more closely[119], it was found that the increased intercalation rate was not due to increased mass transport but an irreversible change in the host. Electron microscopy showed that the immediate effect of sonication is to reduce the particle size from 60-90μm to 5μm within the first 15 minutes. The degree of intercalation reaches its maximum value at this point, implying that this is a major determinant of the reaction length. Sonication has also been found to assist in the process of exfoliation. This appears to be due to the particle size reduction by exposure of the material to weak shearing forces.

1.12.3 Pre-intercalation

The host lattice can be expanded by pre-intercalation of a small molecule or ion to form an intercalation compound which, unlike the original host, will exfoliate. Dispersions of $PbNb_2S_5$ have been prepared[120] by initially treating the $PbNb_2S_5$ with a solution of sodium naphthalide in THF to produce $NaPbNb_2S_5$. When this is reacted with 0.1M HCl, the solid oxidises, hydrogen is liberated and a suspension of dispersed layers of $PbNb_2S_5$ is formed. A similar approach[121] was used for the layered oxide $Zr(HPO_4)_2.H_2O$. Addition of n-propylamine to this material results in the protons undergoing an acid-base intercalation reaction. When 50% of the protons have reacted, the intermediate formed is $Zr(PO_4)(HPO_4)C_3H_7NH_3.H_2O$. This will spontaneously exfoliate in water, but addition of more n-propylamine causes the layers to reflocculate. It is thought that addition of sufficient n-propylamine disrupts the hydrogen bonding between the layers to allow exfoliation, but that going beyond this point results in van der Waals interactions between the alkyl chains, which replace the strong hydrogen bonds but have the same effect. The exfoliation is specific to particular polar solvents, no exfoliation being observed in methanol.

1.13 ORGANIC/INORGANIC HYBRIDS

Many examples of this type of compound have already been mentioned; in particular, the ammonia, pyridine and amine intercalates of the transition metal dichalcogenides. A great deal of work has been carried out on the investigation of low-dimensional inorganic conductive materials owing to their unusual electronic properties. More recently this has extended to organic systems, stimulated by the discovery of the organic metal TTF-TCNQ. However, although, a great deal of technological interest has arisen in organic metals, their application has been limited due to the fragility of the materials as well as difficulties in synthesis and processing. Hence, the investigations have been extended to organic/inorganic hybrid materials in the search for novel electronic and magnetic properties, created by the interaction of the organic and inorganic components.

New low-dimensional materials have been made via the intercalation of organic electron donors TTF, TMTTF, TTN and TTT into FeOCl[122] to form $FeOCl(TTF)_{0.12}$, $FeOCl(TMTTF)_{0.08}$, $FeOCl(TTN)_{0.11}(toluene)_{0.05}$ and $FeOCl(TTT)_{0.11}(toluene)_{0.04}$. In all cases, the tetrathiolene molecule was found to be oriented perpendicular to the layers with the exception of $FeOCl(TMTTF)_{0.08}$ where the TMTTF molecule is oriented parallel to the layers. Two probe conductivity measurements established the conductivity of these intercalates as being 103-105 times greater than that of the pristine host. However, they remain semi-conducting with band gaps of 0.3-0.4eV. IR spectra indicated the presence of radical cations within the layers and Mössbauer spectra are consistent with 4-6% reduction to Fe^{2+} in the host. FeOCl has also acted as host to pyrrole where in-situ polymerisation of pyrrole produces a conducting polymer-inorganic hybrid material[123]. Powder X-ray diffraction revealed that in a similar manner to $(pyridine)_{0.33}FeOCl$, the C_2 molecular plane is perpendicular to the host layers. Thermoelectric power measurements of the material indicate predominant hole transport near room temperature, similar to that of doped polypyrroles.

The aromatic hydrocarbons pentacene, tetracene and anthracene have been intercalated into the metal dichacogenides TiS_2 and TaS_2 and also into graphite[124], by subjecting a suspension of host material and guest species to ultrasound and then leaving at 60° C for one week. For the intercalation compounds of graphite, the resistivity increases on incorporation of the guest and all materials are diamagnetic. Of the intercalates of TaS_2 and TiS_2, $(pentacene)_{0.66}TaS_2$ showed a superconducting transition temperature of 7.05K whereas the other intercalates exhibited either an increase or no change in the resistivity relative to the host material.

All these examples have referred to layered host materials, since these naturally provide the greatest flexibility when attempting to incorporate bulky organic molecules into an inorganic system. Other hosts that are being investigated include zeolites and related phases where Al/Si have been replaced by Be, B, Ga, Ge, Zn and P. This area of work is expanding, as new techniques for synthesising hosts develop combined with the large range of guest species incorporation possible with these wide pore systems[76, 134].

1.14 EXFOLIATION TECHNIQUES AS APPLIED TO MoS_2.

Single layer dispersions of the transition metal disulphide MoS_2 (denoted as $\{MoS_2\}_{exf}$ in this work) have been produced by the intercalation of lithium followed by exfoliation in water. The interlayer interactions have been manipulated to the extreme case of separating the layers into discrete units. The individual structural elements completely disperse to form colloidal suspensions containing highly anisotropic particles and a significant number of individual layers. As such, this is the limiting case of lattice expansion when the S-M-S layers have been separated completely. These suspensions have been used for the formation of novel intercalation compounds by addition of the guest species to the colloidal dispersion of single layers, followed by flocculation of these layers, trapping the guest species in between the S-M-S slabs in the process. It has been found to be a particularly useful technique for the incorporation of large guest species such as organic molecules. This method of exfoliation provides a novel route to the synthesis of intercalation compounds of MoS_2. It affords access to materials containing molecules that are neither electron donors or Lewis bases, both of which have hitherto been prerequisites for guest species to be incorporated into MoS_2.

This method has been successfully applied to the insertion of sterically disfavoured molecules such as those investigated by Kanatzidis and co-workers[125]. They successfully made a family of new materials based on layered transition metal dichalcogenides of the type $[Co_6Q_8(PR_3)_x]_y[MoS_2]$ where Q=S, Se, Te and R=Et, Bu, Ph. Magnetic susceptibility data indicated Curie-Weiss law behaviour and their electrical conductivity data showed semiconducting behaviour. Preliminary variable temperature thermopower data from two of the intercalates suggest that the predominant charge carriers in these materials are holes.

Other species that have been incorporated into MoS_2 using the technique of exfoliation-flocculation include substituted aromatics, metallocenes and polymers. This technique has also allowed intercalation at room temperature of alkylammonium and phenanthrolinium ions, and transition and rare earth metal cations. It was found with 1,10-phenanthroline, studied over the pH range 0-11, that only protonated phenanthroline initiates flocculation of the MoS_2 dispersion[126]. The transition metal and rare earth ions caused immediate flocculation on addition to the suspension of MoS_2. The resulting intercalation compounds have interlayer spacings between 4.9Å and 11.5Å, implying that insertion of the hydrated cations occurs[127]. Magnetic data indicate that Ni and Co intercalates contain octahedral divalent ions, Co(II) being in the high spin state[128].

This technique has been used to intercalate the more bulky ferrocene and substituted derivatives[129]. These show a systematic increase in the interlayer expansion with increase in bulk of the substituent. It was proposed that the ferrocene molecule is oriented with the C_5 axis perpendicular to the MoS_2 layers. In contrast, when inserting ruthenium cationic complexes, on the basis of powder X-ray diffraction and EXAFS, the arene ligands in $[(arene)Ru(H_2O)_3]SO_4$ cationic complexes were reported as being oriented perpendicular to the MoS_2 layers.

One of the most interesting areas currently being investigated is that of apparently neutral species which are poor electron donors being inserted into MoS_2. Amongst this group in particular, the insertion of polymers is producing compounds which show interesting electronic and mechanical properties. Bissessur and co-workers inserted poly-ethylene oxide (PEO), poly-propylene glycol (PPG), methylene cellulose and other high molecular weight polymers into MoS_2[131]. They observed semi-conducting behaviour for $(PEO)_{0.92}MoS_2$, but corresponding thermoelectric power measurements indicated that the material was a p-type metallic conductor. Magnetic susceptibility data confirmed the metallic character after temperature independent Pauli-like behaviour from 50-300K was established. Electrical conductivities of 0.1 and 0.2

Scm^{-1} were obtained for the $(PEO)_xMoS_2$ and $(PPG)_xMoS_2$ compounds at room temperature. The work of Lemmon and Lerner[132] confirmed the semi-conducting nature of the $(PEO)_xMoS_2$ intercalate in their work. They also examined the polymer extracts by GPC, which indicated that the polymer had not fragmented to low molecular weight sections, although evidence for crosslinking was present.

1.15 AIMS OF THIS WORK

The aims of this work were two-fold. Firstly, the project sought to extend the applicability of the exfoliation-reflocculation route to an investigation of intercalates containing molecules with large π electron densities. The molecules to be investigated are poor electron donors with considerably less functionality than those previously utilised as guest species. MoS_2 was chosen as the host material, since the intercalation chemistry using traditional techniques of this semi-conductor is limited. The project sought to expand the intercalation chemistry of this host to a new area in an effort to produce materials with interesting structural, electrical and magnetic properties. Hence, this thesis describes the successful synthesis and initial characterisation of intercalation compounds of MoS_2 containing small, electron-rich organic molecules, some of which are both poor electron donors and non-polar.

The second broad aim of the project was to investigate the potential of a relatively new technique, neutron Compton scattering, for the study of the dynamical properties of intercalated species, initially using $LiTiS_2$ as a model system. The project sought to extend the applicability of the technique from relatively simple atomic and molecular systems to species in more complex chemical environments. Data collected on a variety of systems provided an opportunity to assess the nature and quality of the information provided by neutron Compton scattering in comparison with complimentary techniques.

Chapter Two

Experimental

2.1 INTRODUCTION

This chapter describes the preparation of starting materials, the techniques used for compositional analysis and the instrumental methods for the measurement of physical properties. It concludes with an account of the theory and experimental procedure for the less routine techniques of Extended X-ray Absorption Fine Structure (EXAFS) and Incoherent Inelastic Neutron Spectroscopy (INS).

2.2 PREPARATIVE ROUTES TO STARTING MATERIALS

2.2.1 MoS_2 Synthesis

2H-MoS_2 was prepared by combination of the elements Mo (Aldrich 99.9%) and S (Alfa 99.99%) in an evacuated silica tube (10^{-4} Torr) at 1150°C for 5 days, with regrinding of the sample after 48 hours. The product was characterised by powder X-ray diffraction and the sulphur content was determined using thermogravimetric analysis.

2.2.2 $LiMoS_2$

$LiMoS_2$ was prepared by adding three equivalents of 1.6M n-butyllithium to a dispersion of 2H-MoS_2 in distilled 60-80 petroleum ether and stirring for 48 hours under N_2. The product, Li_xMoS_2, was washed with several 20ml portions of petroleum ether, dried under vacuum and stored in a glove box. The product was characterised by powder X-ray diffraction and flame emission spectroscopy.

2.2.3 Intercalation of Organic Guests

Optimum conditions for the intercalation of organic guests into MoS_2 were initially established using naphthalene as the guest species. Reaction variables such as concentration of reactants, molar ratio of reactants, use of sonication, pH conditions and reaction length, were varied systematically in order to establish the following general procedure. Sufficient de-ionised water was added to a preweighed sample of Li_xMoS_2 (~0.5g) under N_2 to produce a suspension of 0.08mg/ml exfoliated MoS_2 (denoted $\{MoS_2\}_{ext}$). This suspension was placed in an ultrasound bath for 30 minutes. A solution of naphthalene in dichloromethane was added and the mixture stirred for 24 hours under N_2. Sufficient 6M HCl was added to reduce the pH to below 2 (tested using universal indicator paper). The reaction was then stirred at ambient temperature for periods between 24 hours and 3 weeks. The solid was separated, washed with three portions of de-ionised water and three portions of dichloromethane and dried under vacuum. Initial products were transferred to a dry nitrogen box until it was established that the materials produced were not air sensitive. No previous reports of air sensitivity of similar materials have been made. This procedure was extended to the intercalation of other organic guests by introducing the guest species as a solution in dichloromethane.

2.3 STRUCTURAL AND COMPOSITIONAL CHARACTERISATION

2.3.1 Powder X-ray Diffraction

Powder X-ray diffraction performed on a Philips PA 2000 diffractometer was used for initial characterisation of products. Samples of approximately 50mg were finely ground and loaded into aluminium holders in air. A gas-tight holder was used for air-sensitive samples, the sample being mounted in a dry nitrogen glove box.

Data were collected between 5 and 100° (2θ) using CuK$_\alpha$ radiation (λ=1.5418Å). A step-scan method with an increment of 0.05° in 2θ and a counting time of 1s was used for routine identification of samples; for the determination of lattice parameters the scan conditions were altered to an increment of 0.02° and a counting time of 5s. For the calculation of lattice parameters, accurate peak positions were determined using the "Peak Fit" routine contained in the Philips PC-APD software, lines were indexed and the lattice parameters were refined using the program "Cellref"[80] which minimises the function

$$M = \Sigma_i \left[\omega_i \left\{\sin^2\theta_{i(obs)} - \sin^2\theta_{i(calc)}\right\}^2\right] \qquad (2.1)$$

where the weighting factor ω_i was set to unit.

2.3.2 Infra-Red Spectroscopy

Infra-red spectra were recorded for analytical and/or diagnostic purposes using a Nicolet 400 FT-IR spectrometer. A small amount of sample of approximately 10mg was ground with dry CsI and the mixture pressed into a 13mm pellet using a Specac pellet press. Data were collected between 400 and 4000cm^{-1} at a resolution of 4cm^{-1}.

2.3.3 Chemical Analysis

Determination of sulphur and water content was carried out by thermogravimetric analysis using a Du Pont 951 TGA. For thermogravimetric analysis, samples of 5-10mg were loaded into a Pt boat and heated up to 1000°C under flowing air. For the determination of the organic intercalate content, a combination of TGA and CHN microanalysis was applied. Samples were submitted to the departmental CHN microanalysis service for determination of carbon and nitrogen content. Instrument limitations resulted in the percentage of hydrogen in the sample being quoted as $x\pm0.3\%$.

Since for most products, the actual hydrogen content was in the region of 0.20-0.80%, the %H determinations from CHN microanalysis were therefore not used in calculations of organic content.

Atomic absorption spectroscopy and flame emission spectroscopy were carried out for the determination of V and Li respectively, on a Pye Unicam spectrometer with a calibration range of 10-100ppm. A known mass of sample was dissolved either in 20% HNO_3 or 20% HCl and the solution diluted to a concentration of approximately 10ppm.

2.4 STUDIES OF PHYSICAL PROPERTIES

2.4.1 Magnetic Susceptibility Measurements

Magnetic susceptibility measurements were carried out on crystalline MoS_2 and the intercalated materials. Prolonged instrument failure prevented measurements for the complete series of organic intercalation products.

An Quantum Design MPMS SQUID magnetometer was used to measure the magnetic susceptibility of samples between 5 and 300K. Accurately weighed samples of between 50-100mg were placed in a weighed diamagnetic gelatin capsule. The capsule was then inserted into a plastic drinking straw and the straw attached to a 1.6m stainless steel rod which was lowered into the cryostat. Data were collected over the temperature range $5 \leq T/K \leq 300$ in 5K and 10K intervals both after cooling the sample in zero field (ZFC) and after cooling the sample in the measuring field of 1000G (FC). A schematic of a SQUID magnetometer is shown in Figure 2.1.

The experimental quantity measured on the SQUID is the magnetisation, M_{raw}, of the sample. This can be expressed as

$$M_{raw}=MV \qquad (2.2)$$

where M= magnetisation per unit volume, V= volume of sample

The raw data were corrected for the intrinsic diamagnetic contribution to the magnetisation, κ, of the sample holder and for the diamagnetic contribution to the susceptibility arising from the inner full electron shells of the ions present, χ_{dia}. The molar susceptibility was calculated using the equation below.

$$\chi_{molar} = \frac{M_{raw} - \kappa}{Hm} - \chi_{diamagnetic} \qquad (2.3)$$

where χ= susceptibility per unit volume

H= magnetic field strength

m= moles of sample present

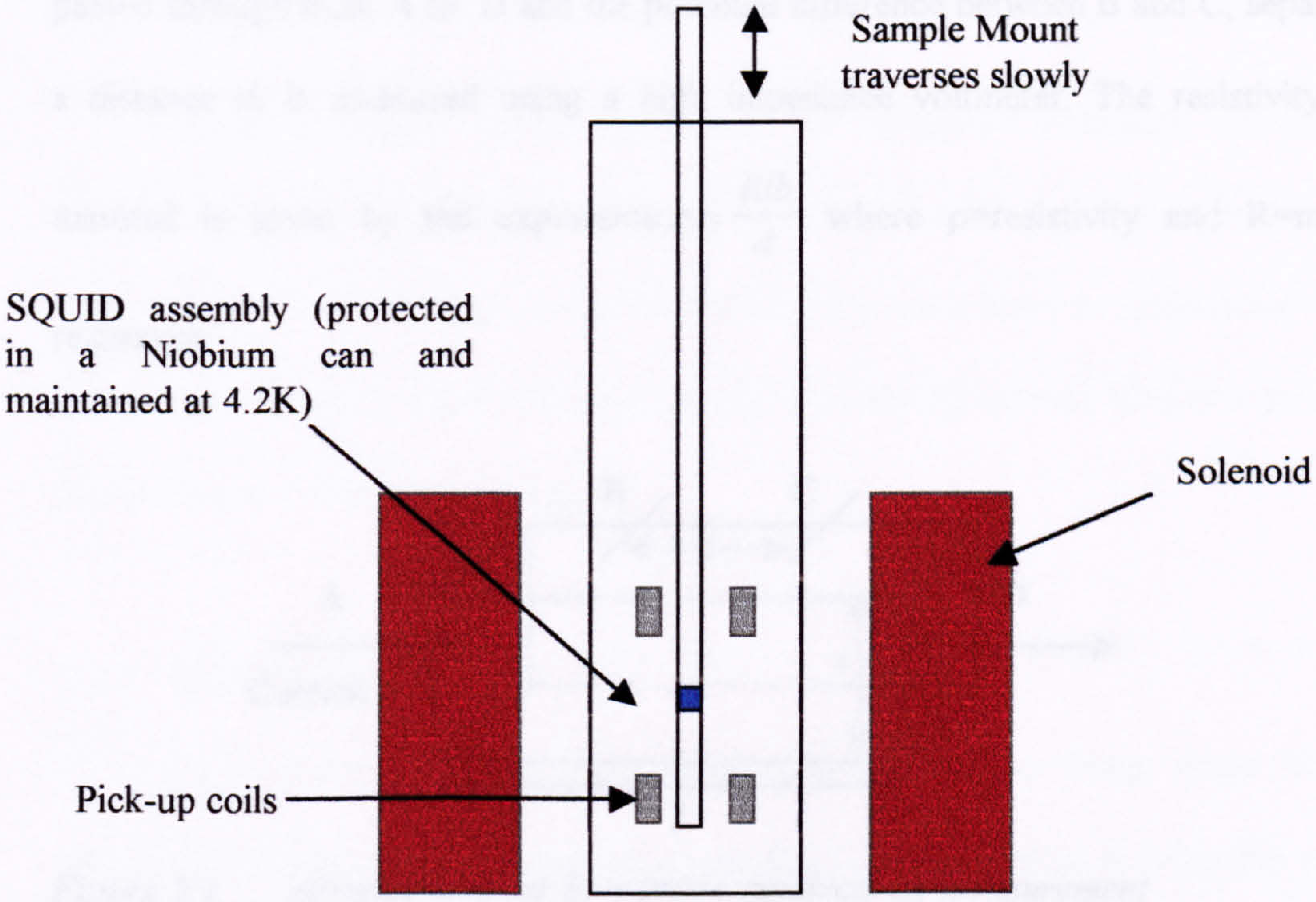

Figure 2.1 Schematic of a SQUID Magnetometer

2.4.2 Four Probe Conductivity Measurements

The transport properties of the products from intercalation of MoS_2 were investigated using 4-probe D.C. conductivity. Such measurements provide information about the nature of the electronic structure of the material.

The conductivity of a material is given by the product of the number of carriers, *n*, and their mobility, μ.

$$\sigma = ne_0\mu \qquad (2.4)$$

where e_0 is the charge on the carrier, which may be positive or negative. A schematic diagram of the experimental set-up is shown in Figure 2.2. A rectangular pellet of the material under study was cut, with effective length *l*, width *b* and thickness *t*. Current is passed through from A to D and the potential difference between B and C, separated by a distance *d*, is measured using a high impedance voltmeter. The resistivity of the material is given by the expression $\rho = \frac{Rtb}{d}$ where ρ=resistivity and R=measured resistance

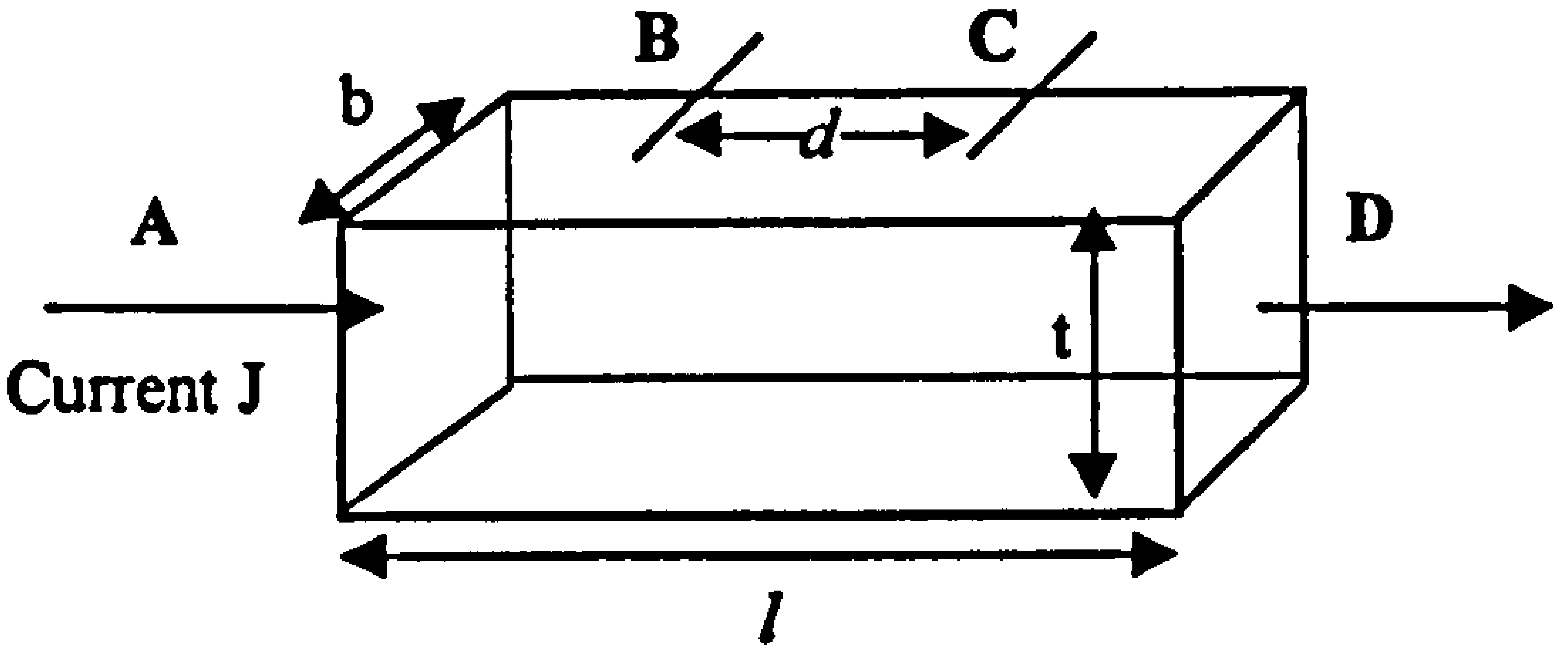

Figure 2.2 Arrangement for four probe conductivity measurement

The rectangular pellet was prepared by pressing the sample in a Specac press under a pressure of 8 tons. For the measurements of crystalline MoS_2, the polycrystalline pellet was then sintered at approximately 75% of the original firing temperature in a evacuated silica tube for 12 hours to improve densification and reduce grain boundary effects. Ambient temperature intercalation compounds however could not be sintered and a rectangular ingot was cut from these pellet. Electrical connections to the pellet were made by means of four 50μm silver wires and attached to the ingot via conducting silver paint. The wires near each end of the pellet acted as the current leads (A and D) while the two contact wires (B and C) were used to measure the potential difference. The pellet was mounted onto a four-pin DIL socket which was placed in an Oxford Instruments CF1200 continuous flow cryostat, using helium or nitrogen as the cryogenic liquid, and connected to an ITC 502 temperature controller. Resistances were measured with a HP34401A multimeter over the temperature range $10 \leq T/K \leq 300$. Data collection was computer controlled.

2.5 EXAFS

Three materials were investigated by EXAFS: restacked MoS_2, MoS_2 intercalated with naphthalene and MoS_2 intercalated with 2-methylnaphthalene. Data were collected and analysed at the SRS, Daresbury Laboratory in conjunction with Dr. R. Strange. Access to the facility was through the DARTS scheme (Daresbury Analytical Research and Technology Service).

2.5.1 EXAFS Theory

X-ray absorption spectra are usually produced in the energy range 200-35000 eV. In this energy range, the main process for X-ray absorption is when the photon is completely absorbed and a core photoelectron is ejected from the absorbing atom, leaving behind a core hole. This excited atom with a core hole may produce further excitation, but in the simple picture this possibility is ignored. The photoelectron will be ejected with an energy equal to the energy of the incoming photon, denoted hν in Equation 2.5, less its binding energy E_0 when in the core.

$$E=h\nu-E_0 \qquad (2.5)$$

This photoelectron interacts with the surrounding atoms in the solid which act as secondary sources of scattering for the photoelectron. Interference effects occur between the out-going photoelectron wave and the back-scattered waves. There is an interference effect on the final state of the photoelectron. Since the absorption coefficient is related to the transition probability between the initial and final state, the interference affects the absorption coefficient. The interference depends upon the phase of the back-scattered wavefunction and so is affected by the phase-shift associated with the back-scattering and hence the distances between the central atom and its neighbours. A change in the kinetic energy of the photoelectron changes its wavelength and thus the phase associated with the backscattered photoelectron at the central atom will alter with the energy of the incoming photon. As a result, the absorption exhibits a periodic modulation when plotted against the electron momentum. From this, information regarding the distances of the back scattering atoms from the central atom and its co-ordination environment can be determined. The application of EXAFS is primarily for the determination of the local environment of an atom; it does not depend therefore on long range crystalline order and so can be applied to poorly crystalline and amorphous materials.

The magnitude of the fine structure of the X-ray absorption spectrum can be expressed as a function of the photoelectron wavevector, *k*.

$$\chi(\vec{k})=\sum_m S_i(\vec{k})\left(\frac{N_m}{\vec{k}a_m^2}\right)\left|f_m(\pi,\vec{k})\right|\exp\left(-2\sigma_m^2\vec{k}^2\right)\exp\left(\frac{-2a_m}{l_m(\vec{k})}\right)\sin\left(2\vec{k}a_m+2\delta_l(\vec{k})+\vartheta_m(\vec{k})\right) \qquad (2.6)$$

N_m is the co-ordination number, a_m is the distance and $f_m(\pi,k)$ is the backscattering amplitude of the neighbouring m^th atom; $S_i(k)$ is an amplitude reduction factor to account for energy loss due to shake up processes caused by multiple excitations at the central atom; $\exp\left(\frac{-2a_m}{l_m(k)}\right)$ is a damping factor dependent on the ratio of the distance travelled,

$2a_m$, to the electron mean free path, $l_m(k)$. These two terms approximate to accounting for the amplitude lost though inelastic scattering; $\exp\left(-2\sigma_m^2 k^2\right)$ is a Debye-Waller factor to account for the static disorder of the atoms and also the thermal vibration of the atoms. Finally, $\delta_l(k)$ is the central atom phaseshift and $\theta_m(k)$ is the phaseshift caused by the neighbouring atom.

2.5.2 EXAFS Experimental

The SRS operates with an electron energy beam of 2GeV and an average current of 150mA. Mo K-edge data were collected in transmission mode on station 9.2. A Si(220) double crystal monochromator was used, detuned to reject 50% of the signal in order to minimise harmonics. The monochromator angle was calibrated by running an edge scan for a 5μm Mo foil before the samples were measured. Ionisation chambers, filled with a mixture of Ar and He at appropriate partial pressures to optimise detector sensitivities, were placed in the beam path in front of and behind the sample to measure the ionization counts (I_0 and I_t) before and after the X-rays passed through the sample. The samples were partially diluted with boron nitride powder to reduce absorption to a satisfactory level, ground and smeared onto Sellotape™. Data collection was carried out at room temperature; four scans were recorded at the Mo K- absorption edge for each sample in the range from 200eV below the edge to 700ev above.

2.5.3 Data Analysis

The programs EXCALIB, EXBACK and EXCURV92 were used to analyse the data[81]. The four scans recorded for each sample were summed using the program EXCALIB to give a high quality averaged spectrum. The monochromator angles were converted to the corresponding X-ray energy and the absorbance from the ion chamber readings were calculated as $\log_e(I_0/I_t)$.

A smooth background was subtracted from the data using EXBACK. The energy was first rescaled around a point E_0 on the absorption edge, taken as the first maximum in the first derivative of the raw data. A pre-edge polynomial was fitted to the data points in the pre-edge region (below E_0) and this was subtracted from the data. A post-edge polynomial, of third order, was fitted through the post-edge region and subtracted. This removed the effect of the slowly varying background from the quickly varying oscillations due to the EXAFS.

The EXAFS data, thus isolated, were analysed using EXCURV92, employing the spherical wave approximation. Phase-shifts were derived from ab-initio calculations using Hedin-Lundqvist potentials and von Barth ground states. The theoretical fits were obtained by adding shells of back-scattering atoms around the central absorbing atom and adjusting the Fermi energy, E_f, the absorber-scatterer distances, a, the Debye-Waller factor, $2\sigma^2$, and the co-ordination numbers, N, in an iterative manner. Least squares refinements of the structural parameters were carried out against the k^3 weighted EXAFS signal to minimize the fit index FI: χ^{theory} and χ^{expt} are the experimental and theoretical EXAFS respectively.

$$FI = \sum_i \left(\vec{k}^3\left(\chi_i^{theory} - \chi_i^{expt}\right)\right)^2 \qquad (2.7)$$

The results of the least squares refinement are reported in terms of the discrepancy index where

$$R = \left(\int\left|\left(\chi^T(\vec{k}) - \chi^E(\vec{k})\right)\right|\vec{k}^3 dk \Big/ \int\left|\chi^E(\vec{k})\right|\vec{k}^3 dk\right)\times 100\% \qquad (2.8)$$

2.6 INELASTIC NEUTRON SCATTERING

TFXA (Time Focused Xtal Analyser) is an inverse geometry time-of-flight spectrometer with a time-focusing analyser operated at a fixed energy of ca. 4meV, situated at the ISIS pulsed neutron spallation source, Rutherford Appleton Laboratory. This instrument was used to obtain the inelastic neutron scattering (INS) spectrum of the intercalation compound $(C_{10}H_8)_{0.15}MoS_2$, restacked MoS_2 and naphthalene in order to investigate the dynamical properties of the guest in the intercalation compound.

A schematic of the TFXA spectrometer is shown in Figure 2.3. A moderated white beam of neutrons is incident on the sample and a fraction of the incident neutrons are scattered inelastically by the sample.

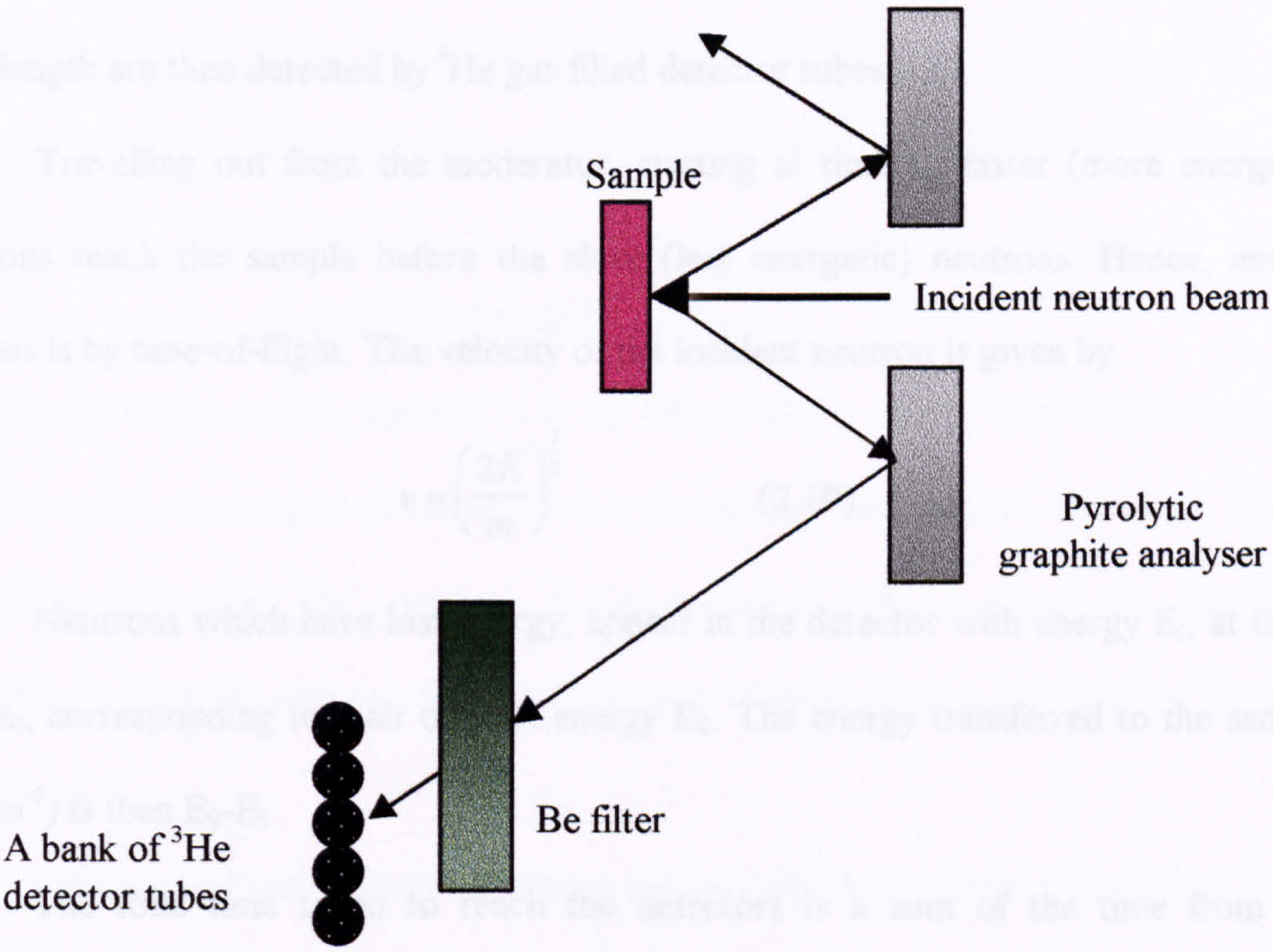

Figure 2.3: Path of Incident Neutron Beam on TFXA. The instrument is symmetric about the sample position.

Neutrons which are backscattered through an angle of 135° are incident on a graphite crystal which is aligned such that Bragg scattering from the 002 planes of graphite. From Bragg's law:

$$n\lambda = 2d\sin\theta \qquad (2.9)$$

where d is the interplanar distance in the crystal

λ is the wavelength of the scattered neutron

θ is the angle of incidence on the graphite crystal

Since d and θ are constant, only one wavelength (and its higher harmonics) are scattered from the graphite analyser. After the graphite analyser, there is a Be filter which absorbs neutrons at multiples of the fundamental wavelength. Neutrons of the fundamental wavelength are then detected by ^{3}He gas filled detector tubes.

Travelling out from the moderator, starting at time t_0, faster (more energetic) neutrons reach the sample before the slow (less energetic) neutrons. Hence, energy analysis is by time-of-flight. The velocity of the incident neutron is given by

$$v = \left(\frac{2E}{m}\right)^{\frac{1}{2}} \qquad (2.10)$$

Neutrons which have lost energy, appear in the detector with energy E_f, at times after t_0, corresponding to their original energy E_0. The energy transferred to the sample E_T (cm^{-1}) is then E_0-E_f.

The total time taken to reach the detectors is a sum of the time from the moderator to the sample, t_i, and the time taken to move around the analyser, t_f, so that

$$T = t_i + t_f = \frac{L}{v_i} + \frac{l}{v_f} = L\sqrt{\frac{m}{2E_0}} + l\sqrt{\frac{m}{2E_f}} \qquad (2.11)$$

The energy transferred to the sample is E_T=E_0-E_f. From, E_f, L and *l*, which are all known hence E_0 is can be calculated by measuring the time-of-flight and the energy transfer can be determined. The resulting spectrum is the inelastic neutron scattering spectrum of the sample. The total number of neutrons detected i.e. the band intensity depends on several instrumental factors and the sample's Scattering Law, S(Q, ν). The Scattering Law can be written as

$$S(Q, \nu) = Q^2.U^2\exp(-Q^2.U^2) \qquad (2.12)$$

This gives the intensity, S, of a vibrational transition with an energy transfer ν(cm^{-1}) observed with neutron momentum transfer of Q(Å^{-1}). U^2(Å^2) is the mean square amplitude of the scattering atom in the mode at ν. The chance that a particular nucleus will scatter a neutron is given by the incoherent cross-section, σ_{inc}, of the atom. This is an experimentally determined parameter and it is dependent on a given isotope. Its value is unrelated to any other nuclear property. Thus the intensity of an INS band is proportional to

$$I_i \propto Q^2 U_i^2 \exp\left(-Q^2 U_{total}^2\right)\sigma_{inc} \qquad (2.13)$$

The exponential term in Equation 2.13 is the Debye-Waller factor. One variable which in part determines the magnitude of this term is the thermal motion of the molecule. During the TFXA experiment, the sample is cooled to below 50K to reduce this effect. By reducing the thermal energy of the nuclei, only neutron energy loss spectra need be considered.

Whereas in IR or Raman techniques the intensity derives from the changes in the dipole moment or polarisability of the molecule during the vibration, in INS the intensity of a mode is strongly weighted by σ_{inc}. For hydrogen, σ_{inc} is very high at ~80 barns but for most other elements it is below 5 barns. Thus all molecular vibrations are "neutron active" and modes are seen which involve motion of hydrogen, either directly or if hydrogen is attached to a vibrating atom. Thus the INS spectrum is different in appearance from either IR or Raman spectra. TFXA records spectra in the range 16-4000cm^{-1} with a resolution of ~2% of the energy transfer.

The high incoherent scattering cross-section of hydrogen was exploited in the measurement of the INS spectrum of $(C_{10}H_8)_{0.15}MoS_2$ as this compound contained approximately 25 atom% of hydrogen and modes which involved significant hydrogen displacements were found to dominate the spectrum. However, because the synthetic procedure was known to result in trace amounts of water not associated with the guest, the INS spectrum of MoS_2 reflocculated in the absence of naphthalene was also recorded for use as a background. A spectrum of pure naphthalene was also recorded in order to provide comparison with the intercalated material.

All samples were pre-weighed. This was to enable spectra to be normalised with respect to hydrogen prior to subtraction of a background spectrum. The samples were then transferred to aluminium sachets. These were attached to the end of the sample stick and cooled to 20K in a closed cycle refrigerator.

Chapter Three

Intercalation of Naphthalene into MoS_2

3.1 INTRODUCTION

This chapter describes the synthesis and characterisation of an organic/inorganic nanocomposite material formed from the incorporation of naphthalene into MoS_2. The synthesis was carried out via "single" molecular layers of the host, produced through the technique of exfoliation. As described in Chapter 1, this involves reaction of a colloidal dispersion of the layered host with a solution containing the guest species. The successful application of this method to the intercalation of naphthalene into MoS_2 is described here. Extension of this work to the insertion of naphthalene derivatives and other aromatic ring systems is described in the following chapter.

Initial studies were directed towards the formation of single layer MoS_2. This was followed by efforts to optimise the reaction conditions required for intercalation of naphthalene. The work continued to structural studies of the product material obtained and to measurements of its physical properties. This investigation illustrates that guest species which are both poor electron donors and non-polar may be introduced by this method.

3.2 MoS_2

At an early stage, magnetic susceptibility measurements indicated that commercial MoS_2 contained paramagnetic impurities. Therefore it was necessary to prepare MoS_2, which was subsequently shown to be diamagnetic and could be used as a starting material for all reactions. The powder X-ray diffraction pattern for MoS_2 synthesised by the author is shown in Figure 3.1. Data were indexed on the basis of a hexagonal unit cell and refined lattice parameters of a=3.1620(2)Å , c=12.3000(3)Å were obtained, in agreement with the literature values for of 2H MoS_2[82]. The 103 and 105 reflections of the prepared MoS_2 are slightly broadened relative to those of the commercially supplied material. Repeated firings at 1423K sharpened these lines to the limit observed in Figure 3.1. Stacking faults originating from random orientation of some layers perpendicular to the c axis cause this weakening and broadening of the h0k reflections. Thus this material may be described as hexagonal MoS_2 with a small number of stacking faults. A stoichiometry of $MoS_{2.01(4)}$ was determined by TGA under flowing oxygen.

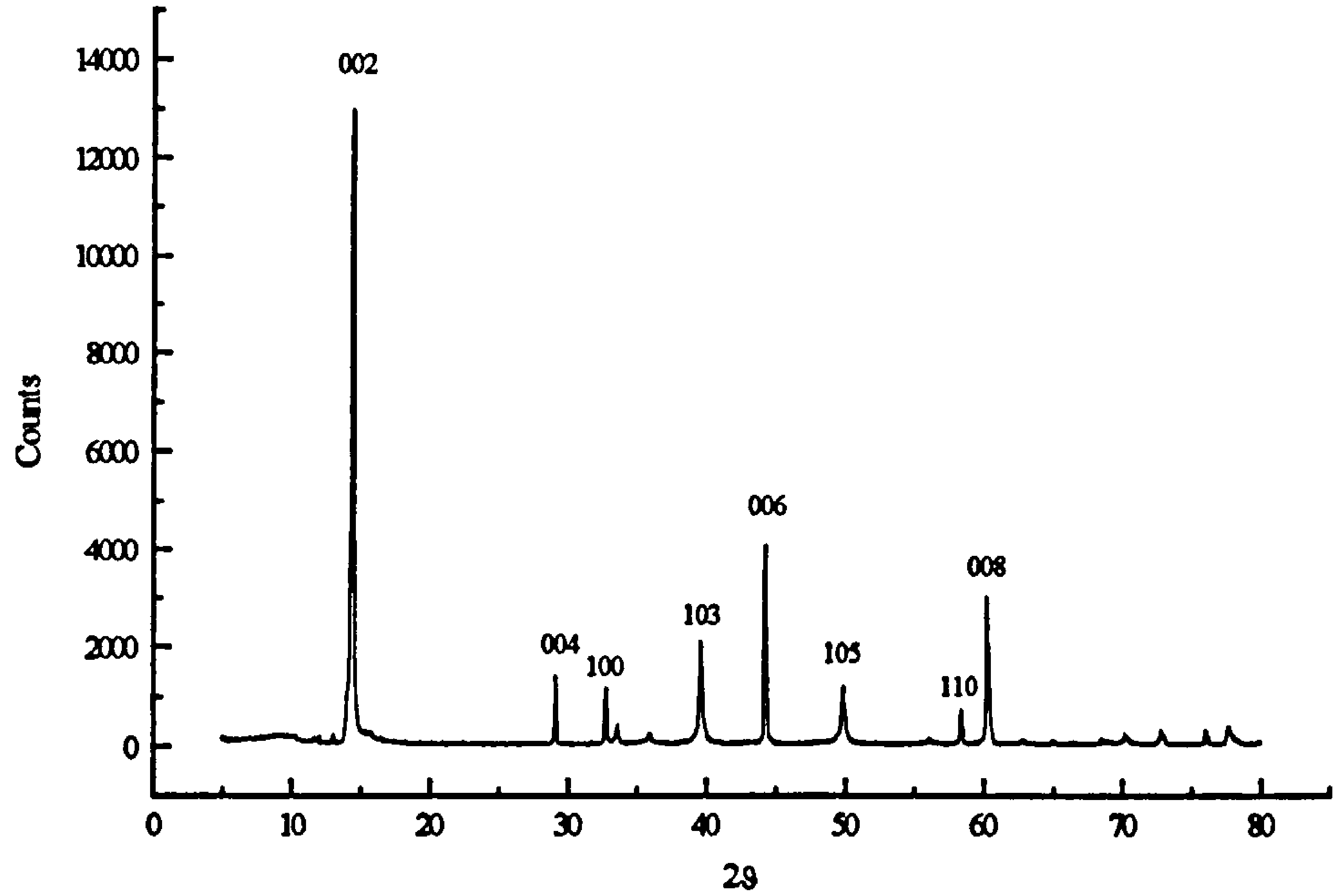

Figure 3.1: Powder X-ray diffraction pattern for synthesised MoS_2

3.2.1 Physical Properties of MoS_2

The electron transport and magnetic properties of synthesised MoS_2 provided a check against literature data on hexagonal MoS_2 and a basis for comparison between the starting material and MoS_2 intercalated with organic species.

Four probe variable temperature electrical conductivity data for polycrystalline pellets of MoS_2 are shown in Figure 3.2. The measured conductivity varies from 0.3 $\Omega^{-1}cm^{-1}$ at room temperature to 3×10^{-4} $\Omega^{-1}cm^{-1}$ at 80K. The material is therefore a semiconductor as anticipated for the calculated band structure 2H-MoS_2[83]. A linear fit to the plot of ln σ versus 1/T, indicates Arrhenius behaviour with an activation energy of 0.13eV.

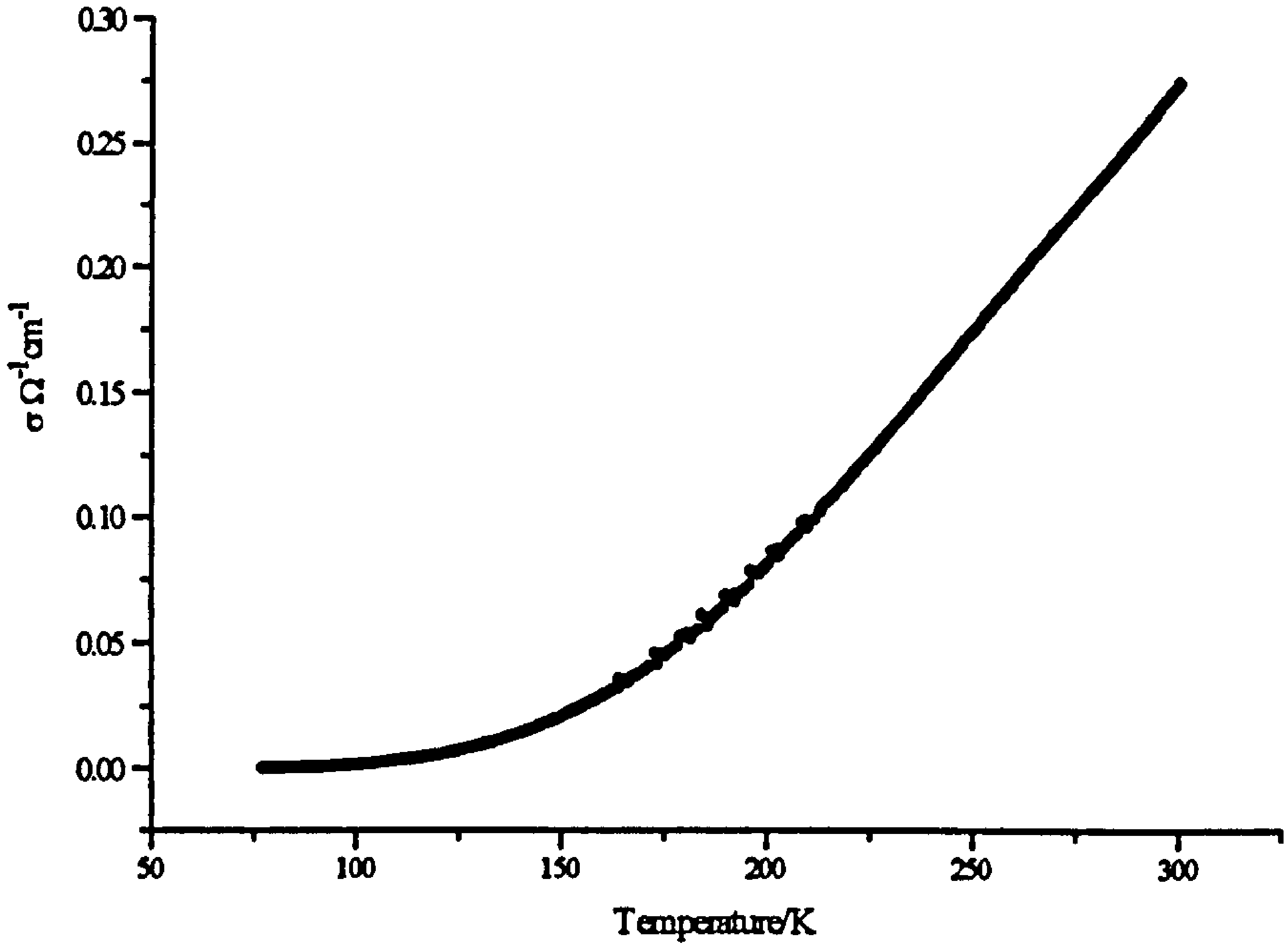

Figure 3.2: Four probe conductivity data for synthesised MoS_2

The conductivity of MoS_2 has previously been interpreted as being intrinsic and predominantly n-type, the conductivity perpendicular to the c axis dominating that parallel to the c axis. In the work by El-Mahalawy[95], two different slopes of the measured conductivity versus reciprocal temperature were observed, when measuring the conductivity perpendicular to the c axis on a single crystal of MoS_2. Below 790K, the activation energy was measured as 0.235eV and above that, as 0.635eV. Other reports of values for the low temperature (<298K) thermal activation energy show a wide variation, ranging from 0.03eV to 0.38eV[95,84,87,89]. The lowest of these values could be indicative of extrinsic conduction processes.

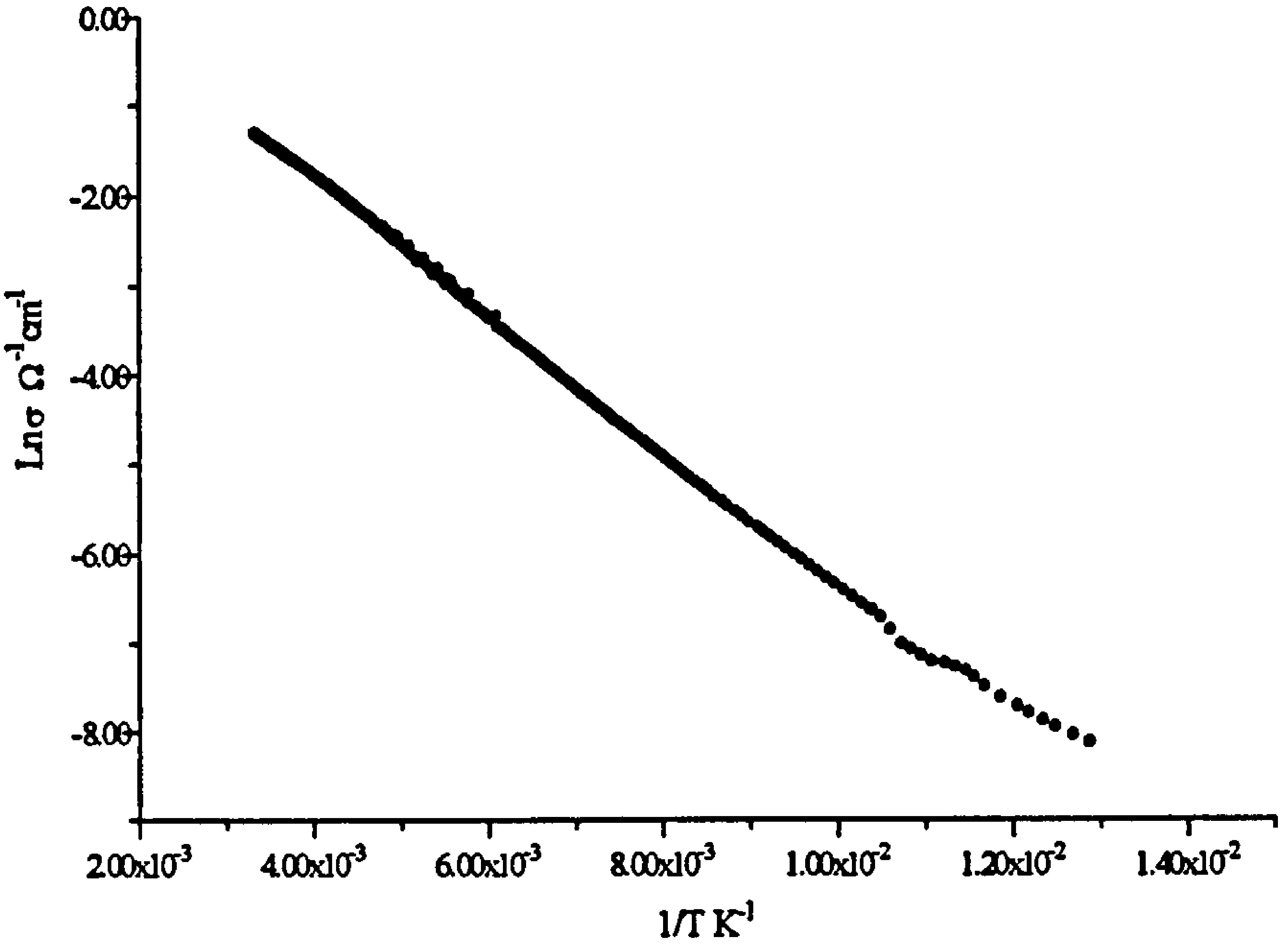

Figure 3.3: Ln σ against reciprocal temperature plot for synthesised MoS_2

Figure 3.4 shows the variable temperature magnetic susceptibility for MoS_2 between 5K and 300K, demonstrating diamagnetic behaviour of the material. This is consistent with the band structure (Figure 1.17) for 2H-MoS_2 i.e. Mo(IV) with a filled dz^2 band.

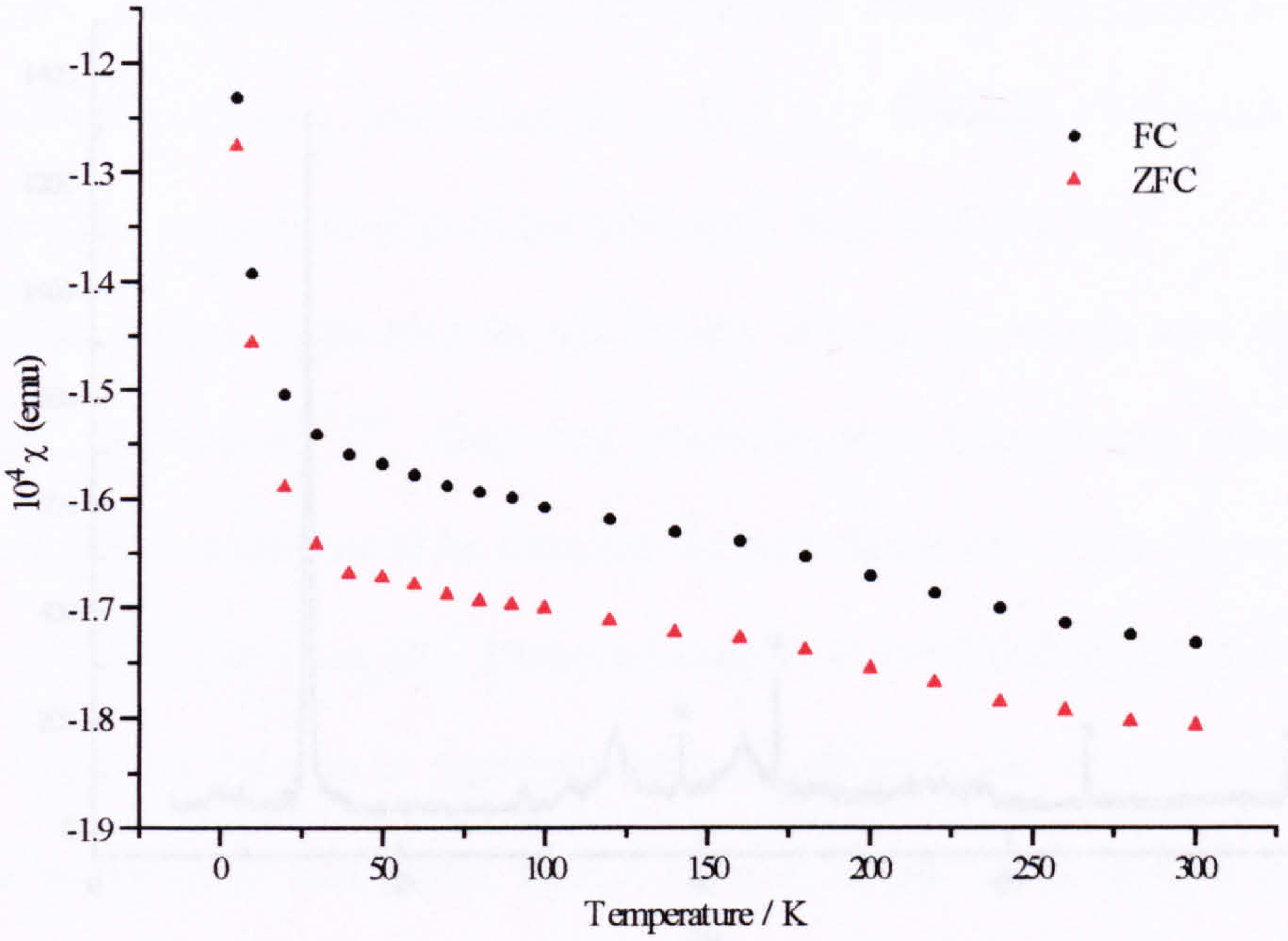

Figure 3.4: Magnetic susceptibility data for synthesised MoS_2

3.3 $LiMoS_2$

Powder X-ray diffraction data (Figure 3.5) indicated that substantial degradation of the lattice occurs on intercalation of lithium. No lines corresponding to unreacted MoS_2 were observed. A shift in the d-space of the 002 reflection of 6.294(49)Å corresponded to a Δc of 0.104Å, where Δc is the increase in interlayer spacing, observed by a movement of the 00*l* reflection to a higher 2θ value in the powder X-ray diffraction pattern. The rest of the pattern comprises unindexable broad diffraction peaks. The lithium content x, was determined to be 1.02(2), by flame emission spectroscopy.

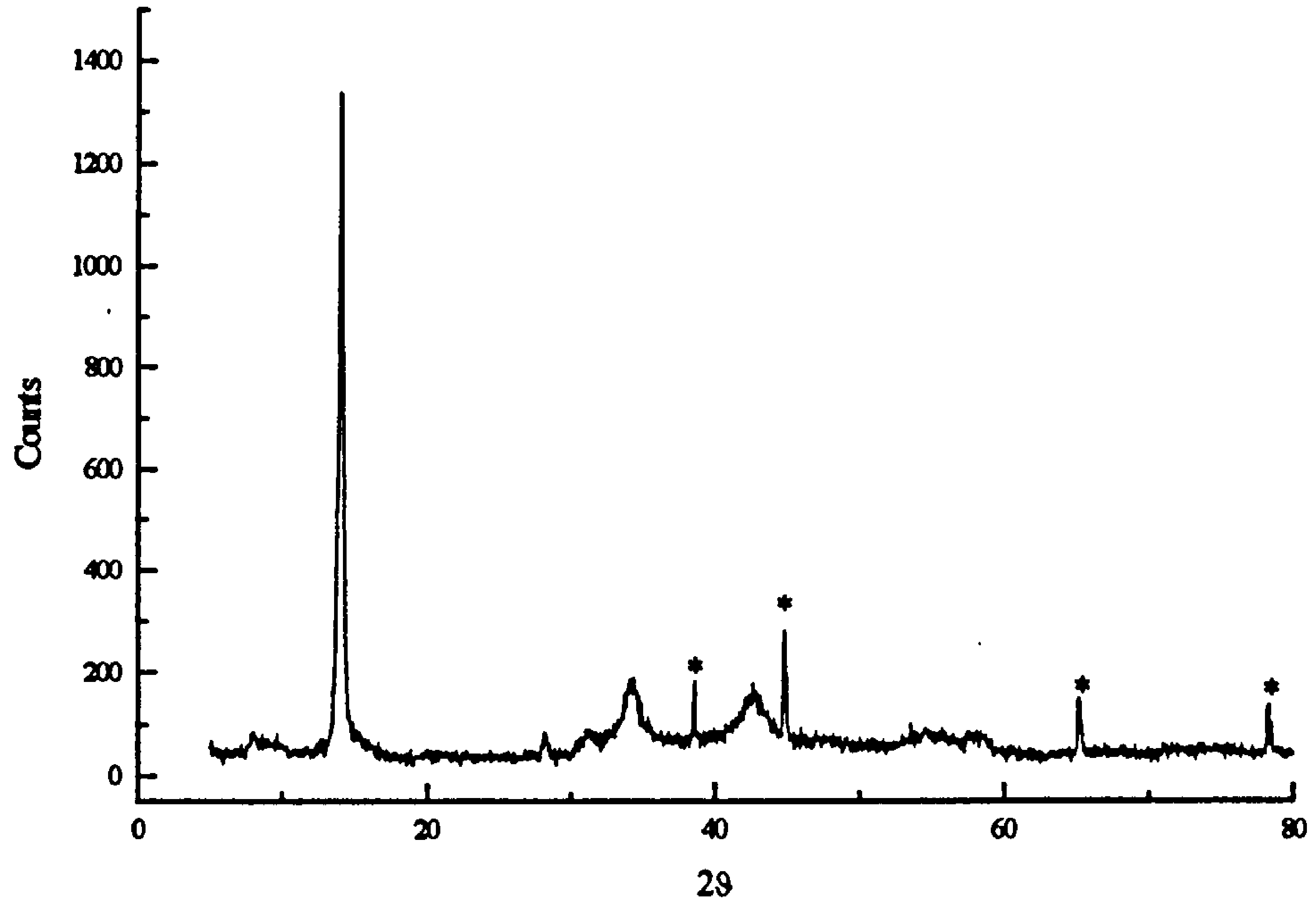

*Figure 3.5: Powder diffraction pattern of $LiMoS_2$. Lines marked * correspond to reflections from Al sample holder.*

3.4 EXFOLIATED MoS_2

This section will provide a brief description of how single layers of MoS_2 are thought to form before describing the experimental observations from this work. The early literature attributed the process of spontaneous exfoliation to the rapid hydrolysis of $LiMoS_2$ in water, the rapid reaction accompanied by this evolution of hydrogen was meant to be sufficient to separate the layers, a process represented by Equation 3.1[91].

$$LiMoS_2 + xH_2O \rightarrow (MoS_2)_{\text{single layers}} + xLiOH + \tfrac{x}{2}H_2 \qquad (3.1)$$

It was concluded that the stability of single layer suspensions arise from the layers possessing negatively charged surfaces which repel each other. At reasonably high pH the charge was considered to arise from the adsorption of OH^- ions onto negatively charged sulphide layers. It was found that reduction of the pH to less than 2 or the introduction of metal cations into the solution caused spontaneous flocculation of the single layers. The positive ions, either by adsorption onto the disulphide layers or by reaction with the OH^- ions, neutralised the surface layer charge and permitted restacking of the layers and the growth of particles sufficiently large to flocculate[130].

An alternative explanation for the stability of single layers was later proposed by Danot and co-workers[144,145]. They had observed that intercalation compounds of dialkylammonium cations could be obtained via flocculation of a MoS_2 dispersion in the presence of R_4NX (X=Cl or Br). Elemental analysis showed that the product contained neither oxygen nor halogen in significant amounts although the alkylammonium cation had been incorporated into MoS_2; from 0.15 to 0.30 per MoS_2 formula unit. It was concluded therefore, that the only anion present in the product was MoS_2^{x-}. For this species to form by hydrolysis of $Li^+(MoS_2)^-$, a fast redox process in which the MoS_2 layer charge changes from 1- to x- per formula unit was proposed, involving reduction of water molecules during exfoliation (Equation 3.2).

$$\{Li^+(MoS_2)^-] + H_2O \rightarrow Li^+ + (MoS_2)^{x-} + (1\text{-}x)OH^- + (1\text{-}x)/_2\, H_2 \qquad (3.2)$$

This proposed mechanism is also consistent with the observation that after washing a fresh single layer suspension in copious amounts of water to attain a neutral pH, the single layer suspension continues to be stable. Therefore, the reduction of water with the concomitant partial oxidation of the $(MoS_2)^-$ layers in $LiMoS_2$ to a state $(MoS_2)^{x-}$ remains the most favoured explanation. It was not the intention of the work carried out here to focus on the single layer suspension and so extensive work was not pursued in this area.

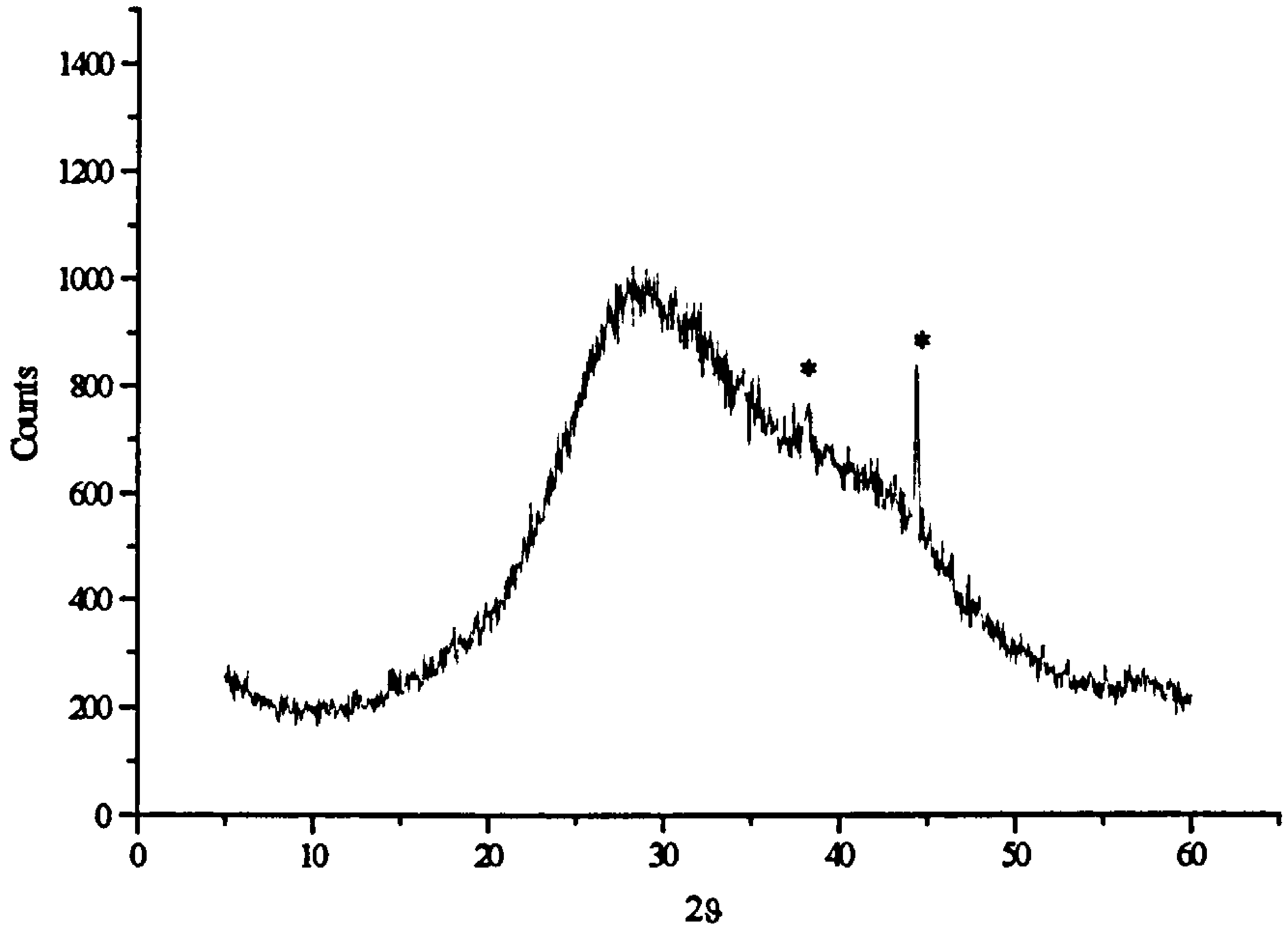

*Figure 3.6: Powder X-ray diffraction pattern of a single layer suspension of MoS_2 obtained in this work. Lines marked * correspond to reflections from Al sample holder.*

Upon exposure of $LiMoS_2$ to water, the evolution of gas was observed together with the formation of a highly opaque black suspension in water. These observations are consistent with previous reports[136]. Powder X-ray diffraction data for MoS_2 single layers in the form of a concentrated suspension are shown in Figure 3.6. Theoretical diffraction patterns of small crystallites of 2H-MoS_2 with different numbers of stacking layers have been calculated[146]. As the number of layers in a stack decreases, the Bragg reflections broaden and for a single layer, the 002 reflection disappears. Good agreement was obtained between the data observed in this work, earlier experimental data from Joensen et al[147] and the modelling study of poorly crystalline MoS_2 by Liang et al[146].

Pristine MoS_2 undergoes a structural transformation upon intercalation with lithium in which the co-ordination of the molybdenum atom changes from trigonal prismatic to octahedral with an accompanying change in oxidation state from Mo(IV) to Mo(III). The main driving force for this transformation is thought to be the minimisation of the total energy by lowering electron occupied conduction bands following electron transfer from lithium into the host upon intercalation. Formation of a $2a_0 \times 2a_0$ superlattice has been observed for lithiated MoS_2[148]. A recent EXAFS study of $LiMoS_2$ showed that the co-ordination environment of a molybdenum atom within the MoS_2 layer is 6 sulphur atoms at 2.44Å, 3 molybdenum atoms at 2.94Å and 3 molybdenum atoms at 3.65Å[15]. The superstructure observed is not caused by the disruption of the host through insertion of lithium ions but appears to be driven by the transfer of an electron into the MoS_2 layer which causes intralayer distortions involving the molybdenum atoms.

A substantial body of evidence suggests that single layer MoS_2 contains octahedrally co-ordinated MoS_2. A modelling study[150] has been carried out on single layer MoS_2. Comparison of peak shapes from experimental powder X-ray diffraction patterns for both octahedrally co-ordinated and trigonally prismatically co-ordinated molybdenum have been made. The conclusion was drawn that the MoS_2 single molecular layers in suspension in water have octahedral co-ordination. Furthermore, STM measurements on thin films of MoS_2 prepared from single layer suspensions showed that the superstructure of a MoS_2 single layer corresponds to a $2a_0 \times a_0$ structure type[151].

3.5 RESTACKED MoS_2

Bulk restacked MoS_2 was prepared from exfoliated material by addition of 6M HCl in order to reduce the pH below 2. The reaction mixture was then stirred for one week to reproduce conditions under which the intercalated materials were prepared. The solid was separated, washed with de-ionised water and dried under vacuum. The powder X-ray diffraction pattern is shown in Figure 3.7. It is dominated by an intense reflection at d=6.20Å and less intense, broadened reflections at larger 2θ. The broadness of the Bragg peaks is due to the small particle size.

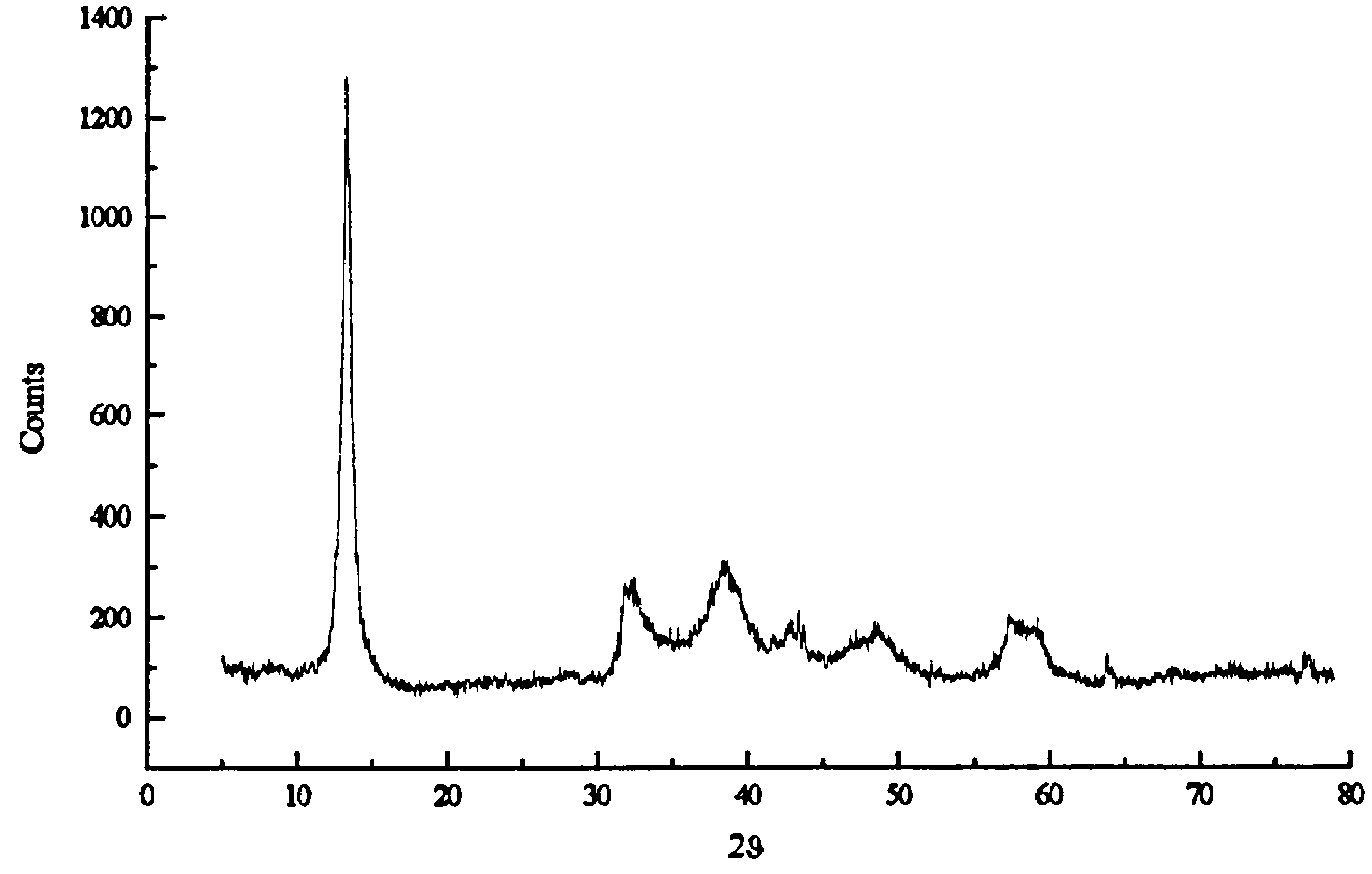

Figure 3.7: Powder X-ray diffraction pattern of restacked MoS_2 ($MoS_2.0.41H_2O$)

A decrease in crystallite size causes asymmetric line broadening, particularly as higher diffraction angles are reached, which gives a "saw-tooth" structure to the peaks. This is a consequence of the Warren effect which arises from the fact that for a two-dimensional structure, the reciprocal lattice becomes a line perpendicular to the layer and so, for higher diffraction angles, a continuous distribution of diffraction intensity appears[152].

Thermogravimetry data for restacked MoS_2 is presented in Figure 3.8. The composition for this sample was calculated as $MoS_2.0.41H_2O$. From the position of the 001 reflection in the diffraction pattern (d=6.202Å), it was concluded that the water is present in the form of surface water and is not intercalated into the host structure. Flame emission spectroscopy confirmed the absence of significant amounts of lithium (<0.004 mole of Li per mole of MoS_2).

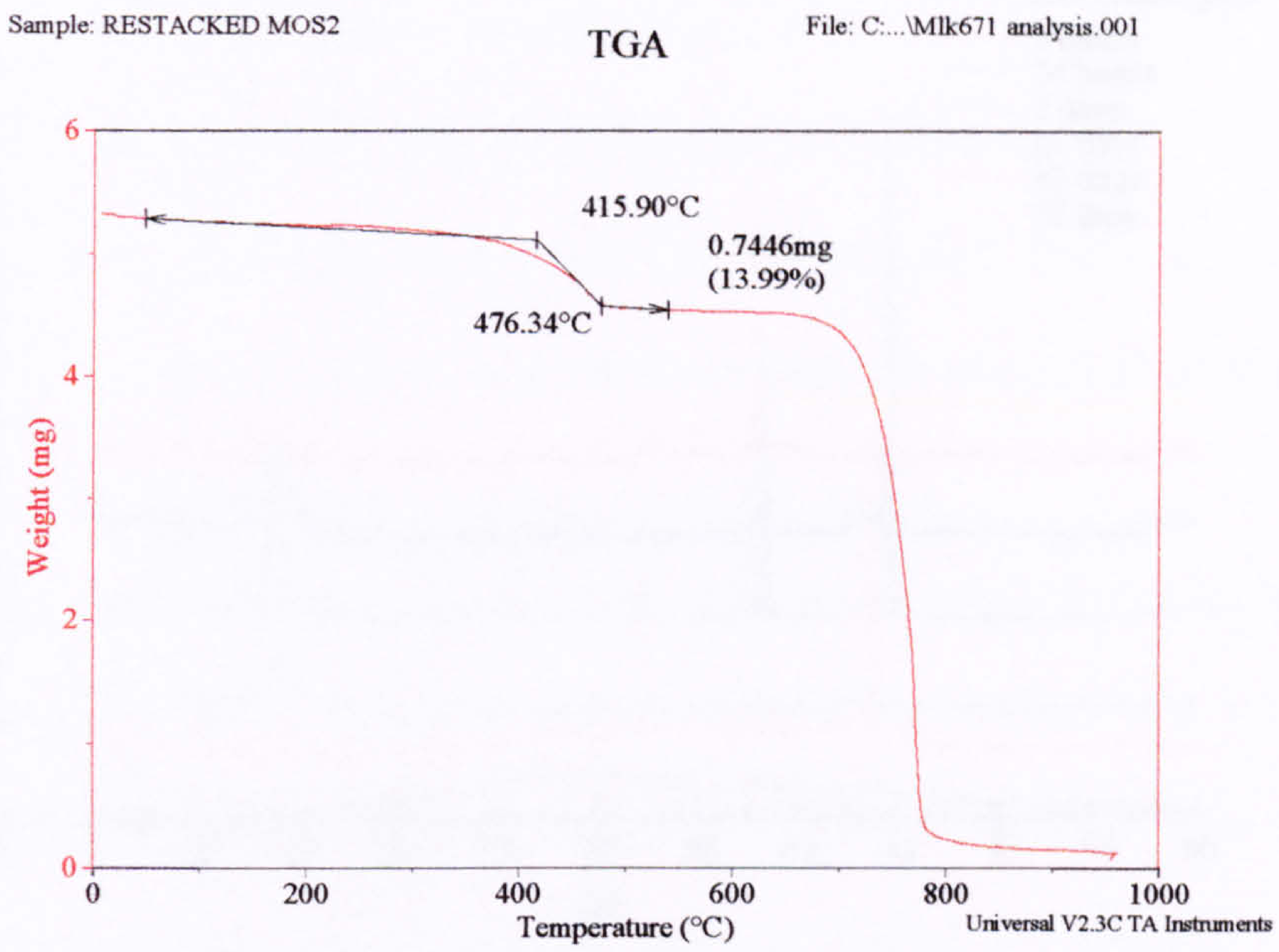

Figure 3.8: TGA for Restacked MoS_2

The process of the restacking of the single layers was investigated by allowing a sample of exfoliated MoS_2 to dry at ambient temperature and humidity on an aluminium X-ray plate. Powder X-ray diffraction patterns of the drying material were collected at regular intervals. The series of powder patterns in Figure 3.9 illustrate the restacking of the MoS_2 layers as the sample dries and the formation of a poorly crystalline phase with no coherent stacking arrangement at ambient temperature.

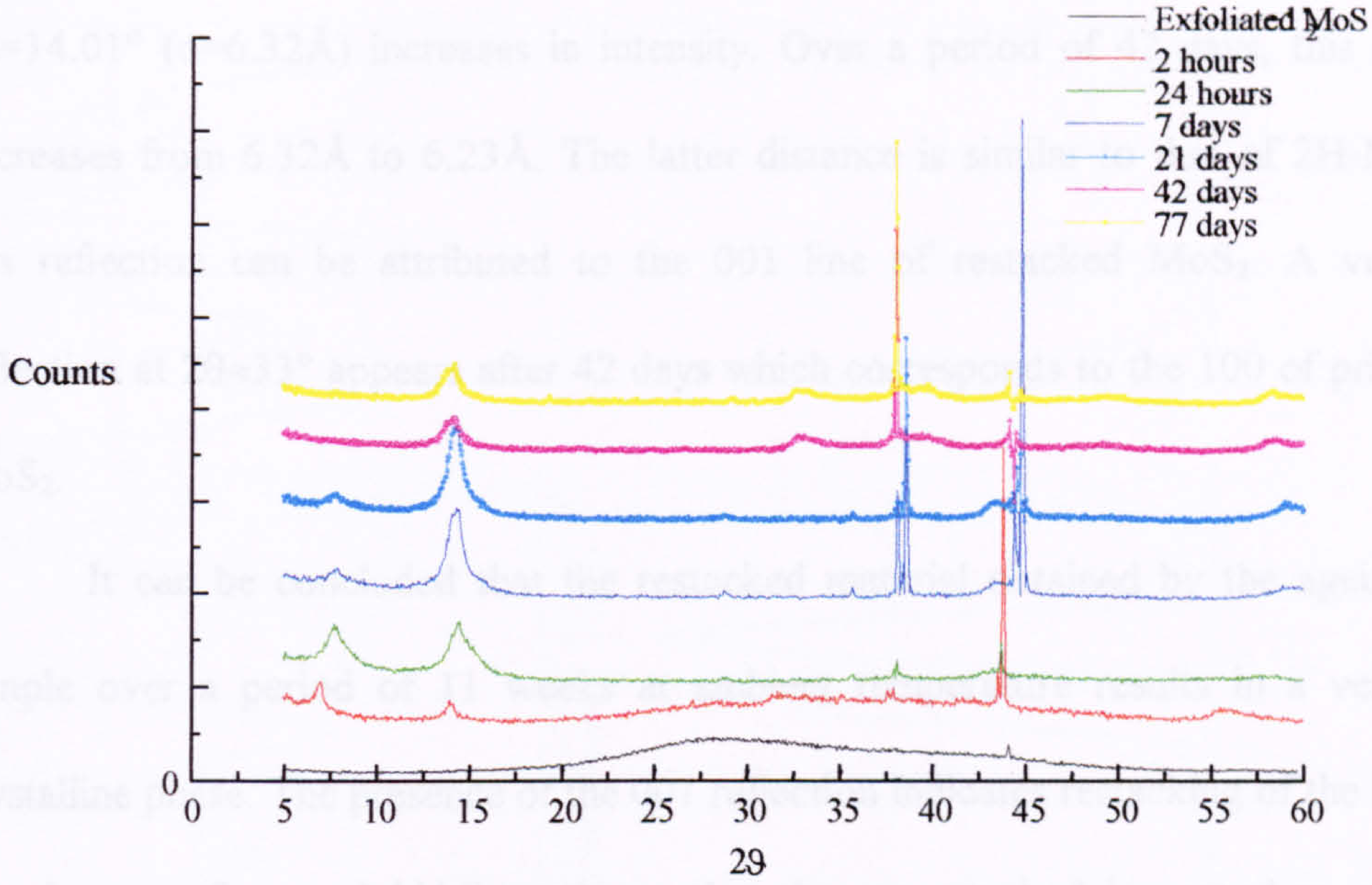

Figure 3.9: Powder X-ray diffraction patterns of restacking MoS_2 over time, patterns have been offset against y-scale and expanded for clarity.

The series of diffraction patterns show two main reflections, the first at 2θ≈7° and the second at 2θ≈14°. These two reflections are due to a mixture of two phases. The latter reflection can be attributed to dry restacked MoS_2 and the other reflection at 2θ≈7° has been identified from earlier work[147] as the 001 reflection for restacked MoS_2 containing a bilayer of water. After 24 hours, the sample is in the form of a thick paste; the most intense reflection occurs at 2θ=7.32° (d=12.07Å). This peak is initially strong and diminishes in intensity with increasing time, being undetectable after 21 days. Trapping bilayers of water in the interlayer space would result in a correspondingly large lattice repeat distance in a direction perpendicular to the layers. Using a value of 6.2Å for the repeat distance between adjacent molybdenum layers, the remaining increase in interlayer distance to be accounted for is therefore approximately 5.9Å. The nominal van der Waals radius for a water molecule is 2.8Å. Hence a bilayer of water in between the layers would be consistent with the observed lattice repeat distance of 12.07Å.

As the intensity of the reflection at d=12.07Å diminishes, the reflection at $2\theta=14.01°$ (d=6.32Å) increases in intensity. Over a period of 42 days, this d-spacing decreases from 6.32Å to 6.23Å. The latter distance is similar to that of 2H-MoS_2 and this reflection can be attributed to the 001 line of restacked MoS_2. A very broad reflection at $2\theta\approx33°$ appears after 42 days which corresponds to the 100 of pristine 2H-MoS_2.

It can be concluded that the restacked material obtained by the ageing of the sample over a period of 11 weeks at ambient temperature results in a very poorly crystalline phase. The presence of the 001 reflection indicates restacking of the layers but the absence of general *hkl* lines shows that they are stacked in a random orientation about the c axis and with poor registry between adjacent lamellae. The saw-tooth shape of the 100 reflection is a result of this turbostratic disorder; caused either by the shearing of the layers or possibly by bending of the layers.

3.5.1 EXAFS spectroscopy of Restacked MoS_2.

The powder X-ray diffraction pattern comprises a strong 001 reflection and less intense reflections whose degree of broadness precludes assignment of *hkl* indices. This indicates that the layers are arranged parallel and equidistant but are random in translation parallel to the layer and in rotation about the axis normal to the layer. More detailed structural information regarding the local molybdenum environment was sought using EXAFS. The sample used for EXAFS had a stoichiometry $MoS_2.0.16H_2O$.

Figure 3.10 shows the k^3 weighted EXAFS data and the Fourier transform for crystalline MoS_2. This material was considered to be a close model to the compounds under study and so the EXAFS of 2H-MoS_2 was used for calibration of three phaseshifts (the absorbing atom Mo phaseshift and the Mo and S backscattering atom phaseshifts) used in the analysis.

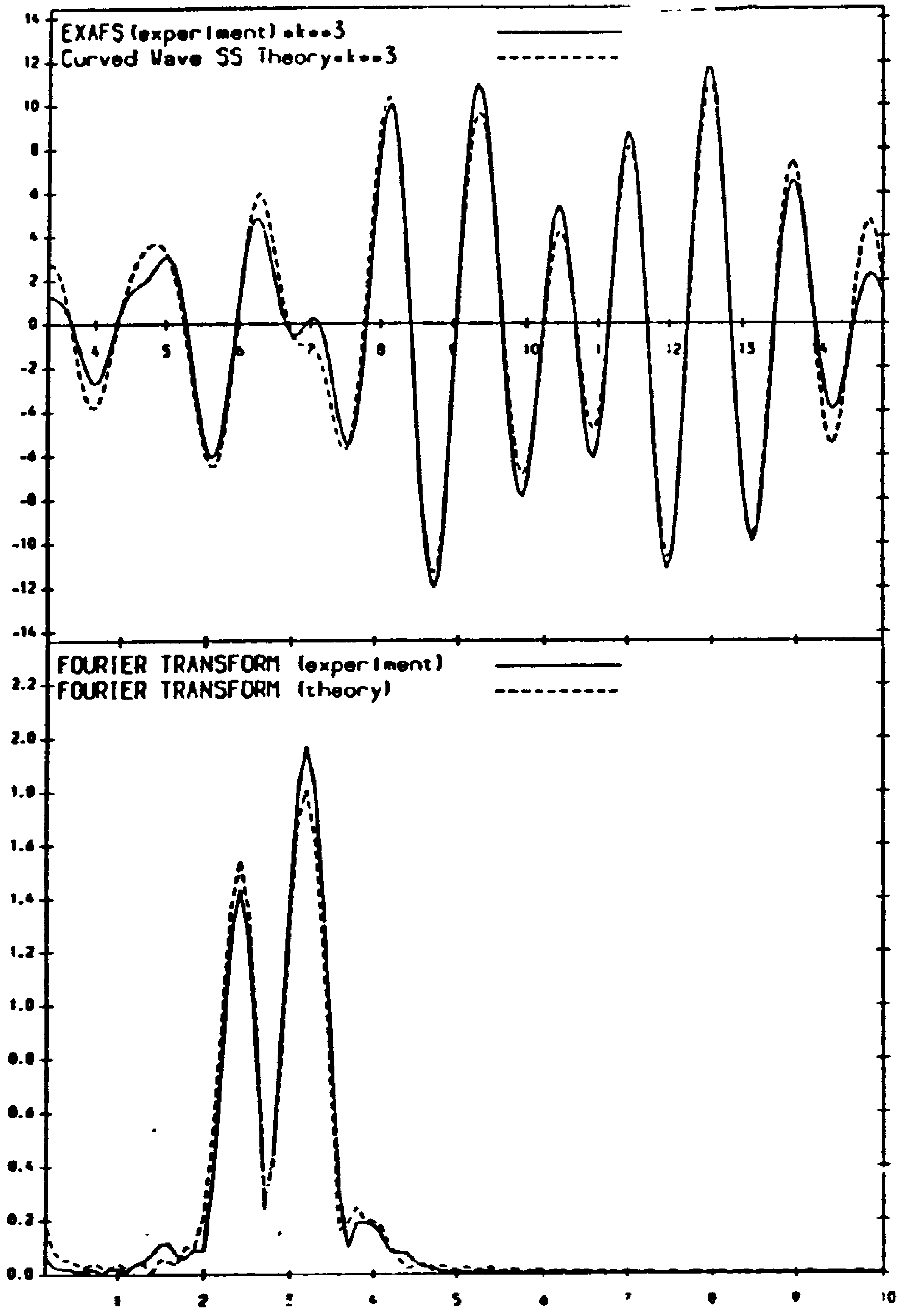

Figure 3.10: EXAFS and Fourier transform data for crystalline MoS_2, for shells< 4Å.

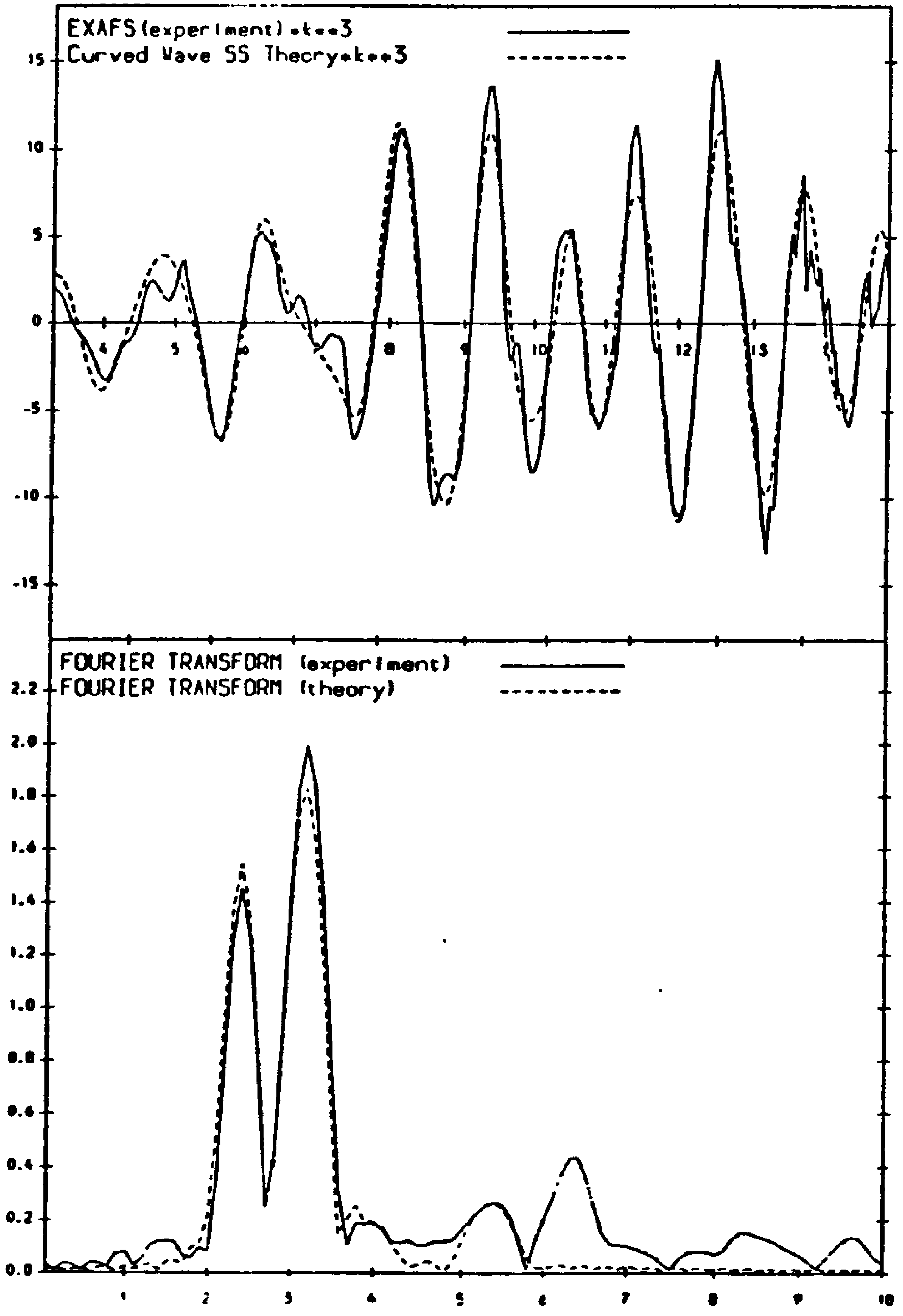

Figure 3.11: *EXAFS and Fourier transform of crystalline MoS_2, fitted with shells according to crystal structure, to 5.5Å.*

The fit to the experimental data in Fig. 3.10 was refined to minimize the fit index, using crystallographic co-ordination numbers. Nearest neighbour distances similar to the crystallographic values were obtained. The data were Fourier filtered to exclude shells >4Å. This was done because the three materials under study only showed scattering contributions for distances <4Å. The more complete EXAFS spectrum for 2H-MoS_2, showing scattering extending to 7Å is shown in Figure 3.11.

Table 3.1: Fitting parameters for MoS_2 model EXAFS.

Coordination numbers	**Crystallographic distances/Å**	**Fourier Filtered refined distance/Å**	**Raw EXAFS refined distance/Å**
6S	2.417	2.405	2.403
6Mo	3.160	3.165	3.163
6S	3.979	3.976	3.962
2S	4.561	-	-
12S	5.081	-	5.149
6Mo	5.473	-	5.479
12S	5.549	-	5.549

Table 3.1 provides a comparison between interatomic spacings taken from the ICSD database, EXAFS refined distances to 4Å and EXAFS refined distances from the full EXAFS spectrum. Although the EXAFS distances are quoted to 3 decimal places, the true errors are more realistically ±0.01Å in the innermost shells and ±0.05Å in the outermost shell. The good agreement between atom-atom distances obtained from EXAFS data and the crystallographic values justified the use of the same phase shifts in refinements using EXAFS data collected for the exfoliated and intercalated materials. For these intercalation compounds, the Mo K-edge data were Fourier filtered, forming a

window from ~1.7Å to 4Å. The lower limit included any possible Mo-Mo bonding distances. The upper limit was chosen because the three compounds under study showed no scattering contributions for distances >4Å.

Figure 3.12 provides a comparison of the EXAFS for restacked MoS_2 and that for a model derived from crystalline MoS_2; there are significant changes in the molybdenum co-ordination on moving from crystalline MoS_2 to the restacked MoS_2, as indicated by the clear differences in amplitude and frequency of the two spectra. The Fourier transforms of the two spectra are shown in Fig. 3.13. The significant reduction in amplitude of the second shell at ca. 3.2Å corresponds to a reduction in the backscattering contribution from molybdenum atoms, indicating a lower co-ordination by molybdenum atoms at this distance from the central atom relative to that observed in the crystalline MoS_2. There is also a small decrease in the first co-ordination shell, as indicated by the narrowing of the first shell peak relative to the same peak in the EXAFS spectrum of 2H-MoS_2. These observations are reflected in the best fit parameters obtained after least squares fit refinement.

The refined distances are shown in Table 3.2. The co-ordination environment of a molybdenum atom was determined as 5.1 sulphur atoms at 2.1Å, 0.3 molybdenum atoms at 2.77Å, 1.5 molybdenum atoms at 3.17Å and 1.0 molybdenum atom at 3.74Å. A fit index of 0.17 was obtained. The best fit is shown in Fig 3.14. Co-ordination numbers are regarded as soft parameters and are accurate to approximately 20%. When fixing the first co-ordination shell to 6 sulphur atoms, refinement led to a slightly poorer fit index of 0.21 although the appearance of the fit did not alter.

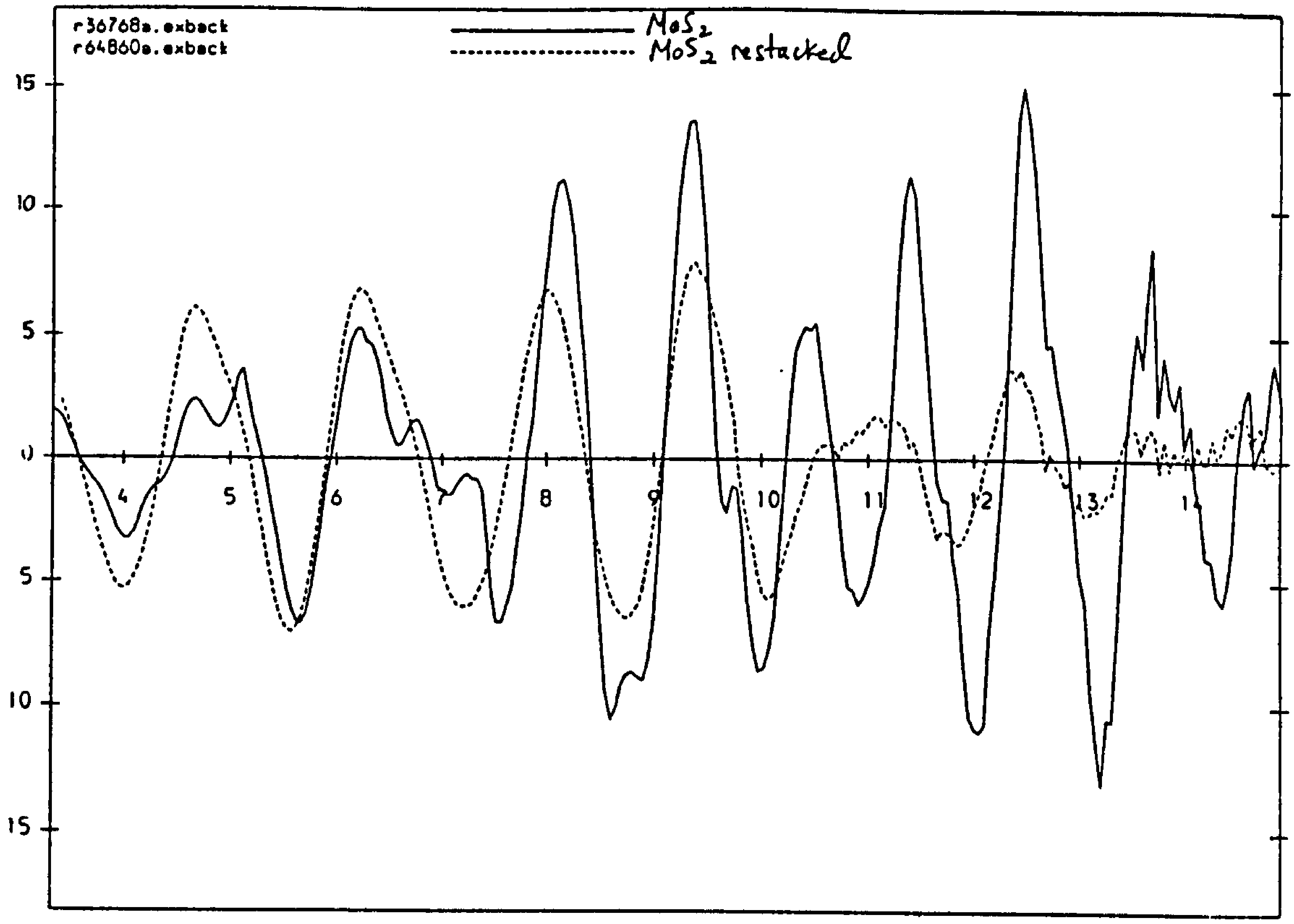

Figure 3.12: EXAFS for restacked MoS_2 and crystalline MoS_2.

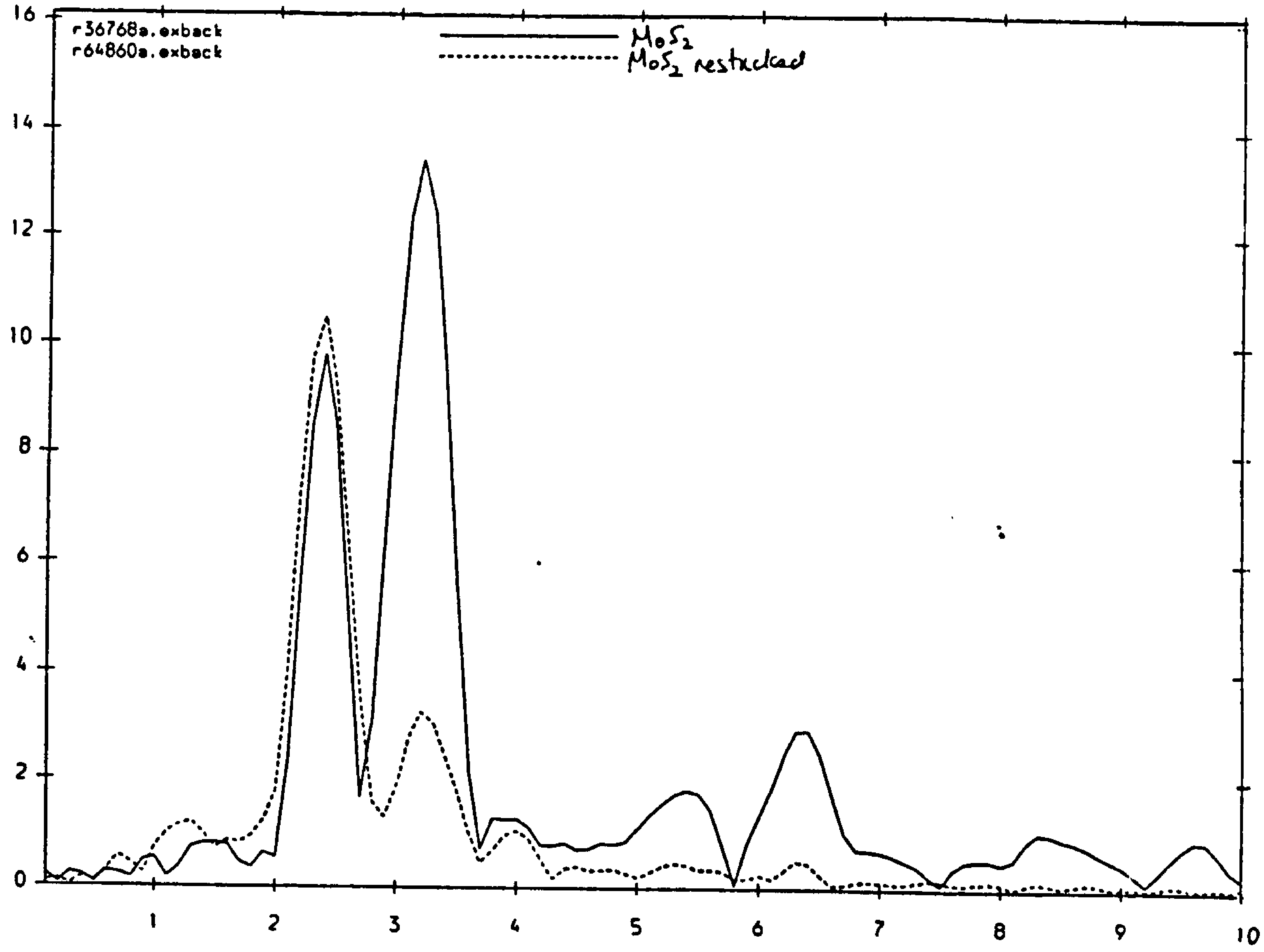

Figure 3.13: Fourier transform plots for restacked MoS_2 and crystalline MoS_2.

Table 3.2: Coordination numbers (N), distances (R) and Debye-Waller factors (A) for restacked MoS_2 with N fitted (column A) and fixed with N=6 for the first shell (column B)

Coordination Shell	**A**			**B**		
	N	**R/Å**	**A/Å^2**	**N**	**R/Å**	**A/Å^2**
Mo-S	5.1	2.409	0.010	6.0	2.409	0.013
Mo-Mo	0.3	2.770	0.002	0.5	2.765	0.005
Mo-Mo	1.5	3.171	0.009	1.4	3.173	0.009
Mo-Mo	1.0	3.737	0.012	0.9	3.740	0.012

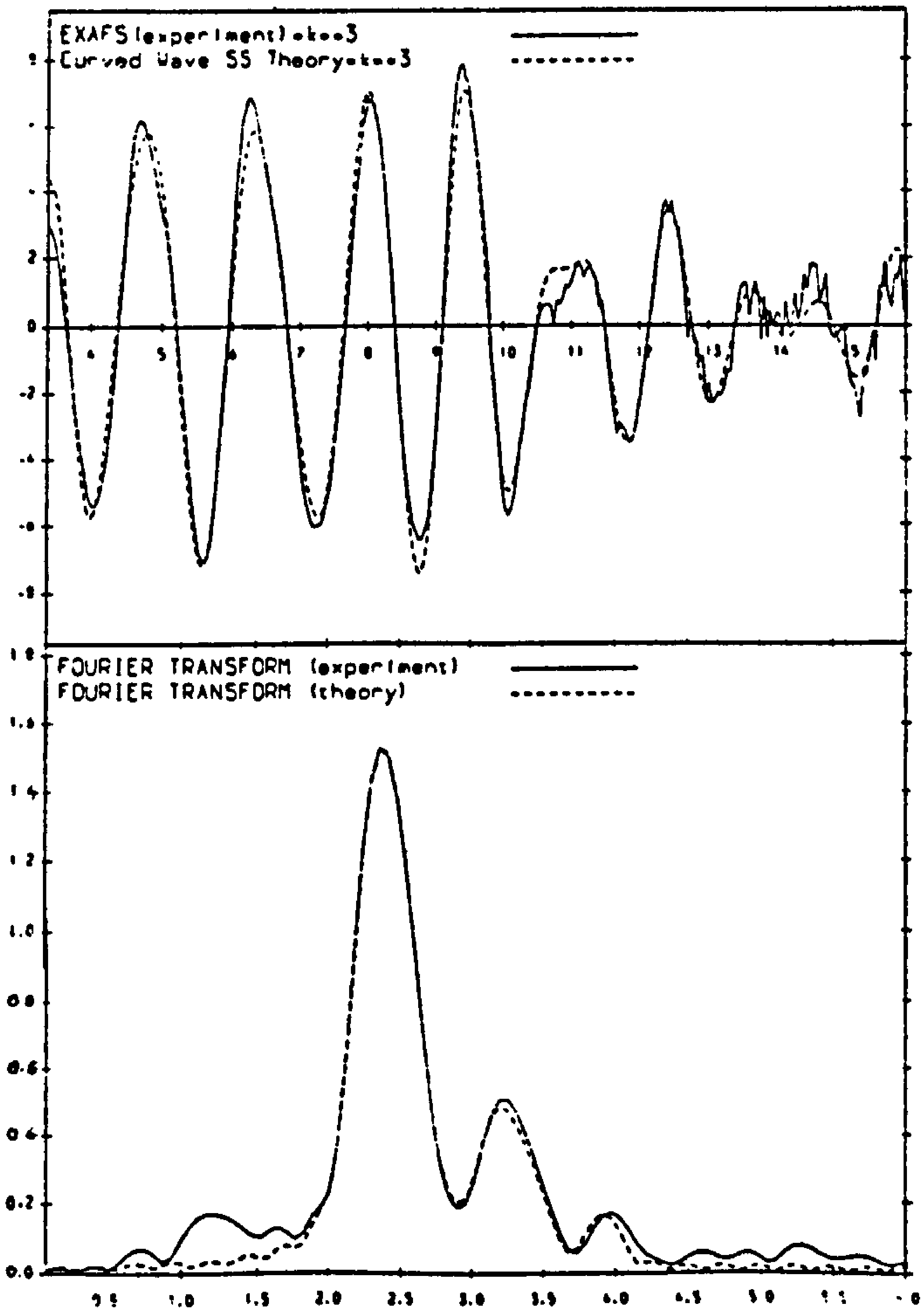

Figure 3.14: Final Fit to EXAFS of restacked MoS_2.

Fixing the co-ordination numbers to more "chemically sensible" integral values (beyond the setting of the first shell to 6 sulphurs) consistently led to a significant increase in the fit index (FI) and a poorer fit to the EXAFS spectrum and Fourier transform data. Notably, omission of the 0.3 molybdenum atoms at a distance of 2.77Å caused an increase in the FI to 0.00038.

The EXAFS data clearly indicate that lithiation of MoS_2, followed by exfoliation leads to substantial structural changes within the S-Mo-S layers. The origins of the relatively large Mo-Mo distortions within the MoS_2 layer is not clear but these distortions must be linked to the reduction in sulphur co-ordination of the molybdenum. Overall the co-ordination number for sulphur within the 1st co-ordination shell in restacked MoS_2 is reduced to approximately 85% of the value for the crystalline material. This can result either from sulphur loss or from static distortions to the structure; since the TGA data indicated a Mo:S ratio of 1:2, the latter is more likely.

A molybdenum atom in the restacked material has a local co-ordination environment of 2.8 molybdenum atoms at distances of 2.77Å, 3.171Å and 3.737Å, and 5.1 sulphur atoms at 2.42Å. Attempts to fit of these peaks using $F_i(k)$ and $\delta_i(k)$ for sulphur or oxygen failed. The first Mo-Mo distance is short and is in the range 2.73-2.83Å observed for Mo-Mo bonds in cluster compounds containing the Mo_3S_4 core structure[153], indicating a degree of Mo-Mo bonding.. It is also similar to distances measured for Mo-Mo bonding in other amorphous molybdenum sulphides[154].

The second Mo-Mo distance approximates to the original Mo-Mo co-ordination shell distance in 2H-MoS_2. This suggests that there is a reduction in the Mo intralayer distortions that were observed for $LiMoS_2$ and that the structure more closely approaches that of 2H-MoS_2. The final Mo-Mo distance is not observed in the pristine material, but has been observed during an EXAFS study of $LiMoS_2$. This shows that intralayer distortions are still present. The sulphur distance of 2.42Å is similar to the Mo-

S bond length in 2H-MoS_2 but does not indicate whether molybdenum is octahedrally or trigonally prismatically co-ordinated.

These data can be interpreted in terms of random defects within the layer rather than systematic regular distortions of the molybdenum lattice. Whether the molybdenum atom is octahedrally or trigonally prismatically co-ordinated, removal of a sulphur atom (A in Figure 3.15) to produce 5 sulphur atom co-ordination around the molybdenum enables the remaining Mo-S-Mo linkages (B) to become more flexible. This can lead to distortion of the local co-ordination environment of the molybdenum centres and could account for the long Mo-Mo distance of 3.77Å observed, resulting from co-ordination defects and the resultant expansion of the MoS_2 layers. The Mo-Mo bonds could either be in chains of molybdenum atoms or correspond to localised clustering, to compensate for sulphur loss.

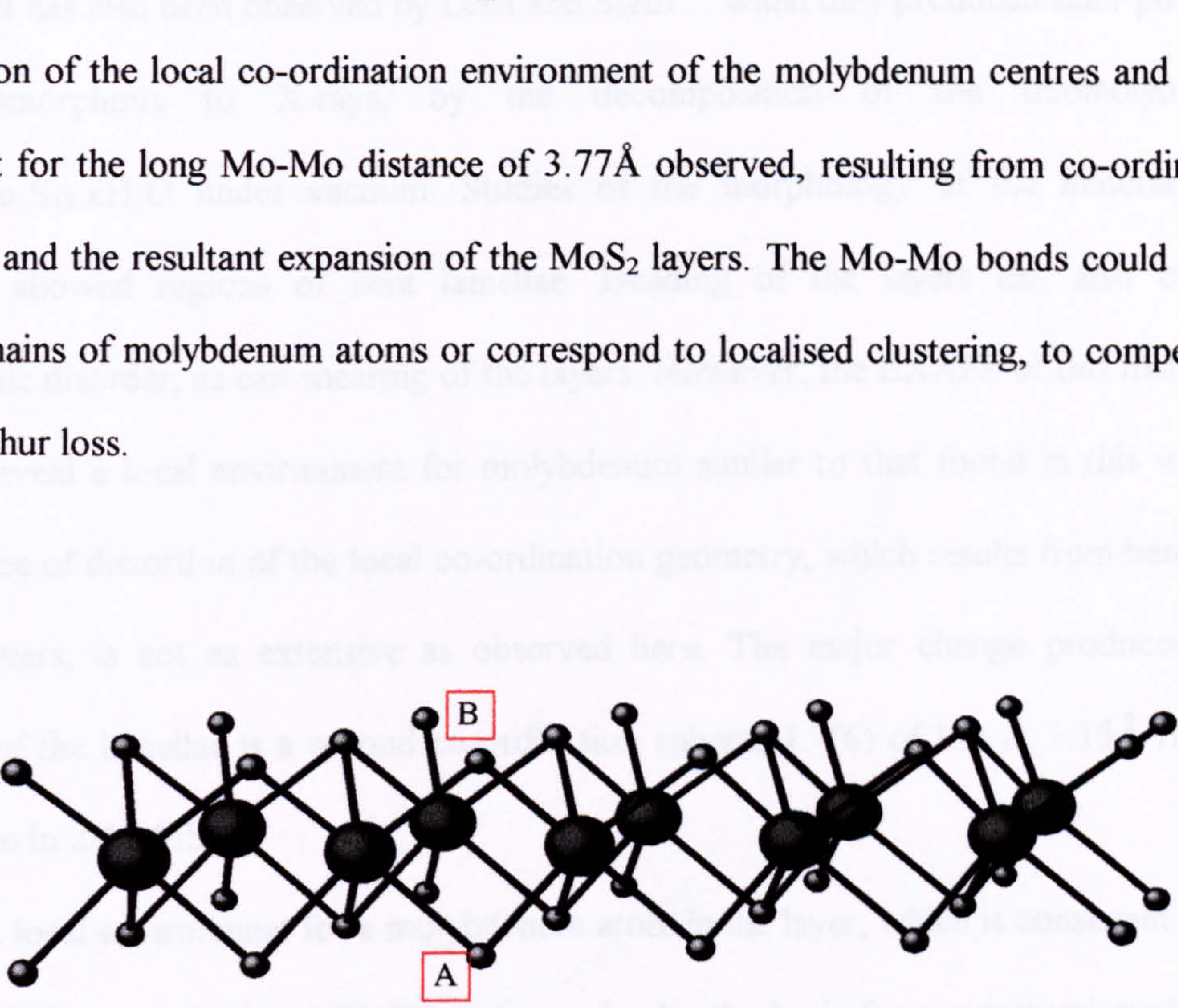

Figure 3.15: A single layer of hexagonal MoS_2.

Another possibility is the introduction of an oxygen atom, which has either replaced a sulphur atom or is situated above a molybdenum atom such that the 3 close sulphur atoms are separated. This would cause a distortion of the bond angles and lead to a strain region of increased Mo-Mo distances, further surrounded by shorter Mo-Mo distances. However, no Mo-O bonds (in region of 2.0-2.1Å) were detected by trying to fit oxygen as a co-ordination shell to the EXAFS data.

Another phenomenon which was considered as a potential contributor to the generation of the range of Mo-Mo distances was the bending of the layers. It has been observed in supported MoS_2 type hydrotreated catalysts that co-ordination defects and a significant decrease in van der Waals interactions lead to a bending of the MoS_2 slabs[155]. This effect has also been observed by Leist and Stauf[156] when they produced semi-porous MoS_2, amorphous to X-rays, by the decomposition of the thiomolybdate $(NH_4)_2Mo_3S_{13}.xH_2O$ under vacuum. Studies of the morphology of the material by HRTEM showed regions of bent lamellae. Bending of the layers can also cause turbostratic disorder, as can shearing of the layers. However, the EXAFS of this material did not reveal a local environment for molybdenum similar to that found in this work. The degree of distortion of the local co-ordination geometry, which results from bending of the layers, is not as extensive as observed here. The major change produced by bending of the lamellae is a second co-ordination sphere; 4.7(6) of Mo at 3.15Å rather than 6 Mo in 2H-MoS_2.

A local environment for a molybdenum atom in the layer, which is consistent with the information provided by EXAFS and can also be the basis for a structural model of the MoS_2 layer has not been possible. Primarily this is because it is difficult to rationalise how the sulphur co-ordination number can be reduced by a small amount relative to 2H-MoS_2, and yet the molybdenum co-ordination shells have been so radically distorted, manifested not only in the Mo-Mo distances but the number of molybdenum atoms present. The best conclusions are that co-ordination defects are producing random strain regions leading to lengthened Mo-Mo distances associated with increased flexibility of the layer and also Mo-Mo bonds. The structural reorganisation within the layer could be caused by the partial reduction of the layer as the molybdenum aims to lower the band gap between the conduction and valence bands to accommodate extra residual charge.

3.5.2 Physical Properties of Restacked MoS_2

Electrical conductivity data for restacked MoS_2 are presented in Figure 3.16. The material exhibits similar semi-conducting behaviour to crystalline 2H-MoS_2, except that there is a sharper increase in conductivity above 150K than in the crystalline material. However, the conductivity is an order of magnitude lower than in 2H-MoS_2, suggesting that the conduction electrons are being scattered by defects.

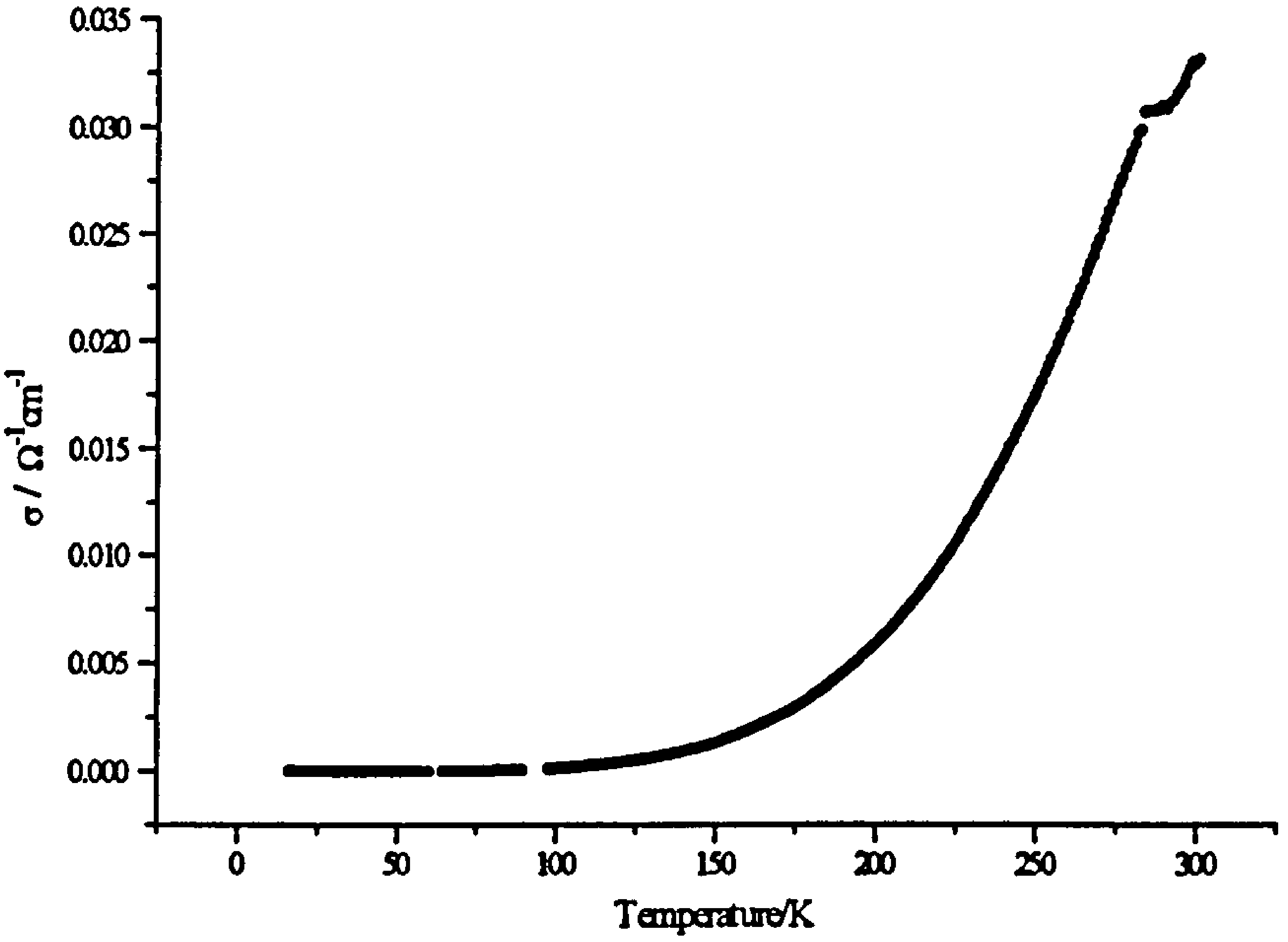

Figure 3.16: Electrical conductivity behaviour for restacked MoS_2 over 10-300K

A plot of ln σ against reciprocal temperature (Figure 3.17), reveals the non-Arrhenius behaviour of this material in contrast to 2H-MoS_2. This indicates that the conduction properties of this material are not simply governed by thermal excitation of electrons across a band gap. The fit to a $T^{-1/4}$ dependence shown in Figure 3.18 suggests that a variable range hopping mechanism between localised states is taking place.

It has been proposed that restacked MoS_2 contains distorted octahedrally co-ordinated Mo and that the restacked MoS_2 layers are partially reduced, charge balancing coming from H^+, H_3O^+ or even Li^+ [157]. With reference to the band structure of transition metal dichalcogenides, octahedral co-ordination would result in a partially filled band and consequently metallic behaviour would be anticipated. The measurements presented here show that in restacked MoS_2, conductivity has decreased relative to 2H-MoS_2 and semi-conducting behaviour is still dominant. These data do not support a change to octahedral co-ordination.

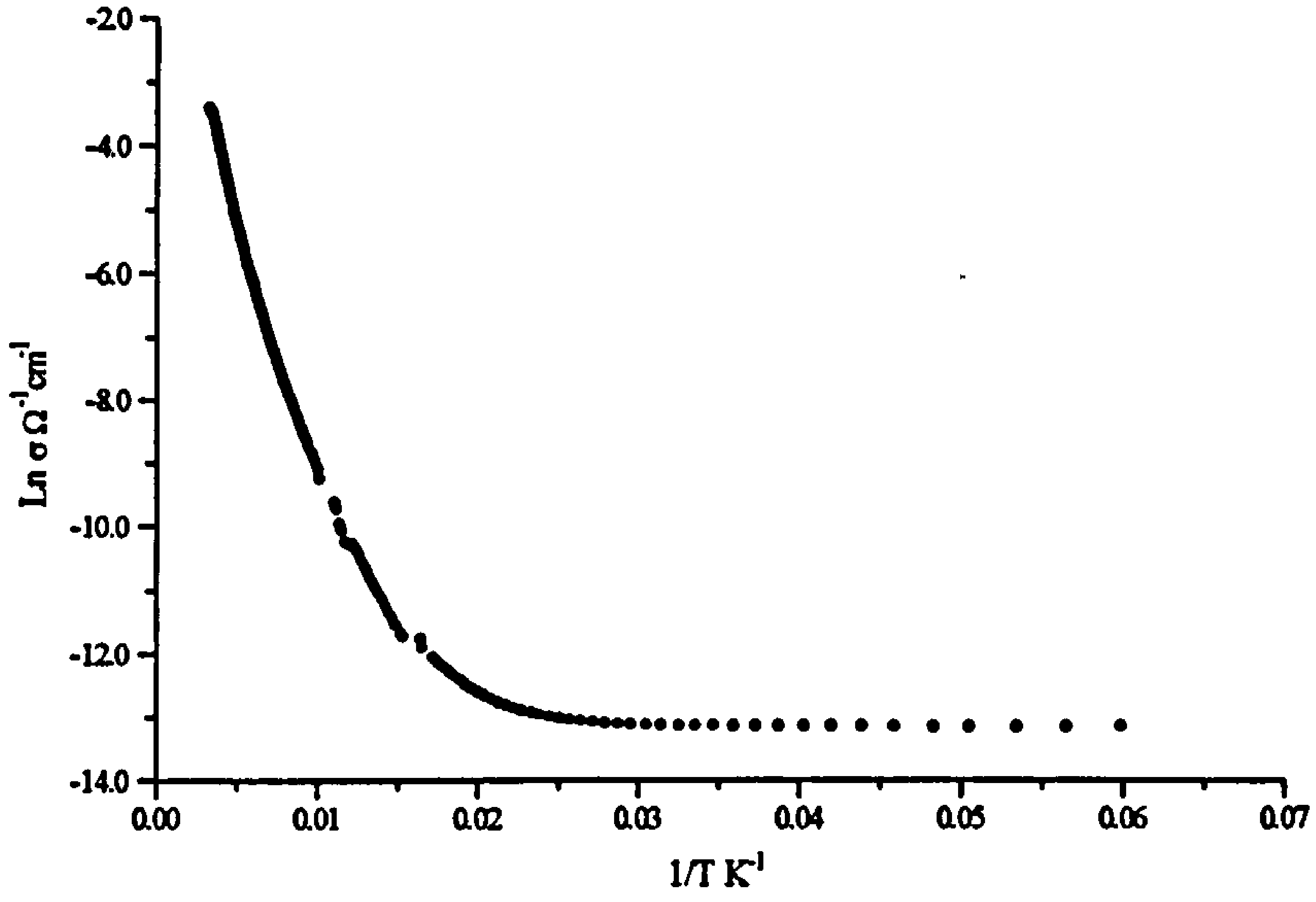

Figure 3.17: Ln σ against reciprocal temperature for restacked MoS_2 showing the difference in behaviour from that of 2H-MoS_2

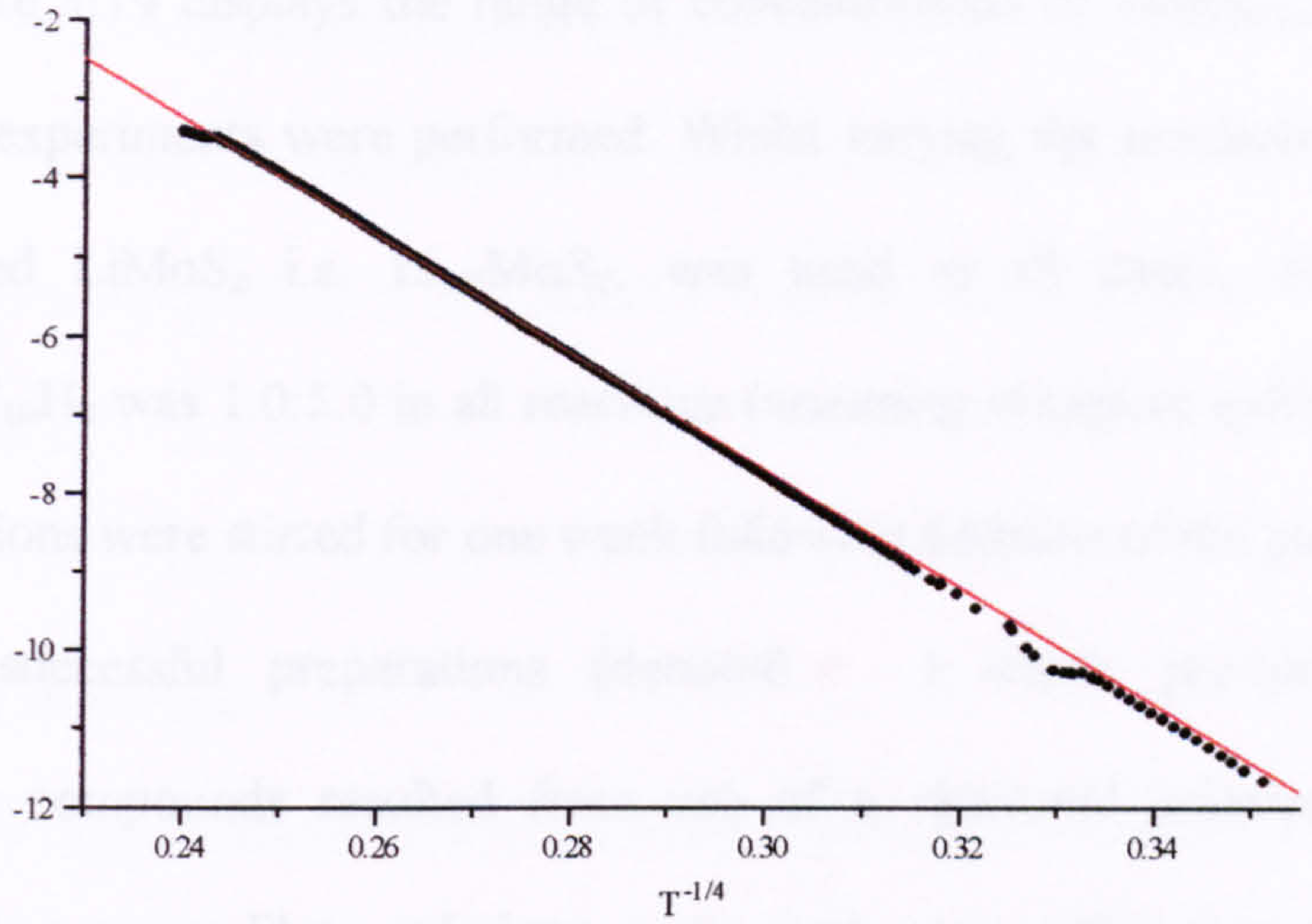

Figure 3.18: Ln σ against $T^{1/4}$ for temperature range 66-300K.

3.6 INTERCALATION OF NAPHTHALENE INTO MoS_2

Reaction variables listed in Table 3.3 were changed systematically in order to optimise the synthetic procedure. A brief account of their influence on the intercalation process will first be given.

Table 3.3: Range of experimental conditions used for preparation of intercalate.

Reaction Variable	**Lower Limit**	**Upper Limit**
$[Li_{1.0}MoS_2]$	0.02M	1.0M
$[C_{10}H_8]$	0.15M	saturated solution in dichloromethane
$\{MoS_2\}_{exfoliated}$: $C_{10}H_8$	2:1	1:30
pH of reaction	<2	pH>7
Length of reaction	24 hours	3 weeks

3.6.1 Concentration of Reactants

Figure 3.19 displays the range of concentrations of $\{MoS_2\}_{exf}$ and naphthalene with which experiments were performed. Whilst varying the concentration of reactants, fully lithiated $LiMoS_2$ i.e. $Li_{1.0}MoS_2$, was used in all cases, the molar ratio of $\{MoS_2\}_{exf}$:$C_{10}H_8$ was 1.0:5.0 in all reactions (assuming complete exfoliation of $LiMoS_2$) and all reactions were stirred for one week following addition of the guest species.

All successful preparations (denoted ◆) which produced well ordered intercalation compounds resulted from use of a saturated solution of naphthalene. Products when more dilute solutions were used, were either restacked MoS_2 or an unidentified material amorphous to X-rays. As not all preparations which utilised a saturated naphthalene solution were successful, it suggests that there is an additional variable which affects the reproducibility of the reaction.

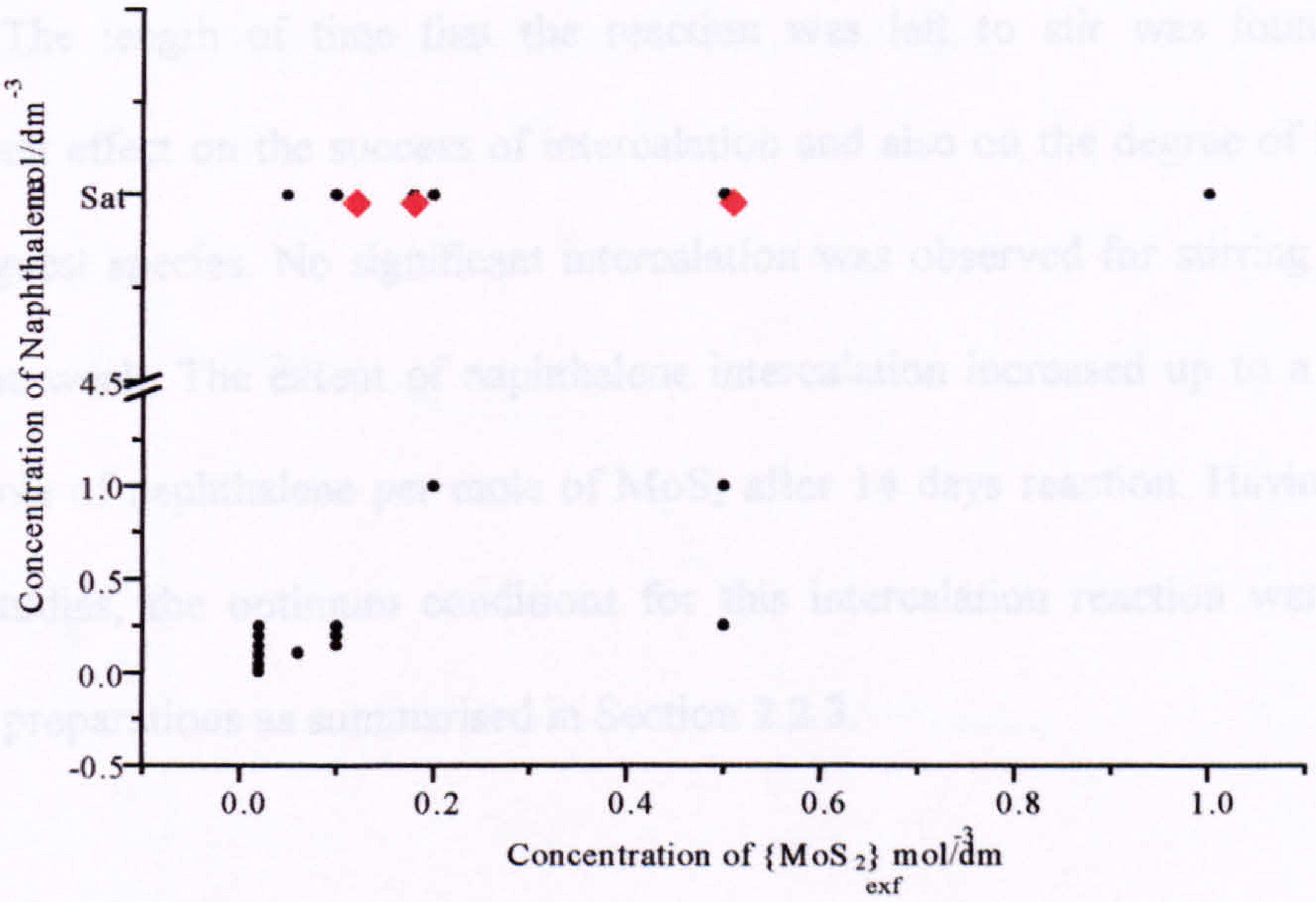

Figure 3.19: Concentrations of reactants used during synthesis optimisation

3.6.2 Molar Ratio

The effect of varying the molar ratio of $\{MoS_2\}_{exf}$: $C_{10}H_8$ was studied using $[MoS_2]_{exf}$ =0.2M and $[C_{10}H_8]$=saturated. Since all preparations were unsuccessful, it implied that the unreliability of the reaction was not determined by the molar ratio of reactants alone.

3.6.3 pH of Reaction

Reactions were carried out in which the addition of acid was omitted. The ratio $[MoS_2]_{exf}$:$[C_{10}H_8]$ was maintained at 1:5 and reactions were left stirring for one week. The powder X-ray diffraction pattern of the products had one sharp reflection at d=6.0Å and the rest of the pattern was featureless. This may correspond to the 001 reflection of a product containing octahedrally co-ordinated molybdenum[97].

3.6.4 Reaction Length

The length of time that the reaction was left to stir was found to have a significant effect on the success of intercalation and also on the degree of incorporation of the guest species. No significant intercalation was observed for stirring times of less than one week. The extent of naphthalene intercalation increased up to a maximum of 0.20 mole of naphthalene per mole of MoS_2 after 14 days reaction. Having carried out these studies, the optimum conditions for this intercalation reaction were adopted in further preparations as summarised in Section 2.2.3.

3.7 NAPHTHALENE INTERCALATED MoS_2

The content of the intercalated naphthalene in all product materials was determined by CH elemental microanalysis and by thermogravimetric analysis. A hydrogen content slightly in excess of that required for a CH ratio corresponding to naphthalene, was found by CH analysis. This suggested that residual water was present. An initial low temperature mass loss observed during thermogravimetric analysis was consistent with this conclusion (Figure 3.20). This residual water appears to be on the surface of the product material, since repeated preparations of samples indicated that there was no relationship between the interlayer expansion and the water content of the sample (Table 3.4). DSC measurements (Figure 3.21) showed an endothermic transition at 110°C, again consistent with surface water and another endothermic transition at 220°C, caused by de-intercalation of naphthalene. It is also unlikely that naphthalene, a hydrophobic molecule, would co-intercalate with water. Atomic absorption analysis of the intercalation product indicated that the levels of lithium present were below the detection levels of the instrument (<0.005 moles of Li per mole of MoS_2). Table 3.4 shows repeated preparations, only varying in the period of stirring following acidification; the corresponding composition (taken from combined TGA and CH analysis) and final interlayer expansion. Stirring times longer than 14 days did not lead to any increase in the degree of intercalation beyond this value.

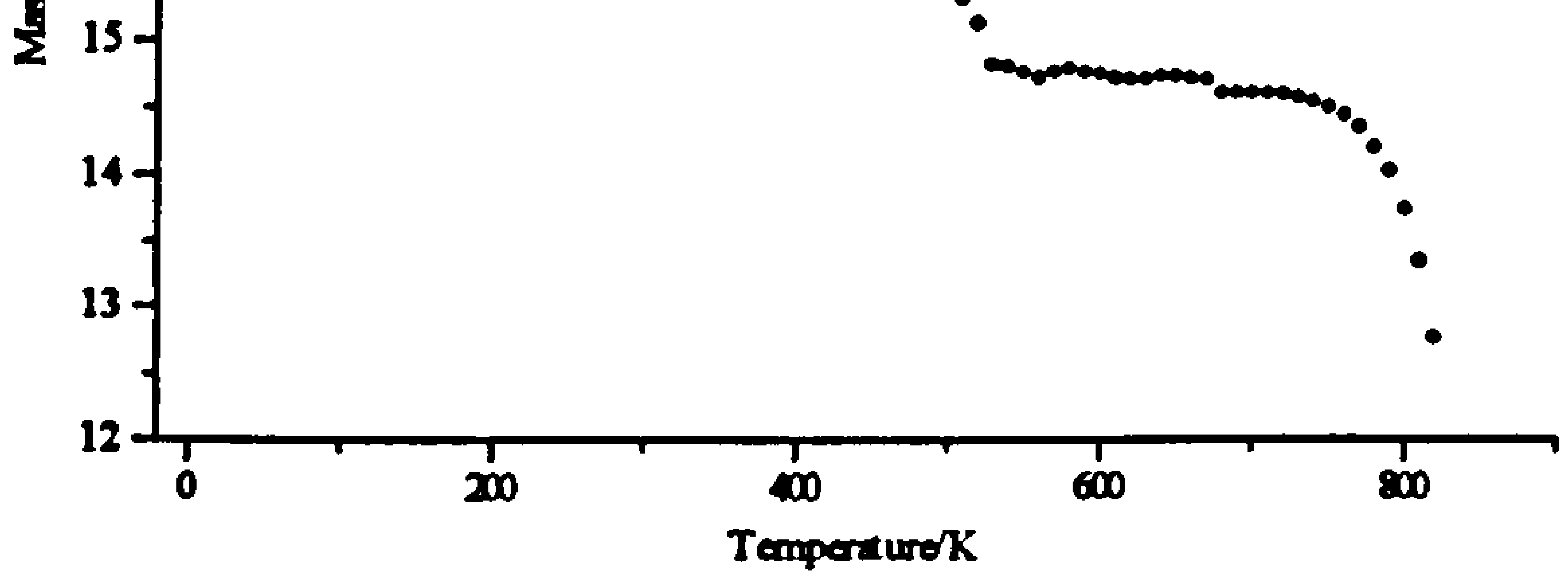

Figure 3.20: TGA plot for $(C_{10}H_8)_{0.13}(H_2O)_{0.05}MoS_2$

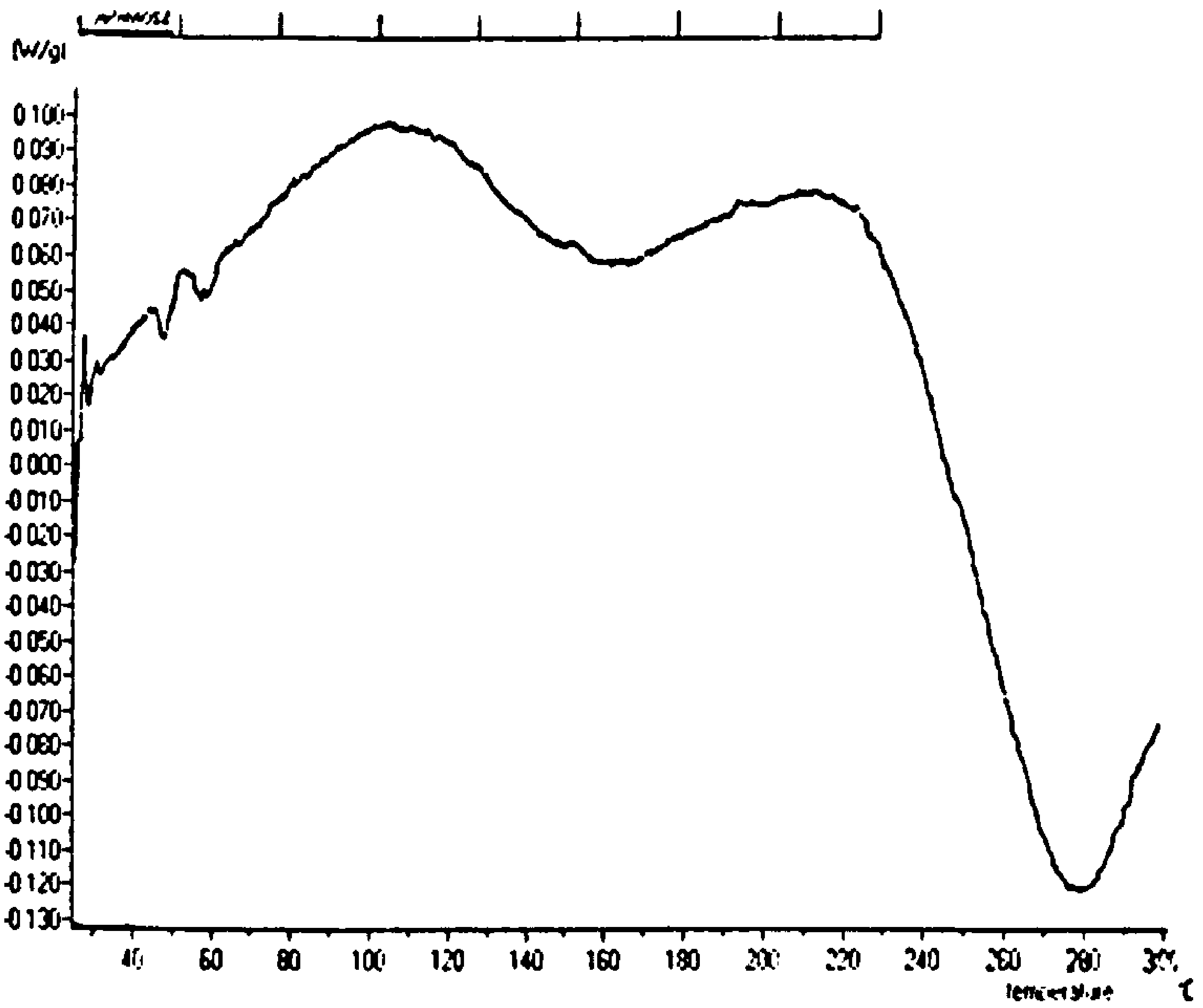

Figure 3.21: DSC of $(C_{10}H_8)_{0.13}(H_2O)_{0.24}MoS_2$

Table 3.4: Compositions of naphthalene intercalates achieved.

STIRRING TIME/DAYS	ΔC/Å	EMPIRICAL FORMULA (CH ANALYSIS)	EMPIRICAL FORMULA (CH+TGA COMBINED)
1	2.43	$(C_{10}H_8)_{0.07}(H_2O)_{0.11}MoS_2$	$(C_{10}H_8)_{0.07}(H_2O)_{0.06}MoS_2$
7	2.91	$(C_{10}H_8)_{0.08}(H_2O)_{0.33}MoS_2$	$(C_{10}H_8)_{0.08}(H_2O)_{0.28}MoS_2$
9	3.74	$(C_{10}H_8)_{0.11}(H_2O)_{0.26}MoS_2$	$(C_{10}H_8)_{0.11}(H_2O)_{0.20}MoS_2$
13	3.53	$(C_{10}H_8)_{0.13}(H_2O)_{0.19}MoS_2$	$(C_{10}H_8)_{0.13}(H_2O)_{0.14}MoS_2$
19	3.85	$(C_{10}H_8)_{0.13}(H_2O)_{0.33}MoS_2$	$(C_{10}H_8)_{0.13}(H_2O)_{0.24}MoS_2$
14	3.81	$(C_{10}H_8)_{0.13}(H_2O)_{0.05}MoS_2$	$(C_{10}H_8)_{0.13}(H_2O)_{0.05}MoS_2$
14	4.26	$(C_{10}H_8)_{0.20}(H_2O)_{0.19}MoS_2$	$(C_{10}H_8)_{0.20}(H_2O)_{0.12}MoS_2$

Having successfully established a synthetic route for the intercalation of naphthalene, the physical properties of the material were investigated. Powder X-ray diffraction provided only limited information (Figure 3.22). The two strong lines corresponding to the 001 and 002 reflections, which provide the interlayer expansion, are both broad. This is due to the small particle size estimated to be ca. 125Å from the

Scherrer formula. All hk0 reflections show pronounced Warren broadening leading to a series of characteristic saw-tooth features in the diffraction pattern. This is an indication of the highly anisotropic nature of this material.

The interlayer expansion with respect to MoS_2 is approximately 3.8Å. Molecular modelling calculations[159] indicate the van der Waals size of naphthalene to be ca. 6.8Å × 5.1Å. Hence the observed Δc value would suggest that the plane of the aromatic species is parallel to the MoS_2 layers. Further evidence for naphthalene intercalation with this orientation is provided by the fact that the p_z orbitals in naphthalene project above and below the plane of the ring in such a way as to give the ring an effective thickness of ca. 3.7Å[160]. This is consistent with the interlayer expansion observed in these products; a $\Delta c<3.7$Å implies some interlayer gaps are unoccupied.

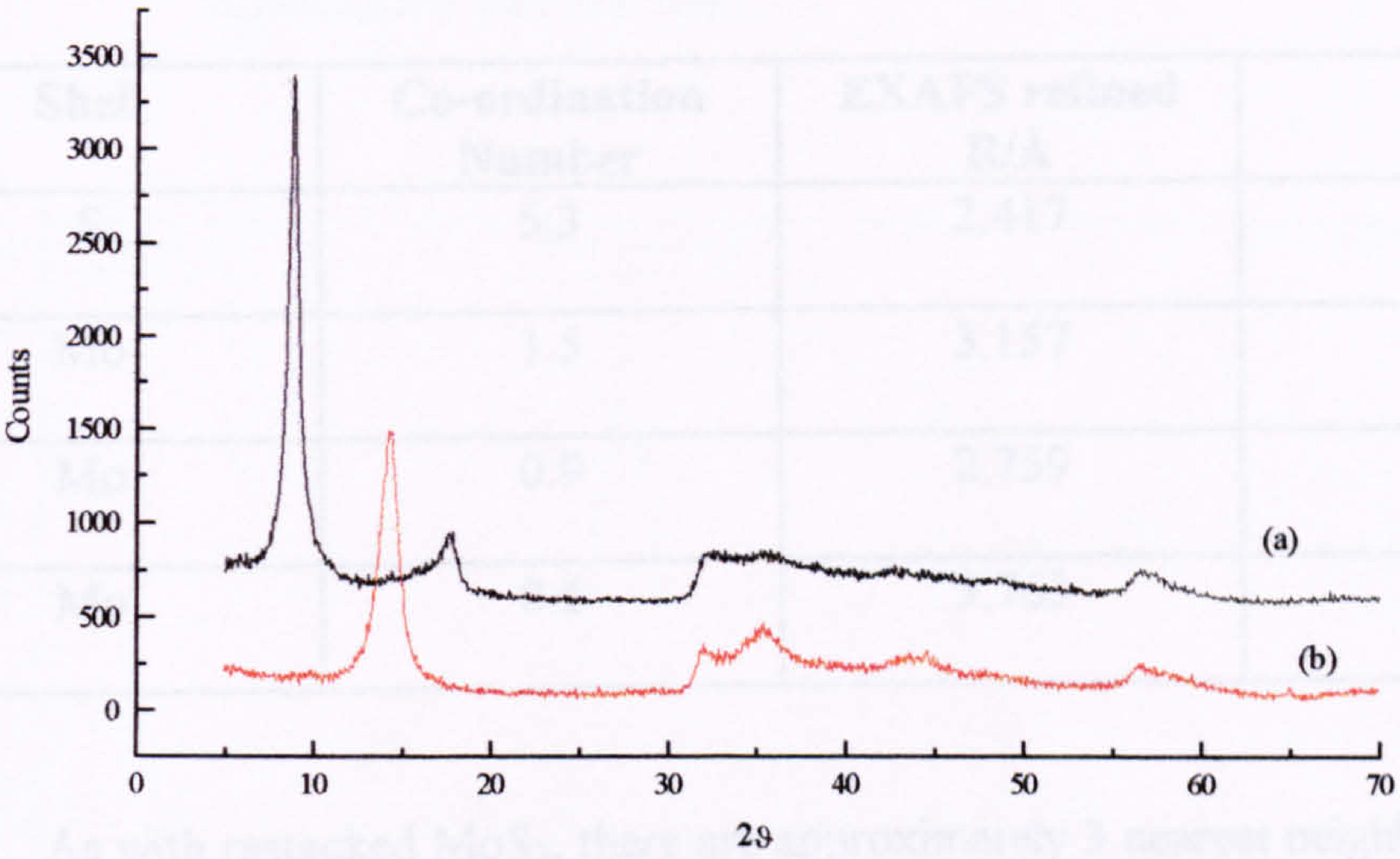

Figure 3.22: Powder X-ray diffraction patterns of (a) $(C_{10}H_8)_{0.13}(H_2O)_{0.05}MoS_2$ *and (b) Restacked* MoS_2 $(MoS_2.0.16H_2O)$

The area of a naphthalene molecule is approximately 35Å^2. This compares with the interlayer area of ca. 8.6Å^2 per molybdenum atom in MoS_2. Geometric constraints suggest therefore that the maximum uptake of naphthalene is approximately 0.25 per molybdenum atom. Steric repulsion effects between neighbouring naphthalene molecules are likely to prevent maximum occupancy of the interlayer space from being attained, resulting in the maximum intercalate content of 0.20 per mole of MoS_2.

3.7.2 EXAFS of Naphthalene intercalated MoS_2

Figures 3.23a and 3.23b show the EXAFS and Fourier transforms of restacked MoS_2, compared with $(C_{10}H_8)_{0.13}(H_2O)_{0.05}MoS_2$. The contribution to the EXAFS from the first shell of sulphur atoms at ca. 2.4Å is very similar in both cases but there are slight differences in the 3.0-3.5Å region.

Table 3.5: *EXAFS refinement data for* $(C_{10}H_8)_{0.13}(H_2O)_{0.05}MoS_2$

FI=0.00020, R=20.19%

Shell	**Co-ordination Number**	**EXAFS refined R/Å**	**A/Å^2**
S	5.3	2.417	0.012
Mo	1.5	3.157	0.013
Mo	0.9	2.759	0.008
Mo	0.6	3.763	0.011

As with restacked MoS_2, there are approximately 3 nearest neighbour Mo atoms, at variable distances. There is a slightly larger molybdenum contribution to the co-ordination shell at 2.76Å and a smaller contribution at a distance of 3.76Å compared to the restacked material. Refinement using these data (Figure 3.24) indicates there appears to be little perturbation to co-ordination environment of molybdenum within the metal sulphide single layer on intercalation of naphthalene.

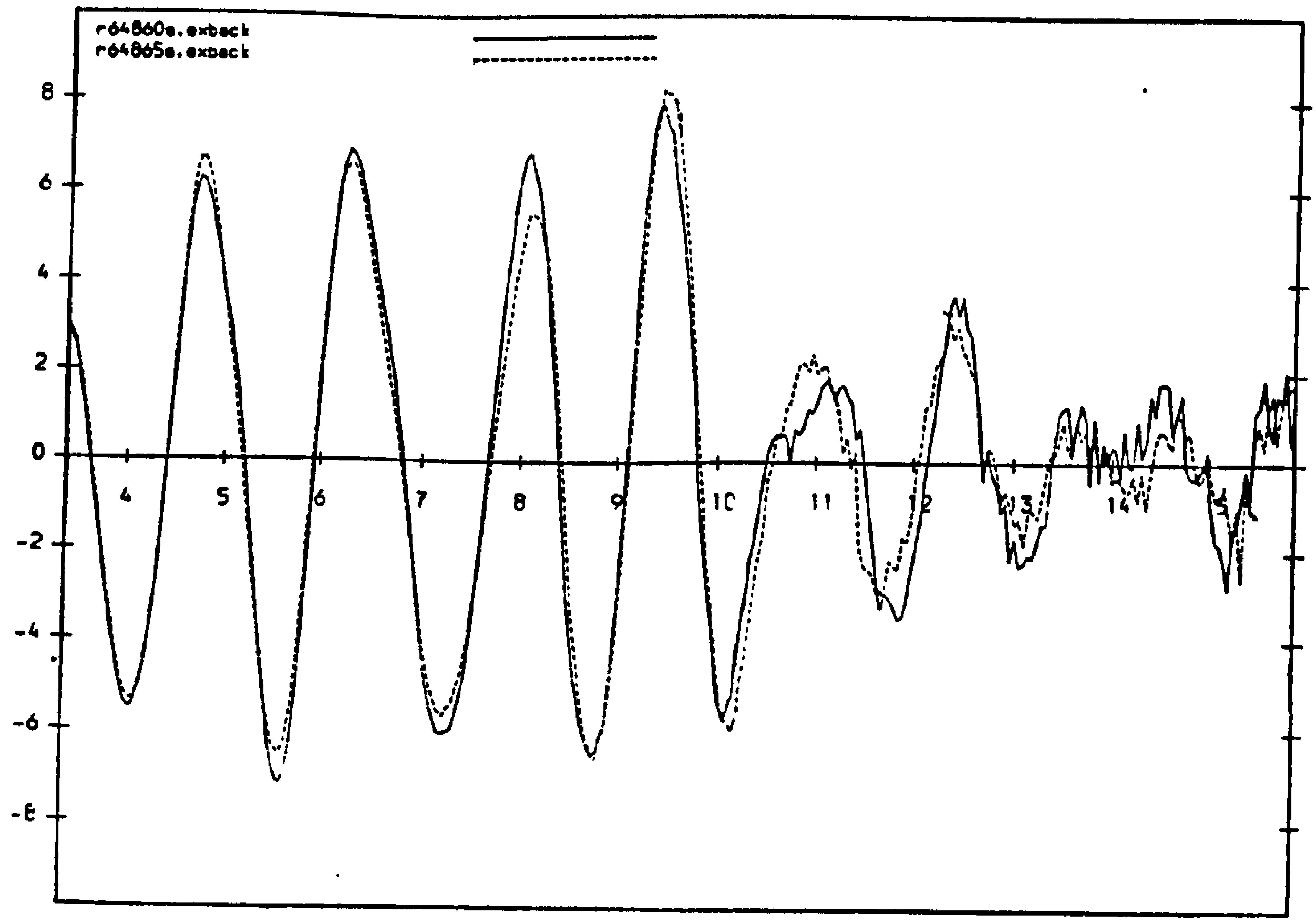

Figure 3.23a: EXAFS for restacked MoS_2 (solid line) and MoS_2 intercalated with naphthalene (dashed line).

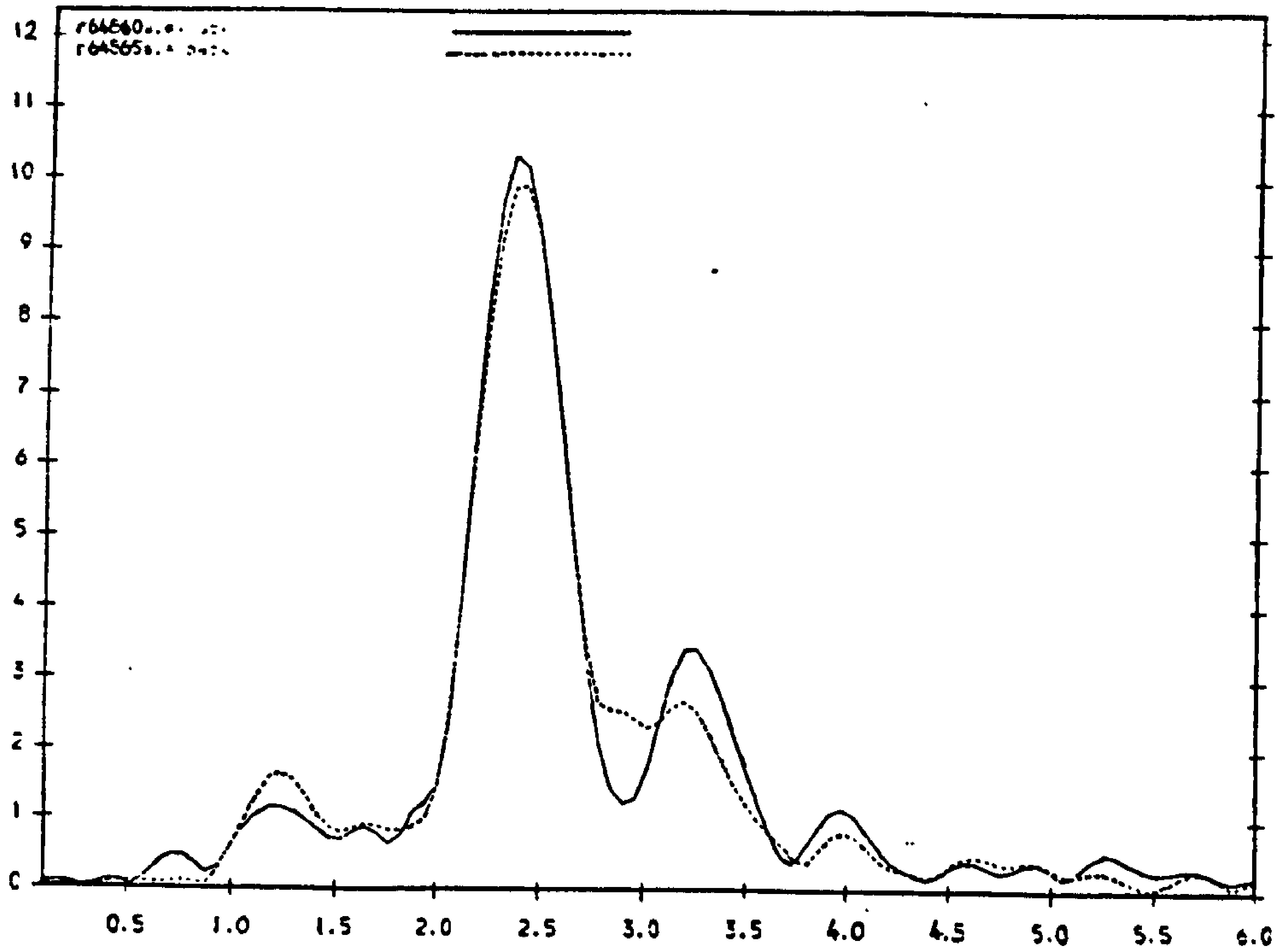

Figure 3.23b: Fourier transforms for restacked MoS_2 (solid line) and MoS_2 intercalated with naphthalene (dashed line).

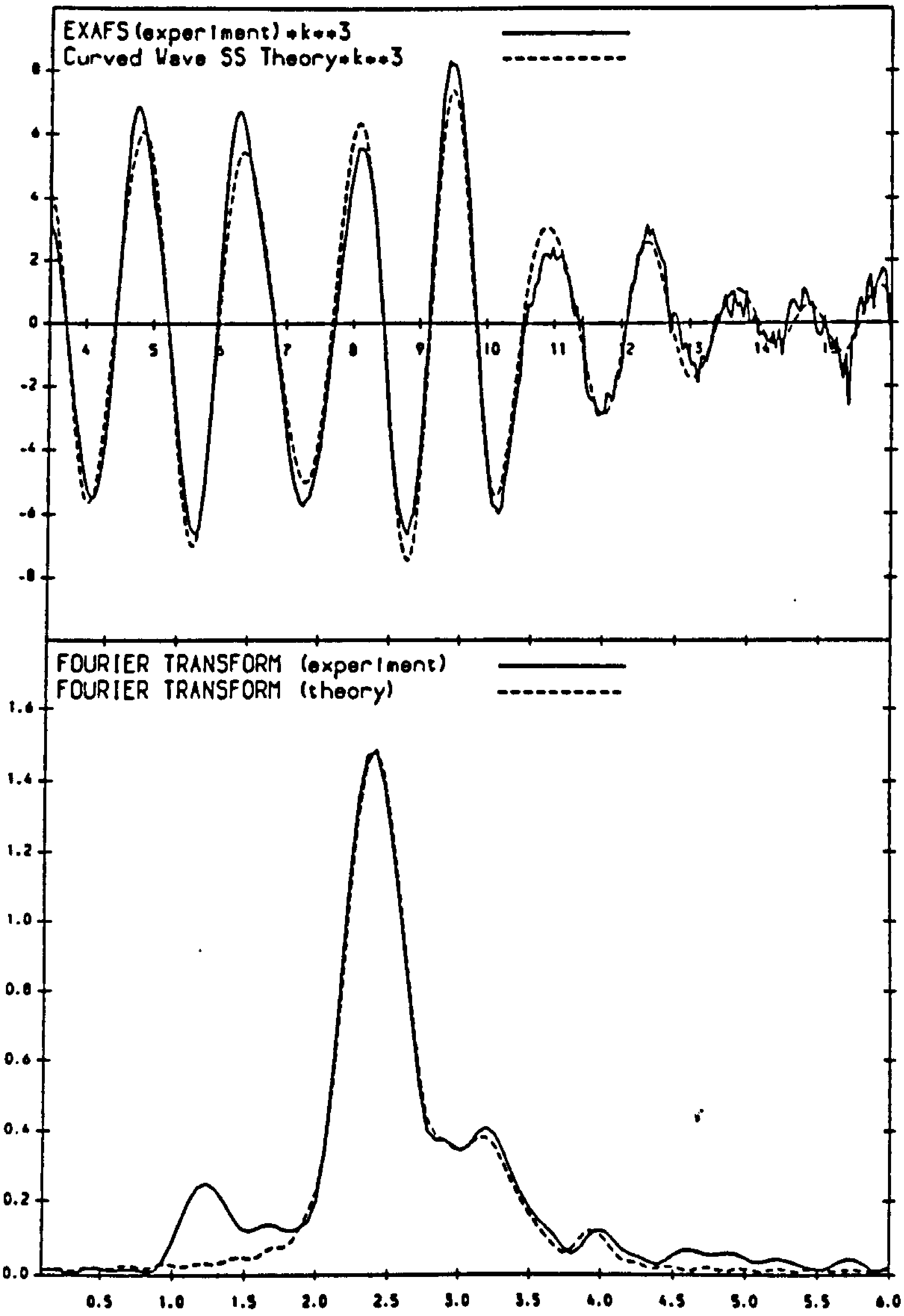

Figure 3.24: Fits to data for $(C_{10}H_8)_{0.13}(H_2O)_{0.05}MoS_2$.

3.7.3 Physical Properties of the Naphthalene Intercalate of MoS_2

Magnetic susceptibility data for an intercalate of composition $(C_{10}H_8)_{0.11}(H_2O)_{0.20}MoS_2$ are shown in Figure 3.25. Surprisingly, this intercalation compound is weakly paramagnetic, with a sharp upturn in the susceptibility below 50K. The source of the paramagnetism could arise from interaction between the π electrons of the naphthalene and the MoS_2 layers, electron transfer being directed into the host structure or from partial reduction of the MoS_2 layer, originating from the single layer suspension which is carried through to this compound.

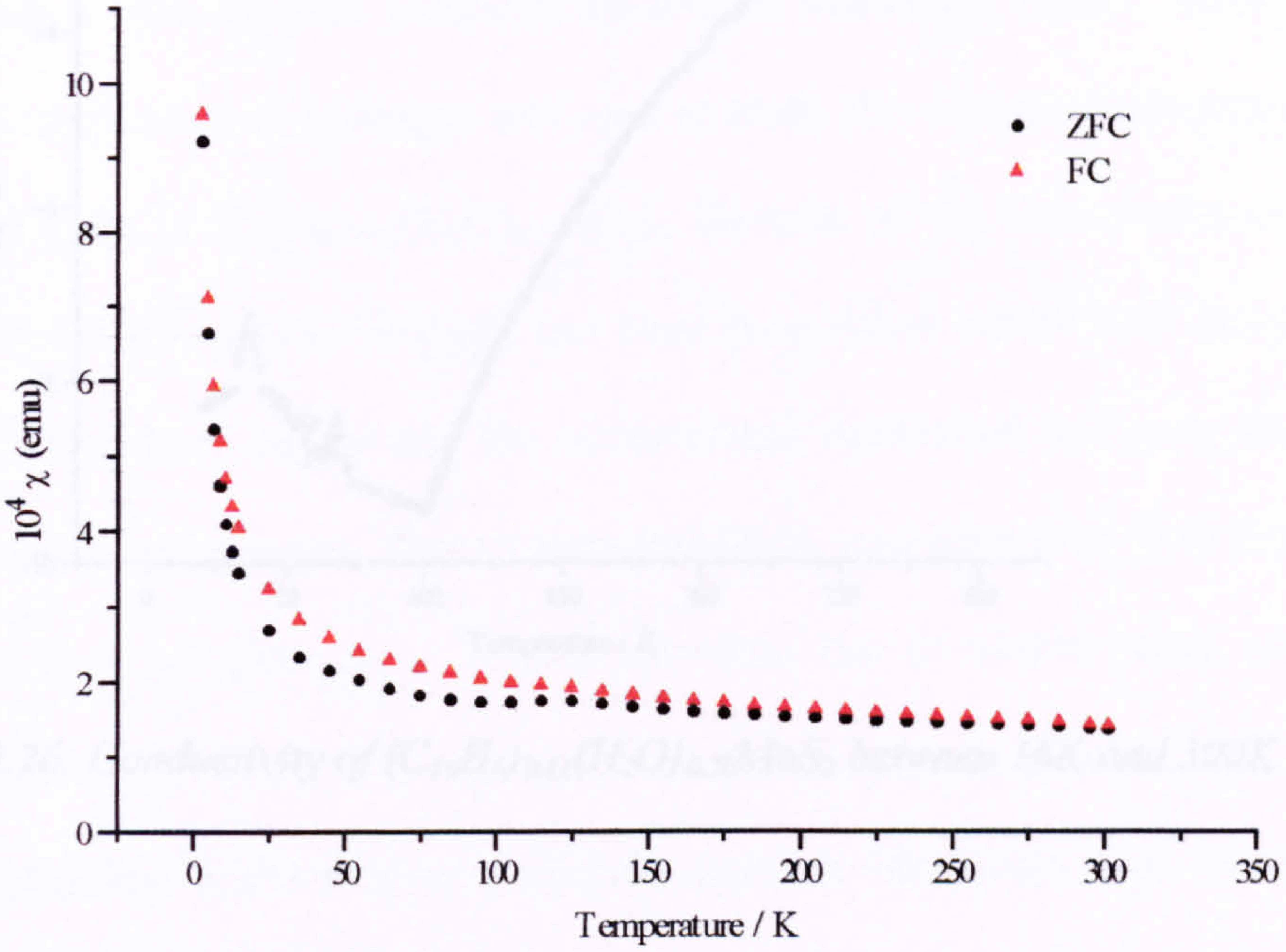

Figure 3.25: Magnetic susceptibility data for $(C_{10}H_8)_{0.11}(H_2O)_{0.20}MoS_2$.

The four-probe conductivity data for this intercalate are presented in Figures 3.26 and 3.27. Figure 3.26 shows measurements recorded over the temperature range 16-300K. Measurements were extended to lower temperatures, using helium as a cryogen. At the time of these measurements at lower temperatures, carbon deposits on the pellet holder were causing sporadic erroneous measurements and less reliable measurements of the conductivity ensued. The intercalate shows unusual behaviour. At high temperatures, a positive $d\sigma/dT$ is consistent with semiconducting behaviour. However, at 100K, the conductivity passes through a minimum and $d\sigma/dT$ changes sign. Extension of the measurements to lower temperatures revealed that the conductivity continues to increase with further cooling to 37K, at which point a second transition is observed. The fit of the data to $T^{-1/4}$ indicates that variable range hopping is taking place as a dominant mechanism of conduction in this temperature region.

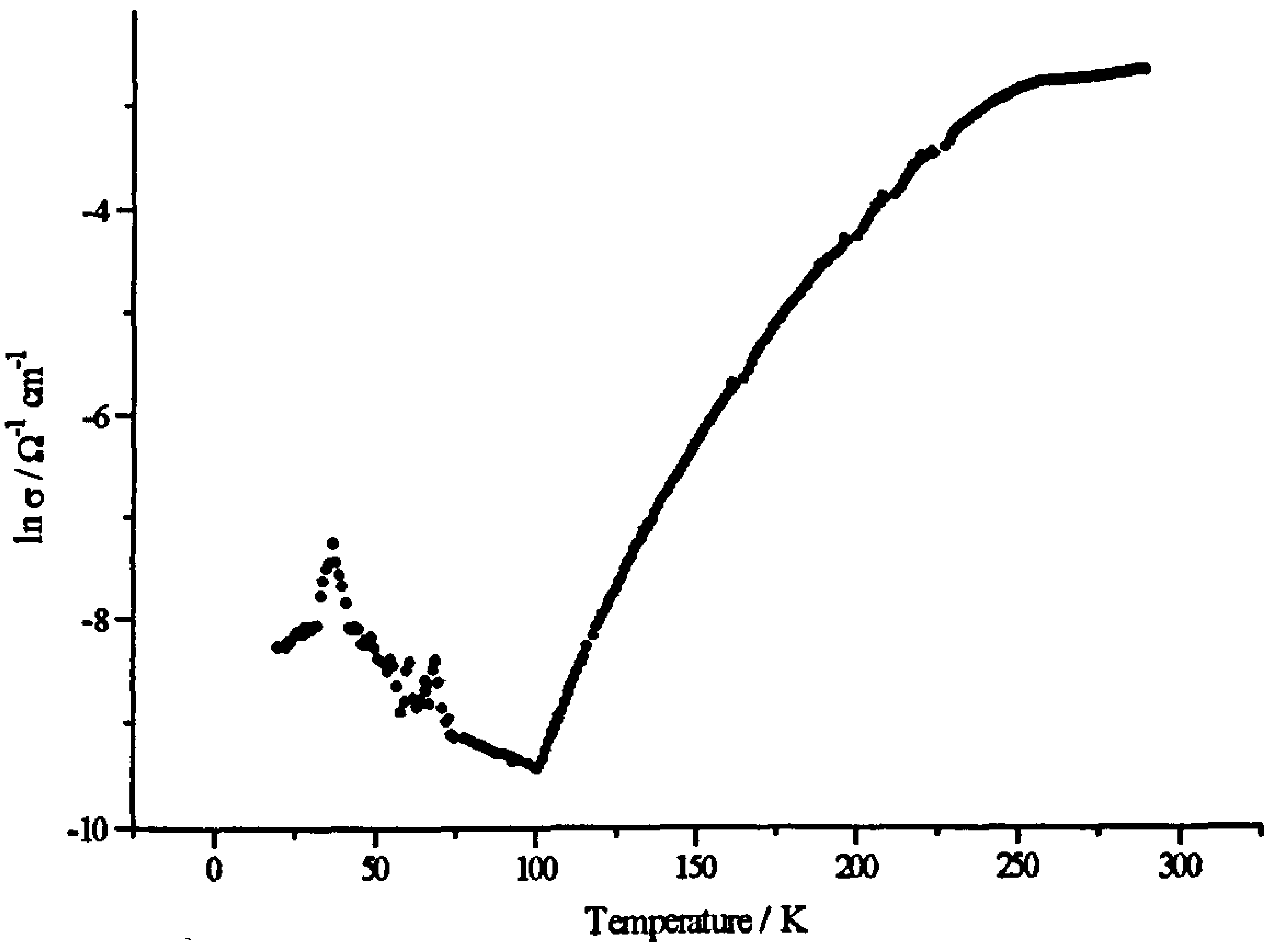

Figure 3.26: Conductivity of $(C_{10}H_8)_{0.11}(H_2O)_{0.20}MoS_2$ between 16K and 300K

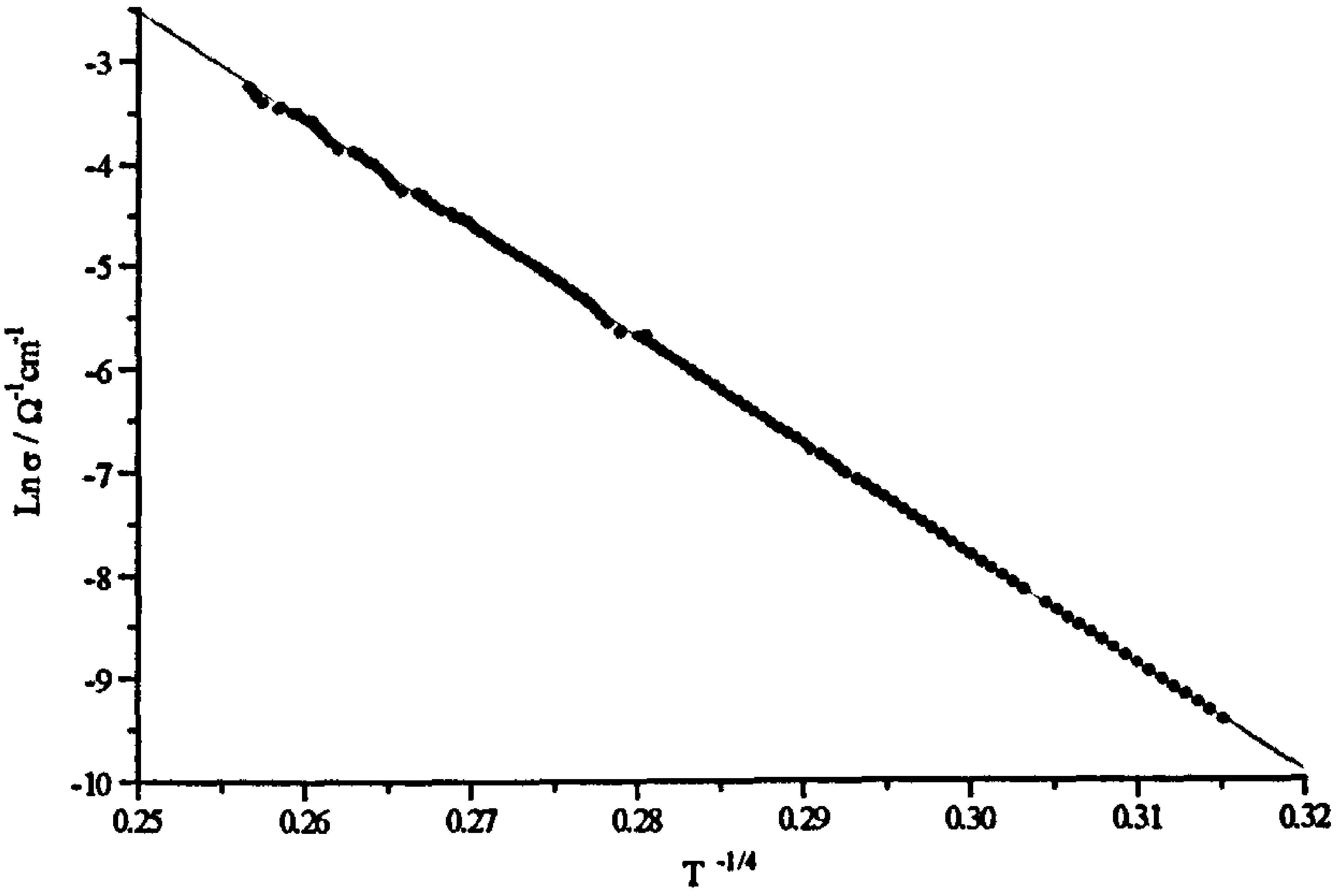

Figure 3.27: Ln σ against $T^{1/4}$ for $(C_{10}H_8)_{0.11}(H_2O)_{0.20}MoS_2$ between 100K and 220K

3.7.4: Inelastic Neutron Scattering Study of $(C_{10}H_8)_{0.15}(H_2O)_{0.10}MoS_2$

Owing to the poorly crystalline nature of the intercalation compound, spectroscopic methods provided an alternative to diffraction methods for sample characterisation. The extreme sensitivity of INS to vibrational modes involving large amplitudes of vibration of hydrogen was used to study the vibrational properties of the naphthalene guest in $(C_{10}H_8)_{0.15}(H_2O)_{0.10}MoS_2$. Samples of the intercalation compound and restacked MoS_2 ($MoS_2.0.05H_20$) had been preweighed before their spectra were collected. Using these masses and the compositions determined for each, the spectra were normalised to hydrogen. That of restacked MoS_2 was subtracted from that for the intercalated material. This was to remove vibrations due to surface water, present on both samples.

Naphthalene is the simplest polycyclic aromatic with fused rings. There are 48 normal modes for the naphthalene molecule, classified according to symmetry types as follows[162]

$$\Gamma_v = 9A_{1g} + 4A_{1u} + 8B_{1g} + 4B_{1u} + 3B_{2g} + 8B_{2u} + 4B_{3g} + 8B_{3u}$$

Recently, numerous normal co-ordinate calculations of naphthalene (as the simplest of the benzenoid hydrocarbons) have been made.[163,164,165,166] Recent improvements in computer power have enabled normal mode calculations to be carried out, using the known molecular geometry and harmonic force constants, which permit assignment of the experimental vibrations to the calculated normal modes to be made with confidence. Vibrational frequencies observed by INS were assigned to normal modes (Table 3.6) calculated by Pauzat[163] and Swiderek[164]. Apart from r(CH) and the α(CCC) modes, no in-plane modes can be assigned to the vibration of any individual bond or angle. This is a characteristic feature of cyclic compounds in general and cyclic aromatics in particular. Figure 3.28 shows the structure of naphthalene and the definition of internal co-ordinates used.

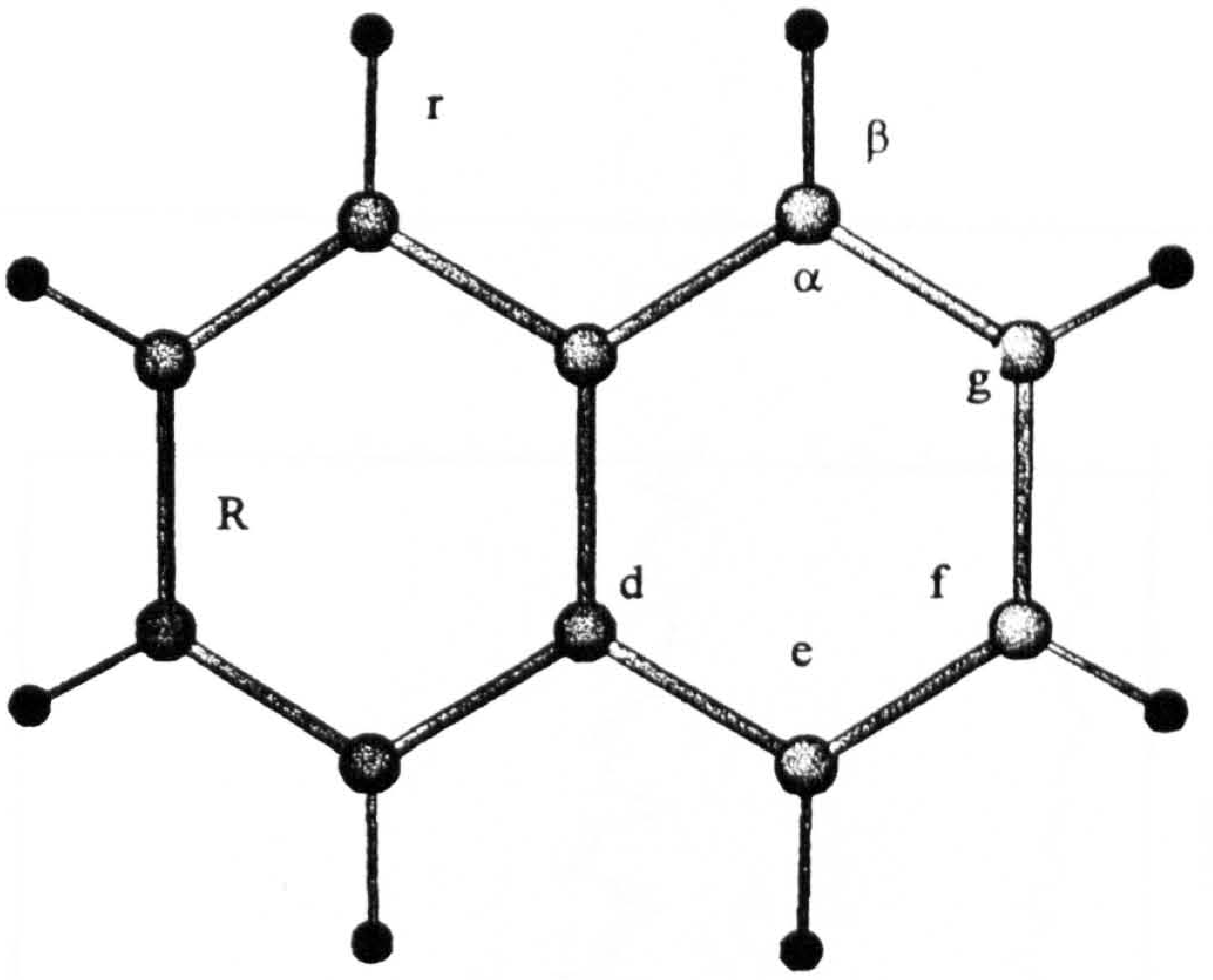

R; C-C bonds; R(C-C)= CC stretching vibrations

r; C-H bonds; r(C-H)= CH stretching vibrations

α; CCC angles $C_dC_eC_f$ and $C_eC_fC_g$; α(CCC)= CCC in-plane bending vibrations

β; β(CH)= in-plane C-H bending vibrations

ε; ε(CH)= out-of-plane bending of C-H

τ; dihedral angle between planes; τ(CCC)= CCC out-of-plane bending vibrations

Figure 3.28: Structure of naphthalene molecule and definitions of vibrational motion.

Figure 3.29 shows that all naphthalene modes are suppressed in the intercalate with the exception of three, identified as:-

B_{2g} → τ (CCC) → 461cm^{-1} B_{2g} → ε (CH) → 959cm^{-1} B_{3g} → β (CH) → 1158cm^{-1}

These normal modes correspond to a dihedral angle bend, an out-of-plane CH bend and a CH in-plane bend respectively. The reduction in intensity for all other modes implies that these motions are inhibited. This is consistent with hindering of the vibrational motions of the naphthalene molecule between the molybdenum disulphide layers. If the naphthalene molecule were located on the surface of the compound, such extended suppression of the vibrational modes would not be expected. The three vibrational bands which do appear in the spectrum are the strongest bands in the INS of pure naphthalene (Figure 3.30).

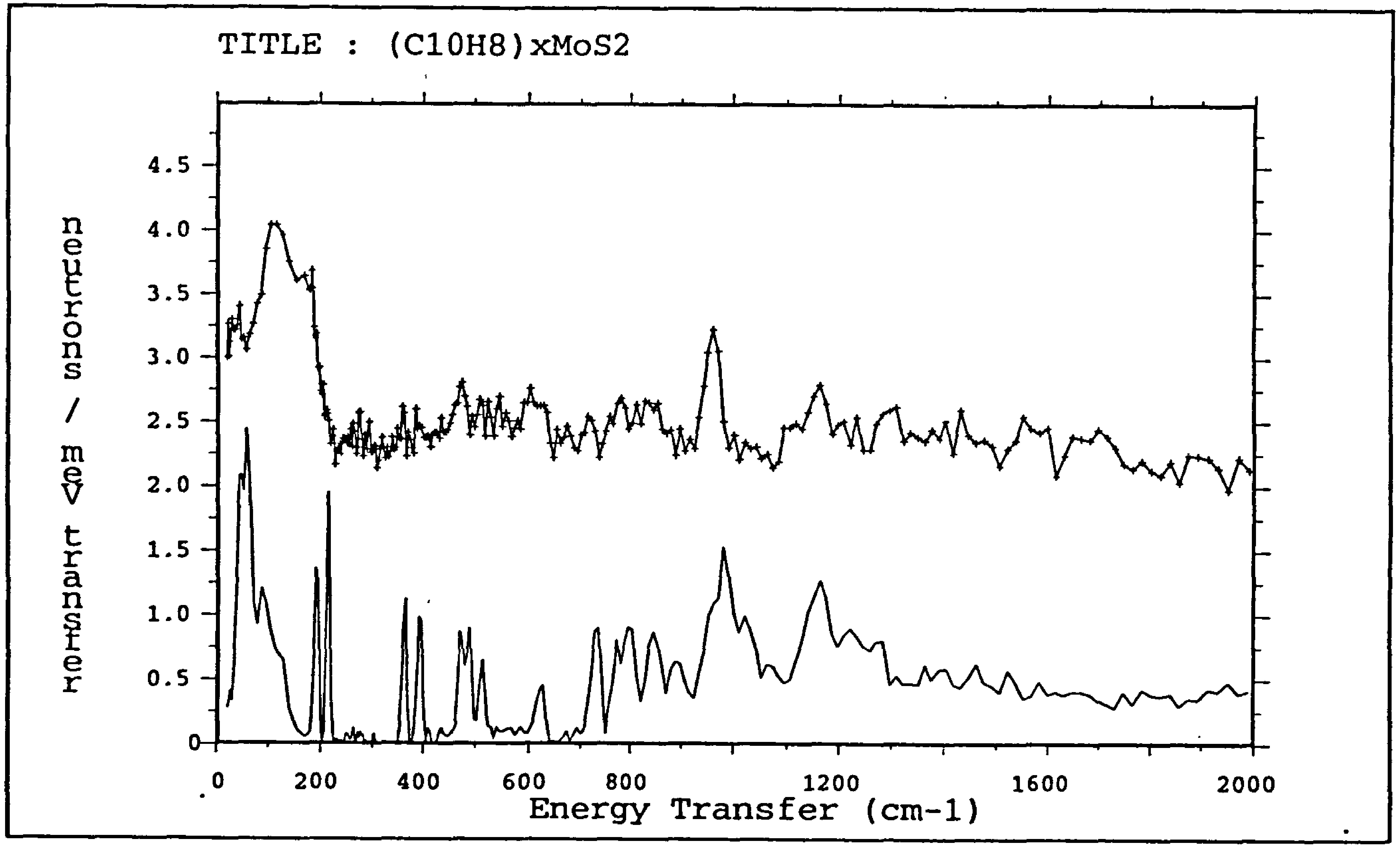

Figure 3.29: INS spectra of $(C_{10}H_8)_{0.15}(H_2O)_{0.10}MoS_2$ *and naphthalene*

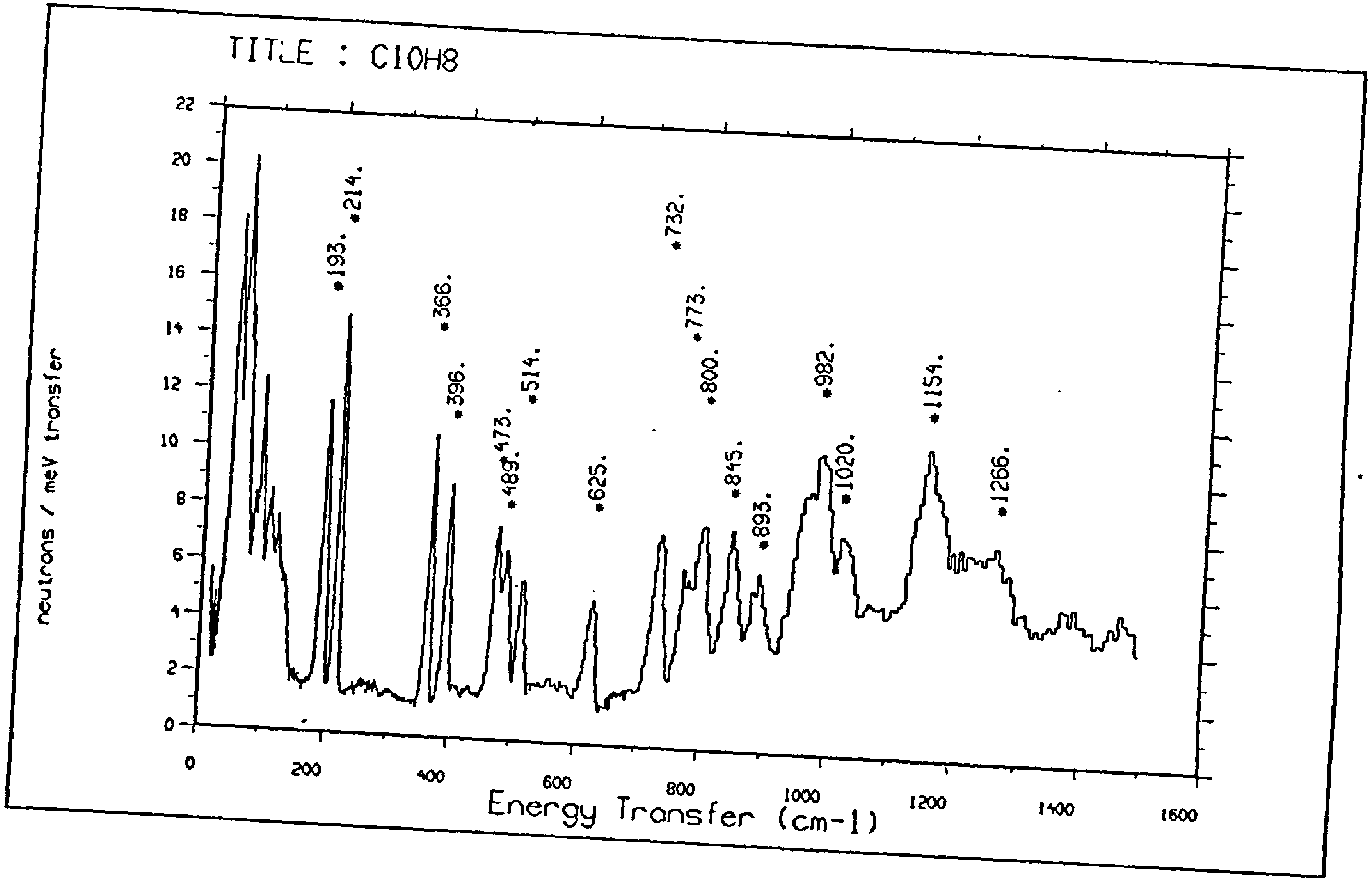

Figure 3.30: INS spectrum of naphthalene

Table 3.6: Observed and calculated frequencies for vibrations of naphthalene.

ν_{obs} / cm^{-1}	ν_{calc}/cm^{-1} Swiderek[164]	ν_{calc}/cm^{-1} Pauzat[163]	Symmetry	Assignment
193			-	
214			-	
366	354	359	b_{1u}	α(CCC)
396	387	386	b_{1g}	τ(CCC)
473	471	461	b_{2g}	τ(CCC)
489	480	476	b_{3u}	τ(CCC)
514	512	512	b_{3g}	α(CCC)
625	626	618	b_{2u}	α(CCC)
732	705	717	b_{1g}	ε(CH)
773	773	770	b_{2g}	τ(CCC)
800	792	782	b_{3u}	ε(CH)
845	825	841	a_{1u}	ε(CH)
893	897	876	b_{2g}	ε(CH)
982	981	970	a_{1u}	ε(CH)
1020	1023	1025	a_{1g}	R(CCC)+β(CH) +α(CCC)
1154	1156	1158	b_{3g}	β(CH)
1266	1272	1266	b_{1u}	R(CC)+β(CH)+ α(CCC)

Chapter Four

Organic Intercalation Compounds of MoS_2

4.1 INTRODUCTION

Chapter Three described the insertion of naphthalene molecules between the MoS_2 layers using the technique of exfoliation of MoS_2 to form "single molecular" layers, followed by reflocculation of the layers in the presence of the intercalating species. This work was subsequently extended to the intercalation of other small electron-rich organic molecules. These include substituted naphthalene derivatives and other fused-ring systems. The primary intention was to establish whether this synthetic method, which had been successful with naphthalene guest species, was generic in its application to other organic molecules. Furthermore it provided an opportunity to investigate systematic trends in the observed physical properties of the nanocomposites formed. Of particular interest was the relationship between structural and physical properties of the material to basic features such as ring size, number of rings or the presence of heteroatoms in the guest species. This chapter presents the results of studies on the insertion of a variety of organic guest species into MoS_2.

4.2 GUEST SPECIES

Slight modifications to the synthetic method that had been used for insertion of naphthalene were introduced in certain cases in order to optimise the procedure. Guest species were selected to allow investigation of the effect of varying ring size, ex-ring functionality and heteroatom within the rings. The intercalation of anthracene was unsuccessful. However, anthracene is only sparingly soluble in polar solvents and almost totally insoluble in water. This lack of solubility results in little intermixing of anthracene and the aqueous suspension of single layer MoS_2 and hence, is thought to be the reason for its failure to intercalate. Intercalation was successful to varying degrees for those organic molecules listed in Table 4.1.

Table 4.1: Guest species intercalated into MoS_2

Organic Species	**Synthetic method**
2-Methylnaphthalene	As for naphthalene
2-Ethylnaphthalene	As for naphthalene
Pyridine	Pyridine added directly to exfoliated MoS_2, no dichloromethane.
Benzofuran	Conc. of benzofuran in dichloromethane = 1.5M
Biphenyl	As for naphthalene
Crystal Violet	a) 1:1 molar ratio of crystal violet: $\{MoS_2\}_{exf}$ b) crystal violet dissolved in $25cm^3$ DCM

Table 4.2 lists the increase in the repeat distance parallel to the c axis (Δc) and the corresponding degree of uptake of guest species. All figures summarising the studies of these intercalates are presented at the end of the chapter; the composition of each intercalate relating to these data is that given in Table 4.2. The powder X-ray diffraction patterns are shown in Figures 4.13-4.18 As with the naphthalene intercalate, these diffraction patterns indicate that poorly crystalline phases have been formed. The 001 and 002 reflections are present in all but that of the 2-ethylnaphthalene intercalate. There is also the characteristic saw-tooth shape to the reflections, which becomes more pronounced with increasing diffraction angle, indicating that there is turbostratic disorder in these products. Thermogravimetric plots for intercalates are presented in Figures 4.7-4.12. As can be seen, there is a gradual mass loss up to a temperature of approximately

690°C that corresponds to three processes: loss of water, de-intercalation of the organic guest species and oxidation of MoS_2 to MoO_3. The difficulty in separating these three decomposition stages resulted in compositional analysis being achieved by a combination of TGA and CHN, as described in Section 2.3.3. The sharp mass loss above 690°C is due to sublimation of MoO_3. Since it was not possible to distinguish weight changes solely from the loss of water from those of the organic guest molecule, the %C was taken from CHN analysis and used to calculate the organic molecule content. The gradual mass loss observed at low temperature on the TGA was then used to determine the water content.

Table 4.2: Compositions of materials with highest degree of intercalation

Guest species	Empirical analysis (TGA+CHN)	Lithium content.	Δc / Å
2-methylnaphthalene	$(C_{11}H_{10})_{0.19}(H_2O)_{0.05}MoS_2$	0.003	4.29
2-ethylnaphthalene	$(C_{12}H_{12})_{0.09}(H_2O)_{0.55}MoS_2$	0.0023	3.51
Pyridinium	$(C_5H_6N)_{0.15}(H_2O)_{1.58}MoS_2$	undetectable	3.35
Benzofuran	$(C_8H_6O)_{0.18}(H_2O)_{0.93}MoS_2$	0.0012	4.84
Biphenyl	$(C_{12}H_{10})_{0.17}(H_2O)_{0.07}MoS_2$	undetectable	5.78
Crystal violet	$(C_{25}H_{30}N_3)_{0.07}(H_2O)_{0.55}MoS_2$	0.009	4.00

The structures and dimensions of the organic molecules were modelled using "Chem 3D Pro"[159] software. For a given molecule, this program determines the configuration of minimal energy. Distances between atoms are measured from between the centres of atoms, schematic drawings of these guest species are presented in Figures 4.1-4.6.

4.3 2-METHYLNAPHTHALENE

Intercalation of 2-methylnaphthalene into MoS_2, resulted in an increase in interlayer spacing of 4.29Å (Figure 4.13). For the naphthalene intercalate with an equivalent degree of guest content, the increase in interlayer spacing was 4.26Å. Initially it was assumed that the extra bulk of the methyl group would produce a greater expansion of the inter-layer space than for naphthalene intercalation. However, computer modelling studies of the methyl derivative revealed that the methyl group does not increase the effective "thickness" of the aromatic rings beyond 3.7Å (due to p_π electron density.) Thus intercalation of 0.19 mole of 2-methylnaphthalene would be expected to increase the interlayer spacing by approximately the same amount as 0.19 mole of naphthalene. Three separate products, containing different amounts of 2-methylnaphthalene were obtained. Table 4.3 lists the compositions, together with the reaction time and the Δc determined from powder X-ray diffraction.

Table 4.3: Products obtained on intercalating 2-methynaphthalene

Composition	Reaction time/days	Position of 001 reflection/Å	Δc/Å
$(C_{11}H_{10})_{0.09}(H_2O)_{0.14}MoS_2$	14	10.16	3.96
$(C_{11}H_{10})_{0.12}(H_2O)_{0.21}MoS_2$	18	10.23	4.03
$(C_{11}H_{10})_{0.19}(H_2O)_{0.05}MoS_2$	21	10.48	4.29

From these reactions, it appears that the uptake of 2-methylnaphthalene shows a similar dependence on reaction time as was observed for naphthalene intercalation. Reaction times longer than three weeks were not used.

Electrical conductivity data for the intercalate $(C_{11}H_{10})_{0.19}(H_2O)_{0.05}MoS_2$ are presented in Figure 4.19. At high temperatures, the material exhibits semi-conducting behaviour similar to that observed for restacked MoS_2. However, like the restacked material, it is not of the Arrhenius simple thermally activated type; variable range hopping occurs from 78K to 300K (Figure 4.25). Furthermore, there is a broad transition between 21K and 33K where the sign of $d\sigma/dT$ changes from positive to negative. Therefore this material exhibits a similar electronic transition to that observed in the naphthalene intercalate, although in the 2-methylnaphthalene case it is not as sharp and occurs at a lower temperature. The magnetic susceptibility data for $(C_{11}H_{10})_{0.19}(H_2O)_{0.05}MoS_2$ are shown in Figure 4.30. The material exhibits weak paramagnetism similar to that of the naphthalene derivative, with a marked increase in measured susceptibility at T=50K. The maximum susceptibility is 1.32×10^{-3} emu at 5K.

The 2-methylnaphthalene intercalate was also investigated using EXAFS. The procedure for measuring the EXAFS spectrum and refinement of the data was similar to that for the naphthalene intercalate. The results of refinement are presented in Table 4.4. Figure 4.32 shows the corresponding EXAFS spectrum and Fourier Transform data.

Table 4.4: Co-ordination numbers (N), distances (R) and Debye-Waller factor (A) for $(C_{11}H_{10})_{0.19}(H_2O)_{0.05}MoS_2$ with N fitted. FI=0.00034, R=24.22%.

Co-ordination Shell	**N**	**R/Å**	**A/Å^2**
Mo-S	5.0	2.415	0.011
Mo-Mo	1.0	2.753	0.009
Mo-Mo	1.5	3.153	0.013
Mo-Mo	0.6	3.766	0.017

The molybdenum environment in this material appears to be very similar to that in the naphthalene intercalate. Refinement indicates 5.0 sulphur atoms at a distance of 2.42Å, 1 molybdenum atom at 2.75Å, 1.5 molybdenum atoms at 3.15Å and 0.6 molybdenum atoms at 3.77Å. There is a slightly larger molybdenum contribution at 2.75Å and a slightly smaller one at 3.75Å compared to restacked MoS_2.

4.4 2-ETHYLNAPHTHALENE

The powder X-ray diffraction pattern of MoS_2 intercalated with 2-ethylnaphthalene exhibits broader 001 reflection than in those of the 2-methylnaphthalene or naphthalene intercalates (Figure 4.14). Furthermore, this 001 reflection has a shoulder at higher diffraction angles, suggesting the presence two closely similar phases. In addition, two weak peaks (marked * in Figure 4.14) are distinguishable at $2\theta = 14.26°$ and $2\theta = 15.79°$. The former corresponds to the 001 reflection of restacked MoS_2 in which no guest species has been incorporated. The latter has not been identified, but does not correspond to the 002 reflection of the intercalate material.

The uptake of the 2-ethylnaphthalene is somewhat lower than found for the naphthalene and 2-methylnaphthalene intercalation compounds. This composition was determined for a product which was subject to a reaction period of three weeks. The increase in interlayer spacing upon intercalation is 3.51Å which is smaller than the estimated effective thickness of an aromatic ring (3.7Å). Furthermore, modelling studies of the 2-ethylnaphthalene molecule revealed that the terminal CH_3 group of the ethyl substituent projects out of the plane containing the aromatic rings (Figure 4.2) which should significantly increase the effective thickness of the aromatic ring above 3.7Å.

The area of a 2-ethylnaphthalene molecule is approximately $43Å^2$, so the maximum content (assuming an interlayer area of $8.6Å^2$ per molybdenum unit) is 0.20

mole of ethylnaphthalene per mole of MoS_2. The reaction length was extended to 4 weeks, but a lower intercalate content of 0.08 was obtained, suggesting that approximately 0.10 guest content per mole of MoS_2 is a limiting value. Therefore, a Δc of 3.51Å together with the relatively low degree of insertion suggests that not all van der Waals gaps are occupied by the guest species, although there is no evidence for long range order which would result from staging.

The electrical conductivity data are presented in Figure 4.20. This intercalate shows very similar behaviour to that of 2-methylnaphthalene. Again it is semi-conducting at higher temperatures with a temperature dependence which is not of the Arrhenius type. The ln σ data show $T^{-1/4}$ dependence in the temperature region 80-195K, suggesting that variable range hopping is the dominant conduction mechanism (Figure 4.26). The conductivity also exhibits a sharp a transition at ca. 22K, at which the sign of $d\sigma/dT$ changes sign.

4.5 PYRIDINE

Modelling studies reveal that the pyridine molecule is almost circular, as shown by Figure 4.3. The powder X-ray diffraction pattern (Figure 4.15) indicates a single phase material in which there is an increase in interlayer spacing of 3.35Å. As the synthetic method involves addition of hydrochloric acid to lower the pH below 2, it is likely that the pyridine molecule is actually present in its protonated form i.e. the pyridinium ion. The composition in Table 4.4 has been calculated on this assumption. The smallest increase in repeat distance between the MoS_2 layers would result if the aromatic ring of the pyridine molecule were parallel to the MoS_2 layers. The relatively low value of Δc supports this orientation and probably represents an average of occupied and unoccupied van der Waals gaps. The theoretical uptake of pyridinium ions when adopting this arrangement, is 0.44 mole per mole of MoS_2, which supports the conclusion that only a fraction of vacant interlayer sites are occupied.

Electrical transport properties of the pyridine intercalate are shown in Figure 4.21. On warming from 10K, the conductivity follows thermally activated behaviour, although non-Arrhenius, and the ln σ data can be fitted to a variable range hopping model up to 82K. At this temperature, there is a slight decrease in conductivity up to 125K before it gradually increases as the temperature approaches ambient. Measurements were not made above room temperature because of the risk of decomposition to the intercalate, which would render any data meaningless. No magnetic susceptibilty measurements could be made on this material owing to equipment failure.

4.6 BENZOFURAN

The powder X-ray diffraction pattern of this intercalate is shown in Figure 4.16. A broad 001 reflection at 2θ=8.03°, corresponding to an increase in the interlayer spacing of 4.84Å, dominates this diffraction pattern. There is a broad 002 reflection at 2θ=16.2°. The broadness of the 00*l* reflections indicate that this compound comprises a smaller particle size than the other intercalates. The dimensions of the benzofuran molecule are illustrated in Figure 4.4. The increase in the interlayer spacing is 4.84Å which can be interpreted as resulting from occupation of the interlayer spaces in a similar orientation to that of naphthalene and its alkylated derivatives. Alternatively, the plane containing the aromatic and furan rings of benzofuran could be perpendicular to the molybdenum sulphide layers with the C_2 axis of the molecule parallel to the layers. This orientation would result in a Δc of 5.10Å. However, if some van der Waals gaps remain unoccupied, a Δc of 4.84 Å might be observed.

The electrical transport data of the benzofuran intercalate (Figure 4.22) reveal that at 10K, as the temperature is increased, σ increases in a similar manner to the naphthalene intercalate. $T^{1/4}$ dependence is shown between 82K and 230K (Figure 4.28). There is then a sharp transition at 230 K with $d\sigma/dT$ changing sign. This is in contrast to the behaviour of the other intercalated materials. With increasing temperature, $d\sigma/dT$ changes from being positive to negative for the benzofuran intercalate whereas for the other intercalates exhibiting such transitions, $d\sigma/dT$ changes from negative to positive; none of the other intercalates show such a sharp decrease in conductivity as the temperature approaches ambient.

4.7 BIPHENYL

The biphenyl molecule consists of two unfused aromatic rings. Its structure and dimensions are shown in Figure 4.5. Analysis of the powder diffraction pattern in Figure 4.17 yields an increase in inter-layer distance of 5.78Å. This suggests that the orientation of the guest molecule in the van der Waals gap is with the C-C bond which links the two aromatic rings lying parallel to the MoS_2 layers and with the plane of the aromatic rings perpendicular to the host layers i.e. "on its side." The area of the biphenyl molecule is approximately 40$Å^2$, when the two aromatic rings are co-planar. This would mean that if the aromatic rings were parallel to the Mo-S layers, the geometrically limiting extent of insertion would be ca.0.21 mole of biphenyl per mole of MoS_2. The maximum degree of insertion obtained was 0.17 moles per mole of MoS_2. The distance between H_1 and H_2 (Figure 4.5) obtained from the modelling study is 4.32Å, whereas a Δc of 5.78Å is somewhat different. However, there is one structural feature that differentiates this biphenyl molecule from the organic guest species so far discussed, in that the aromatic rings are not fused. Intra-molecular rotation about the C-C linkage is possible and would allow the two aromatic rings to rotate into a non-coplanar orientation. This would result in an increase in the effective area of the molecule and could explain the marked difference between the gas phase dimensions of the molecule and the Δc observed.

The electrical conductivity data for this material were measured between 80 and 300K and are presented in Figure 4.23. This material is semi-conducting and its conductivity is of a magnitude similar to that of the other intercalates produced. There is no observable transition for this material over this temperature range but, given the behaviour demonstrated by the other products at low temperatures, measurements should be extended to lower temperatures.

The magnetic susceptibility data for the biphenyl intercalate, shown in Figure 4.31, indicate similar behaviour to that of the naphthalene intercalate over the temperature range 5-300K. Although for the biphenyl intercalate, the weak paramagnetism observed is of an order of magnitude greater than that for the naphthalene intercalate at low temperatures.

4.8 CRYSTAL VIOLET

This molecular ion is a triarylmethine dye, existing as dark green glistening crystals. Its molecular dimensions are large compared to the other guest species as it possesses three aromatic rings which radiate out from a central carbon atom in a pseudo-fan blade structure (Figure 4.6). The molecule is a Lewis acid; the site of the positive charge is either an ammonium or a carbenium ion. Such a compound cannot lose a proton like a Brönsted acid, but can abstract a hydroxyl group at the carbenium carbon, forming a carbinol. The symmetrically substituted crystal violet does not have a regular propeller shaped geometry. Polarisation measurements[167] by Davidson and Norden indicate that one of the aminophenyl rings is twisted out of the molecular plane more than the others. This fan blade structure is caused by the steric congestion between the o-hydrogen atoms of the phenyl groups.

This molecule was selected in order to investigate the scope for intercalating large molecules between the layers. Following the lack of success with anthracene, this molecule also offered the advantage of high solubility in dichloromethane, and to a lesser extent, in water. This was considered to be important for facilitating the mixing of the host and guest. A small degree of intercalation occurred; a content of 0.07 moles of crystal violet per mole of MoS_2 was achieved.

The powder diffraction pattern (Figure 4.18), indicates a single phase material and a Δc of 4.0Å. Computer modelling gave approximate dimensions to the molecular ion, from which a surface area of approximately 80$Å^2$ was calculated. This corresponds to a maximum uptake of 0.11 mole of methyl violet per mole of MoS_2, if the guest is oriented with the aromatic rings parallel to the MoS_2 layers. This is close to the observed degree of uptake, determined as 0.07 moles of guest species per mole of MoS_2.

The conductivity data for this intercalate, in Figure 4.24 is comparable in magnitude that of the other intercalates. Generally, it is semiconducting, but shows significant anomalies at 50K and 100K. The data could not be fitted to the variable range hopping model over any temperature range. These two transitions at 50K and 100K suggest that there is a change in the band structure, possibly resulting from a change in the interaction between the guest and the host.

The intercalation of the substituted derivatives of naphthalene and other electron-rich molecules into MoS_2 via exfoliation-reflocculation has been described. In all cases, insertion has results in an increase in the interlayer spacing and a perturbation to the electrical properties of the host to varying degrees. This work will be discussed in Chapter Six.

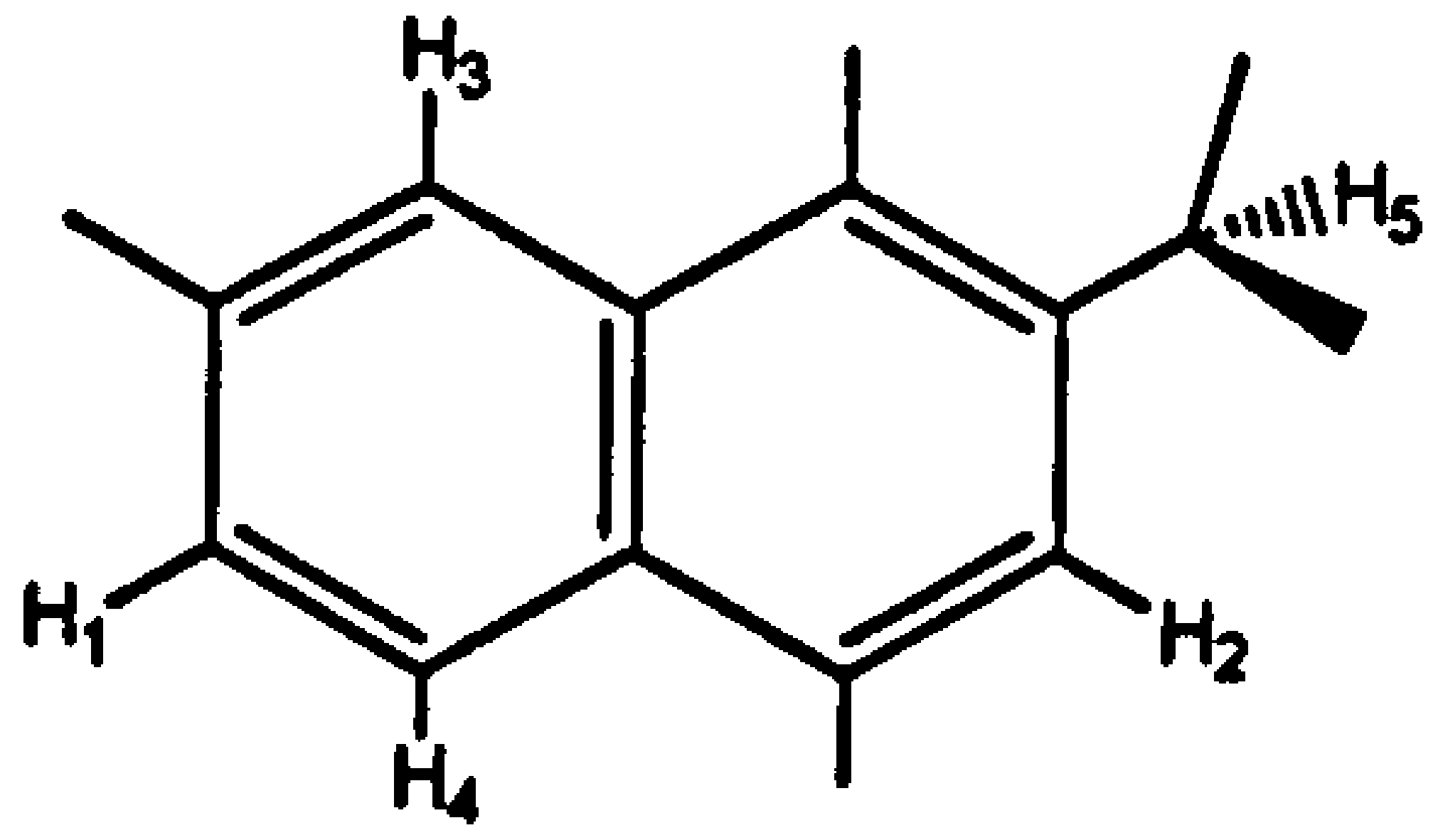

Figure 4.1

H_1-H_2 = 6.78
H_3-H_4 = 5.00
H_1-H_5 = 8.10

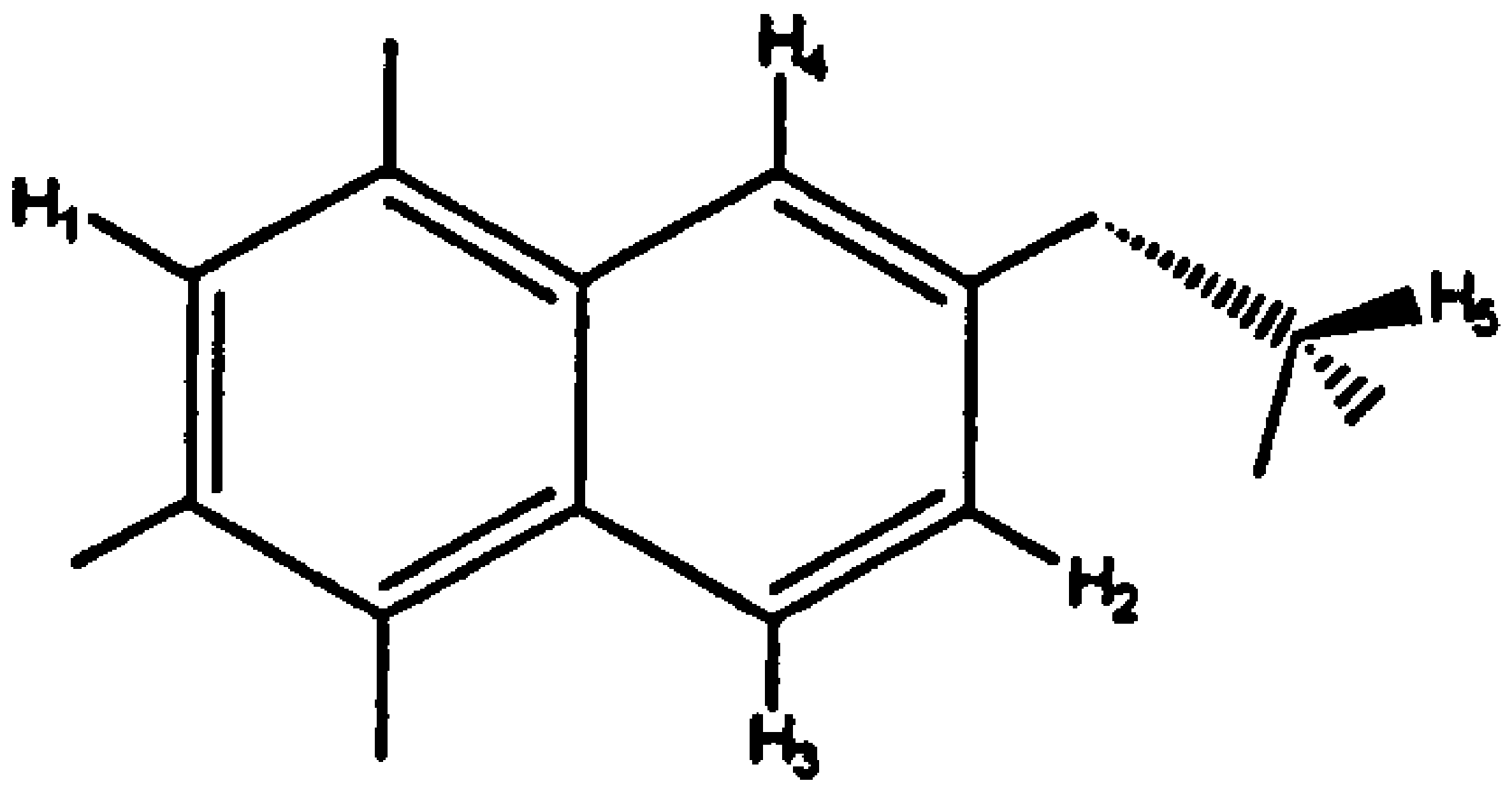

Figure 4.2

H_1-H_2 = 7.22
H_1-H_5 = 8.66
H_3-H_4 = 5.01

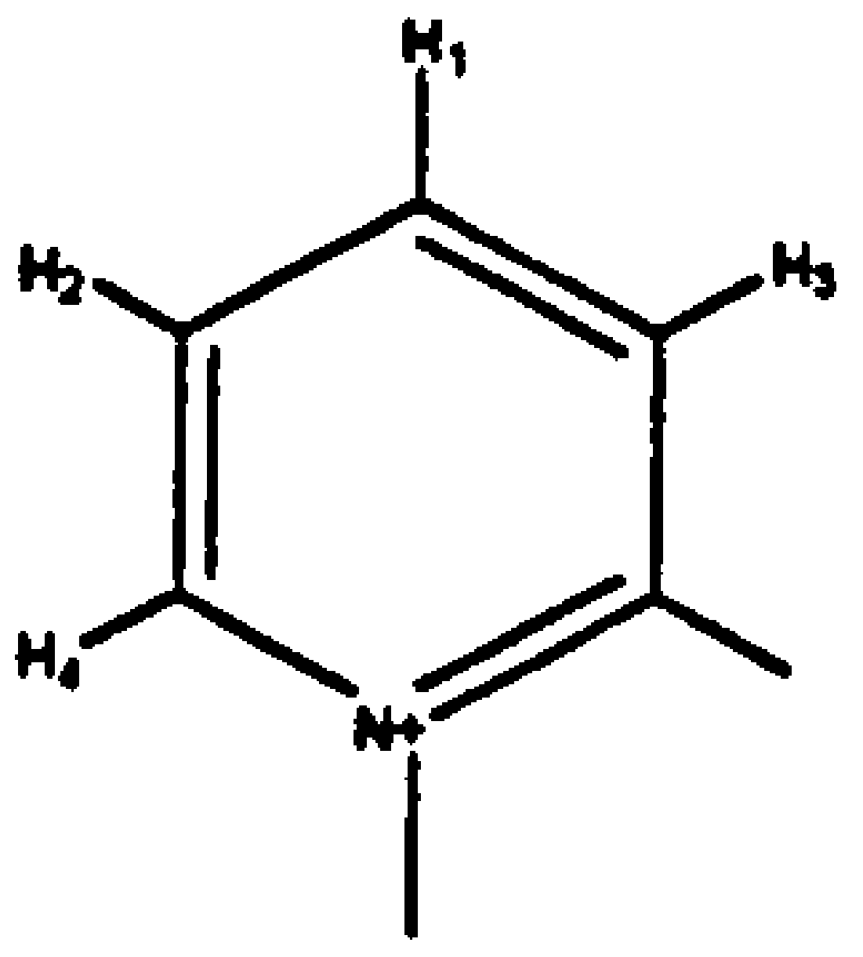

Figure 4.3

H_2-H_3 = 4.33
H_2-H_4 = 4.33

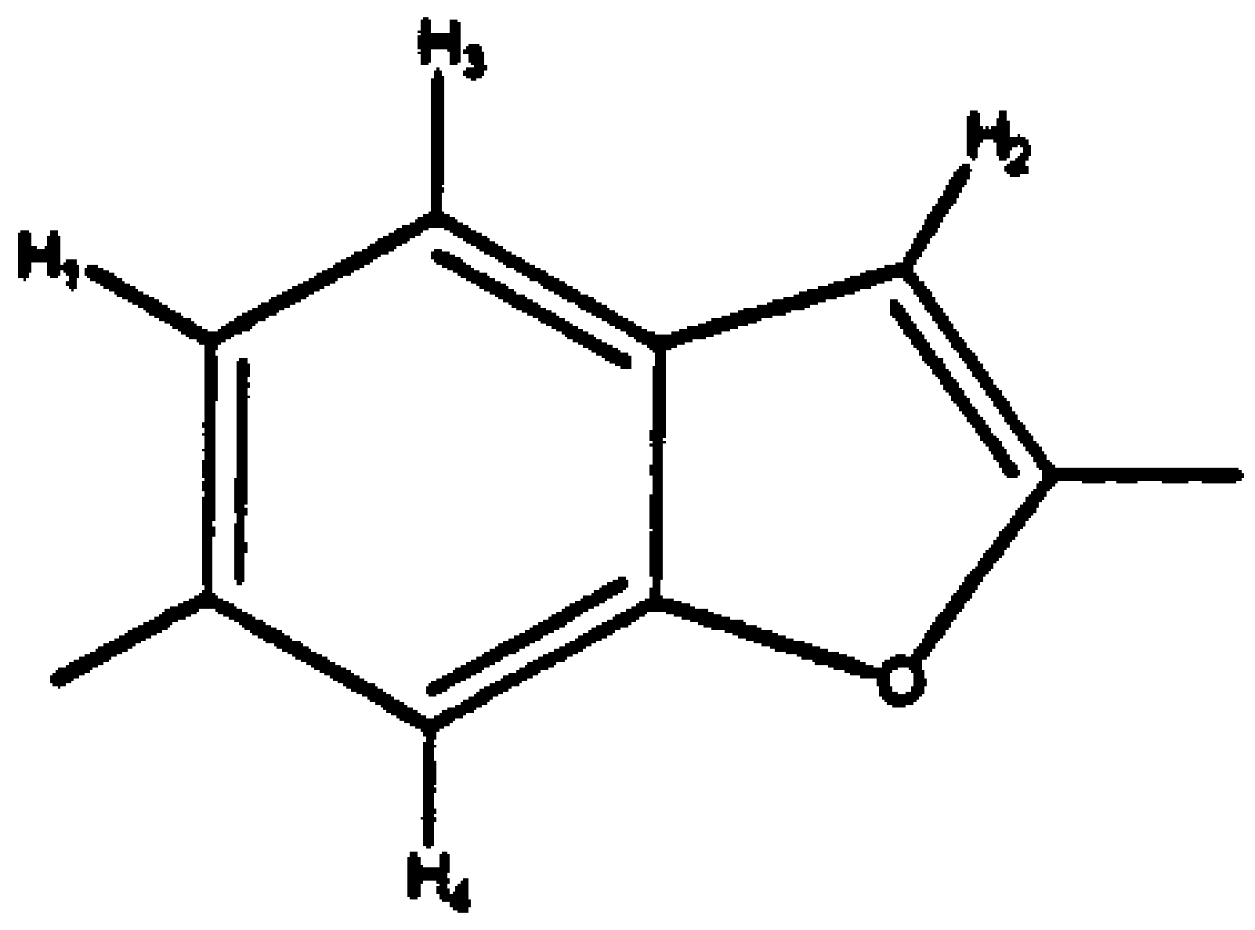

Figure 4.4

H_1-Lp(O) = 6.22
H_1-H_2 = 5.63
H_3-H_4 = 5.10

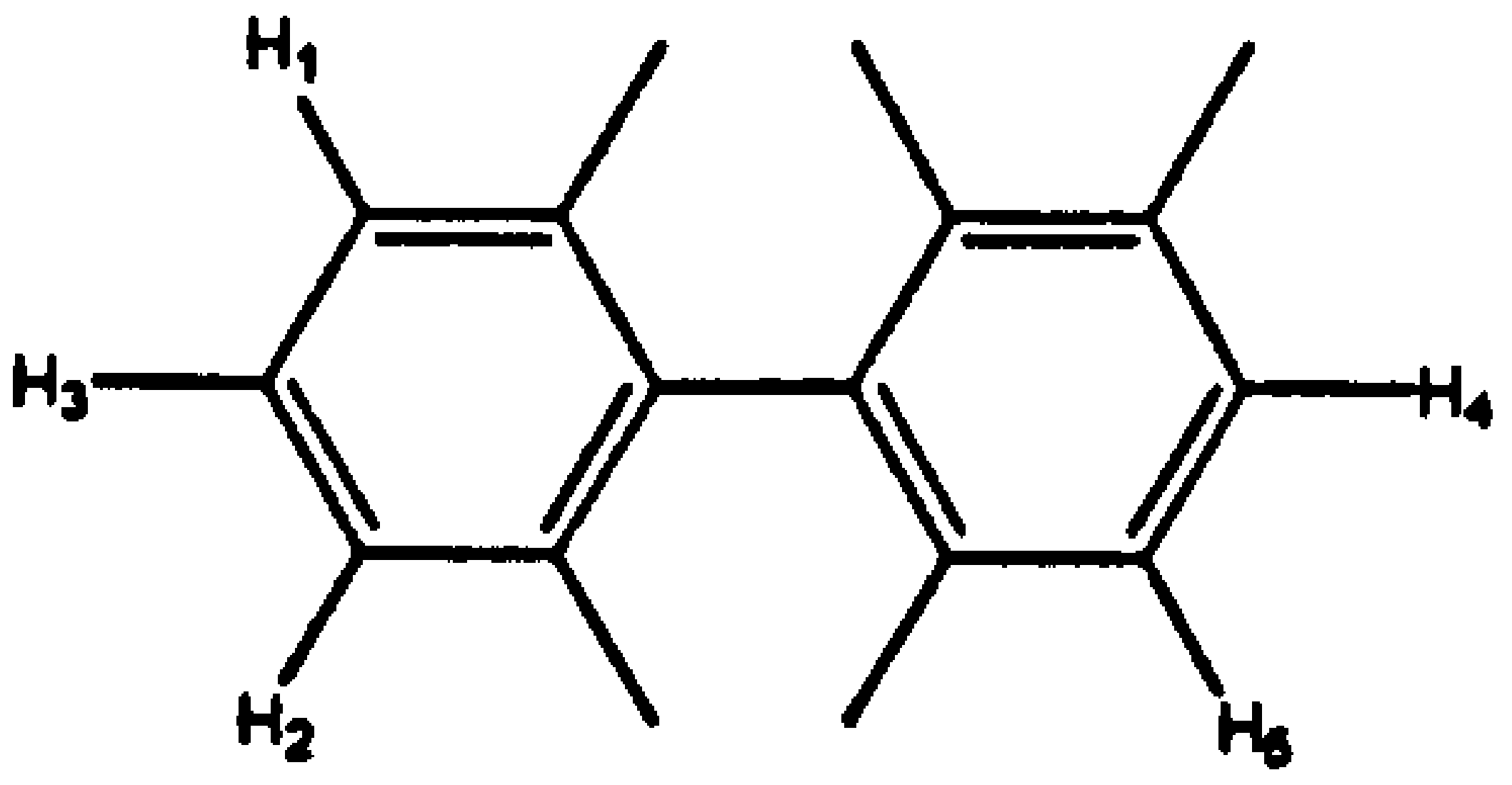

Figure 4.5

H_1-H_2 = 4.32
H_3-H_4 = 9.32
H_1-H_3 = 7.92

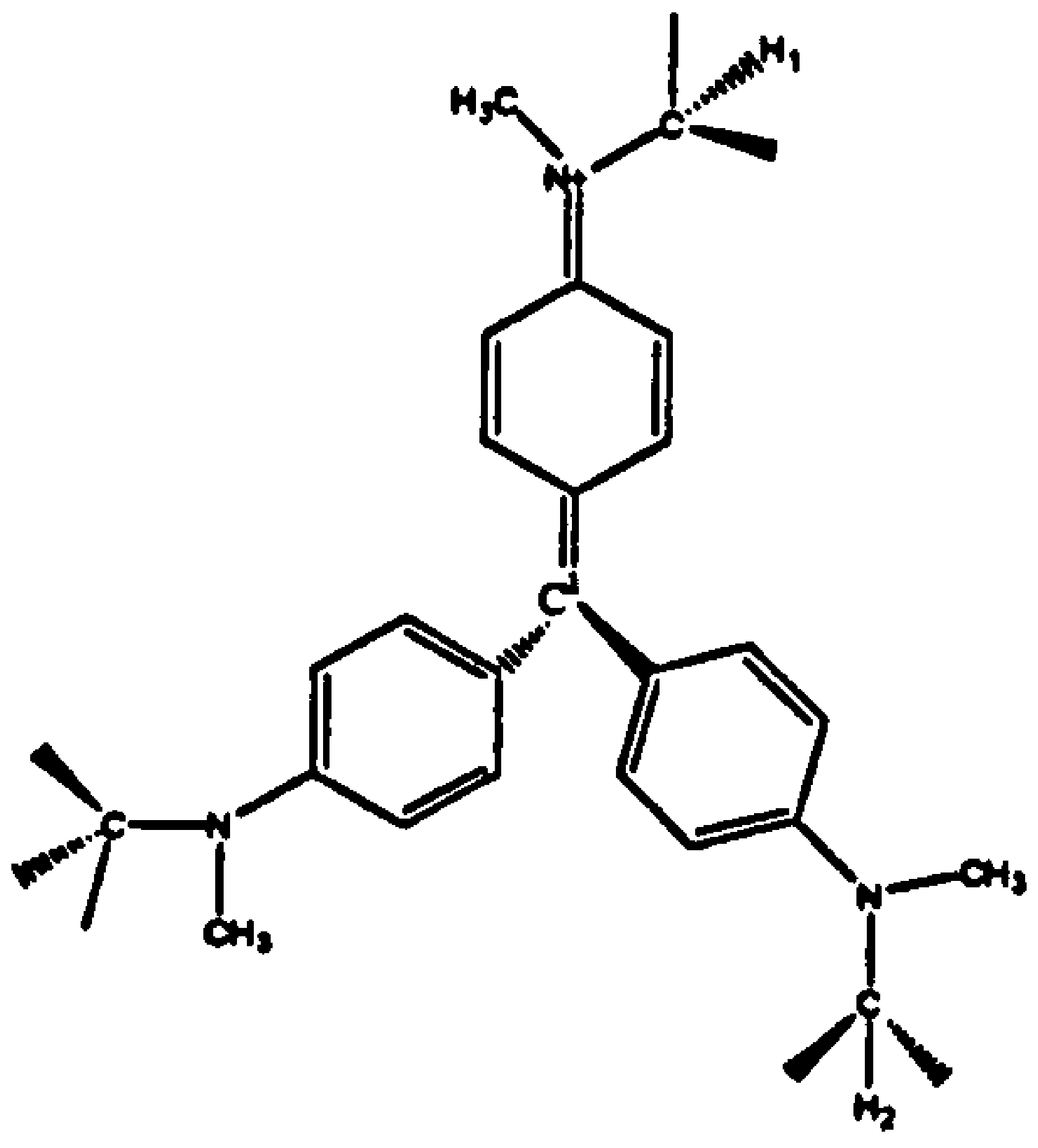

Figure 4.6

H_1-H_2 = ca. 13.4
C_1-H_2 = ca. 7.6
C_1-H_1 = ca. 7.5

Distances are given in Angströms

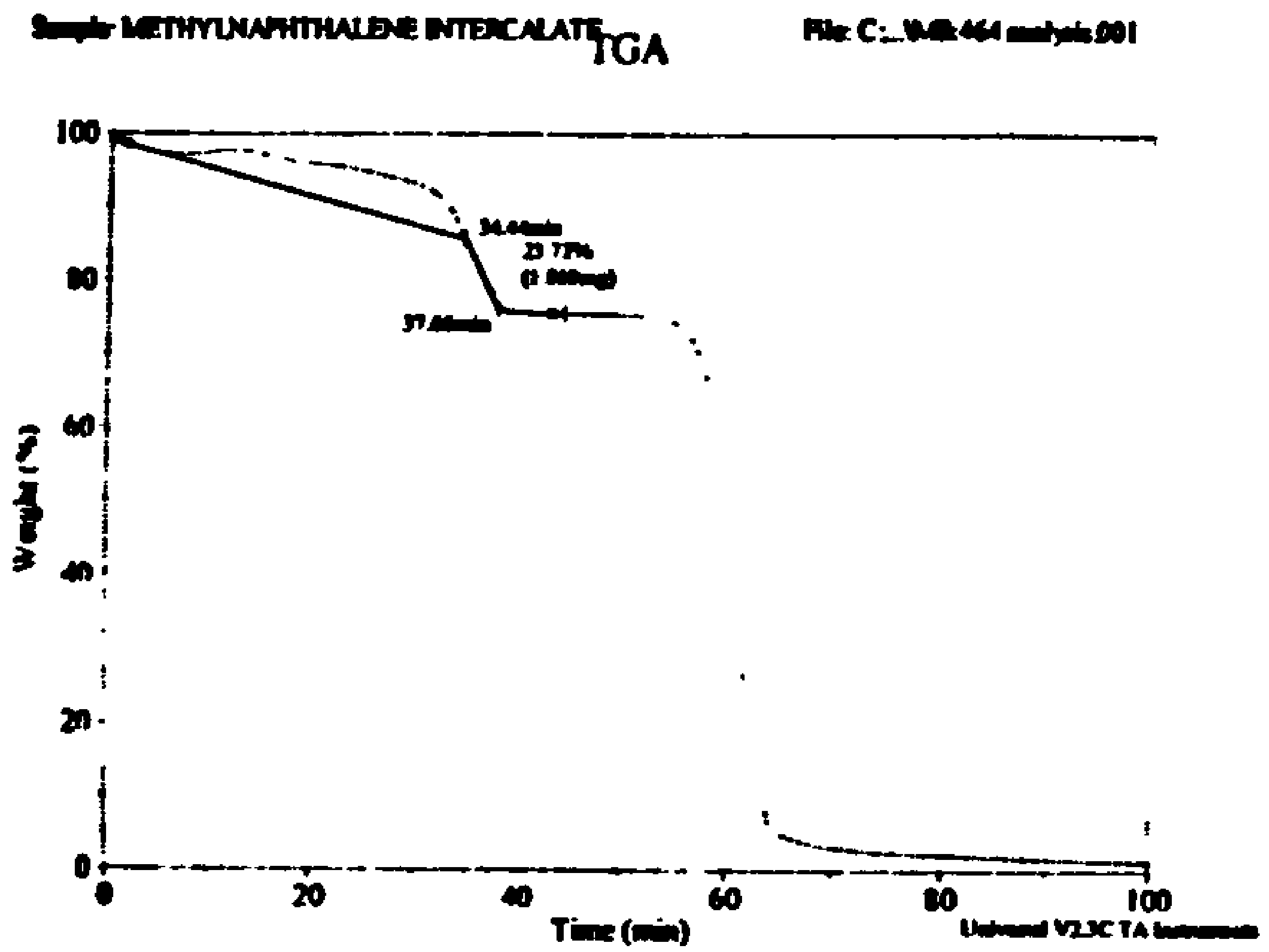

Figure 4.7: 2-methylnaphthalene intercalate

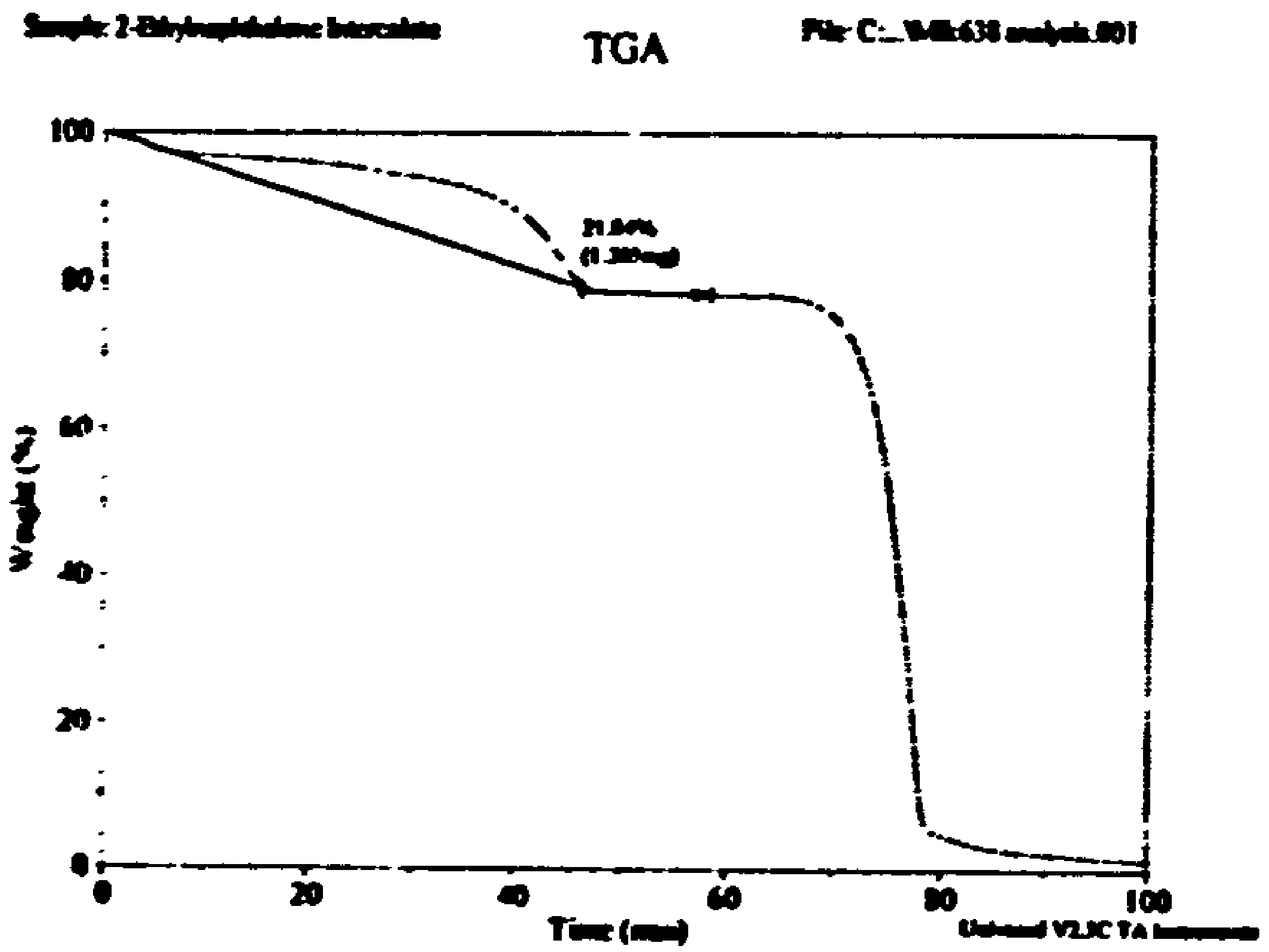

Figure 4.8: 2-ethylnaphthalene intercalate

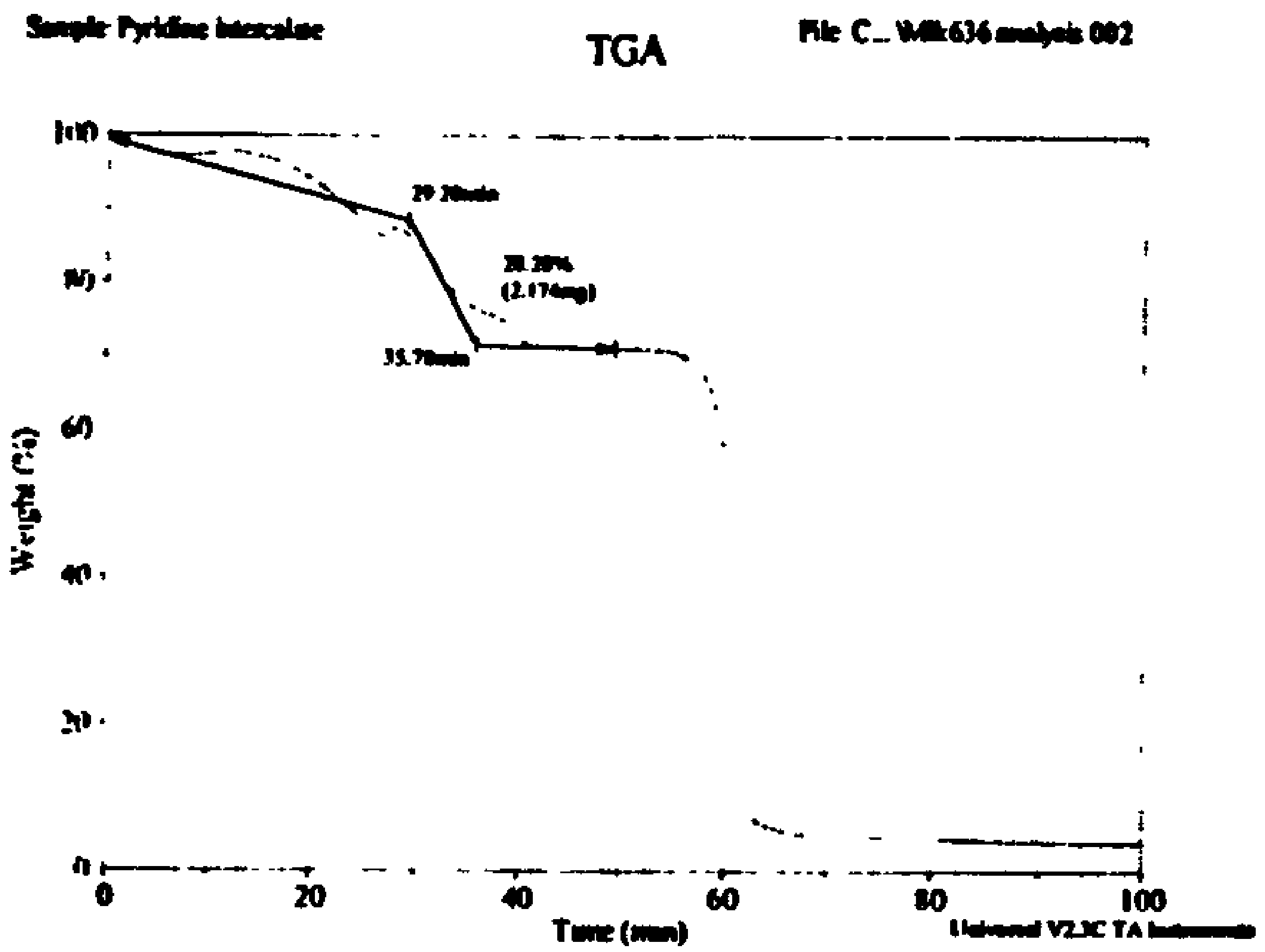

Figure 4.9: Pyridinium intercalate

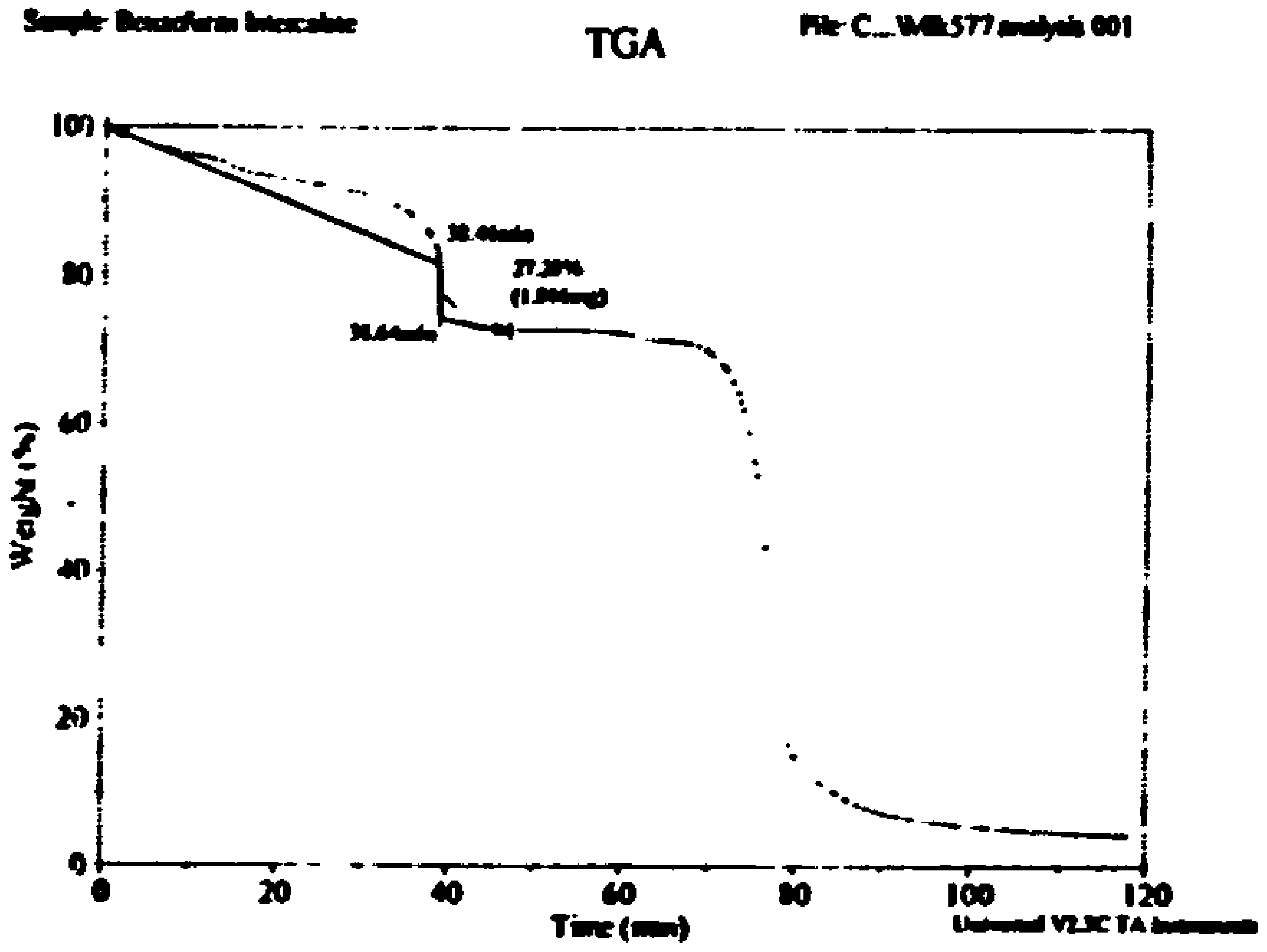

Figure 4.10: Benzofuran intercalate

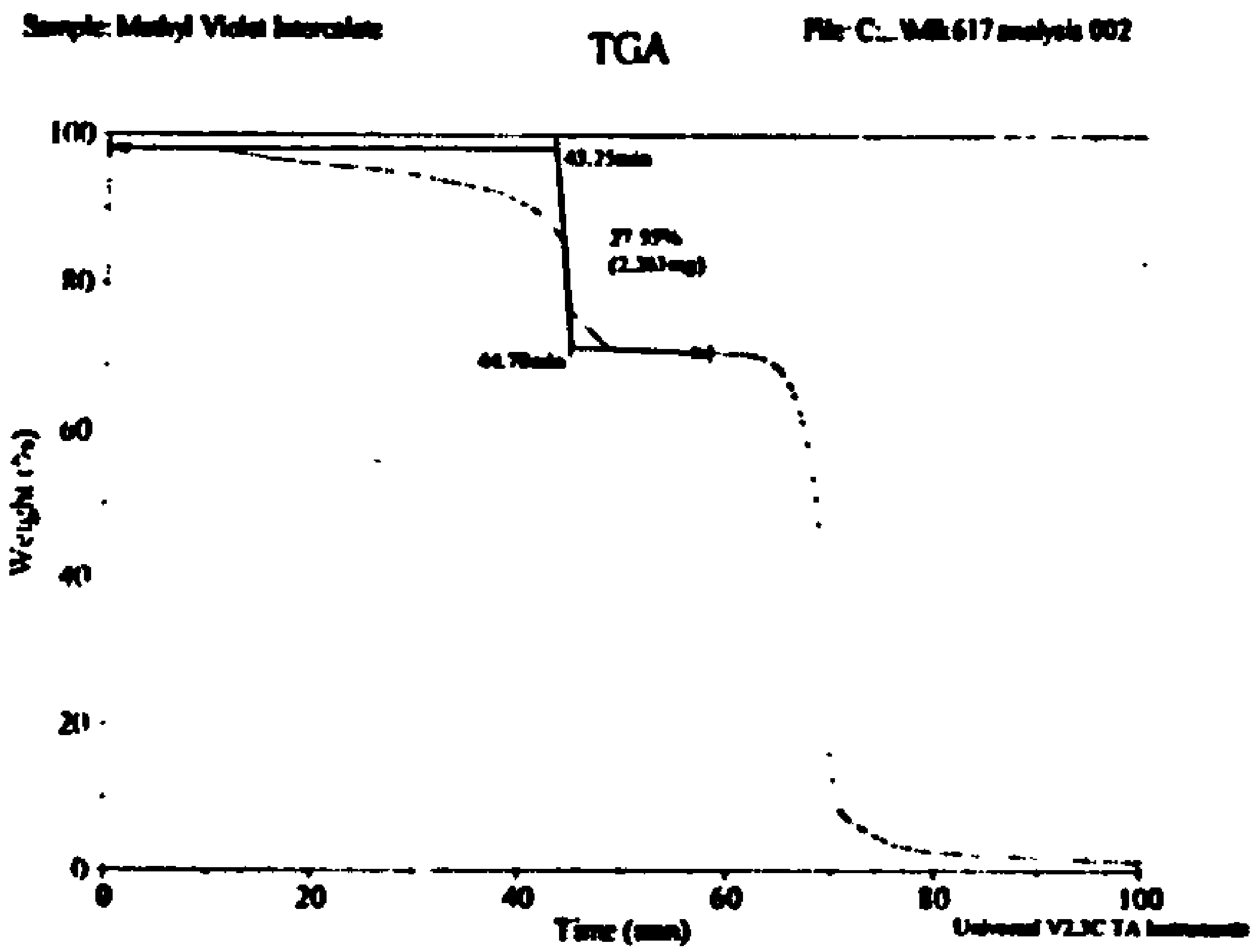

Figure 4.11: Crystal violet intercalate

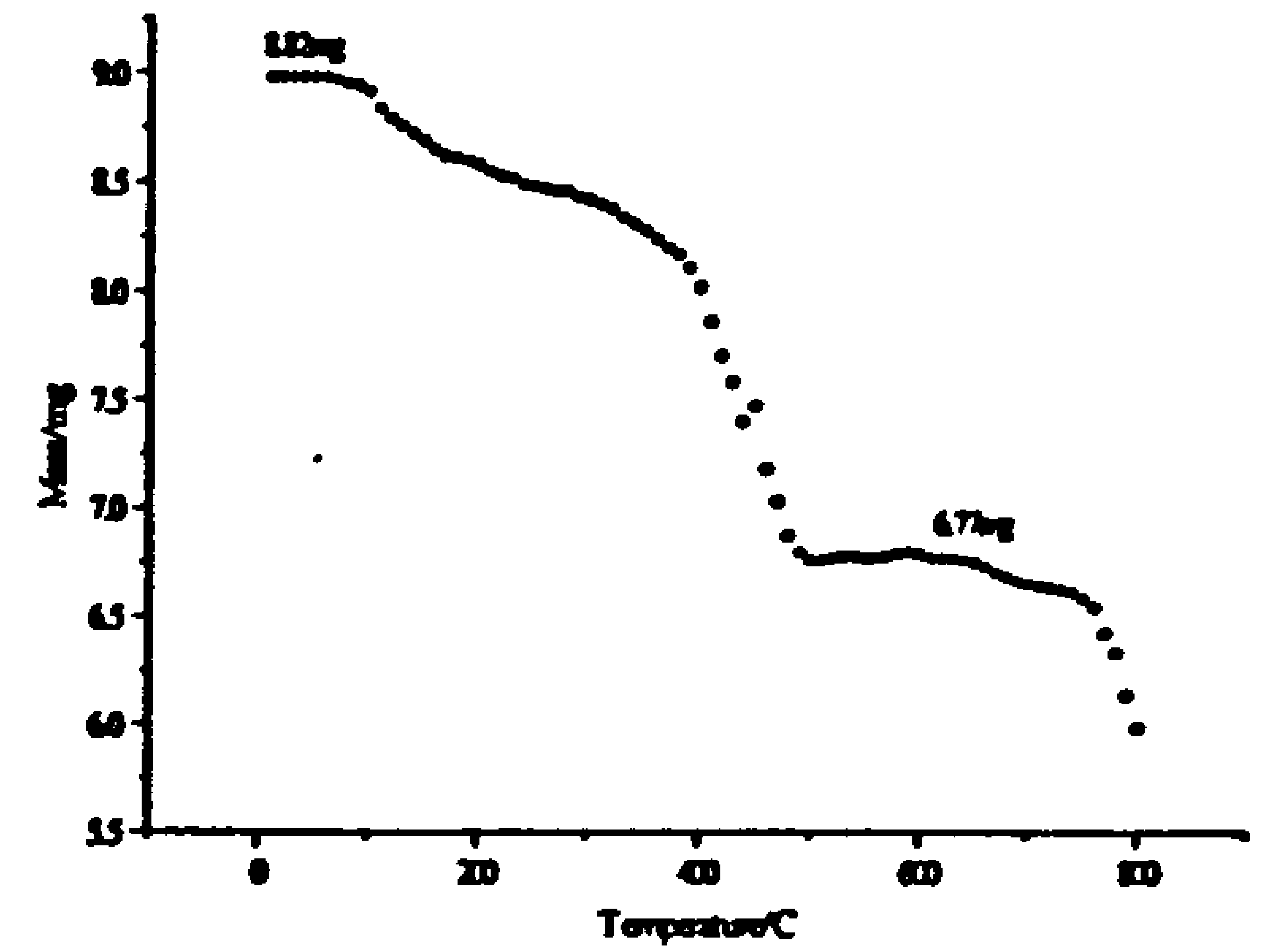

Figure 4.12: Biphenyl intercalate

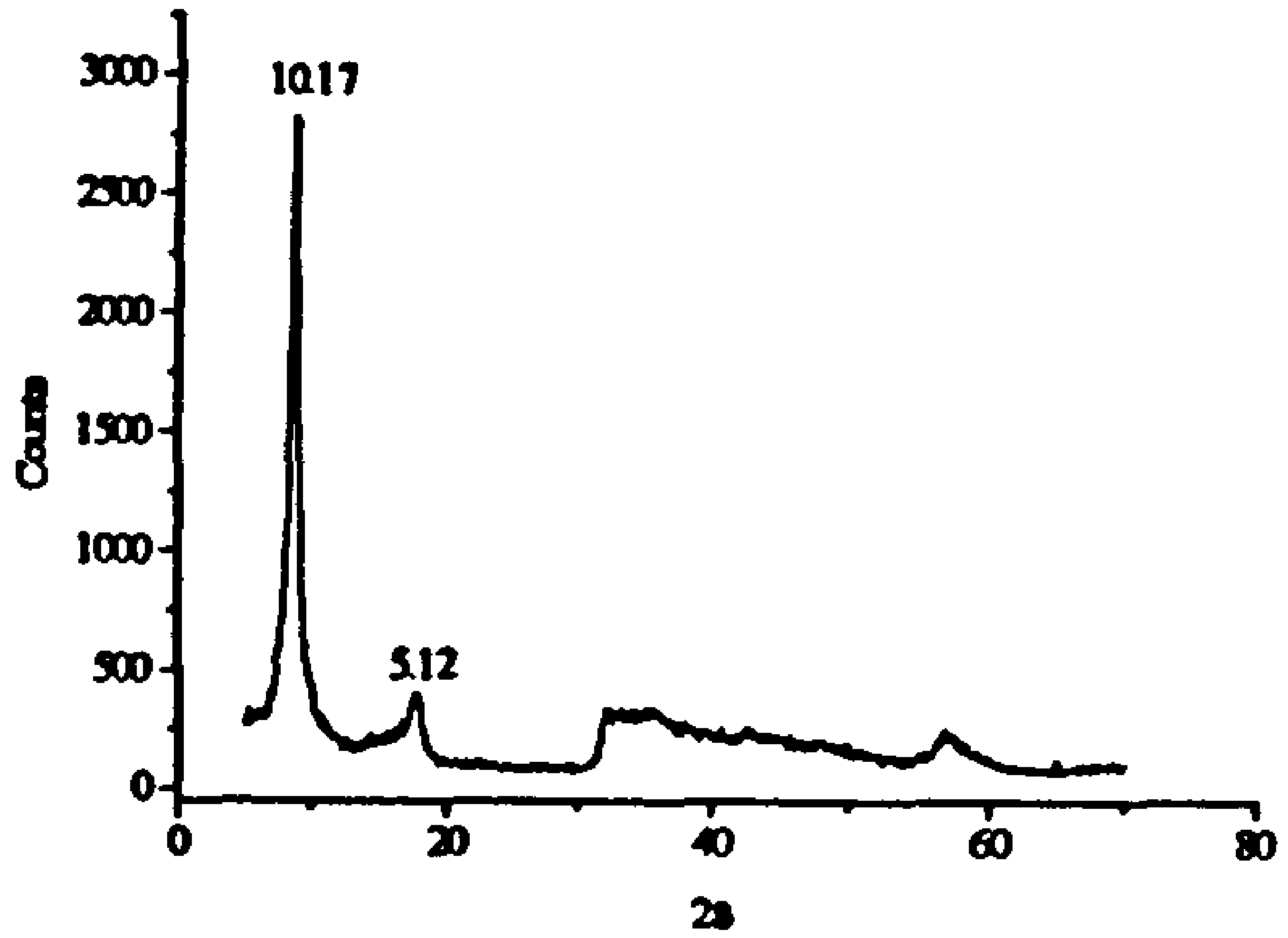

Figure 4.13: 2-Methylnaphthalene

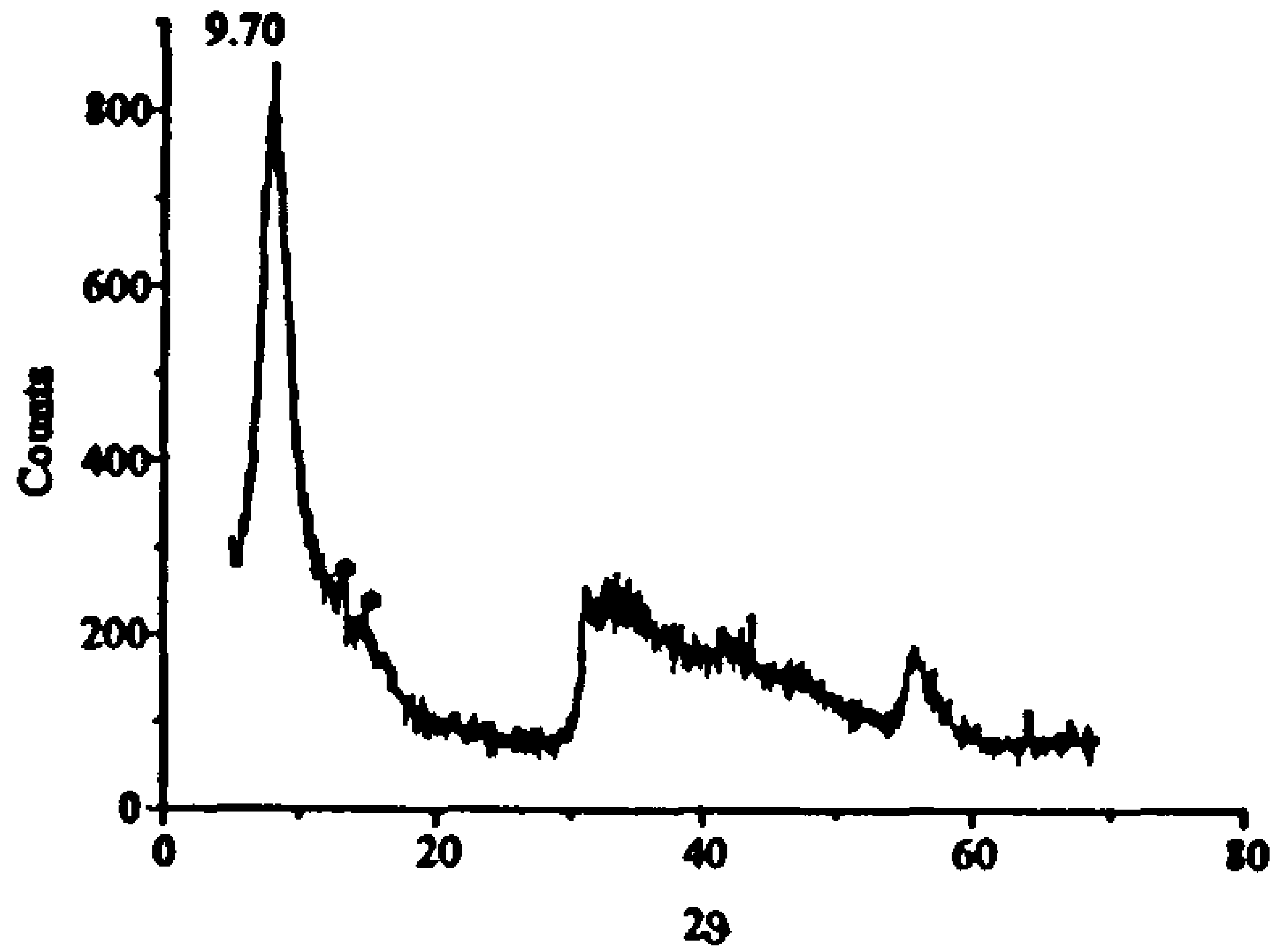

Figure 4.14 : 2-Ethylnaphthalene

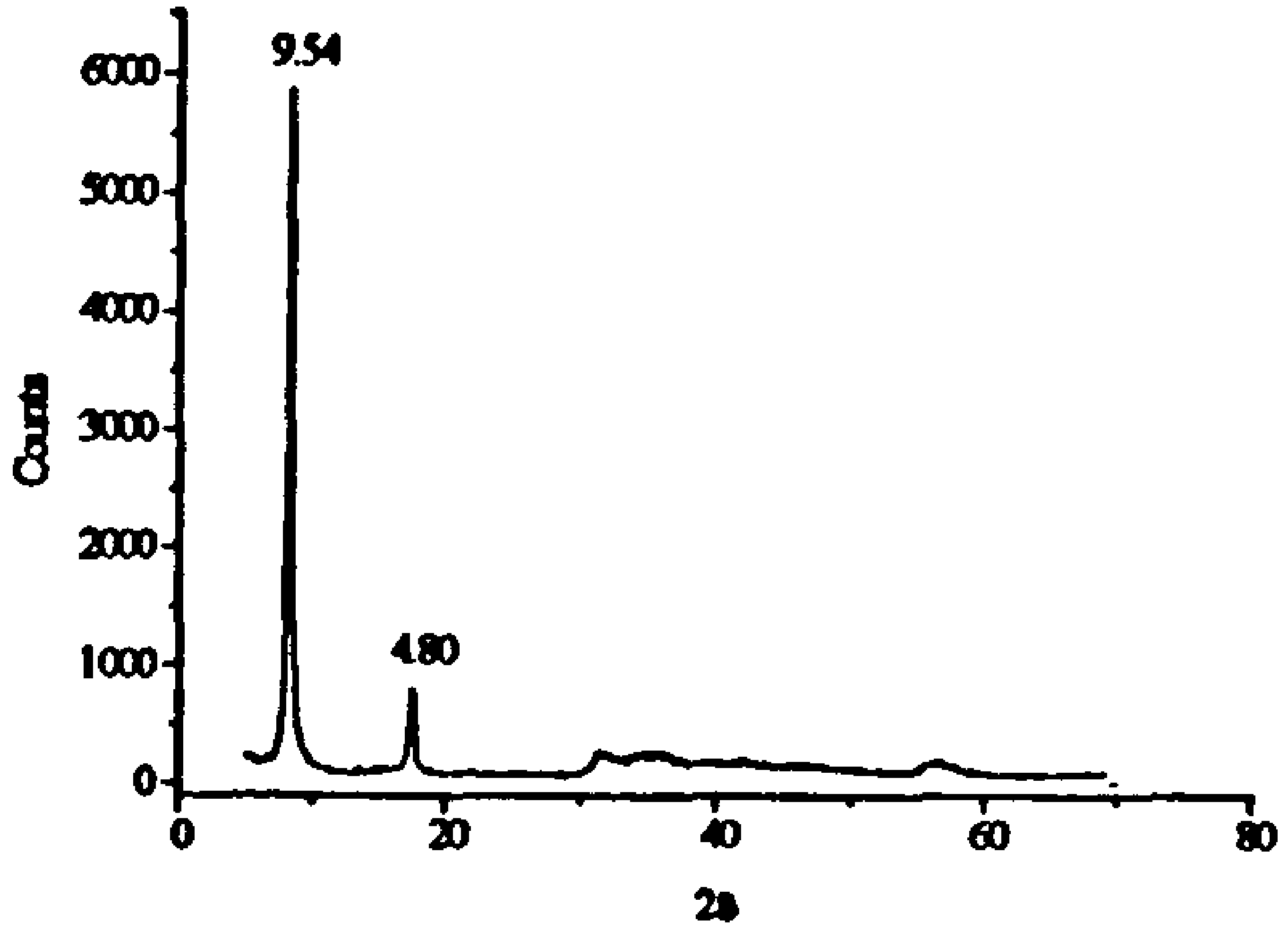

Figure 4.15: Pyridinium

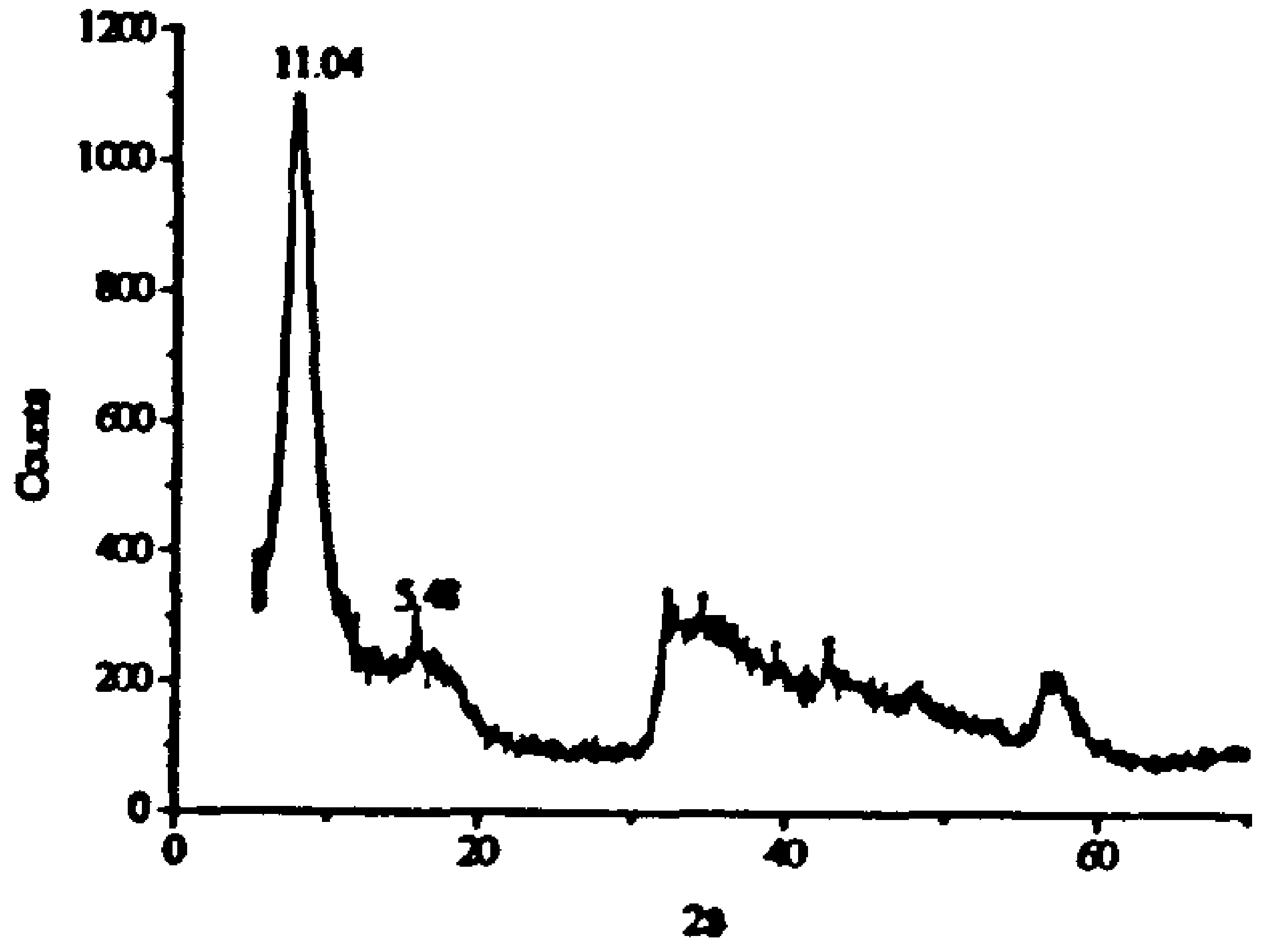

Figure 4.16: Benzofuran

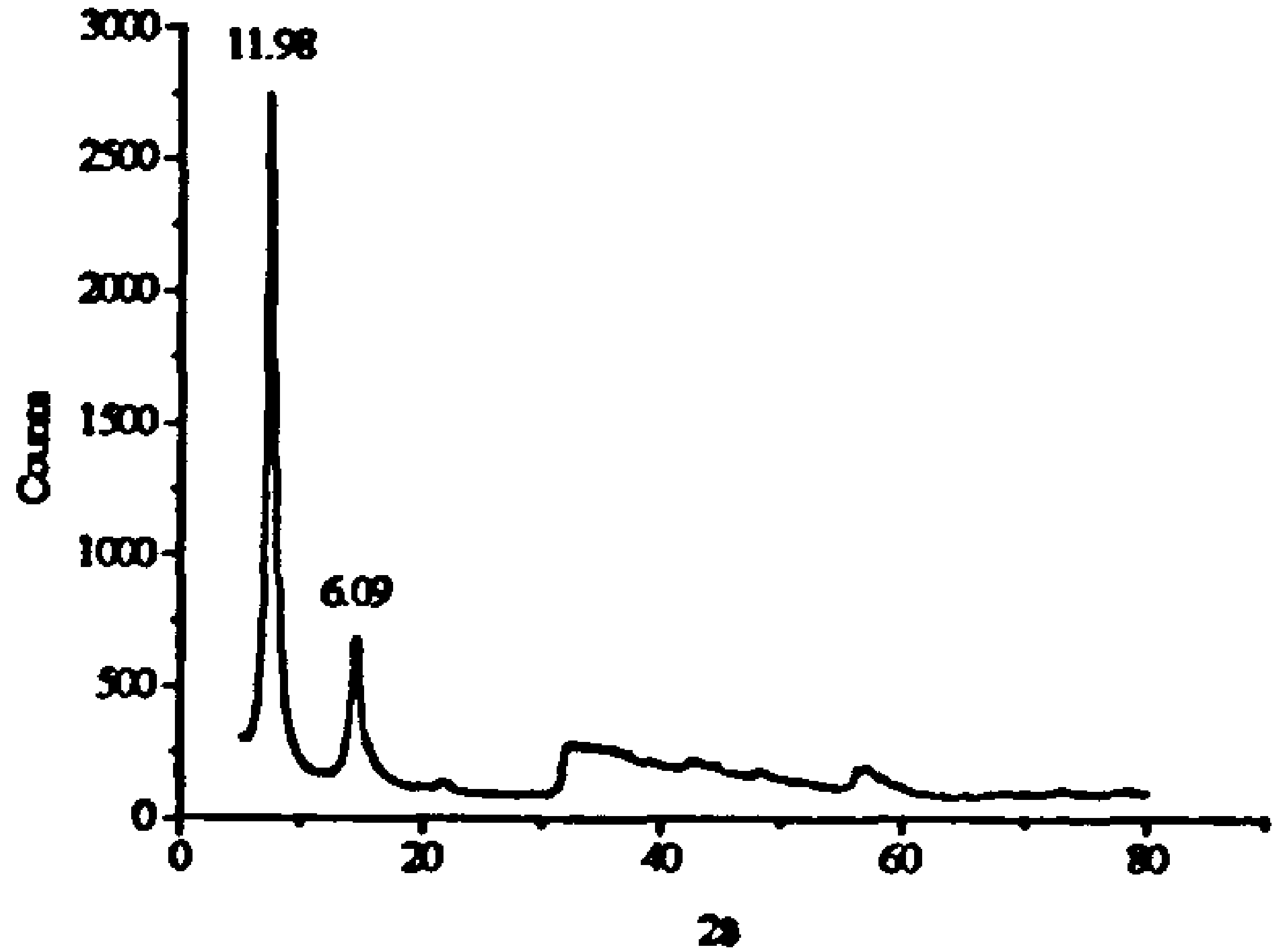

Figure 4.17: Biphenyl

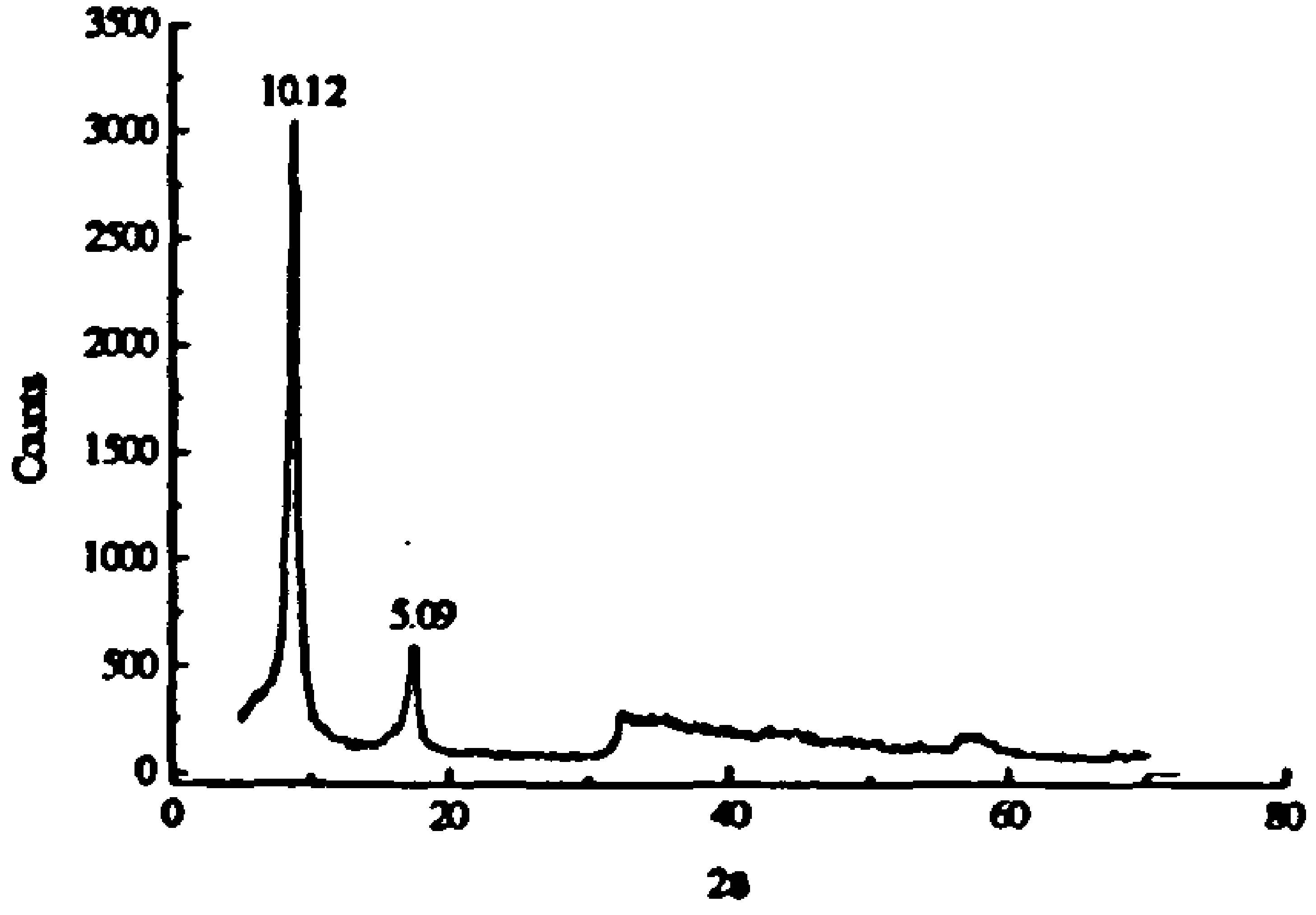

Figure 4.18: Crystal violet

Powder X-ray diffraction patterns for intercalates; marked values on diffraction patterns are d-spacings.

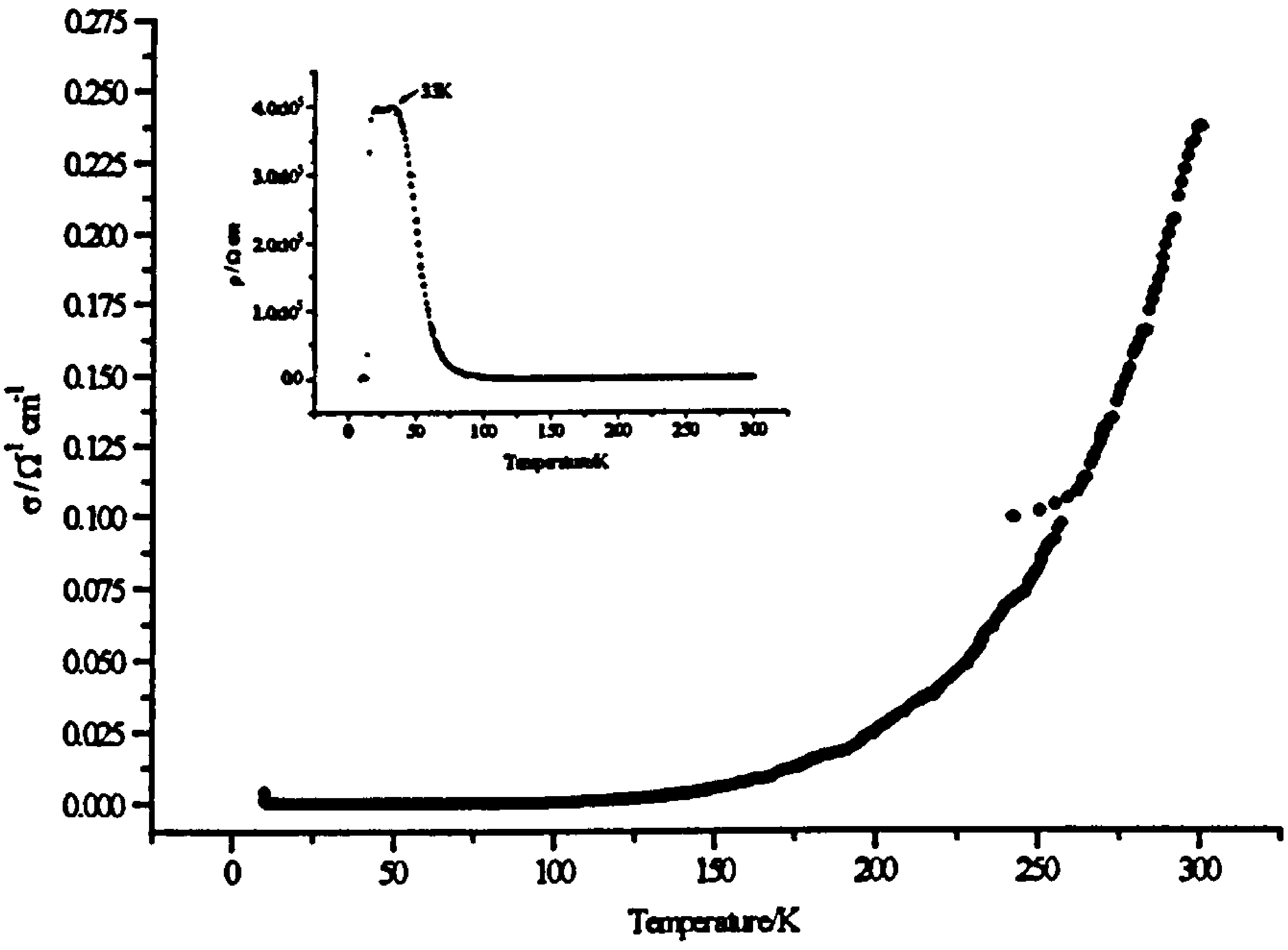

Figure 4.19: 2-Methylnaphthalene intercalate

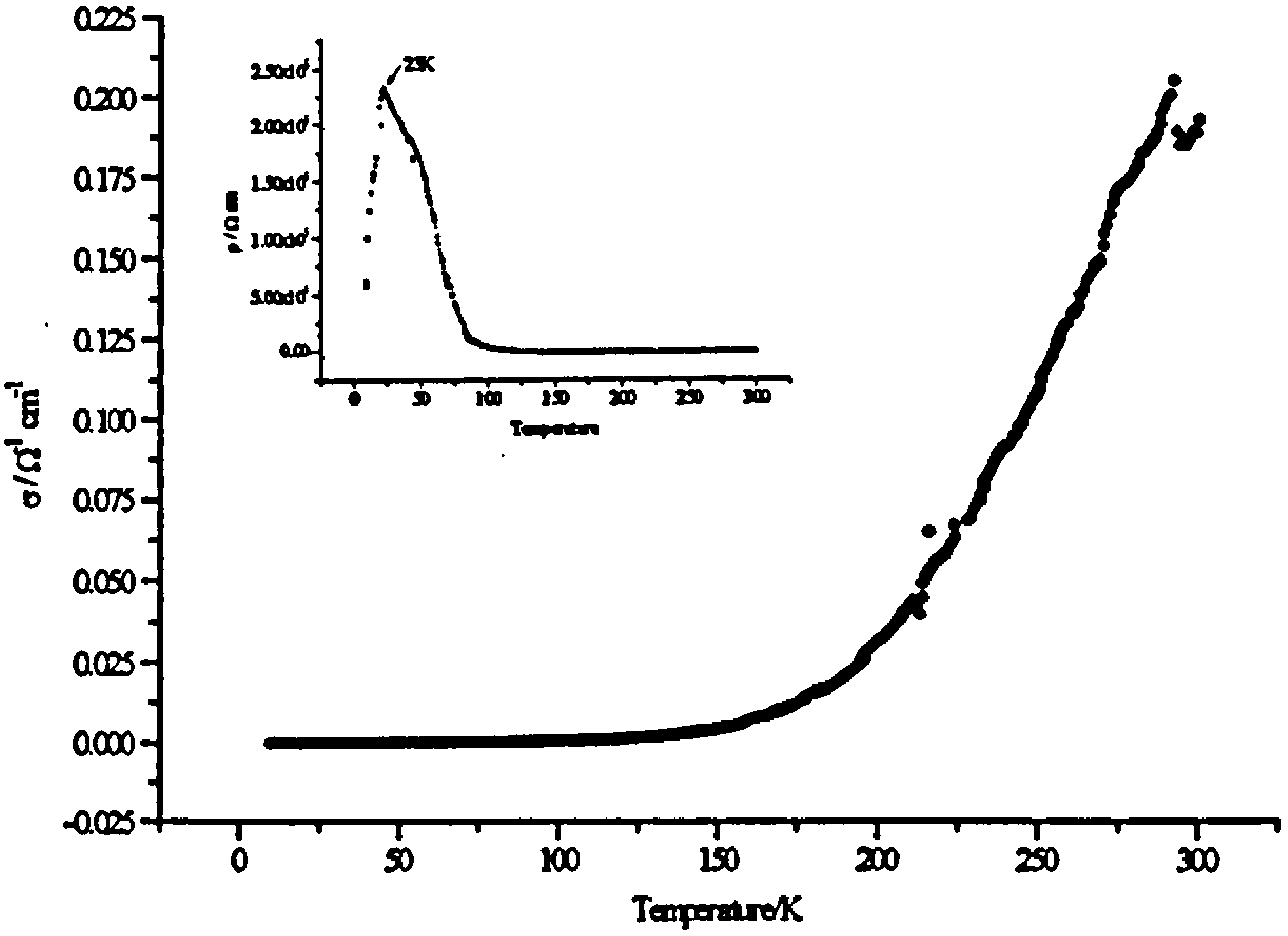

Figure 4.20: 2-Ethylnaphthalene intercalate

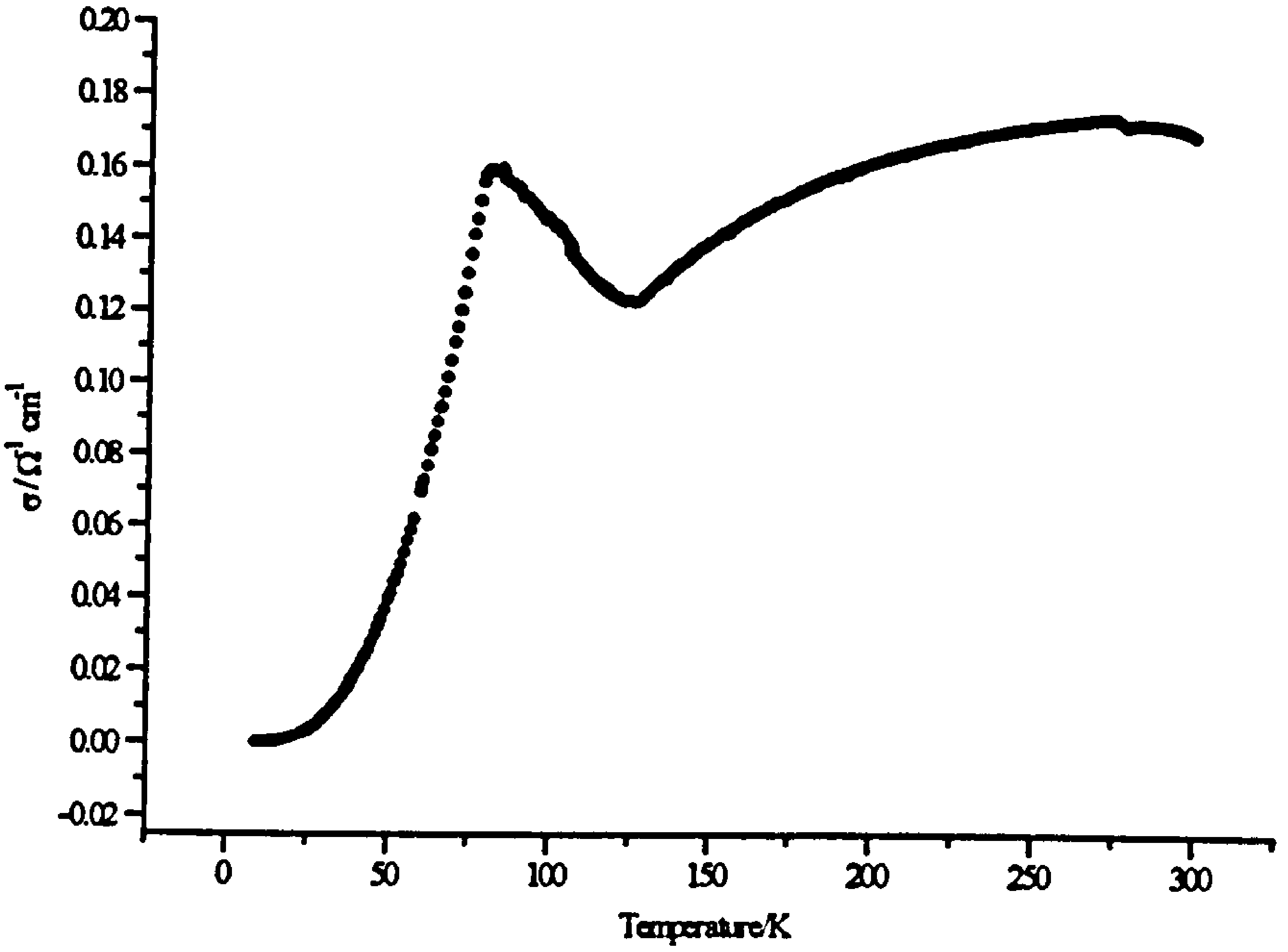

Figure 4.21: Pyridine intercalate

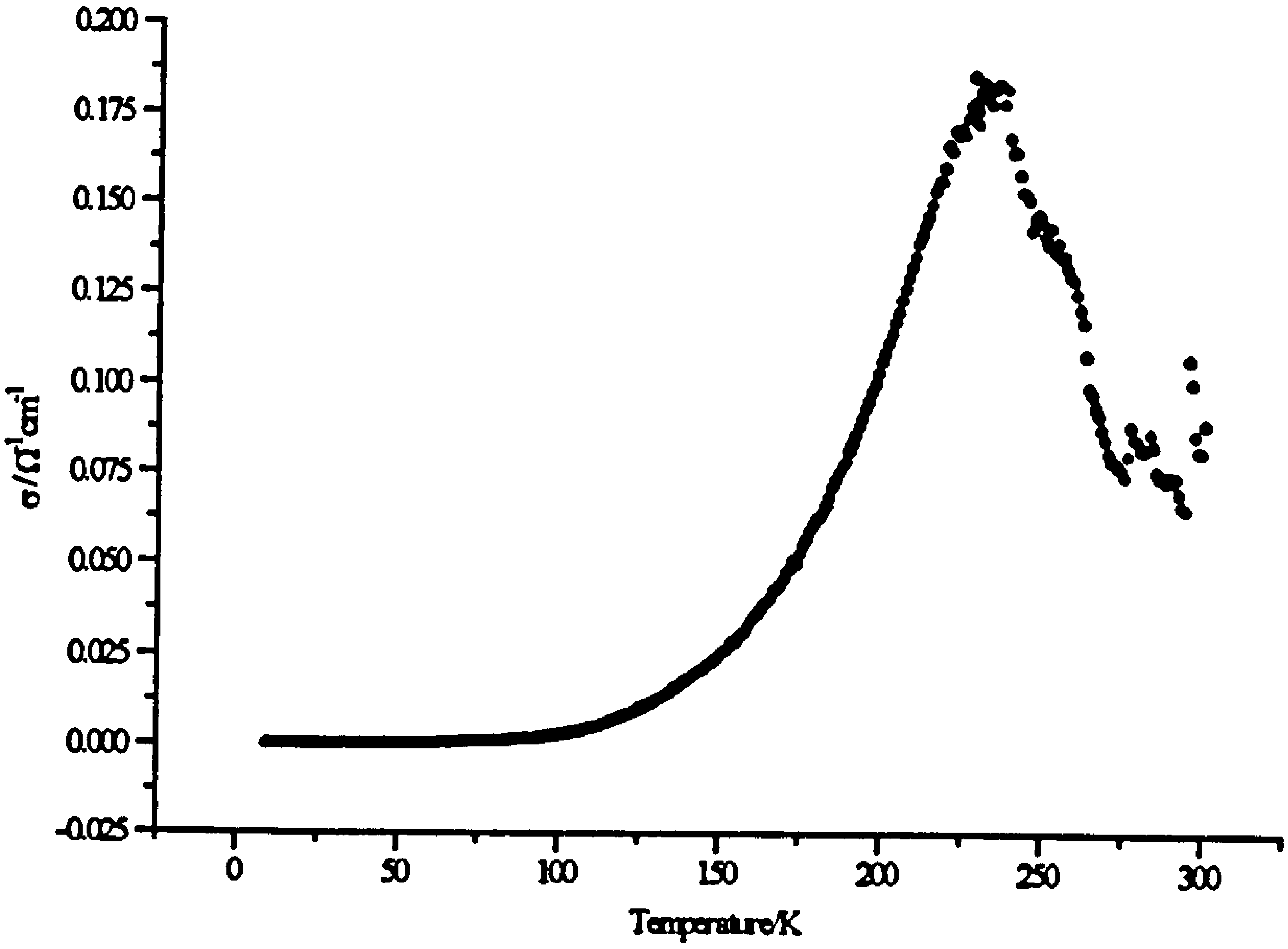

Figure 4.22: Benzofuran intercalate

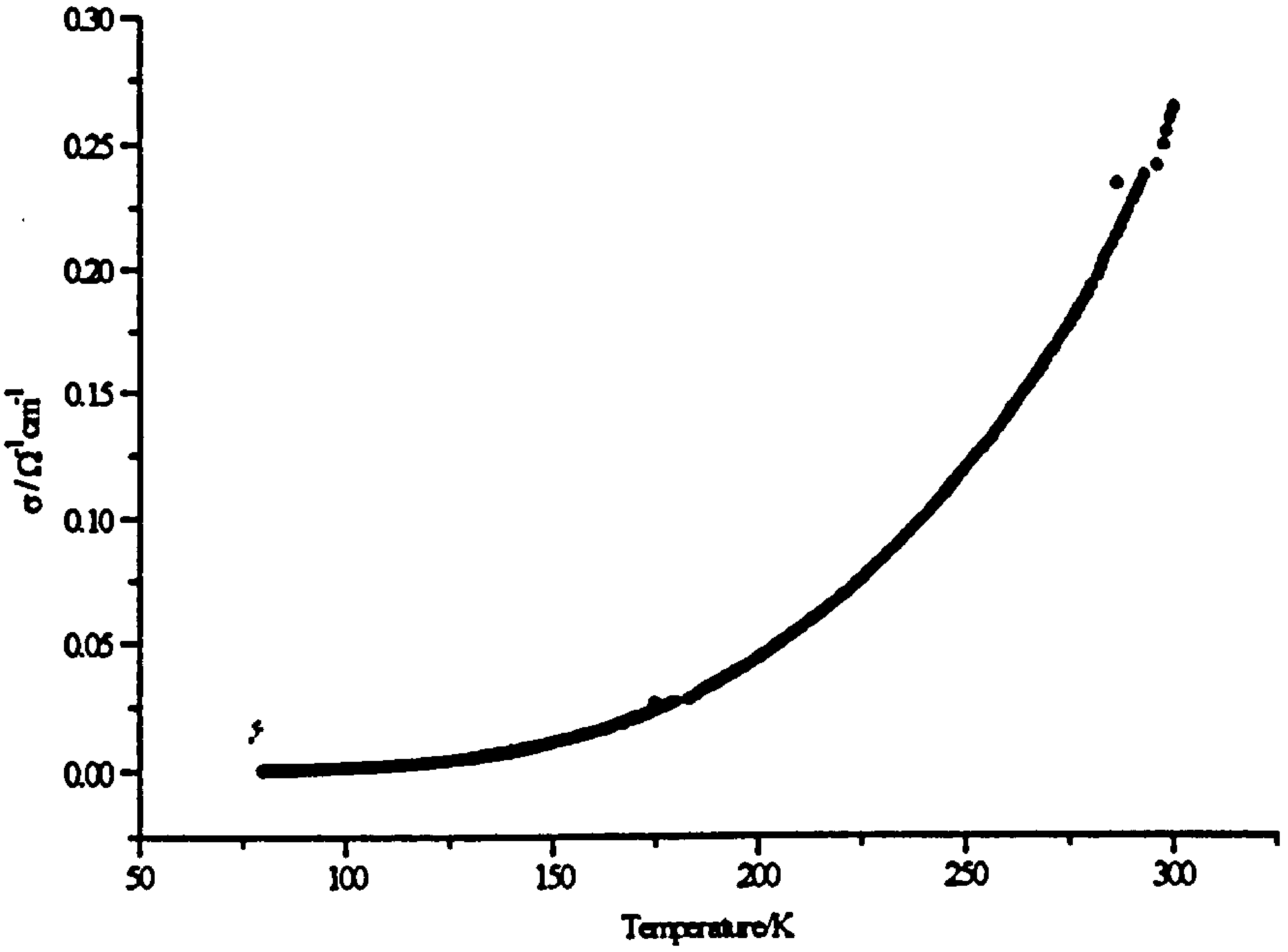

Figure 4.23: Biphenyl intercalate

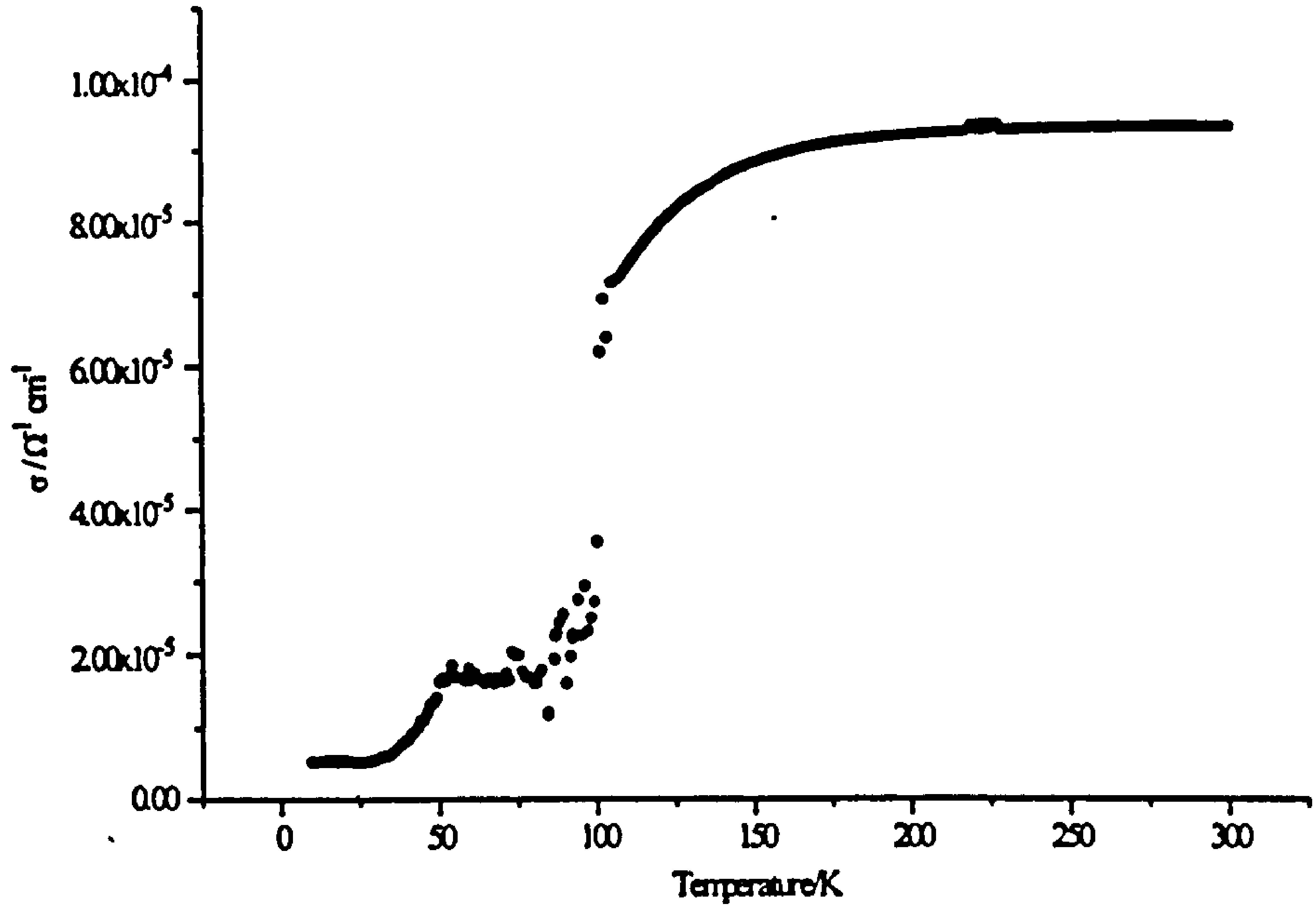

Figure 4.24: Crystal Violet intercalate

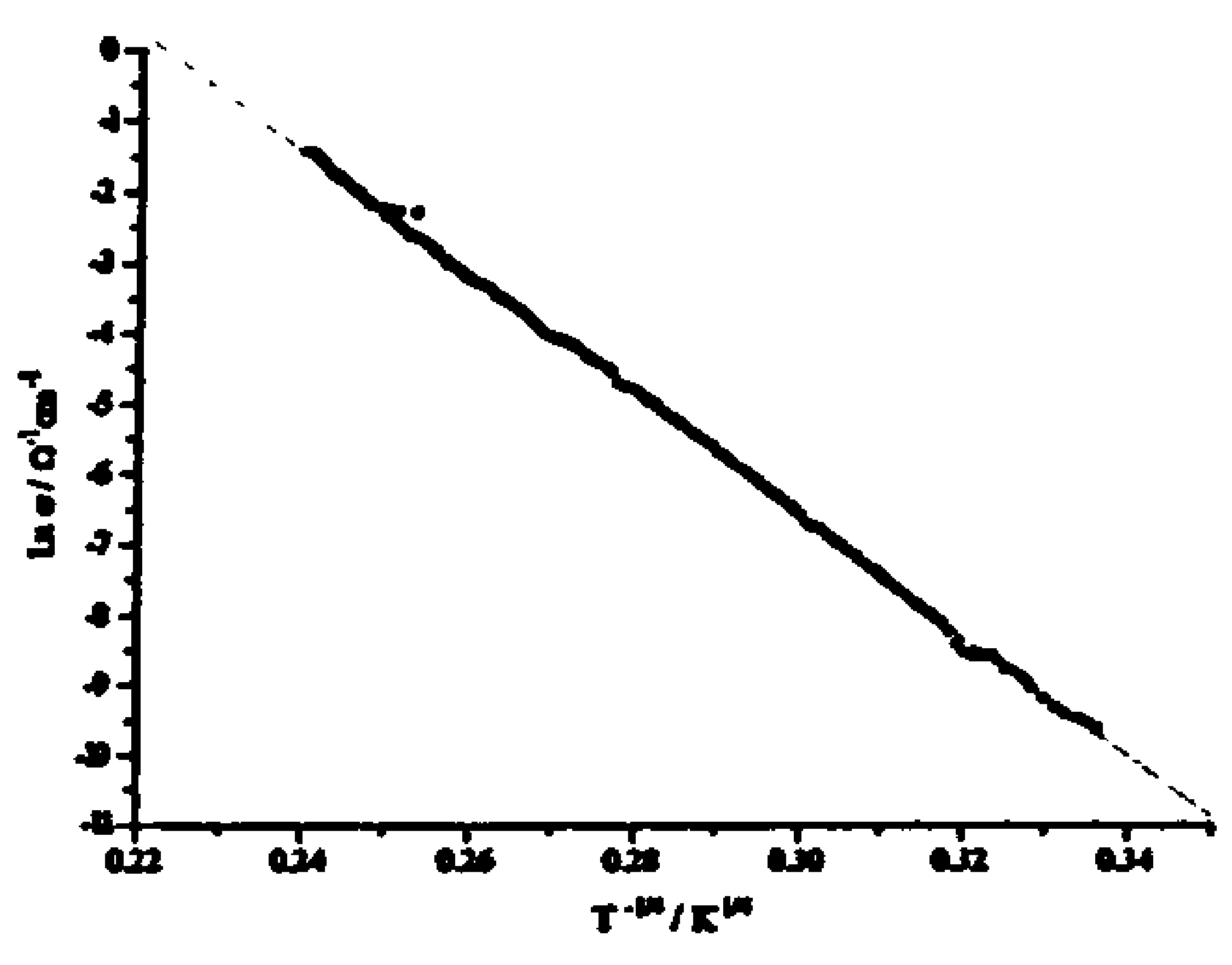

4.25: 2-Methylnaphthalene intercalate

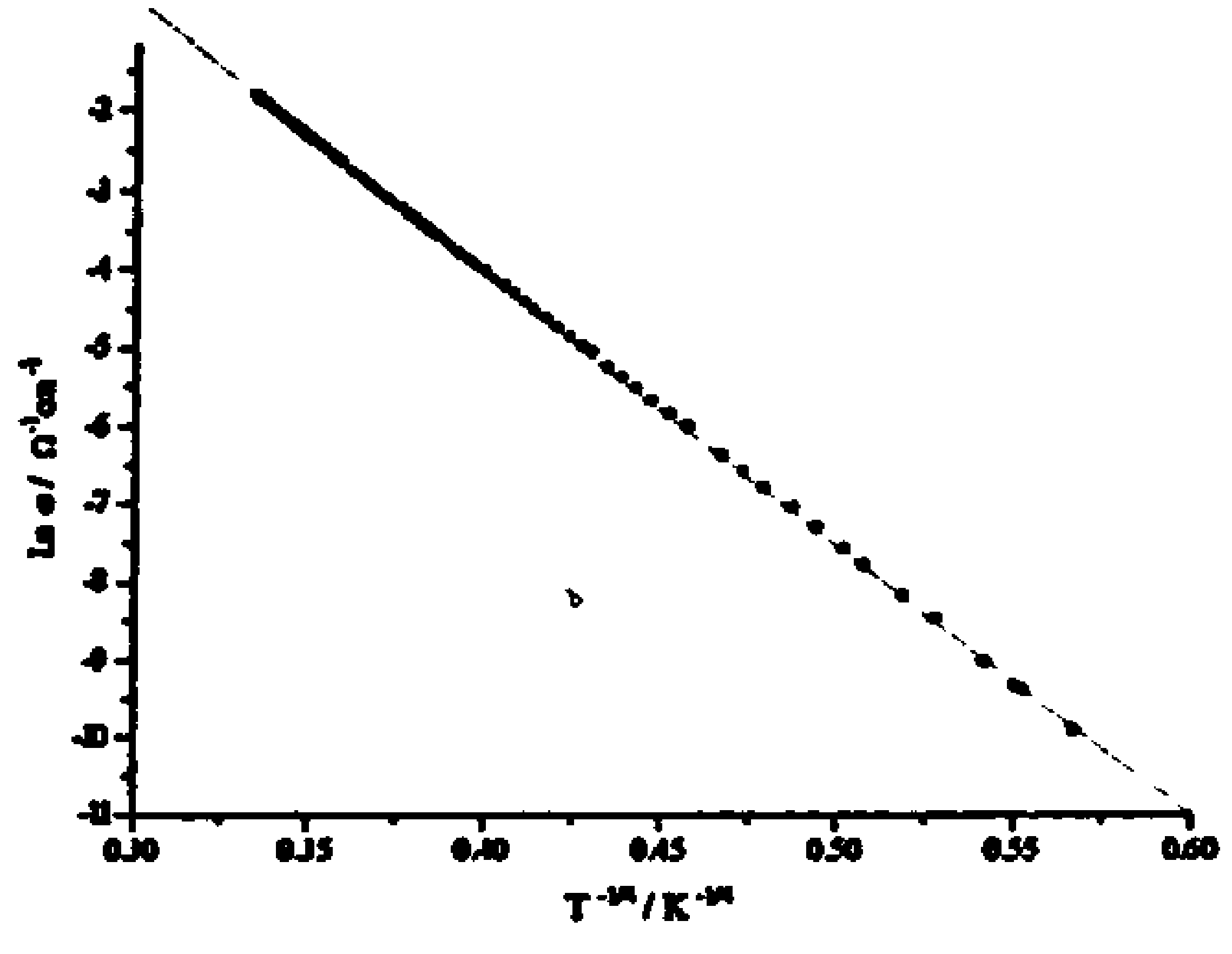

4.27: Pyridine intercalate

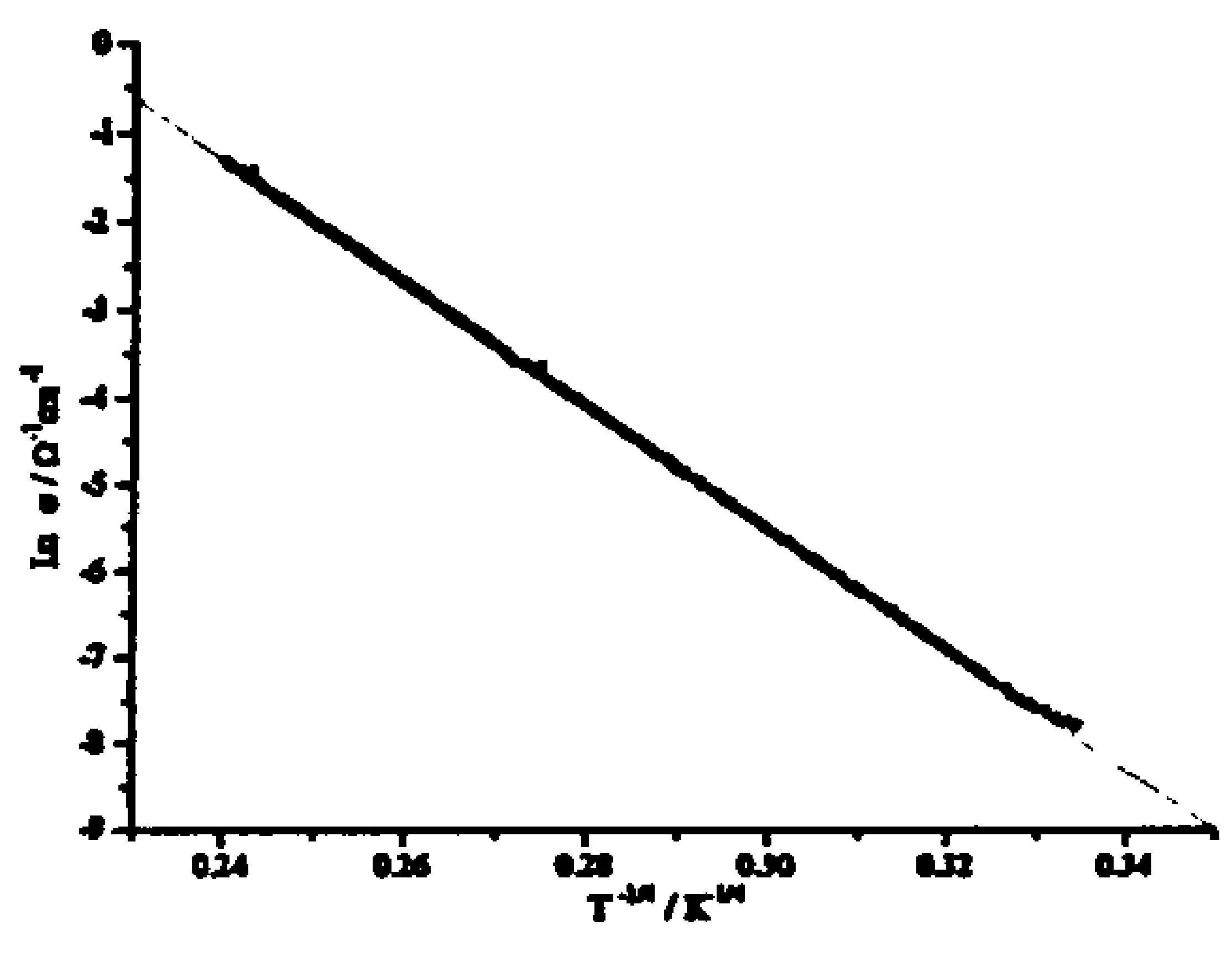

4.29: Biphenyl intercalate

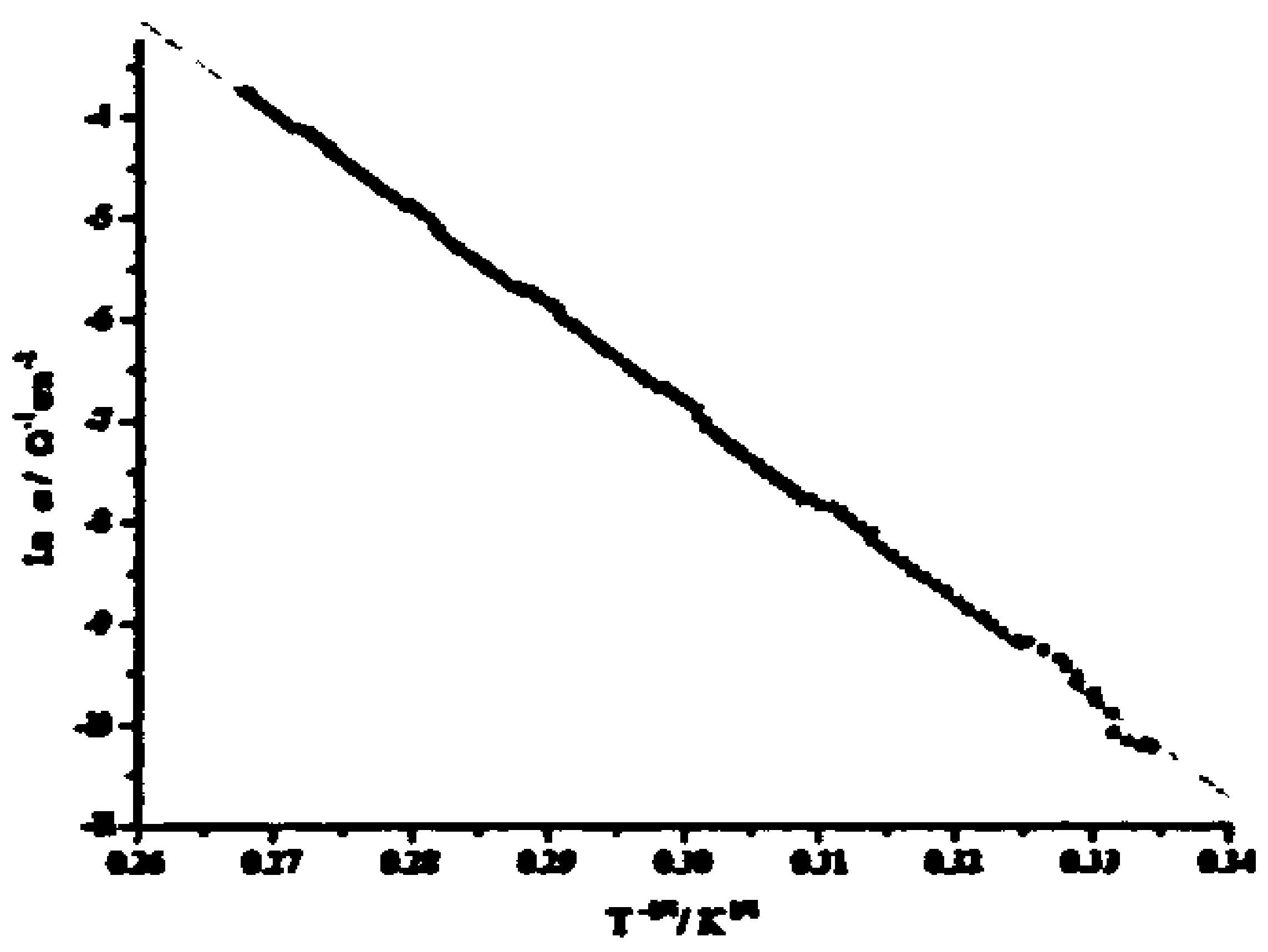

4.26: 2-Ethylnaphthalene

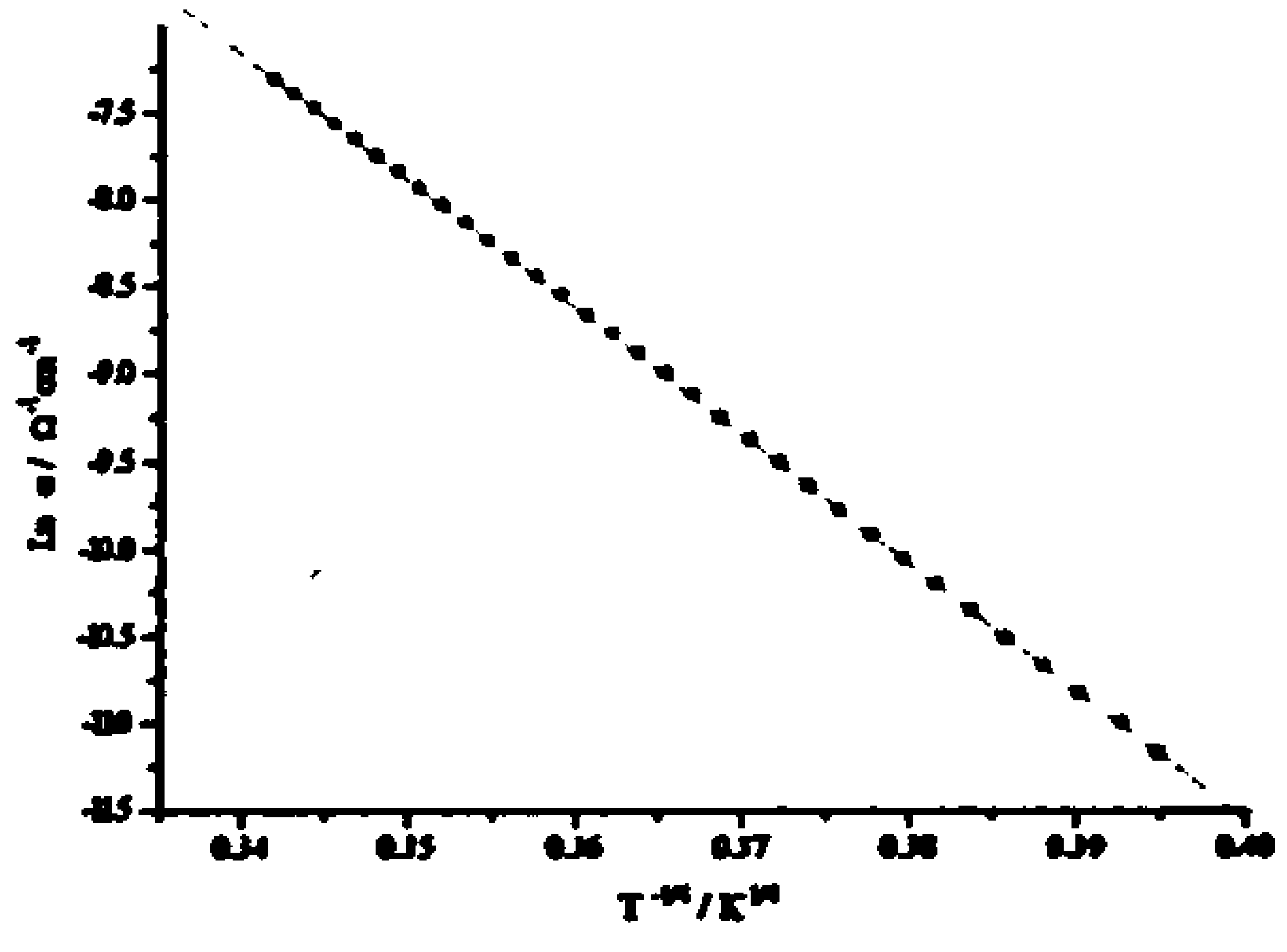

4.28: Benzofuran intercalate

Plots of Ln σ showing $T^{1/4}$ dependence, indicative of variable range hopping.

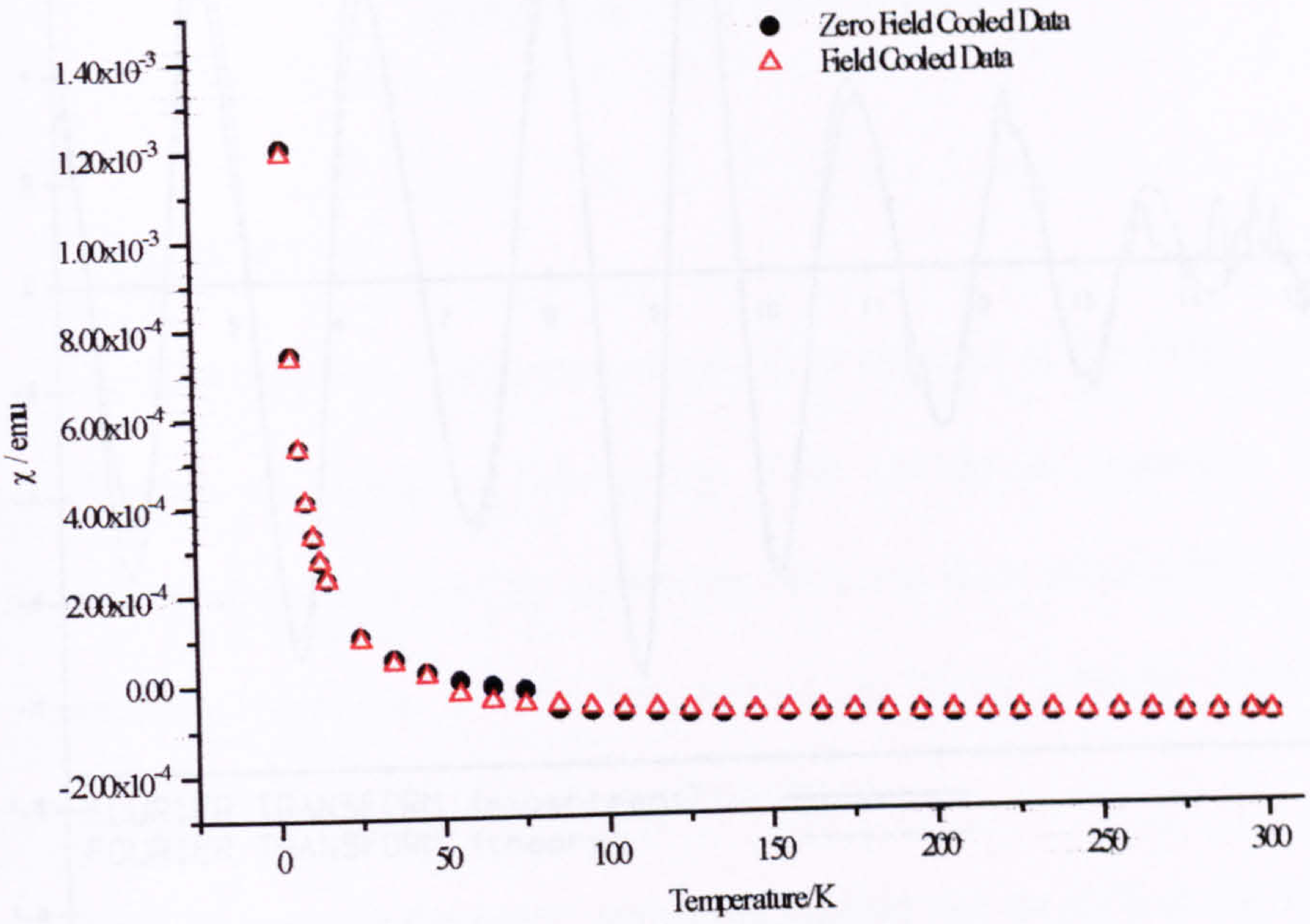

Figure 4.30: *2-Methylnaphthalene*

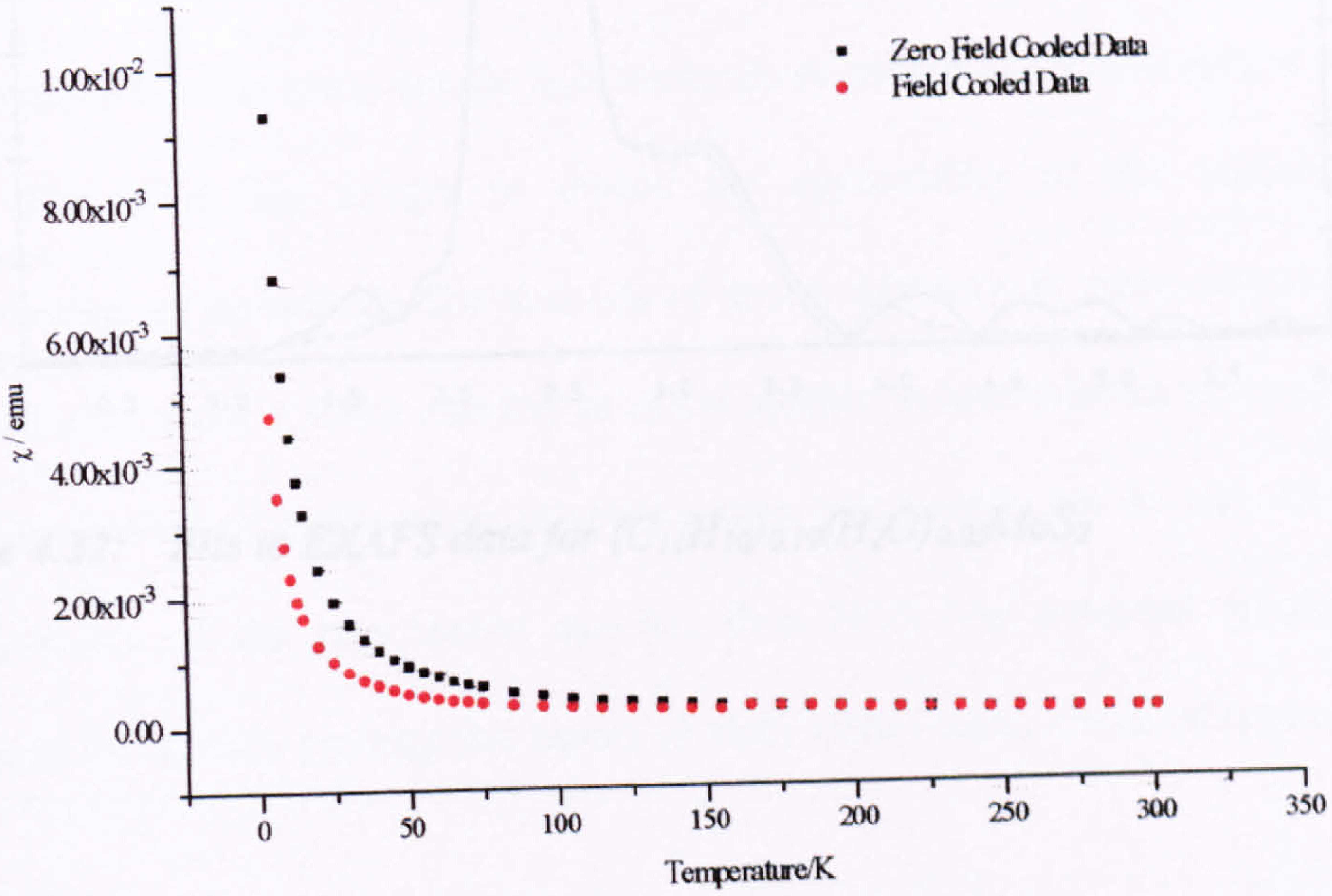

Figure 4.31: *Biphenyl*

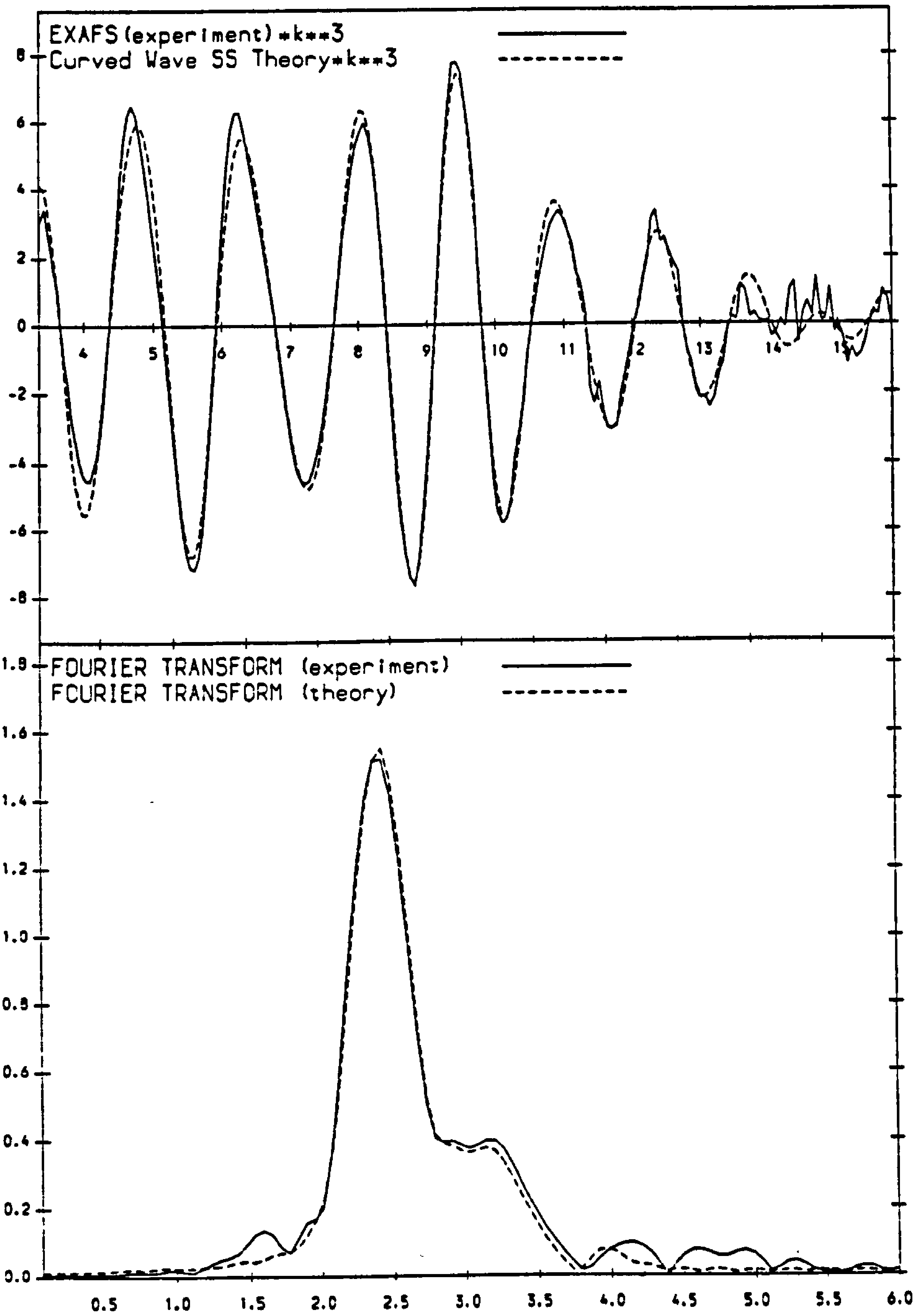

Figure 4.32: Fits to EXAFS data for $(C_{11}H_{10})_{0.19}(H_2O)_{0.05}MoS_2$

Chapter Five

Electron Volt Spectroscopy

5.1 INTRODUCTION

The Electron Volt Spectrometer (eVS) is situated at the ISIS neutron spallation source, Rutherford Appleton Laboratory. This instrument measures the momentum distribution of atoms and ions by scattering neutrons from atomic nuclei at high energy and momentum transfers; a technique known as "deep inelastic neutron scattering" (DINS) or "neutron Compton scattering" (NCS).

To date, neutron Compton scattering carried out on eVS at the ISIS facility, has provided a direct measurement of the momentum distribution of atoms and ions in a wide range of condensed matter systems e.g. hydrogen bonds[168], quantum liquids and solids including helium and hydrogen[169,170], amorphous materials[171,172] metals and metal hydrides[173,174] and molybdenum disulphide[175]. This technique has thus proved successful in the studies of what are primarily light elements or simple condensed matter systems.

This work has sought to extend the applicability of this technique to the measurement of momentum distributions of atoms and ions in more complex chemical environments: namely those existing as guest species in intercalation compounds. Many of the technological applications of intercalation compounds are in part determined by the dynamics of the intercalated species, thus NCS has potential application as a technique for directly probing this aspect of these complicated chemical systems.

5.2 PRINCIPLES OF EVS.

5.2.1 Recoil Scattering

In neutron Compton scattering, neutrons are scattered from atomic nuclei at high energy and momentum transfers. Neutron Compton scattering is similar to Compton scattering of photons, as in both cases, the momentum distribution of target particles (nuclei or electrons respectively) are being measured by the inelastic scattering of incident particles of high energy (neutrons or photons). With large q (momentum transfer) i.e. the wavelength of the neutron is much less than the separation between the particles of the scatterer, the neutron probes the properties of individual particles. It is assumed that no electronic transitions are excited by the neutron and accordingly the electrons are treated as if they are rigidly attached to the nuclei. Thus, the momentum distribution of the nuclei can be regarded as that of the atom.

5.2.2 The Impulse Approximation

Over thirty years ago, it was suggested[176] that NCS could be used on ^{4}He to measure directly its atomic momentum distribution. It was proposed that, by working within the limits of the Impulse Approximation (IA), the dynamic scattering function, S(q,ω), could be directly related to the single particle momentum distribution, n(p). The IA assumes that the potential experienced by the particle due to its interaction with other particles of the system is unchanged over the time-scale of its interaction with the neutron. It also assumes that during a collision, a neutron scatters from a single atom with conservation of kinetic energy and momentum.

The interpretation of experimental NCS data relies upon the validity of the IA and this is approached as the momentum transfer q tends to infinity. Necessarily high values of q are only attainable at pulsed neutron sources which can provide the intense flux of epithermal neutrons required (1<ω (energy)<100eV).

The neutrons scatter from individual nuclei independently and only respond therefore, to a single particle momentum distribution. The differential cross-section for nuclear scattering can be written as

$$\frac{d^2\sigma}{d\Omega d\omega} = Nb^2 \frac{k_f}{k_i} S(q,\omega)$$

where N is the number of scatterers, b is the scattering length and k_i and k_f are the incident and final neutron wavevectors. Within the IA, the incoherent dynamic scattering factor is determined by the single particle momentum distribution and can be expressed as

$$S_{IA}(q,\omega) = \int_{-\infty}^{\infty} n(p)\delta\left[\omega + \frac{p^2}{2M} - \frac{(\bar{p}+\bar{q})^2}{2M}\right]dp \qquad (5.1)$$

where $\bar{p}$= atomic momentum

$\bar{q}$= momentum lost by neutron

M= the nuclear mass

n(p) = probability distribution for the nuclear momentum

ω=energy lost by neutron scattering from an atom

The δ function restricts the integration to those states where the total kinetic energy of the neutron and the atomic nucleus is conserved. In a scattering event, in which the neutron loses momentum $\bar{q}$ and energy ω when scattering from an atom of mass M, if the momentum of the atom is $\bar{p}$ prior to collision, then it will be $\bar{p}+\bar{q}$ after collision and the energy transfer is given by

$$\omega = \frac{(\bar{p}+\bar{q})^2}{2M} - \frac{p^{\ 2}}{2M} \qquad (5.2)$$

The component of atomic momentum along $\vec{q}$ is denoted y where

$$y = \bar{p}.\hat{\vec{q}} = \frac{M}{q}\left(\omega - \frac{q^2}{2M}\right) \qquad (5.3)$$

Thus $S(\vec{q},\omega)$ can be written as

$$S(\vec{q},\omega) = \frac{M}{q} J(\hat{\vec{q}},y)$$

$$\text{where } J(\hat{\vec{q}},y) = \int n(p)\delta(\bar{p}.\vec{q} - y)d\bar{p}$$

From a measurement of $\vec{q}$ and ω, the component of atomic momentum along direction $\vec{q}$ can be determined. Measuring a large number of scattering events, recording $\vec{q}$ and the value of y for each event, builds up a distribution $J(\hat{\vec{q}},y)$. $J(\hat{\vec{q}},y)\mathrm{d}y$ is the probability that the nucleus has momentum component along $\vec{q}$ with magnitude between y and $y+dy$. If *n(p)* is isotropic, there is no dependence on the direction of $\vec{q}$ and $J(\hat{\vec{q}},y)\mathrm{d}y$ reduces to $J(y)dy$; this is termed the "Compton profile."

For a scatterer comprising a number of different masses, the contribution from atoms of mass M is given by

$$S_M(\hat{\vec{q}},\omega) = \frac{M}{q} J_M(\hat{\vec{q}},y_M) \qquad (5.4)$$

J(y) should be symmetric about y_M=0, reflecting its interpretation as a probability distribution for components of atomic momentum along $\vec{q}$ and that atoms are equally likely to have negative or positive directions of movement. y_M can be used as a fitting parameter. If the IA is satisfied, then the fits should give y_m=0. Thus non-zero values of y_M are evidence of deviations from the IA. $S_M(\hat{\vec{q}},\omega)$, at constant q, has a maximum centred at y=0, i.e. at $\omega = \frac{q^2}{2M}$. This is termed the recoil energy and corresponds to a neutron scattering from a stationary atom. Doppler broadening from atomic motion produces a distribution of energy transfers centred at ω_{re}. When the system is bound by harmonic forces and is isotropic, *n(p)* can be treated as a Gaussian distribution and

$$J(y)=\left(\frac{1}{\sqrt{2\pi\sigma_m^2}}\right)\exp\left[\frac{-(y-y_m)^2}{2\sigma_m^2}\right] \qquad (5.5)$$

The profile centroid "y_m" is the position of the peak; the standard deviation "σ_m" is the energy width centred on the recoil energy. The mean atomic kinetic energy can be determined from σ_m from the relationship

$$\langle K\rangle=\frac{3\sigma_m^{\ 2}}{2M} \qquad (5.6)$$

The factor of three in the numerator is to account for three equivalent directions in space for an isotropic system and σ_m is the rms momentum component along one of these directions. Hence by building up a distribution "$J(\vec{q},y)$" and fitting a Gaussian (for atoms in an approximate harmonic potential) convoluted with the instrument resolution function, a direct measurement of the mean atomic kinetic energy can be obtained.

5.2.3 Final State Effects

The IA is exact when $\vec{q}$ and ω are infinite and scattering is taking place from non-interacting particles. For real systems however, the effect of collisions between the recoiling atom and other atoms in the system means that the IA is never satisfied completely. At high $\vec{q}$ and ω on eVS, systematic deviations from the IA can be observed. These are known as "final state effects" (FSE's) and their effect on data interpretation has been extensively investigated.[177] FSEs produce asymmetries in the measured momentum distribution and shift the peak position to negative y values. The procedure to reduce the error incurred, into the measured value of σ_M is to symmetrise the measured *J(y)* about y_M=0. Sears[178] has given a justification for this procedure which will not be recounted here but is recognised as eliminating most of the error from FSE's.

5.2.4 The Electron Volt Spectrometer

A schematic diagram of eVS is shown in Figure 5.1. It is an inverse geometry instrument in which the energy of the scattered neutron is fixed and $\vec{q}$ and ω are determined from time-of-flight techniques. A powder sample is loaded into a flat rectangular aluminium sachet which is secured to an open aluminium frame. This is mounted on an aluminium rod and suspended centrally in the eVS sample tank with the plane of the sachet and frame perpendicular to the incident beam. Both sample tank and beam-line are evacuated.

A pulsed white epithermal neutron beam is incident on the sample. Neutrons scattered by the sample are filtered by analyser foils which are fixed to supports and placed between the sample and the detectors. The thin foils are made of gold or uranium and absorb neutrons strongly over a narrow band of energy centred at E_1.

The foils are cycled in and out of the beam every five minutes, thus two time-of-flight spectra are recorded; one with the foils between the sample and detectors and the second with the foil removed. The difference between these two spectra is due to the neutrons absorbed by the foil and is effectively the time-of-flight spectrum for neutrons scattered with final energy E_1. The scattered neutrons are detected by 32 ^{6}Li doped glass scintillators, arranged as four banks of eight around the incident beam. These detectors are movable; generally for hydrogenous systems, the dynamics of the scattering interaction restricts the scattering to angles $\theta<90°$ and detectors are placed in forward scattering positions. By taking the difference between spectra collected with foil-in and foil-out, data are collected for neutrons scattered with energy E_1.

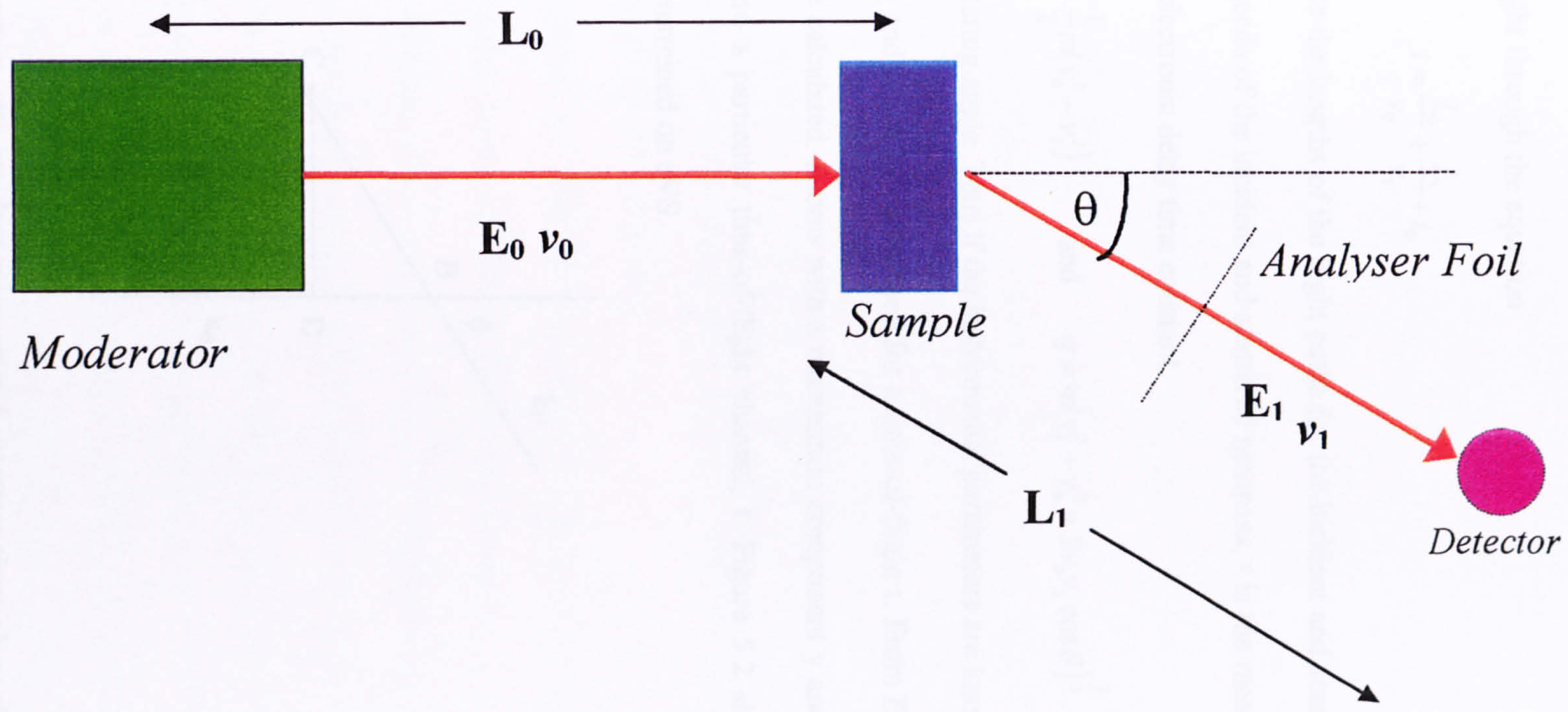

Figure 5.1: *Schematic diagram of the Electron Volt Spectrometer*

The velocity of the scattered neutrons, v_1, can be calculated from $E_1 = \frac{1}{2}mv_1^2$ where m is the neutron mass. The velocity of the incident neutron, v_0, is determined from the neutron time-of-flight through the equation

$$t = \frac{L_0}{v_0} + \frac{L_1}{v_1} + t_0$$

where L_0 and L_1 are the lengths of the flight paths for the incident and scattered neutron, v_0 and v_1 are the speeds of the incident and scattered neutrons, t is the measured time-of-flight and t_0 is the electronic delay time constant.

Thus $$\omega = \frac{1}{2}m\left(v_0^2 - v_1^2\right) \qquad \text{and} \qquad q = m\left(v_1^2 + v_0^2 + 2v_0v_1\cos\theta\right)^{\frac{1}{2}} \qquad (5.7)$$

where θ is the scattering angle. Thus if the instrumental parameters are known i.e. E_1, L_0, L_1, t_0 and θ, then q and ω can be determined for a time-of-flight t. From Equation 5.3, a value for y_m can be calculated. Atoms with a momentum component y and mass M will scatter neutrons into a particular time-of-flight channel, t. Figure 5.2 shows how the direction of $\vec{q}$ is determined on eVS.

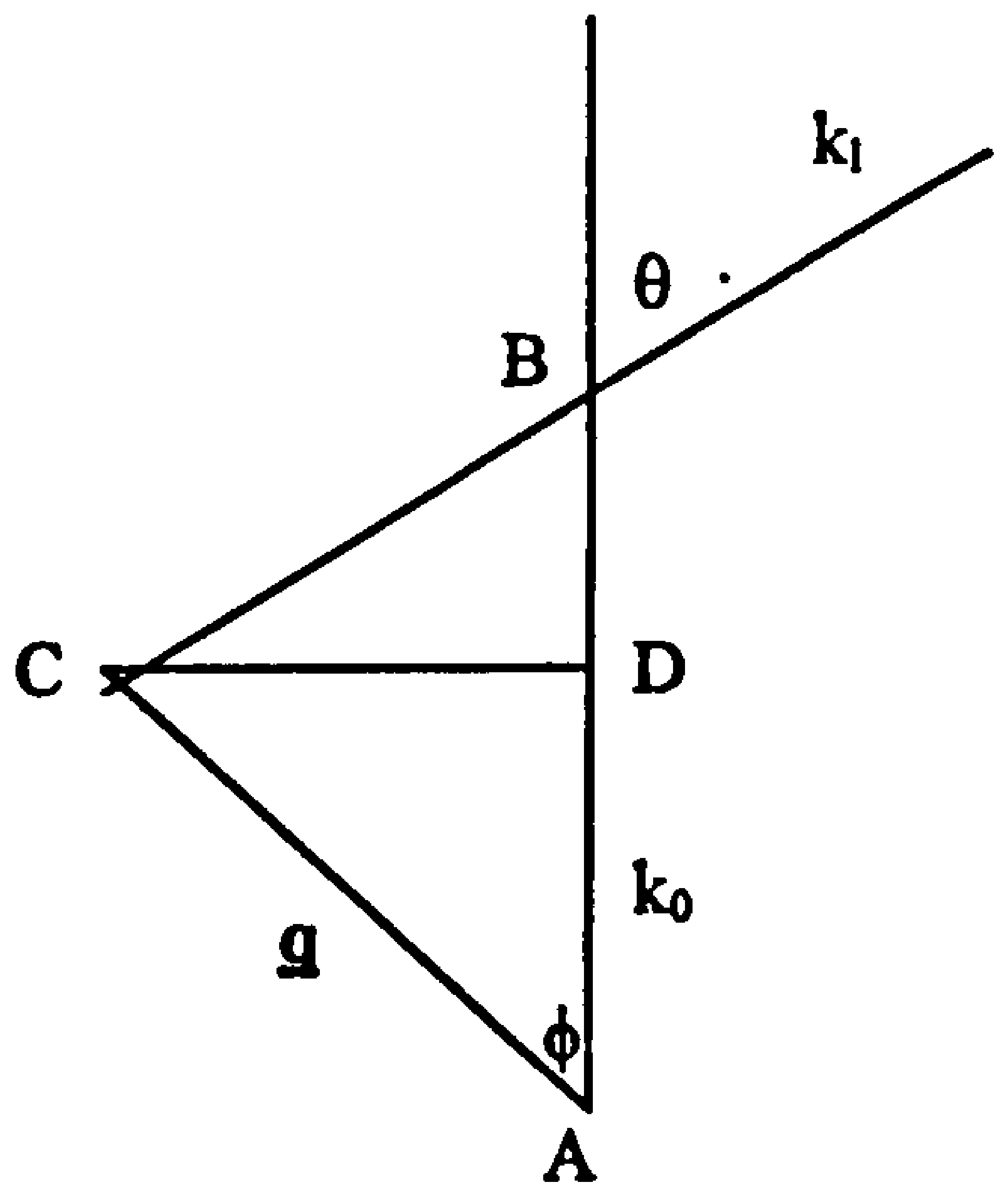

Figure 5.2: A neutron with incident momentum $\underline{k}_0$ scatters through angle θ and has final momentum $\underline{k}_1$. ϕ can be expressed as cos ϕ= (AB-BD)/AC = (k_0-$k_1$cosθ)/q.

5.2.5 Data Analysis

Full data analysis routines for eVS are described elsewhere[179] and only the principles will be described here. For a powder sample with no preferred orientation, time-of-flight spectra at different angles each provide an independent measurement of $J_M(y_M)$ for each atomic mass in the sample. The scattering from a particular atomic mass appears as a peak centred at the recoil time-of-flight for that mass. Distributions obtained at different scattering angles can be averaged to improve statistical accuracy. This is performed by the following procedure. In the analysis routines, each peak can be characterised by three parameters:-

1- The standard deviation, σ_M, of the assumed Gaussian momentum distribution corresponding to mass M. This can be set or used as a fitting parameter.

2- The peak area A_M. This is related to the product of the concentration and the scattering cross-section for mass m. It can be fixed if the sample composition is known. If it is used as a fitting parameter, the resulting values of A_M can be used to determine the sample composition.

3- The peak position, y_M. This can be accurately calculated from the atomic mass and is always fixed by the mass which is input to the program.

The individual time-of-flight spectra are fitted using N_M, the number of atoms of mass M in the sample and σ_M as fitting parameters. The fitted peaks of all masses other than that corresponding to the mass of interest are subtracted from the time-of-flight spectra, leaving only the single peak corresponding to the atom of mass M. This is converted into momentum space. A weighted mean of the spectra from individual detectors can be obtained from $J_M(y_M)$ convoluted with a mean resolution function for mass M, to give the true Compton profile. The resolution function takes into account detector intensities at the scattering angle θ, resulting from variations in detector efficiency, the angular distribution of scattered intensity and the instrument geometry.

Errors which are reported, originate from finite resolution of experimental parameters. These parameters which define the eVS resolution function in y space are uncertainties in L_0, L_1, θ, E_1 and t, the time-of-flight of the neutron. The distributions of all resolution components are assumed to be Gaussian except the energy resolution of the gold foil which is treated as a Lorentzian and the standard deviations of these distributions are determined by calibration procedures.

The approach to studying intercalation compounds on eVS was to begin with a hydrogenous system, where the large scattering cross section of hydrogen would result in a well defined recoil peak. The study then progressed to investigations of lithium ions as guest species in a variety of hosts, as these systems are numerous and technologically important, with the aim of investigating the effects of the host environment on the dynamics of the lithium ion. Finally a molecular ion situated within a cavity was studied to extend the complexity of the system under investigation.

5.3 H_xMoO_3

The aim of this work was to measure the hydrogen momentum distribution in three of the phases: $H_{0.3}MoO_3$, $H_{1.7}MoO_3$ and $H_{2.0}MoO_3$. The evidence for hydrogen existing as hydroxyl groups in the phase $H_{0.3}MoO_3$ is fairly conclusive[183]. It was hoped to observe differences in the momentum distribution resulting from the site of attachment of the hydrogen atoms within the lattice of the other two phases; either as hydroxyl groups attached to bridging oxygen atoms or as $-OH_2$ groups as co-ordinated to Mo atoms. The transition metal oxide, MoO_3, has a unique layer structure (Figure 1.13).

Glemser and Lutz[180] showed that the reduction of MoO_3 in aqueous acidic media leads to the formation of a series of phases $MoO_{3-x}(OH)_x$ or H_xMoO_3 with $0.5 \leq x \leq 2.0$. A more detailed study by Dickens and Birtill[181] established the presence of four distinct phases for which $0 \leq x \leq 2.0$. Single phase materials have been identified in the following composition ranges: blue, orthorhombic, $0.23 \leq x \leq 0.4$; blue, monoclinic, $0.85 \leq x \leq 1.04$; red, monoclinic, $1.55 \leq x \leq 1.72$. A fourth, green monoclinic line phase has been identified at $x=2.0$. Comparison of the lattice parameters for each of these phases with those of MoO_3 indicates that hydrogen is inserted into the MoO_3 host matrix with minimal structural rearrangement.

These H_xMoO_3 phases are deeply coloured, the colour depending on the degree of reduction of the metal centre. Their electrical conduction properties range from semiconducting to metallic, the latter being accompanied by weak temperature independent paramagnetism. H_xMoO_3 bronzes, by analogy with the tungsten bronzes, have been studied for possible applications as gas sensors, electrochromic materials, hydrogen storage materials and hydrogenation catalysts.

Information concerning the hydrogen atom positions has come from powder neutron diffraction and inelastic neutron scattering studies[182]. A full structural determination of the lowest hydrogen-content phase has been reported[183]. Neutron diffraction on this orthorhombic phase shows that the hydrogen is incorporated as hydroxyl groups without any major structural changes to the MoO_3 lattice. These groups are not involved in hydrogen bonding between the layers but are located within MoO_3 layers, attached to bridging oxygen atoms in the form of -OH groups. The presence of hydroxyl groups has been confirmed by INS experiments.

The hydrogen positions in the higher hydrogen-content phases is the subject of greater debate. A structural study of the deuterated phase $D_{1.7}MoO_3$ by powder neutron diffraction located the hydrogen in sites about the terminal oxygen with an increase in the Mo-O bond length[195]. The presence of $-OH_2$ groups in the interlayer space would require partial occupancy of the four sites about each terminal O with each -OH group directed at a terminal oxygen of the adjacent layer. Normal co-ordinate analysis based upon a structure containing -OH_2 groups is consistent with the measured INS spectrum.[196] However, several NMR studies on both $H_{1.7}MoO_3$ and $D_{1.7}MoO_3$ have led to different conclusions. The proposed sites for the hydrogen atoms have ranged from models which possess two -OH groups[197] to ones which require a combination of -OH and Mo-H groups[198]. The presence of a fraction of -OH groups might have been masked by the high background of the IINS spectrum. Proton mobility in the phases $H_{0.36}MoO_3$ and $H_{1.7}MoO_3$ have been studied using NMR techniques[139] which indicate rapid hydrogen motion in the latter phase with much lower proton mobility in the former.

5.3.1 Experimental

Pure phases of H_xMoO_3 (x~0.3, 1.6, 2.0) were prepared following the method of Glemser and Lutz. In an effort to prepare the most highly reduced phase, it was necessary to maintain MoO_3 in a highly reducing environment. Approximately 3g of finely ground MoO_3 (Aldrich 99.99%) was heated under reflux with 200ml of 50% HCl and an excess of zinc pellets. On addition of Zn/HCl, the white MoO_3 immediately turned blue and progressed to a burgundy colour after about two hours under reflux. An excess of Zn was maintained throughout. After prolonged heating, a green solid was formed. However all attempts to isolate this green phase as a clean, dry powder were unsuccessful. Attempts to stabilise the product by isolation in an evacuated tube consistently led to decomposition to the less reduced burgundy phase on evacuation of the tube. It was concluded that the instability of the phase H_2MoO_3 resulted in decomposition to the more stable $H_{1.6}MoO_3$ phase. As a result no neutron Compton scattering data were collected for this material as a pure phase could not be transported to the ISIS facility.

Red monoclinic H_xMoO_3 ($x\approx1.6$) was also prepared by treatment of MoO_3 with zinc and HCl. After reduction to the green phase ($x\approx2.0$), this material was dehydrogenated in vacuo at 383K for 16 hours. Powder X-ray diffraction showed the product to be a single phase. When indexed on a monoclinic unit cell, lattice parameters of a=13.9840(63)Å, b=3.7723(12)Å, c=4.0575(14)Å and β=93.84(20)° were obtained, consistent with those of Birtill and Dickens[181]. Thermogravimetric analysis gave a stoichiometry of $H_{1.56\pm0.02}MoO_3$ and combustion analysis one of $H_{1.57\pm0.03}MoO_3$.

The blue orthorhombic phase ($x\approx0.3$) was prepared from a mixture of $H_{1.57}MoO_3$ and MoO_3 so as to create an overall composition of $H_{0.3}MoO_3$ in an aqueous slurry. This was heated in a Teflon-lined bomb at 353K for three weeks, with regular shaking of the mixture. The powder X-ray pattern was indexed on an orthorhombic unit cell and refined lattice parameters of a=3.8838(5)Å, b=14.0695(16)Å and c=3.7338(5)Å were obtained. Thermogravimetric and combustion analysis determined the degree of incorporation of hydrogen to be 0.29(0.03) and 0.31(0.02) per atom of molybdenum respectively. NCS data were collected for 1.5g each of $H_{0.30}MoO_3$ and $H_{1.57}MoO_3$, at both room temperature and at 4.5K. Data collection times were approximately 8 hours per sample at each temperature. Gold analyser foils with a strong absorption cross-section centred at 4908meV and a FWHM of 134meV were used: these maximised the neutron count rate but resolution of the oxygen and molybdenum recoil peaks was sacrificed. All thirty-two detectors were placed at forward scattering angles for detection of scattering from hydrogen.

5.3.2 Data Analysis and Results

The foil-in and foil-out time-of-flight spectra for each detector were suitably normalised and subtracted. Figures 5.3 and 5.4 show typical time-of-flight difference spectra for $H_{0.3}MoO_3$ and $H_{1.57}MoO_3$ respectively, each the summation of one bank of detectors.

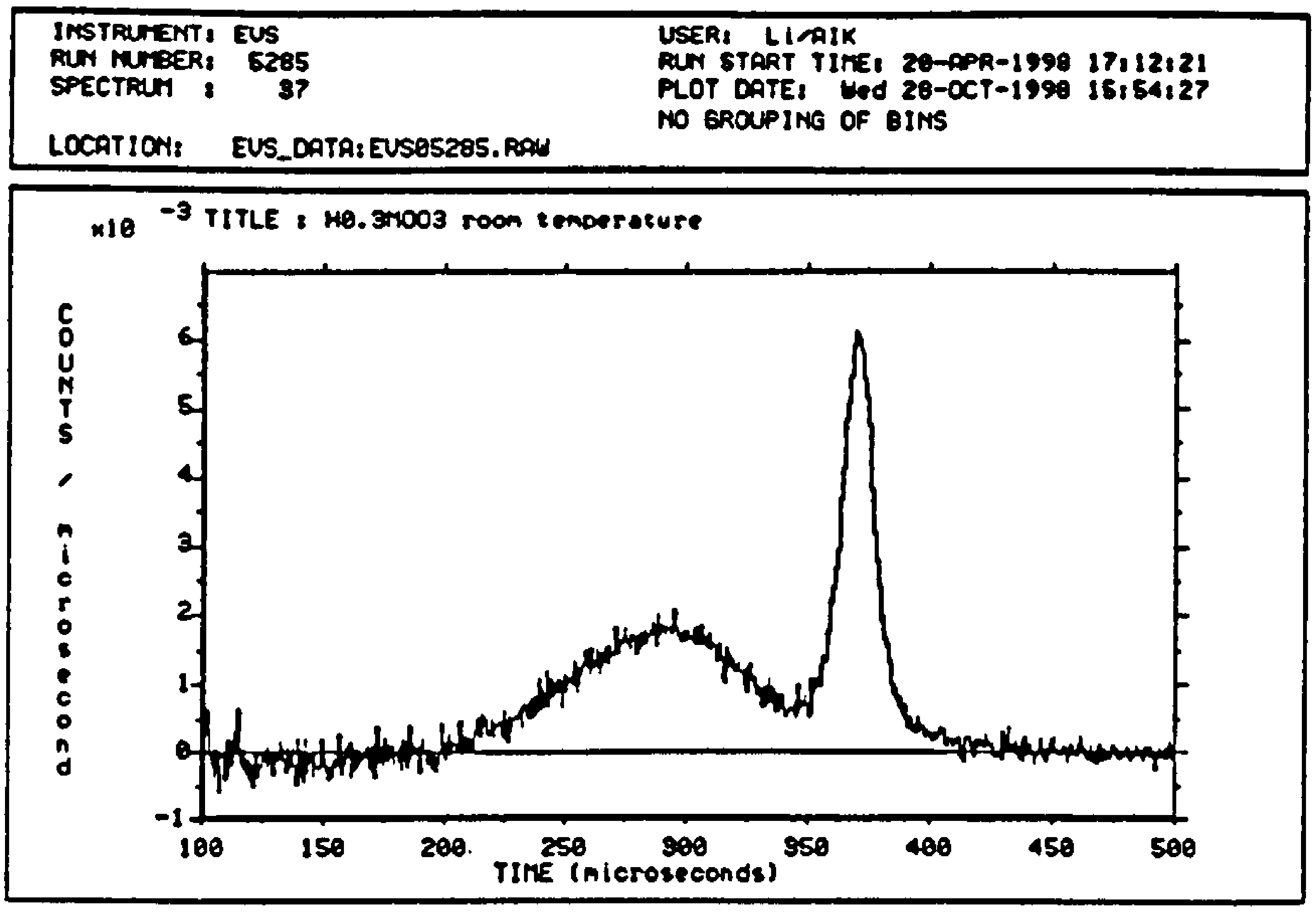

```
INSTRUMENT: EVS                             USER:  LI/AIK
RUN NUMBER:  5285                           RUN START TIME: 20-APR-1998 17:12:21
SPECTRUM  :    37                           PLOT DATE:  Wed 28-OCT-1998 15:54:27
                                            NO GROUPING OF BINS
LOCATION:    EVS_DATA:EVS05285.RAW
```

Figure 5.3: Time-of-flight spectrum for room temperature $H_{0.3}MoO_3$ summed over one bank of detectors.

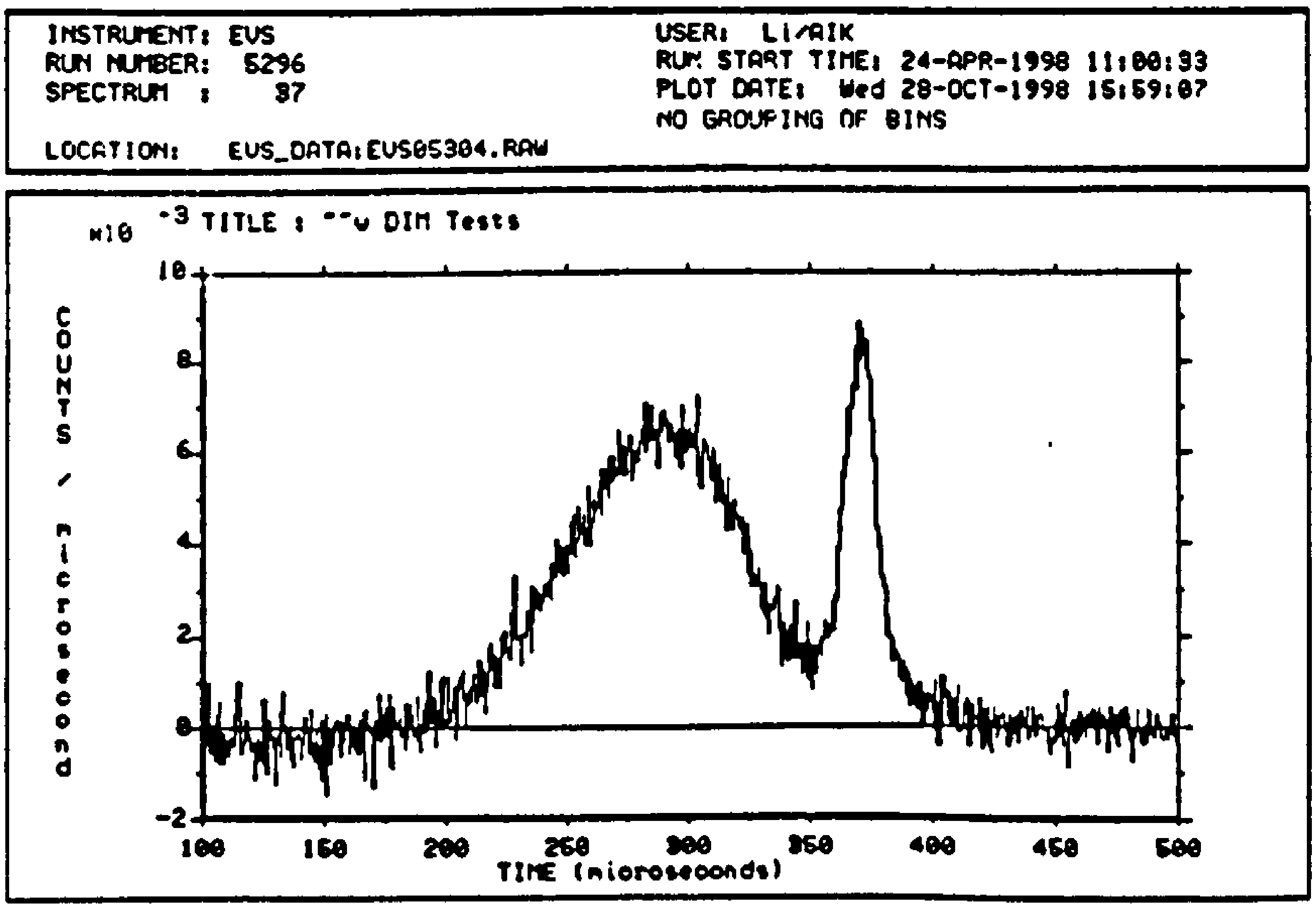

```
INSTRUMENT: EVS                             USER:  LI/AIK
RUN NUMBER:  5296                           RUN START TIME: 24-APR-1998 11:00:33
SPECTRUM  :    37                           PLOT DATE:  Wed 28-OCT-1998 15:59:07
                                            NO GROUPING OF BINS
LOCATION:    EVS_DATA:EVS05304.RAW
```

Figure 5.4: Time-of-flight spectrum for room temperature $H_{1.57}MoO_3$ summed over one bank of detectors.

Two features are visible in each spectrum. The broader peak between 150-350μs corresponds to recoil scattering from hydrogen. The narrower and more intense feature between 350-425μs is the superposition of recoil scattering from O, Mo and Al nuclei. The Al contribution originates from the Al foil sample holder.

Contributions to the Compton profile from aluminium, molybdenum and oxygen were subtracted from the data; each element's contribution being a function of the atom % in the sample and it's total neutron scattering cross-section. Aluminium subtraction was achieved by subtracting a normalised background spectrum for a sample of an empty aluminium sachet. The resulting hydrogen time-of-flight profiles for each detector were transformed into momentum space and fitted to Equation 5.5. Typical fits to the data for $H_{0.30}MoO_3$ and $H_{1.57}MoO_3$ are shown in Figs. 5.5 and 5.6. Tables 5.1 and 5.2 in Appendix A summarise the momentum values obtained for $H_{0.30}MoO_3$ and $H_{1.57}MoO_3$ at the respective θ values, for both symmetrised and unsymmetrised data. Only 16 detectors out of a total of 32 were used for analysis. Problems with electronics in two banks resulted in the time-of-flight spectra from these detectors being unsatisfactory for analysis.

It has been reported that deviations from the IA on measurements of hydrogen using the eVS spectrometer typically introduce errors of less than 1% in the measured kinetic energy of the proton[184]. The statistical errors of those reported here are approximately 2% and symmetrisation of the recoil peaks has little effect on the value of the peak width obtained as demonstrated by the similarity of results for symmetrised and unsymmetrised data. However, after symmetrising the data about $y_M=0$ and repeating the fitting procedure, the value of σ_M obtained is usually slightly lower than for the unsymmetrised data.

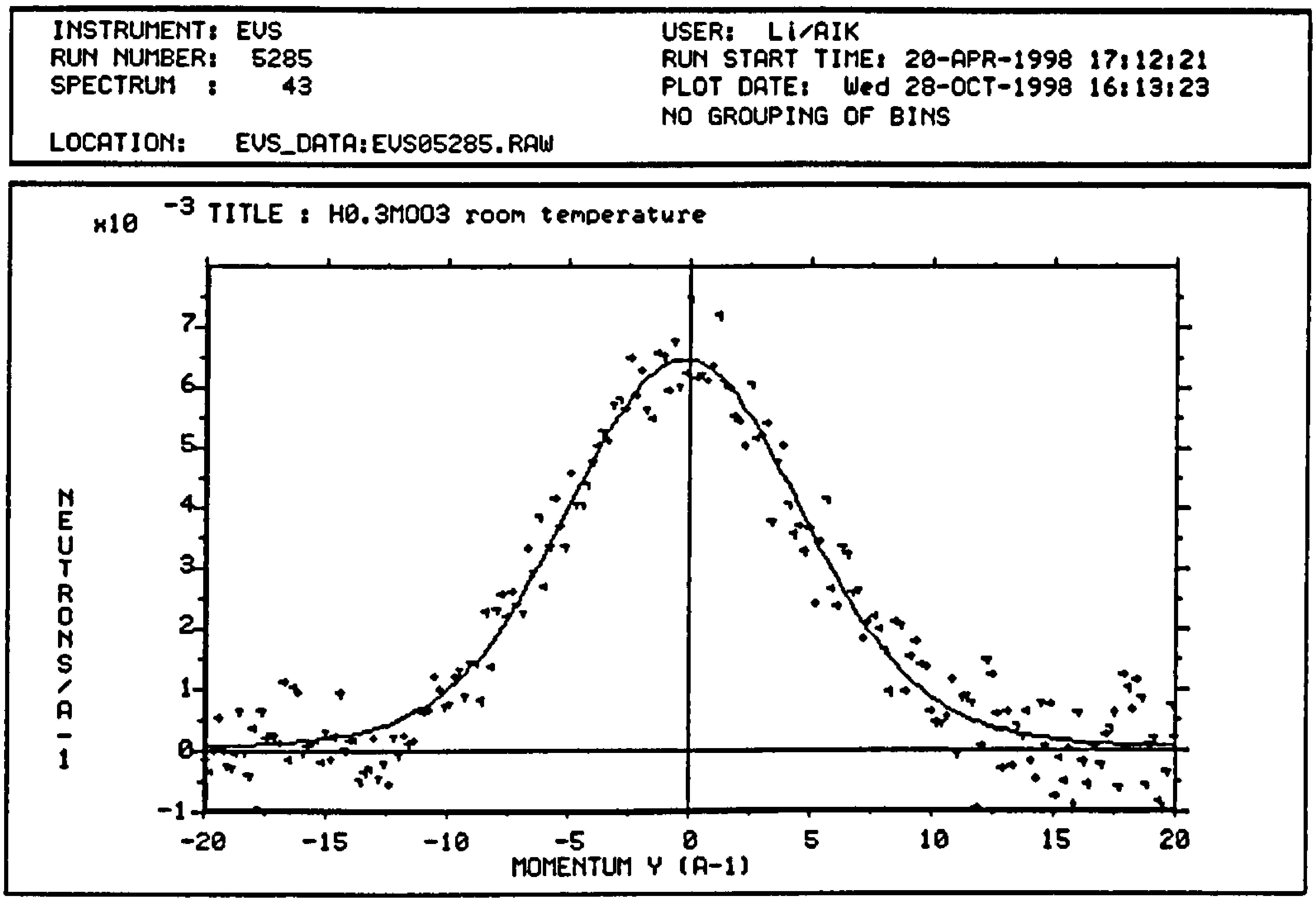

```
INSTRUMENT: EVS                        USER:  Li/AIK
RUN NUMBER:  5285                      RUN START TIME: 20-APR-1998 17:12:21
SPECTRUM  :    43                      PLOT DATE:  Wed 28-OCT-1998 16:13:23
                                       NO GROUPING OF BINS
LOCATION:    EVS_DATA:EVS05285.RAW
```

Figure 5.5 Typical fit to hydrogen recoil peak for $H_{0.3}MoO_3$.

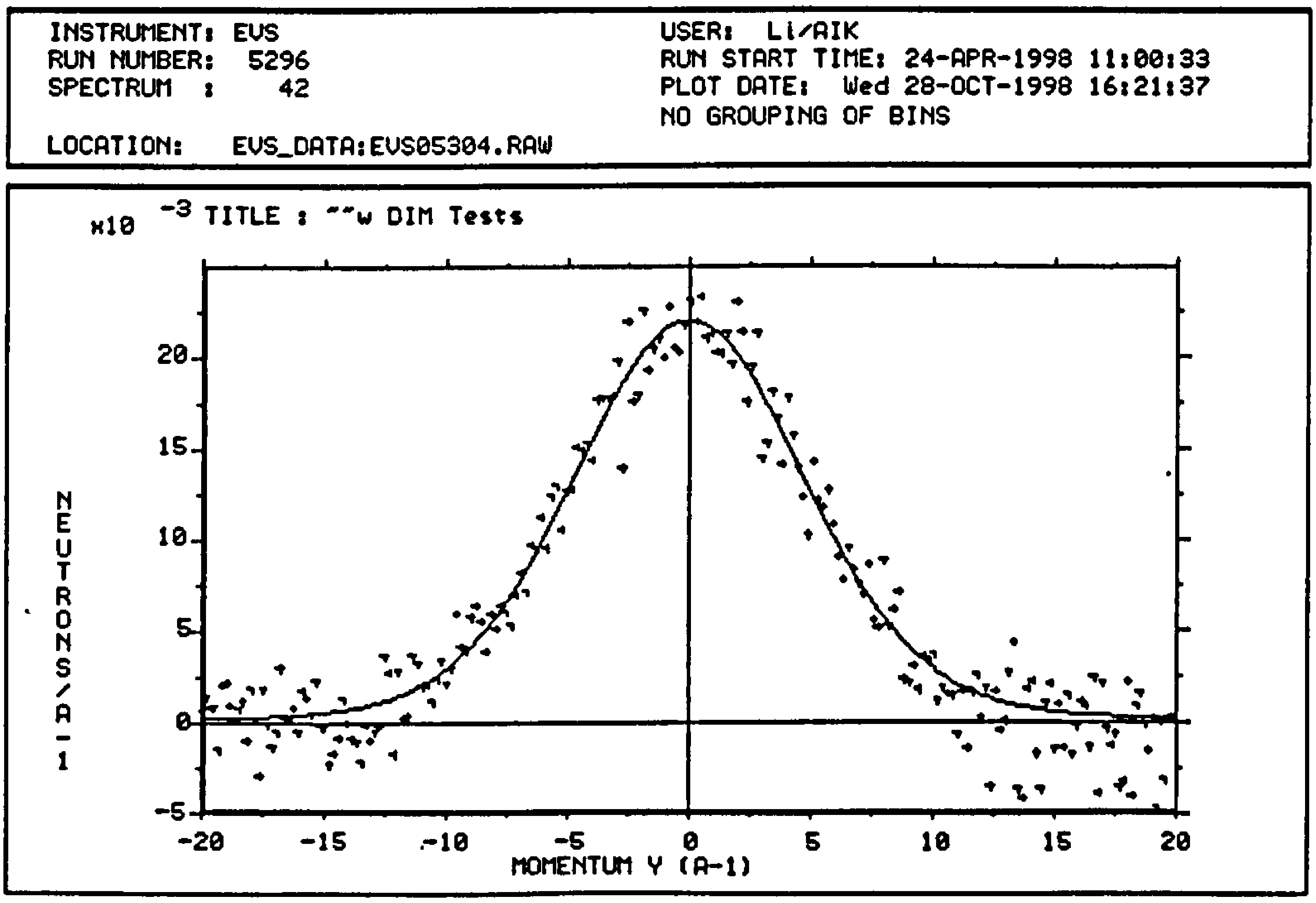

```
INSTRUMENT: EVS                        USER:  Li/AIK
RUN NUMBER:  5296                      RUN START TIME: 24-APR-1998 11:00:33
SPECTRUM  :    42                      PLOT DATE:  Wed 28-OCT-1998 16:21:37
                                       NO GROUPING OF BINS
LOCATION:    EVS_DATA:EVS05304.RAW
```

Figure 5.6: Typical fit to hydrogen recoil peak for $H_{1.57}MoO_3$

The kinetic energy of the hydrogen can be calculated using Equation 5.6: Table 5.1 lists the mean value of σ_M from symmetrised data, excluding those detectors which clearly were not fitting the data correctly, owing to instrumental problems. The corresponding kinetic energy is also quoted. Values of σ_M from symmetrised data were used as the uncertainties in the values are marginally lower.

Table 5.1: *σ_{sym} values for $H_{0.30}MoO_3$ and $H_{1.57}MoO_3$*

	4.3K		295K	
	σ_{sym} /Å^{-1}	E_K /cm^{-1}	σ_{sym} /Å^{-1}	E_K /cm^{-1}
$H_{0.30}MoO_3$	4.54±0.06	1381±35	4.42±0.04	1304±25
$H_{1.57}MoO_3$	4.26±0.03	1213±18	4.34±0.04	1262±21

5.3.3 Discussion

NCS measurements for $H_{0.30}MoO_3$ and $H_{1.57}MoO_3$ at 4.3K and 295K produce Compton profiles which are Gaussian in shape and give the square roots of the powder average mean square momentum.

For $H_{0.3}MoO_3$, there is a decrease in kinetic energy of the protons with increasing temperature which can be regarded as marginal after taking the errors into consideration. In contrast, there is a small increase in the measured kinetic energy of the protons in $H_{1.57}MoO_3$ when increasing the temperature from 4.3K to 295K.

This contrast in their respective behaviours with temperature can be explained after consideration of the factors which can cause the change in kinetic energy. The atomic momentum distribution for heavy atoms or molecules is determined primarily by the thermal energy of the atom or molecule. However, for light atoms and molecules, such as hydrogen, the momentum distribution has a large component originating from the zero point motion of the atom. The zero point motion of light hydrogen is very sensitive to small changes in the potential such that a modest alteration will affect the zero point motion of the proton; thus the proton's local environment has a dominant role in determining the atomic momentum distribution. Hence any temperature change that changes this local environment of the proton can cause an increase or a decrease in the momentum of the proton.

Only very small changes in kinetic energy have been observed in this experiment. This is because for a low mass system such as hydrogen, the binding potential of the proton is deep and the energy level separations are large; promotions to eigenstates where a change in momenta would be observed would require significant temperature rises beyond the increase from 4.3K to 295K used in this experiment. At 4.3K, the momentum values of hydrogen atoms in $H_{0.30}MoO_3$ and $H_{1.57}MoO_3$ are 4.54Å^{-1} and 4.26Å^{-1} respectively. These momentum values arise almost entirely from their respective zero point motions, reflecting slightly different environments of the hydrogen atoms in these two phases.

Several studies have been made on eVS of the momentum distribution of hydrogen atoms in various environments e.g DINS from chemisorped hydrogen in potassium intercalated graphite produced a mean kinetic energy of the hydrogen of 980±300K and 1060±120K in $C_8K_{0.9}H_{0.13}$ and bulk potassium hydride respectively[199]. The corresponding values for this work are between 1300-1500K which imply that hydride species are not present in the two phases $H_{0.30}MoO_3$ and $H_{1.57}MoO_3$. Data obtained for related hydrogenous systems on eVS are listed in Table 5.2.

Table 5.2: Collation of data for hydrogenous systems.

Material	**Nature of hydrogen species**	**Mean momentum value /Å^{-1}**	**Ref**
ZrH_2	Hydride	σ_H=4.15±0.01*	174
$C_8K_{0.9}H_{0.13}$	Hydride	σ_H=2.99±0.91*	199
$CD_3CONHCD_3$	Hydrogen bond N-H...O	σ_H=4.67±0.06(4.5K)	168
$KHCO_3$	Hydrogen bond O-H...O	$\sigma_H(\perp)$=4.14±0.08* $\sigma_H(\parallel)$=4.91±0.19*	186
Amorphous hydrogenated carbon	Hydrogen film	σ_H=4.84±0.02*	200
LiOH	Hydroxyl group	σ_H=4.27±0.01*	201

*room temperature measurements

Direct comparison between the values obtained in this work and previous studies is difficult. At present there is no "catalogue" of data for hydrogen in different environments and as can be seen from the range of momentum values in Table 5.2, the momentum of hydrogen is highly environment-specific.

Inelastic neutron scattering studies on $H_{0.34}MoO_3$ and $H_{1.7}MoO_3$ at 80K and 20K respectively have been reported [182,196]. These compositions occupy the same phase regions as $H_{0.30}MoO_3$ and $H_{1.57}MoO_3$ studied in this work. For $H_{0.34}MoO_3$, the inelastic spectrum showed one intense band at 1267cm^{-1} in the central region of the spectrum which is compatible with classification of this compound as containing hydroxide units, the 1267cm^{-1} excitation being due to the Mo-O-H deformation.[202] The spectrum of $H_{1.7}MoO_3$ is more complicated. The two most intense peaks at 979cm^{-1} and 883cm^{-1} were assigned to rocking and wagging vibrations respectively of the $-OH_2$ group and a further strong feature at 1652cm^{-1} was characterised as the scissors vibration of an -OH_2 group.

The physical basis for the IA stems from the energy transfer being much greater than the typical excitation energy of the system; hence the interaction time between the neutron and struck atom is small on the atomic time scale and the atom does not have time to move. This means that all the energy transfer is kinetic as the potential energy of the struck atom does not change. The period of internal mode vibrations is long relative to NCS and the kinetic energy measured is that of the approximately free atom, uncoupled from the dynamical motion of the lattice. In reality, changes to the effective oscillator mass manifest themselves as deviations from the struck particle being entirely free. However, this does mean that direct comparison of the INS data and NCS data must be treated with caution because in the former, dynamical information is limited to the vibrational modes whereas in the latter, all translational energy is being observed. The kinetic energy comes from both the energy of all the -O-H vibrations and the motion of the oxygen atom to which the hydrogen is attached and so, even though it is known that the hydrogen exists as -OH in this phase, the measured kinetic energy for $H_{0.3}MoO_3$ at base temperature (where lattice motion will be reduced) will still be greater than the 1267cm^{-1} stretching vibration in $H_{0.34}MoO_3$ observed in the INS spectrum.

The kinetic energy of 1213cm^{-1} for $H_{1.57}MoO_3$ at 4.3K is lower than would be expected for hydrogen attached as -OH. The metal-oxygen frameworks for $H_{0.3}MoO_3$ and $H_{1.57}MoO_3$ are similar (apart from greater reduction of the metal centre in the latter material). The significantly reduced kinetic energy implies that hydrogen in this phase is less tightly bound than in $H_{0.3}MoO_3$.

In conclusion, it is known that the protons in the former phase are attached to bridging oxygen atoms in the form of -OH groups and it has been proposed that in the latter phase, the hydrogen atoms are co-ordinated to Mo atoms as OH_2 units. Differences in their respective kinetic energies have been observed but the presence of OH_2 groups in the higher hydrogen content phase cannot be categorically assigned from the momenta values. The paucity of NCS data on hydrogenous systems containing $-OH_2$ groups makes it difficult to draw unambiguous conclusions from this pilot study. However, a potentially productive alternative approach would be to compare kinetic energies of hydrogen in $H_{0.3}MoO_3$ and $H_{1.57}MoO_3$ with those in $H_{2.0}MoO_3$ and α-$MoO_3.H_2O$, by recording NCS spectra for the latter two phases. Inelastic neutron scattering data on the line phase $H_{2.0}MoO_3$ show that this phase contains hydrogen in the form of $-OH_2$ units. α-$MoO_3.H_2O$ has a structure which consists of isolated double chains of MoO_6 octahedra with each molybdenum bearing an $-OH_2$ projecting into the interlayer space. Direct comparison of the measured momentum of hydrogen in these materials would be the most productive approach due to the structural similarity of all three phases.

Proton NMR relaxation times (T_1,T_2 and $T_{1\rho}$) for the compounds $H_{1.71}MoO_3$ and $H_{0.36}MoO_3$ in the temperature range $77K<T<450K$ indicate that hydrogen diffusion occurs with $E_A=22$ kJ mol^{-1} and $\tau_c^o \approx 10^{-13}$sec for $H_{1.71}MoO_3$ and $E_A=11$ kJ mol^{-1} and $\tau_c^o \approx 3\times10^{-8}$sec for $H_{0.36}MoO_3$. $H_{1.71}MoO_3$ demonstrates diffusion parameters typical of fast hydrogen diffusion whereas corresponding figures for $H_{0.36}MoO_3$ show it to have poor ionic conductivity. The NCS kinetic energy measurements reflect the differences in the potentials of the protons in each of these phases. Hydrogen was found to be less tightly bound in $H_{1.57}MoO_3$ than in $H_{0.30}MoO_3$ which is consistent with the higher content phase exhibiting faster hydrogen diffusion.

5.4 $LiTiS_2$

The pilot study of $H_{0.30}MoO_3$ and $H_{1.54}MoO_3$ demonstrated that NCS was an applicable technique to the study of the dynamics of hydrogen within a complex chemical environment. It was possible to distinguish, at 4.3K at least, the different potentials experienced by protons when incorporated into MoO_3 in two different forms but because of the light mass of hydrogen, its kinetic energy is insensitive to temperature changes in the range 4-300K.

The investigation was subsequently extended to the study of lithium intercalates. To date, little work had been carried out on lithium on eVS. Lithium is an important guest species in intercalation chemistry. Lithium ions can be intercalated into both layered transition metal dichalcogenides and layered transition metal oxides, occupying vacant sites in the van der Waals gap between successive MX_2 or MO_n layers[187,188].

$LiTiS_2$ was chosen for study because of its technological importance and also because it is well characterised, having been studied by a battery of physical techniques. TiS_2 consists of hexagonally close-packed chalcogen layers between which titanium atoms occupy octahedral sites (Figure 1.2). Lithium ions can be incorporated into the TiS_2 lattice to form a single non-stoichiometric phase for the entire range of $0 \leq x \leq 1$.

5.4.1 Experimental

Polycrystalline TiS_2 was synthesised by combination of the elements in an evacuated silica tube at 590°C for three days. Powder X-ray diffraction data of the product were indexed on a hexagonal unit cell. Refined lattice parameters of a=3.40697(5), c=5.6969(4)Å were obtained for the product. This material was lithiated by reaction with three equivalents of 1.6M n-butyllithium to produce a single-phase material Li_xTiS_2. X was determined as 1.012±0.024 using flame emission spectroscopy.

Powder X-ray diffraction data of the lithiated phase were indexed on the basis of a hexagonal unit cell. Refined lattice parameters of a=3.4518(9), c=6.1858(6)Å for $LiTiS_2$ were obtained. No reflections arising from a hydrated phase were evident in the diffraction pattern of $LiTiS_2$. Neutron Compton scattering data were collected for $LiTiS_2$ at ambient temperature and also at four lower temperatures between 12 and 298K. Measurements at forward scattering angles with gold analyser foils were used to check for hydrogen as $LiTiS_2$ is susceptible to hydration. Back-scattering spectra were recorded using uranium analysers for good separation of the metal and sulphur. Gold analyser foils at back-scattering angles provided the best resolution of the lithium recoil peaks. Figure 5.7 shows the room temperature NCS profile for $LiTiS_2$, summed over a bank of eight detectors at back-scattering angles, obtained with gold analyser foils.

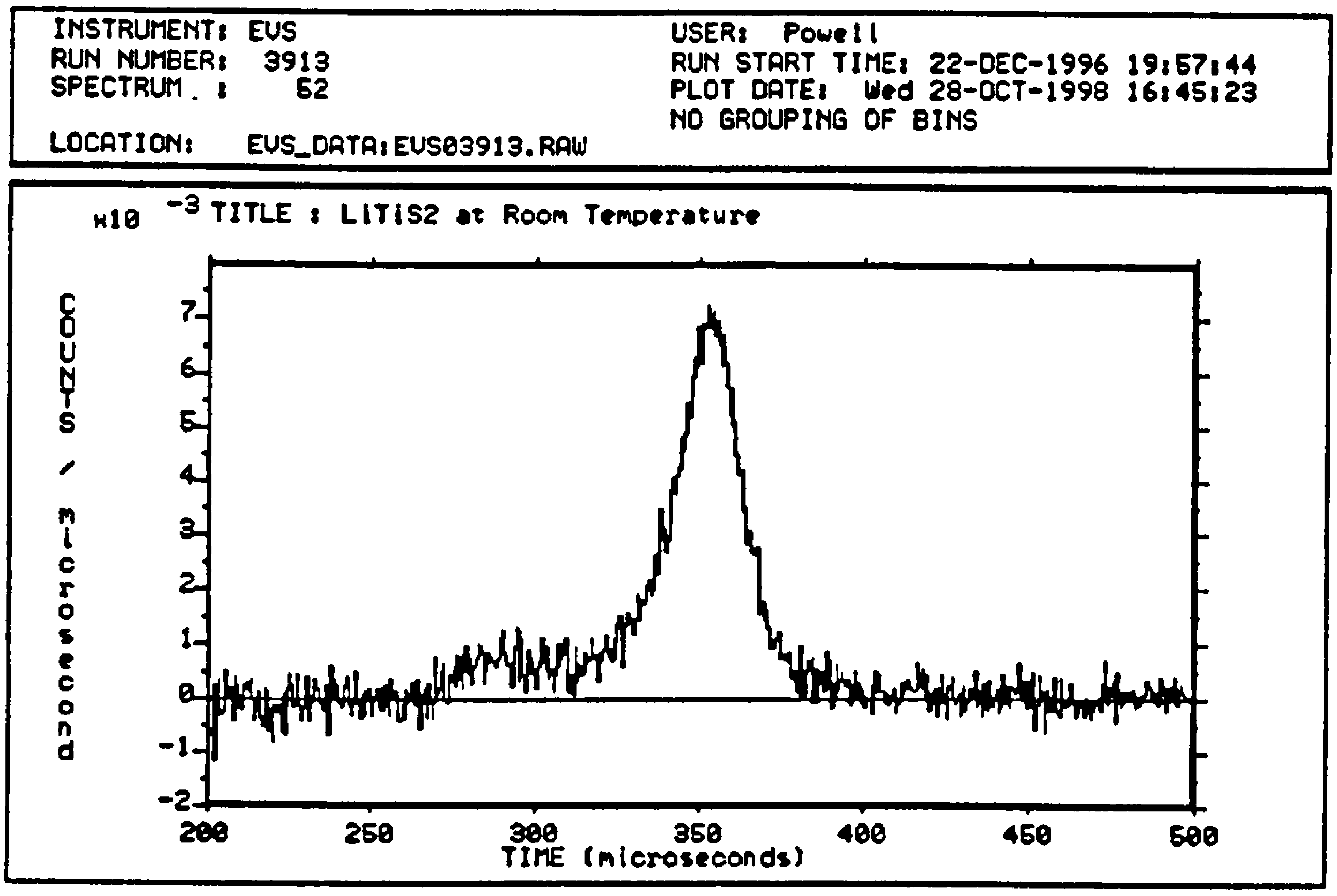

```
INSTRUMENT: EVS                          USER: Powell
RUN NUMBER:  3913                        RUN START TIME: 22-DEC-1996 19:57:44
SPECTRUM . :    62                       PLOT DATE: Wed 28-OCT-1998 16:45:23
                                         NO GROUPING OF BINS
LOCATION:    EVS_DATA:EVS03913.RAW
```

Figure 5.7: Room temperature time-of-flight spectrum for $LiTiS_2$.

5.4.2 Data Analysis and Results

The recoil peak due to lithium appears between 270μs and 320μs, essentially as a shoulder on the side of the main peak at 340-410μs. This intense feature comprises overlapping recoil peaks of sulphur, aluminium and titanium. Scattering contributions from these elements were subtracted from the spectra resulting in lithium time-of-flight profiles for each detector. Values for the kinetic energy were initially determined by fitting Equation 5.5 to the data in y-space. At each temperature, after performing a symmetrisation procedure on each profile to account for deviations from the IA, values of the peak width were determined. These widths were averaged over back-scattering detectors to give a mean value, denoted averaged data in Table 5.3. In an alternative analysis procedure, spectra from the individual back-scattering detectors were focused in momentum space and the resulting single profile fitted to a Gaussian convoluted with the instrument resolution function. These values are denoted "focused data" in Table 5.3. Differences between values of the peak width derived from the two different approaches to data analysis are not statistically significant, although errors in values derived from focused data are, in general, marginally lower. Errors in the values determined are between 6 and 15%. This relatively large error is primarily due to the low neutron count rate for lithium as a result of its small total scattering cross-section and its very high neutron absorption cross-section (ca. 70 barns).

Table 5.3: Values of peak widths for lithium in $LiTiS_2$.

	Averaged data		**Focused Data**	
Temperature/K	σ/Å^{-1}	E_k/meV	σ/Å^{-1}	E_k/meV
13	4.47±0.28	18.05±2.28	4.83±0.36	21.04±3.17
70	4.51±0.47	18.33±3.83	4.87±0.26	21.44±2.31
160	5.16±0.36	24.08±3.38	5.18±0.24	24.27±2.26
220	5.04±0.44	22.91±4.02	5.27±0.31	25.13±3.30
298	6.08±0.49	33.37±5.39	6.16±0.29	34.25±3.21

5.4.3 Discussion

NCS measurements on elemental lithium[173] report figures for the kinetic energy of 21.6meV at 69.5K and 42.03meV at 300K. Values obtained for $LiTiS_2$ at 70K and 298K are 21.4meV and 34.3meV respectively. Similar low-temperature kinetic energies of lithium atoms in the bulk elemental phase, and lithium ions in $LiTiS_2$, are consistent with the kinetic energy arising almost entirely from zero-point motion at these temperatures. However, at room temperature, the measured kinetic energy of lithium ions in $LiTiS_2$ is only 81±7% of that of the atoms in the metal. This may reflect the highly anisotropic environment of lithium ions in the intercalation compound, where the lithium ion sub-lattice is effectively two-dimensional, rather than three dimensional as in the metal. However, the lithium recoil peak is fitted to a Gaussian, based upon the assumption that the particle is in an isotropic environment. The only current way to resolve this problem would be to perform the same experiment on a single crystal of $LiTiS_2$ and thus determine the kinetic energy of the lithium ion in specific crystallographic directions. This would enable the momentum value of lithium ions perpendicular to the sulphur layers to be separated from those parallel to the sulphur layers. This is experimentally impossible at the moment because no lithium would be detected in a sample the size of a single crystal. Uncertainties in the values determined here for the kinetic energies are considerably greater than those measured for lithium in the bulk elemental phase. This is a consequence of the lower number of scattering species in $LiTiS_2$.

As the first experiment to study the applications of NCS to the momentum distribution of lithium ions in intercalation compounds, this experiment proved to be very useful. Observation of a lithium recoil peak is difficult owing to two factors; the element's very low total scattering cross-section and its very high neutron absorption (ca. 70 barns). A higher neutron count rate is observed using gold analyser foils and these are necessary when collecting data on lithium. However, gold foils result in almost complete overlap of metal and sulphur peaks and consequently their use prohibits kinetic energy analysis of metal and sulphur in metal sulphides. However, the ability to resolve oxygen peaks with gold foils was demonstrated in the experiment on H_xMoO_3. Simulation of time-of-flight spectra carried out for various lithiated metal oxides indicated that the systems Li_xMoO_3 and LiV_2O_5 were promising candidates for study on eVS.

5.5 Li_xMoO_3

Lithium can be intercalated into the van der Waals gap of MoO_3 with an accompanying charge transfer from guest to host as with TiS_2. Li_xMoO_3 can be synthesised at ambient temperature; up to $x \approx 0.54$, a single phase is formed but higher lithium contents result in an equilibrium two-phase region for $0.5<x<1.5$ and a second phase is formed for $x>1.528$[185]. Li_xMoO_3 with $x \approx 0.4$ was the selected stoichiometry as this would be comfortably within the single phase region. Lithium dynamics for the two phase region would be easier to measure as the lithium content would be higher but any data would be an average kinetic energy for lithium existing in two phases and so comparison with data collected for $LiTiS_2$ would be meaningless.

5.5.1 Experimental

Approximately 5g of MoO_3 (Aldrich 99.99%) were finely ground, dried and degassed in a Schlenk. 20ml of 60-80 pet. ether, distilled over sodium wire, was added, followed by dropwise addition of a stoichiometric amount of 1.6M n-butyllithium (Aldrich Inorganics). On addition of the n-buyllithium, the white powder of MoO_3

changed to a dark blue colour. The mixture was stirred vigorously for 48 hours and washed repeatedly with distilled pet. ether. The powder X-ray diffraction pattern of the product was similar to that of the parent oxide. The relative intensities of the strongest reflections of MoO_3 were reproduced in the lithiated derivative but their positions were displaced. Sample inhomogeneity was evidenced by lines that could be attributed to MoO_3. This was thought to be due to incomplete equilibration arising from the irreversible nature of lithiation with n-butyllithium. The product was therefore left to equilibrate in a 0.5M solution of $LiBF_4$ in acetonitrile at 50°C for two weeks. Powder X-ray diffraction indicated that the product was predominantly a single-phase material although there were a few lines of very low intensity (<2% intensity of strongest peak) that could not be indexed. Refined lattice parameters of a=3.6885(94)Å, b=16.624(56)Å and c=13.797(11)Å were obtained, in good agreement with Dickens and Reynolds[189]. The overall composition was determined as $Li_{0.450\pm0.005}MoO_3$ from flame emission spectroscopy. Room temperature Compton scattering data were collected for $Li_{0.45}MoO_3$ using gold analyser foils and all detectors placed at back-scattering angles.

5.5.2 Data Analysis and Results

Figure 5.8 shows the NCS profile obtained, summed over all back-scattering detectors. The lithium recoil peak appears as a slight shoulder at a shorter time-of-flight to the intense oxygen peak at 330μs. There was extremely good separation between the oxygen and molybdenum peaks but the lithium recoil peak was swamped by its oxygen neighbour. As a consequence, the lithium peak could not be isolated and no measurement of the kinetic energy of lithium ions in this material could be made. A bank of forward scattering detectors showed that hydrogen was present. Compositional analysis indicated slight hydration of the sample, potentially picked up from the surface of the aluminium foil. The ratio of water to molybdenum was found to be 0.049:1 (assuming a 1:3 Mo:O ratio).

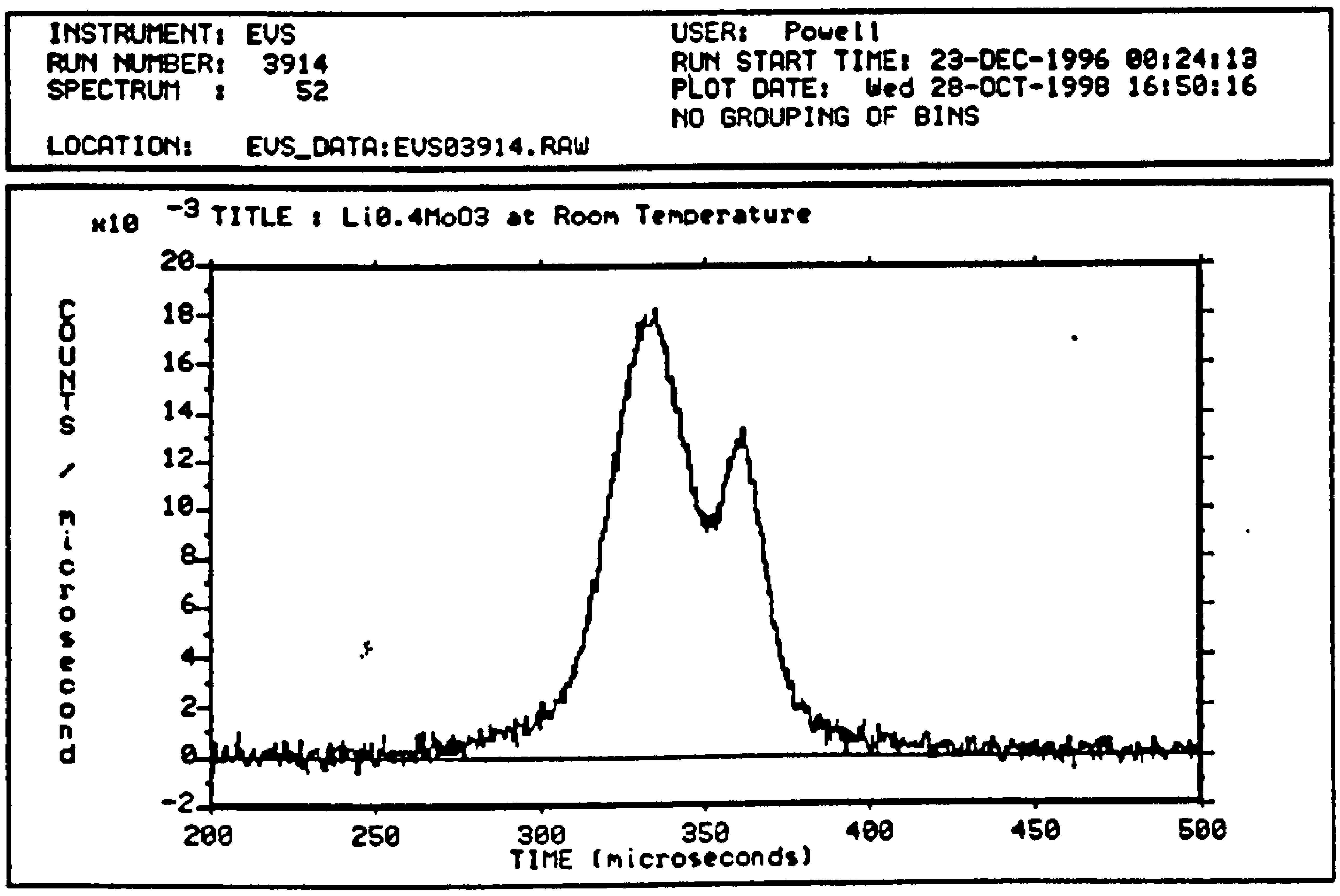

Figure 5.8: Room temperature time-of-flight spectrum for $Li_{0.45}MoO_3$.

5.5.3 Discussion

This experiment demonstrated a new problem not previously encountered in the $LiTiS_2$ measurements. The severity of the problem of considerable overlap of oxygen and lithium recoil peaks had not been anticipated. An immediate remedy for this would be to use uranium analyser foils as these have the effect of separating out recoil peaks and are particularly effective for overlapping peaks from low mass elements. However, the neutron count rate decreases by a factor of approximately ten on changing from gold to uranium foils. This decrease, coupled with the already low intensity of the lithium recoil peak using gold foils, would render the recoil peak undetectable. The atom% of lithium in $Li_{0.45}MoO_3$ is 10% compared with 25% in $LiTiS_2$: clearly this is a crucial factor in the success of lithium detection on eVS. The other sample for study was LiV_2O_5 which has 12.5 atom percent of lithium. By exploiting the higher resolution offered by uranium foils, it was thought that it might be possible to isolate the lithium recoil peak from that of neighbouring oxygen by using a larger sample and longer counting time. These measures were to compensate for the reduction in neutron count rate due to uranium foils.

5.6 $Li_xV_2O_5$

Vanadium cations in V_2O_5 (Figure 1.14) are in a highly distorted octahedral environment in which the shortest metal-oxygen bond is perpendicular to the layers. Three single-phase regions for $Li_xV_2O_5$ have been identified by electrochemical measurements[8,9]: the compound under study was $Li_{1.0}V_2O_5$ which exists on the edge of the $0.9<x<1.0$ phase region[190]

5.6.1 Experimental

Chemical lithiation using the method of Murphy and Christian[9] produced a polycrystalline sample of $Li_xV_2O_5$ which was equilibrated in 0.5M $LiBF_4$ in distilled acetonitrile for a week. Powder X-ray diffraction data were indexed on the basis of an orthorhombic unit cell and refined lattice parameters of a=11.2614(9)Å, b=4.9625(5)Å and c=3.3916(3)Å were obtained. The composition was determined as $Li_{0.98(3)}V_2O_5$ using flame emission spectroscopy, no water could be detected either through combustion analysis or FT-IR. Room temperature neutron Compton scattering data were collected on 9.25g of sample in an aluminium sachet. Sixteen detectors at forward scattering angles with uranium analyser foils were used to check for the presence of hydrogen, as this sample, like $Li_{0.45}MoO_3$, was susceptible to hydration. A further sixteen detectors were placed at back-scattering angles, again with uranium analyser foils.

5.6.2 Data Analysis and Results

Forward scattering detectors indicated that no hydration of the sample had occurred. Normalised data summed over a bank of eight back-scattering detectors are shown in Figure 5.9. The lithium recoil peak is expected to lie in the 240-260μs region. Although a slight increase in neutron count rate can be seen to the left of the dominant oxygen peak at 280μs, data were of too low an intensity to permit analysis. Spectra from detectors 17 to 24 were the most promising, as these profiles demonstrated the best separation between lithium and oxygen.

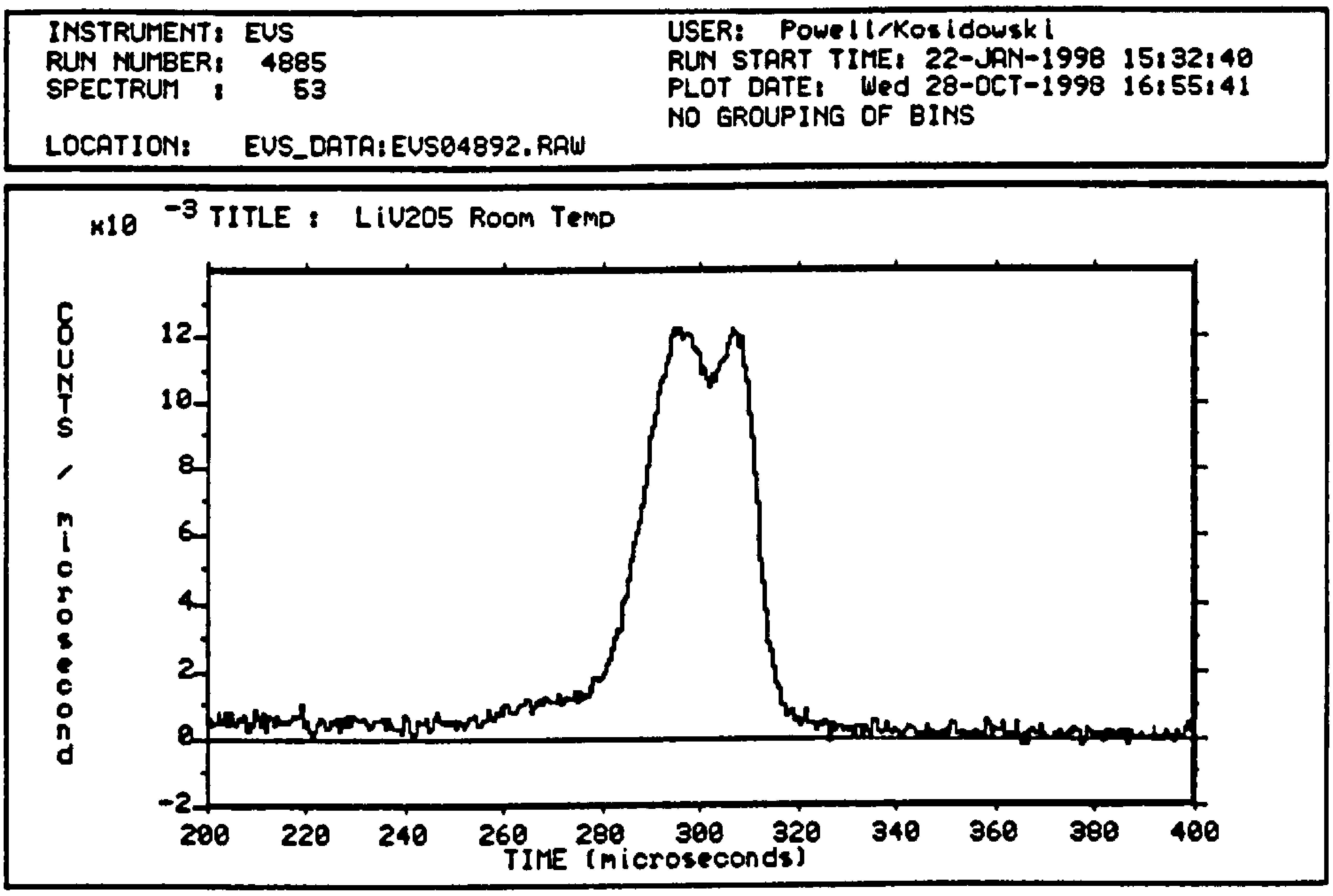

INSTRUMENT: EVS
RUN NUMBER: 4885
SPECTRUM : 53
LOCATION: EVS_DATA:EVS04892.RAW
USER: Powell/Kosidowski
RUN START TIME: 22-JAN-1998 15:32:40
PLOT DATE: Wed 28-OCT-1998 16:55:41
NO GROUPING OF BINS
TITLE : LiV2O5 Room Temp

Figure 5.9: Room temperature time-of-flight spectrum for LiV_2O_5

The data were analysed by two procedures. The first involved fitting the peaks in each time-of-flight Compton profile, fixing the composition and allowing the peak widths to vary. The lithium peaks widths were then averaged over the eight detectors; a mean profile width for the lithium recoil peak was determined as 5.16±0.22Å^{-1}. The second procedure consisted of subtracting the oxygen and vanadium recoil peaks, focusing the data from the eight detectors in momentum space and fitting the resulting peak to a Gaussian: a profile width of 8.17±0.60Å^{-1} was obtained. Poor fitting by the analysis routines in both cases results in the large variation in values and reflects the poor quality of the data. However, good separation of the oxygen and vanadium peaks permitted measurement of their respective areas and from this a V:O ratio of 2:5.3 was obtained.

At this stage in the study of eVS, it was concluded from the experiments described above that lithium, with the current instrument configuration, cannot be detected with sufficiently good statistics to permit analysis using standard eVS routines. Another possible route would be to isolate the lithium peak by performing a background subtraction of the host material; in the case of LiV_2O_5, this would mean subtracting the spectrum of V_2O_5 form that of LiV_2O_5 after suitable normalization.

5.7 NH_4TaWO_6 and $HTaWO_6$

The more complex motions of a molecular ion was the next area of study, using the same approach to data analysis i.e. background subtraction of the host framework. The system chosen for study was the motion of the ammonium ion within the defect pyrochlore structure NH_4TaWO_6. This has a cubic structure (a≈10Å), consisting of vertex-linked MO_6 octahedra which produces a network of interlinked tunnels comprising as series of bottlenecks and cavities (Figure 1.11). These cavities are occupied by migratory ions NH_4^+ in NH_4TaWO_6 and H_3O^+ in H_3OTaWO_6 and result in these materials being proton conducting ceramics. Dehydration of H_3OTaWO_6 produces $HTaWO_6$ in which protons form spirals running along the channel walls. Two sites are relatively close, located at a distance of approximately 2.65Å, enabling the proton to jump relatively easily from site to site.

Measurement of both the spin-lattice and spin-spin relaxation time for protons in NH_4TaWO_6 suggest rapid ionic motion in this compound[203], the results of which were used to propose that NH_4TaWO_6 is an ionic conductor where conduction proceeds via motion of protons. A vehicle mechanism for the ionic conductivity in the ammonium pyrochlore is not supported by experimental data[205]. Structural data[204] shows the ammonium molecule to sit in the centre of the cavity and not in the regions of the bottlenecks, which constitute an impediment to their mobility through the channels. Proton hopping from one ammonium molecule to another is therefore the most likely mechanism. A direct jump between one group and another is possible, as is one via an intermediate stage where the proton is located on the oxygen framework. The transfer of protons may then proceed via tunnelling through the hydrogen bonds.

It was anticipated that the NCS profile of NH_4TaWO_6 would comprise one feature corresponding to overlapping tungsten and tantalum recoil peaks, a second due to overlapping nitrogen and oxygen recoil peaks and a third strong hydrogen recoil peak. To measure the kinetic energy of the ammonium ion, it would be necessary to isolate the peak due to nitrogen. Nitrogen has a sufficiently large mass that any kinetic energy increases should be observed in the temperature range 4-300K compared with lithium in $LiTiS_2$. When considering the product of the relative atom% and scattering power for both oxygen and nitrogen, it was clear that the nitrogen contribution in this region would be ca. 40% that of oxygen. The NCS profile of $HTaWO_6$ was to be used to provide a suitable background for subtraction in the N/O region as it has an identical metal oxide framework with oxygen having a similar binding energy to that in NH_4TaWO_6. Subsequent subtraction of the $HTaWO_6$ spectrum from that of NH_4TaWO_6 should isolate the nitrogen recoil peak. This subtraction would also overcome the problem of tungsten and tantalum resonance peaks which would appear in both NCS profiles. Other than background subtraction, there is no method available on eVS to remove such peaks from a spectrum.

The hydrogen atoms in the ammonium ion possess two components of kinetic energy; the first resulting from the internal vibrational modes of the ammonium ion and the second from the translational motion of the ammonium ion. The former have been analysed in terms of normal co-ordinates from INS data collected at ISIS[192]. The vibrational motion of the hydrogen atoms comprise stretching, rotational and deformation modes. The stretching fundamentals are observable in the infra-red, so using the information from INS and IR, it was considered possible to calculate the kinetic energy of the hydrogen atoms due to their internal vibrational modes.

5.7.1 Experimental

The method of Butler and Biefeld was used to prepare samples of NH_4TaWO_6 and $HTaWO_6$[193] via ion-exchange of $KTaWO_6$. A stoichiometric mixture of dried WO_3, Ta_2O_5 and K_2CO_3 was fired in a platinum crucible at 400°C, reground and heated at 850°C for a further 72 hours. The powder X-ray diffraction pattern indicated the product to be cubic with a lattice parameter of 10.4900(8)Å. One weak line at d=2.79Å (intensity <3% intensity of main peak) was unidentifiable. The $KTaWO_6$ was ion-exchanged by stirring for 2 days in 3M HCl; atomic absorption of the washings confirmed that ion exchange was completed to 97±2%. Dehydration of the H_3OTaWO_6 at 325°C for 12 hours produced $HTaWO_6$ which was sealed in an evacuated quartz tube. A second sample of H_3OTaWO_6 was further ion-exchanged with 2M NH_4Cl under reflux, maintaining the pH at 7, adjusting it when necessary with $NH_3(aq)$. The resulting white solid was washed with deionised water, centrifuged, dried in air and characterised by powder X-ray diffraction, hydrogen and nitrogen combustion analysis and room temperature FT-IR. Powder X-ray diffraction showed the product to be cubic with a lattice parameter of 10.3528(9)Å, in good agreement with the previously quoted value of

10.358Å[31]. Elemental analysis gave 0.81%H and 2.93%N which compared with calculated values of 0.84% and 2.92% respectively. The infra-red spectrum (Figure 5.10) showed lattice vibrations between 400-800cm^{-1}, attributable to the metal-oxygen framework, a strong absorption at 1414cm^{-1} resulting from an NH_4^+ deformation mode and features at 2800-3300cm^{-1} due an IR active fundamental and overtones/combinations.

Neutron Compton scattering data were collected on $HTaWO_6$ and NH_4TaWO_6 at 4.4K, 150K and room temperature. At a given temperature, similar data collection times for $HTaWO_6$ and NH_4TaWO_6 were used to aid normalisation of the data. Three banks of detectors were at back-scattering angles and one bank placed in a forward scattering position; gold foils were used at all scattering angles.

5.7.2 Data Analysis and Results for $HTaWO_6$

Neutron Compton scattering data, summed over eight forward-scattering detectors and eight back-scattering detectors are shown in Figures 5.11 and 5.12 respectively. In Figure 5.12, the peak between 350-400μs is due to overlapping recoil peaks of Ta and W; W resonances appear as a sharp feature at longer times-of-flight, on the side of the Ta/W peak. The oxygen recoil peak produces the strong feature between 300-350μs. No hydrogen recoil peak is detectable at these back-scattering angles. Figure 5.11 shows a broad recoil peak which dominates the spectrum; this is due to hydrogen. The abnormal measurement of negative intensity at times-of-flight just below 200μs is a consequence of severe detector problems which were being experienced at this time which included saturation of the detectors at short times-of-flight. The sharper, more intense feature at longer times-of-flight arises for overlapping O, Ta and W recoil peaks.

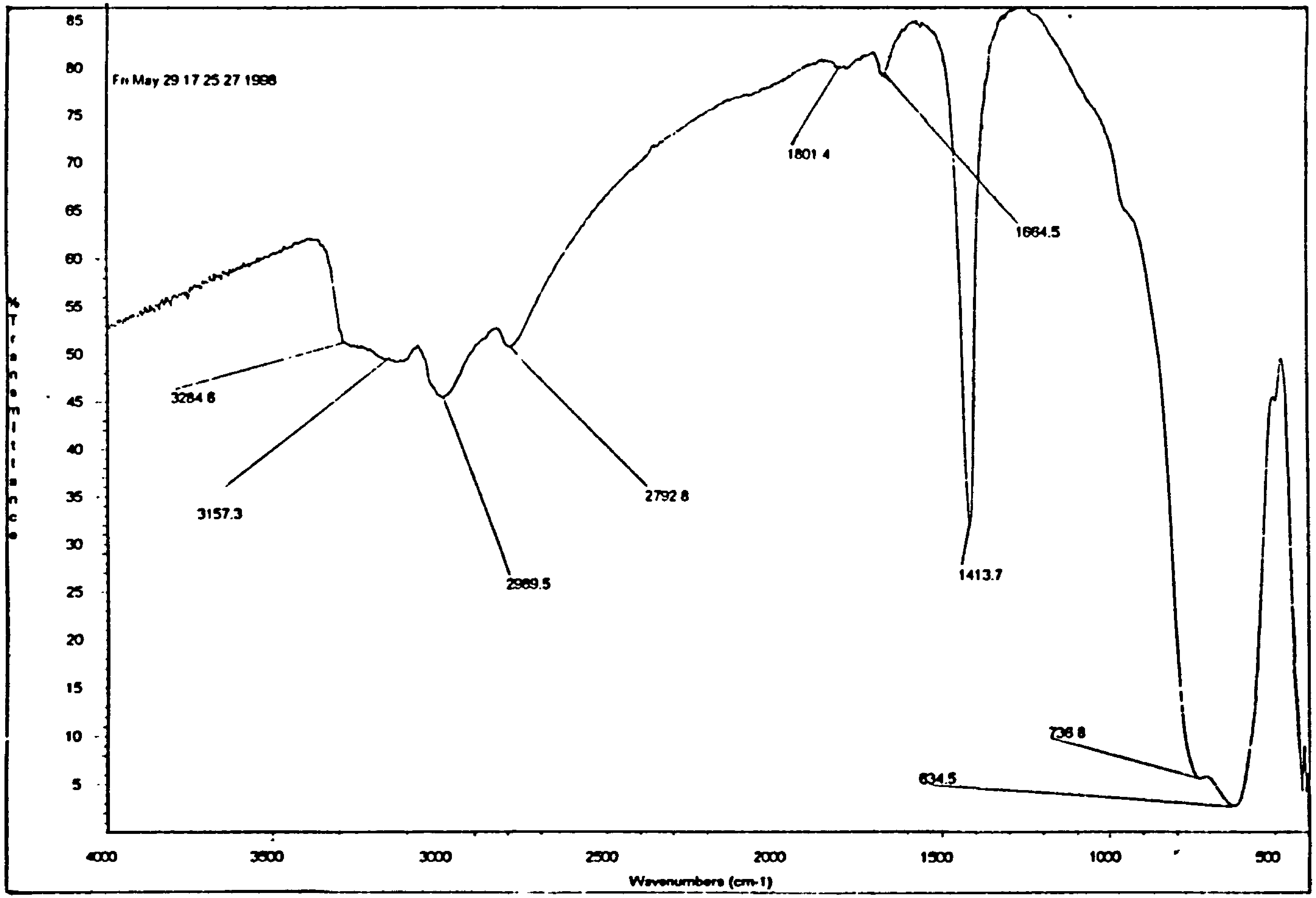

Figure 5.10: *Infra-red spectrum of* NH_4TaWO_6.

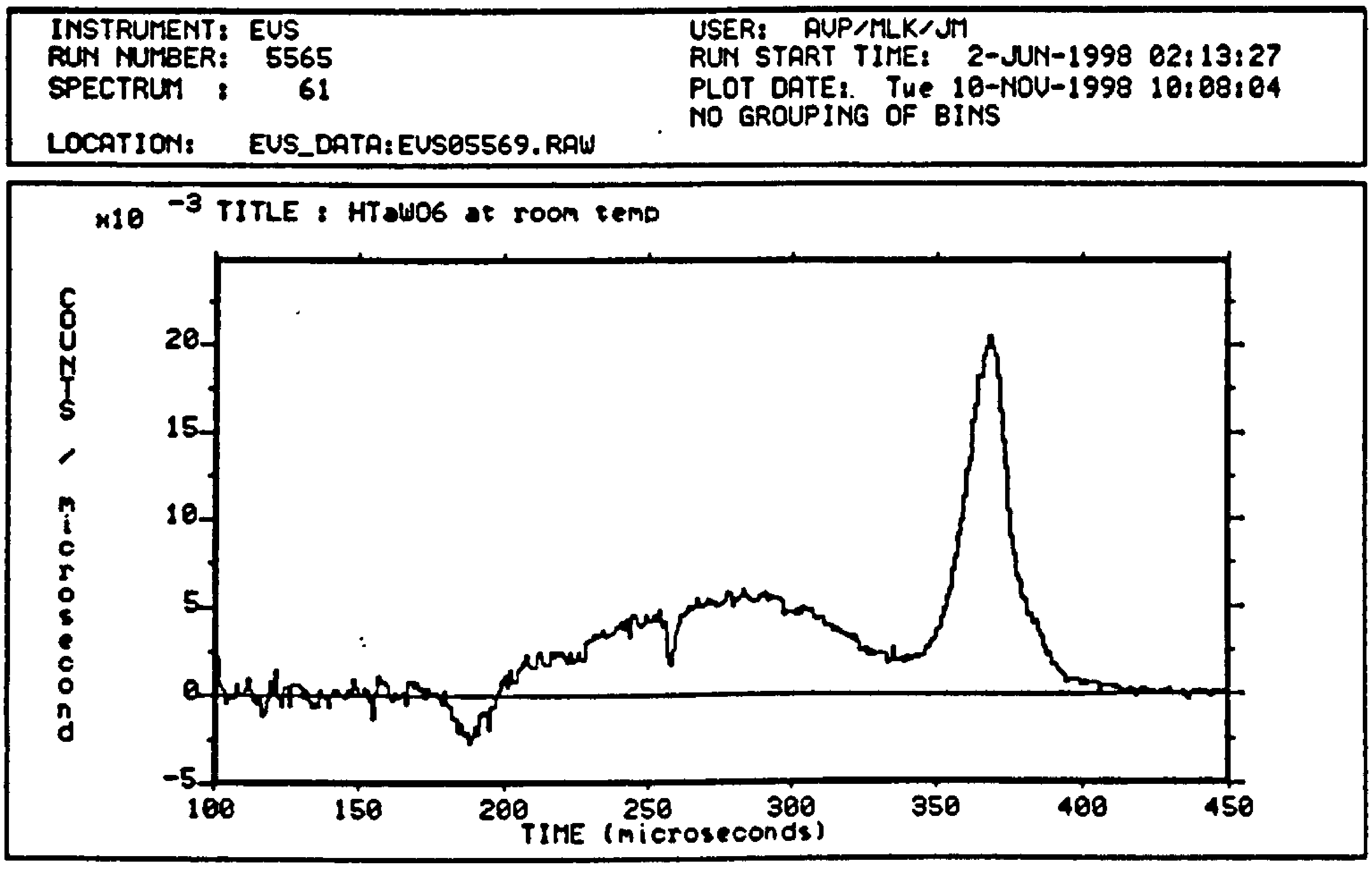

INSTRUMENT: EVS
RUN NUMBER: 5565
SPECTRUM : 61
LOCATION: EVS_DATA:EVS05569.RAW
USER: AVP/MLK/JM
RUN START TIME: 2-JUN-1998 02:13:27
PLOT DATE: Tue 10-NOV-1998 10:08:04
NO GROUPING OF BINS

Figure 5.11: Room temperature spectra for $HTaWO_6$ summed over forward scattering detectors.

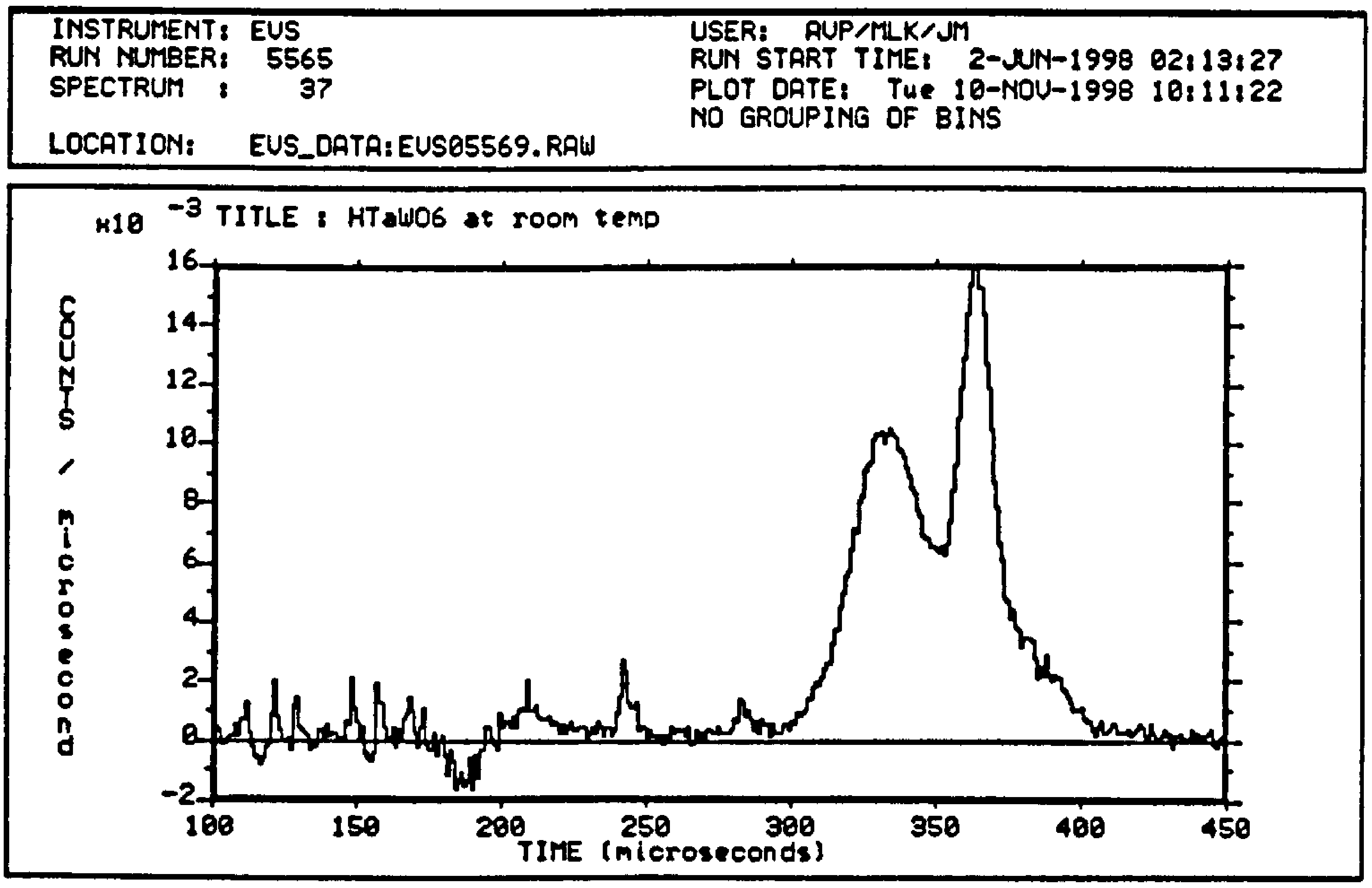

INSTRUMENT: EVS
RUN NUMBER: 5565
SPECTRUM : 37
LOCATION: EVS_DATA:EVS05569.RAW
USER: AVP/MLK/JM
RUN START TIME: 2-JUN-1998 02:13:27
PLOT DATE: Tue 10-NOV-1998 10:11:22
NO GROUPING OF BINS

Figure 5.12: Room temperature spectra for $HTaWO_6$ summed over back scattering detectors.

Standard eVS routines were used to isolate the hydrogen recoil peak for the forward scattering bank of detectors, by subtraction of the cryostat background and recoil peaks due to the metal-oxygen framework. The resultant hydrogen peak was fitted by a Gaussian form in momentum space. The hydrogen recoil peak for detectors 26 and 31 are shown in Figure 5.13 and 5.14; although the fitting routines would attempt to fit a Gaussian peak shape to those like detector 26, such poor data sets were excluded when averaging results. Residual intensity due to resonances from tungsten could not be completely removed but were well separated from the hydrogen recoil peak and therefore did not interfere with the measurement of the peak width.

The measured peak widths and kinetic energies of the protons in $HTaWO_6$ are listed in Table 5.4. From these data, it can be seen that the kinetic energy of the proton within the defect pyrochlore structure $HTaWO_6$, as measured on eVS, is independent of temperature over the temperature range 4-300K.

Table 5.4: Peak widths and kinetic energies for protons in $HTaWO_6$

Temperature/K	**σ/Å^{-1}**	**Kinetic Energy/meV**	**Kinetic Energy/cm^{-1}**
4.4	4.3691±0.0788	118.7±4.3	1276.8±46.1
150	4.3706±0.0272	118.8±1.5	1277.7±15.9
298	4.3738±0.1203	119.0±6.6	1279.5±70.4

Similar conclusions to those drawn about the protons in $H_{0.3}MoO_3$ and $H_{1.57}MoO_3$ can be made. Namely that it is predominantly the zero point energy of these protons which is being measured. These protons in $HTaWO_6$ are situated on the cavity walls of the metal-oxygen framework, attached to the oxygen atoms and are known to undergo rapid ion exchange in solution. In an NMR study of the proton motion in

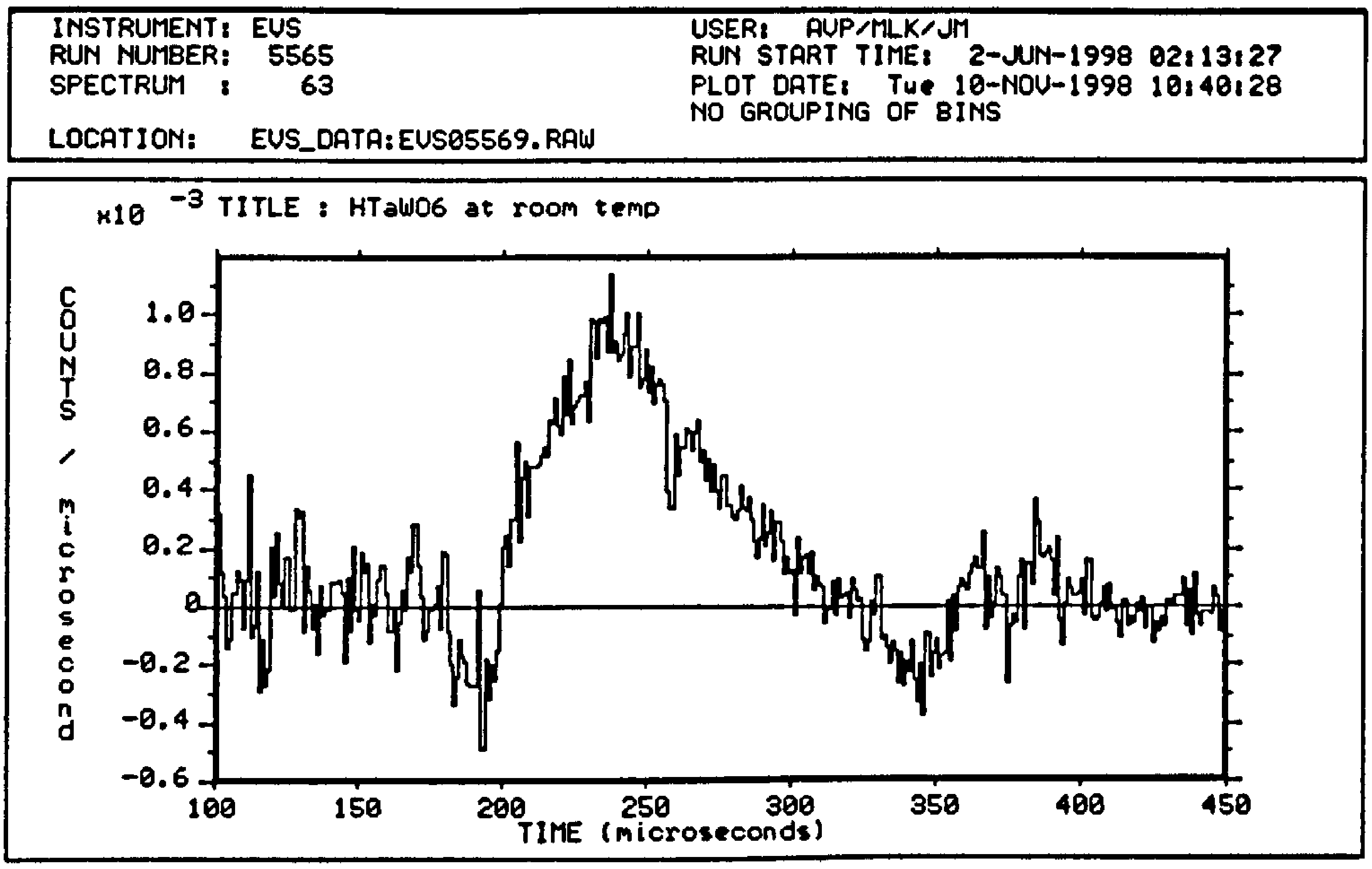

```
INSTRUMENT: EVS                         USER:  AVP/MLK/JM
RUN NUMBER:  5565                       RUN START TIME:  2-JUN-1998 02:13:27
SPECTRUM  :    63                       PLOT DATE:  Tue 10-NOV-1998 10:40:28
                                        NO GROUPING OF BINS
LOCATION:    EVS_DATA:EVS05569.RAW
```

Figure 5.13: Hydrogen recoil peak for detector 26 after subtraction of metal-oxygen framework for $HTaWO_6$.

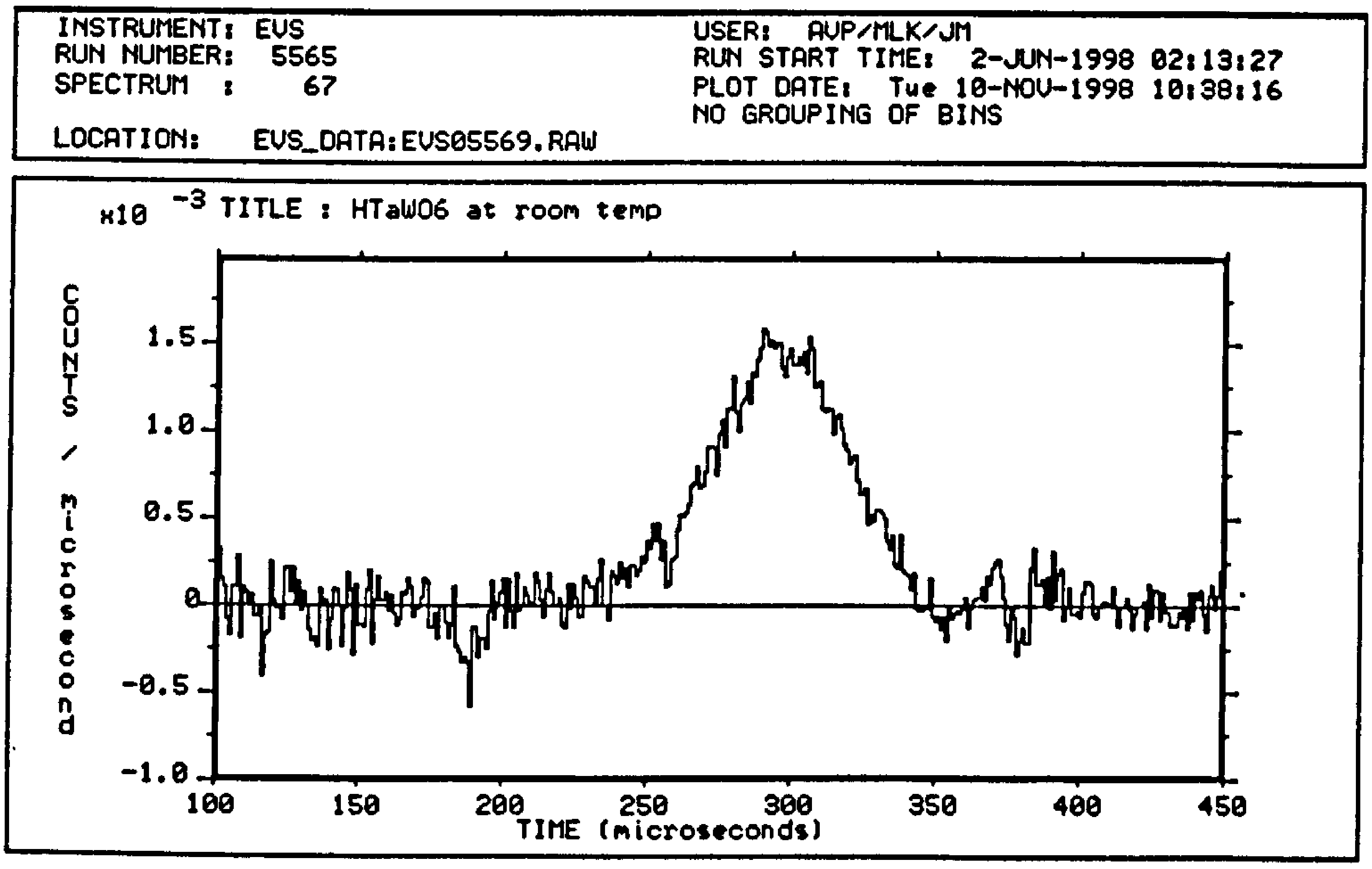

```
INSTRUMENT: EVS                         USER:  AVP/MLK/JM
RUN NUMBER:  5565                       RUN START TIME:  2-JUN-1998 02:13:27
SPECTRUM  :    67                       PLOT DATE:  Tue 10-NOV-1998 10:38:16
                                        NO GROUPING OF BINS
LOCATION:    EVS_DATA:EVS05569.RAW
```

Figure 5.14: Hydrogen recoil peak for detector 31 after subtraction of metal-oxygen framework for $HTaWO_6$.

$HTaWO_6$, a small "attempt" frequency ($3\times10^{10}sec^{-1}$) based upon a random walk model was determined[193]. This value, combined with a small activation energy (0.27eV) led to the suggestion that proton motion proceeds via a tunnelling mechanism rather than the classical picture of proton hopping. The eVS data obtained in this work do not support this mechanism. If tunnelling were a dominant mechanism operating in this material, it would be expected that an overall decrease in the kinetic energy of the proton with increased tunnelling would be observed which has the effect of spreading out the wavefunction and decreasing the average momentum of the proton. However, the eVS data indicates that proton mobility is independent of temperature. Whether this interpretation is a consequence of the insensitivity of the technique to determining such information is not known.

5.7.3 Data Analysis and Results for NH_4TaWO_6

Room temperature NCS profiles summed over all back scattering detectors is shown in Fig. 5.15 and over forward scattering detectors in Figure 5.16. From the back scattering detectors, the areas of the N/O and Ta/W peaks were measured and the ratio of N+O:Ta+W was determined as 1.8:1 against a theoretical value of 3.5:1. This can be attributed to the unusual features of the neutron Compton profile for this material, in that the tungsten resonances cannot be subtracted from the spectrum. The tantalum and tungsten recoil peaks are indistinguishable by virtue of their masses, but the tungsten resonance appearing at longer times of flight to this recoil peak, is included in the measurement of the tantalum/tungsten peak area. The overestimate by the analysis routine of the tungsten peak area consequently results in a reduced N+O to Ta+W ratio.

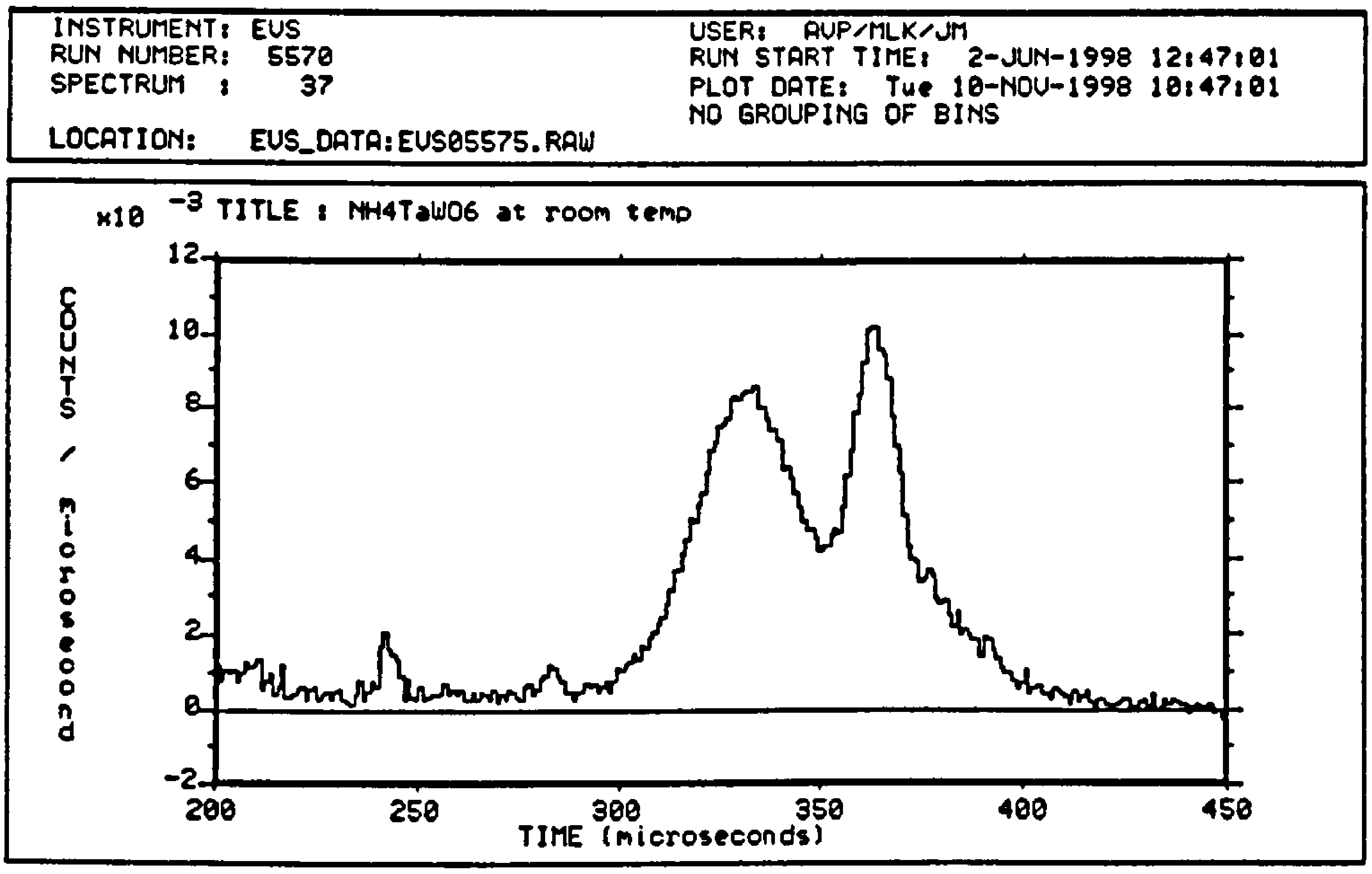

INSTRUMENT: EVS
RUN NUMBER: 5570
SPECTRUM : 37
LOCATION: EVS_DATA:EVS05575.RAW
USER: AVP/MLK/JM
RUN START TIME: 2-JUN-1998 12:47:01
PLOT DATE: Tue 10-NOV-1998 10:47:01
NO GROUPING OF BINS

Figure 5.15: Room temperature NCS profile for NH_4TaWO_6 summed over back-scattering detectors.

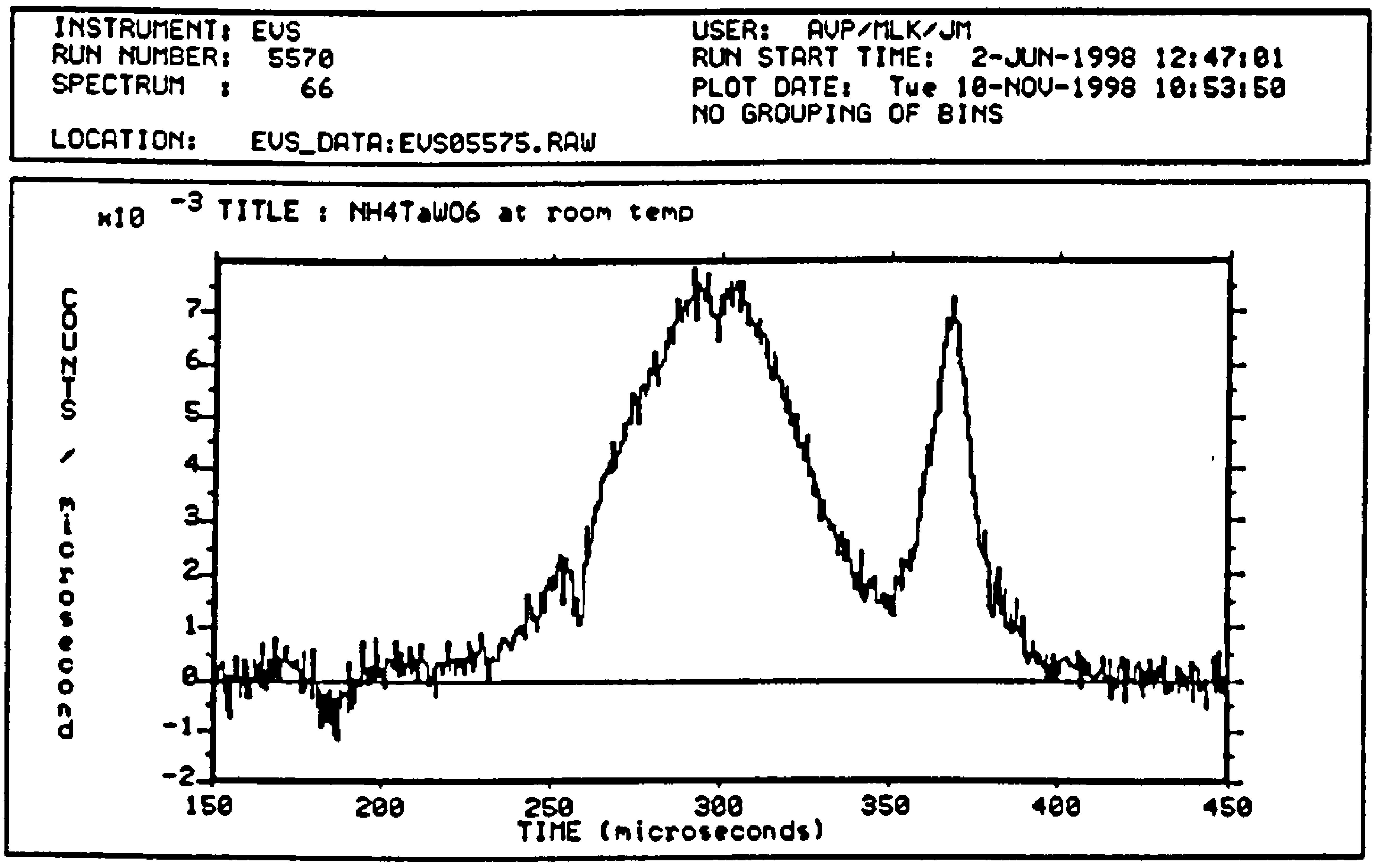

INSTRUMENT: EVS
RUN NUMBER: 5570
SPECTRUM : 66
LOCATION: EVS_DATA:EVS05575.RAW
USER: AVP/MLK/JM
RUN START TIME: 2-JUN-1998 12:47:01
PLOT DATE: Tue 10-NOV-1998 10:53:50
NO GROUPING OF BINS

Figure 5.16: Room temperature NCS profile for NH_4TaWO_6 summed over forward scattering detectors.

Nitrogen Peak Separation

To isolate the nitrogen recoil peak, it was necessary to subtract the overlapping recoil peak due to oxygen. To do this, the NCS spectrum of $HTaWO_6$ was subtracted from that of NH_4TaWO_6 for back-scattering detectors. Initial normalisation of the data was first carried out. Detectors were summed over banks 1-8, 9-16 and 17-24 (25-32 were at forward scattering angles.) both for NH_4TaWO_6 and $HTaWO_6$. Subtraction of the oxygen peak was carried out for each summed spectrum. The resulting spectrum resulted in a peak fit and the peak area was measured. The ratio of the Ta/W peak areas in the spectra from NH_4TaWO_6 and $HTaWO_6$ was measured for each set of detectors and the individual NCS spectra for $HTaWO_6$ were scaled by this factor. Subsequent subtraction of the $HTaWO_6$ spectra from those of NH_4TaWO_6 resulted in a residual nitrogen recoil peak as in Figure 5.17. Having transformed these to momentum space and fitted a Gaussian to them, peak widths and corresponding kinetic energies were obtained and are tabulated in Table 5.5. The data from bank 9-16 were of too poor quality after subtraction of the $HTaWO_6$ spectra from those of NH_4TaWO_6 to be used for analysis. (Figure. 5.18) This is thought to stem from the poorer separation of the O peak from that of Ta/W for this bank of detectors because they were positioned close to 90° scattering angles.

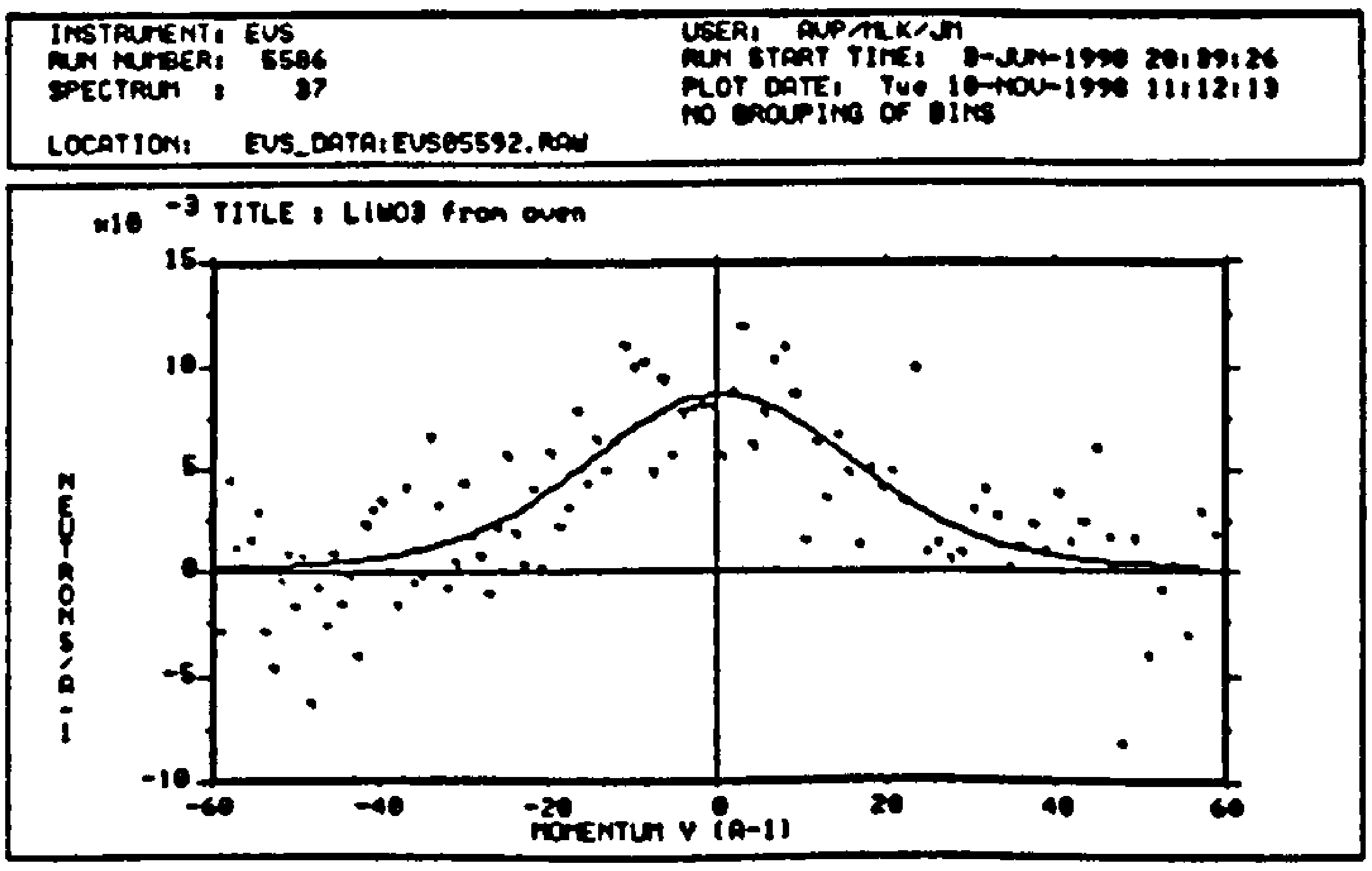

Figure 5.17: Fitted Gaussian to nitrogen recoil peak after subtraction of $HTaWO_6$.

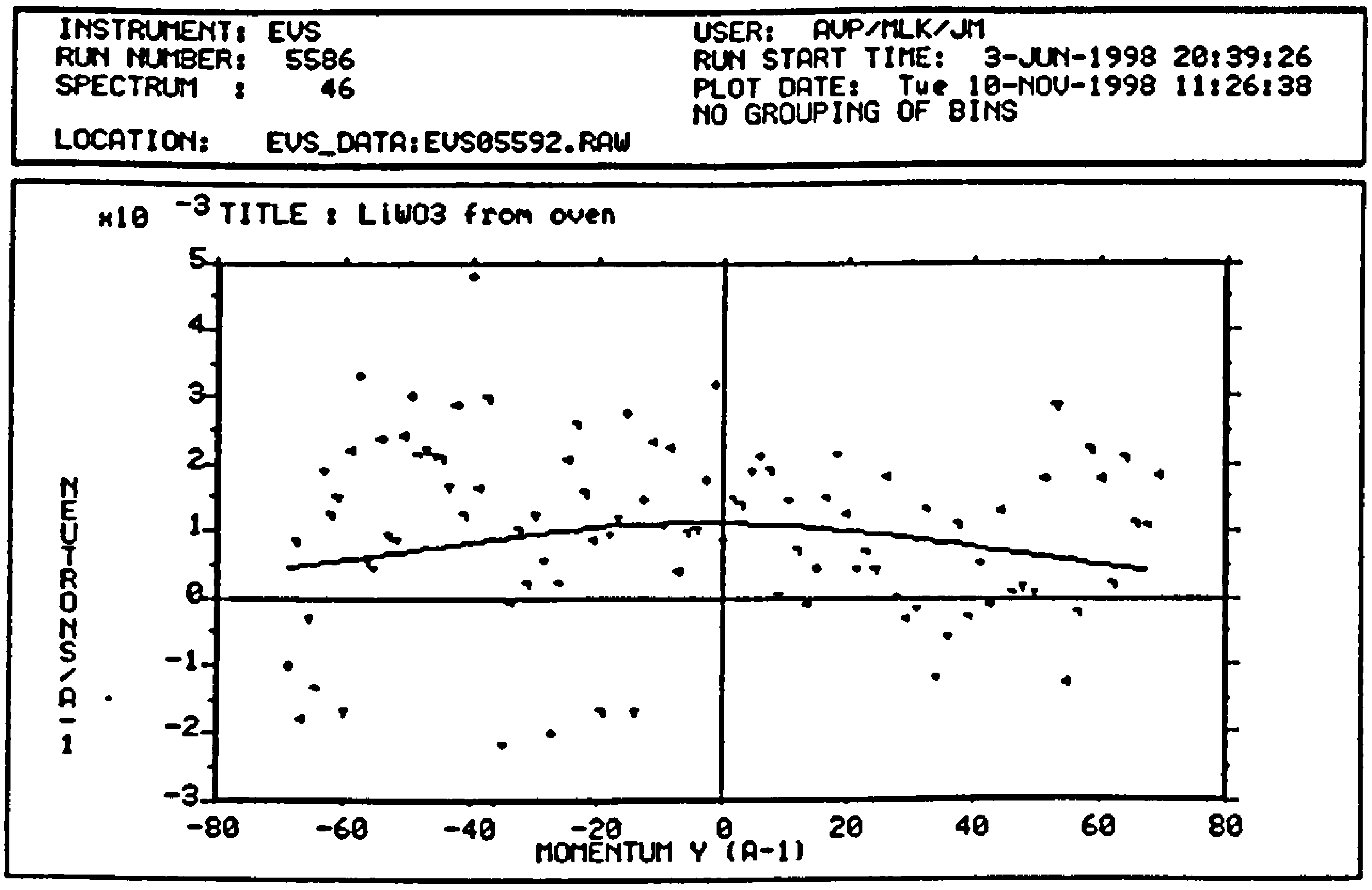

Figure 5.18: Fitted Gaussian to nitrogen recoil peak after subtraction of $HTaWO_6$; detector at 90° scattering angle.

Table 5.5: Peak widths and kinetic energies measured for nitrogen in NH_4TaWO_6

Detector Bank	**4.4K**	**Kinetic Energy /meV**	**Kinetic Energy /cm^{-1}**
1-8	14.2091±0.7468	90.4±9.5	972.1±102.2
17-24	15.1987±0.9065	103.4±12.3	1112.3±132.7

Detector Bank	**150K**	**Kinetic Energy /meV**	**Kinetic Energy /cm^{-1}**
1-8	14.4256±0.5422	93.2±7.0	1002.0±75.3
17-24	13.3534±0.5912	79.8±7.1	858.6±76.0

Detector Bank	**295K**	**Kinetic Energy /meV**	**Kinetic Energy /cm^{-1}**
1-8	12.7891±0.6260	73.2±7.2	787.5±77.9
17-24	12.2144±0.5990	66.8±6.6	718.4±70.5

The eVS data indicate that the kinetic energy of the nitrogen increases with decreasing temperature. This is consistent with conclusions from structural information that there is increasing delocalisation of the ammonium ion from the cavity centre as the temperature is reduced. Kuntz et al[204], having performed neutron diffraction studies on ND_4TaWO_6 at 523K, 300K and 4.2K, reported that refinement using room temperature data, resulted in a high isotropic thermal parameter for the nitrogen atom, indicating some rotational/positional disorder. Data collected at 4.2K indicated that delocalization from the centre of the cavity increases on lowering the temperature to an extent which causes a phase transition between 295K and 4.2K.

Hydrogen Recoil Peak Separation

The hydrogen recoil peak in NH_4TaWO_6 was analysed by the same method as for $HTaWO_6$ and the results are given in Table 5.6. Although the measured peak widths increase slightly with increasing temperature, consideration of the errors on these values leads to the conclusion that they are essentially invariant over the whole temperature range studied. The higher kinetic energy of the protons in NH_4TaWO_6 than in $HTaWO_6$ reflects the different sites of attachment; the ammonium ion for the former and the cavity walls in the case of the latter. The equivalent harmonic vibrational energy is similar to fundamentals observed in the inelastic neutron scattering spectrum of NH_4TaWO_6. These fundamentals were assigned as H-N-H deformation modes; observed at $1465cm^{-1}$ and $1407cm^{-1}$. Here, the kinetic energy measured is the total translational energy but can be compared to the result obtained by Fillaux et al (see Table 5.2) for $CD_3CONHCD_3$. In N-methylacetamide in the crystalline state, the NH group of one molecule hydrogen bonds to the C=O group of another to create a N-H...O bridge with $R_{N..O} \approx 2.8Å$. A momentum value of 4.67Å at 4.5K was obtained for the hydrogen bonded proton as compared with 4.54Å for those in NH_4TaWO_6. Neutron diffraction studies on ND_4TaWO_6 place the ammonium ion in the centre of the cavities of the defect pyrochlore structure, with the deuterium atoms aligned towards the nearest oxygen atoms; a possible indication of a weak hydrogen bonded interaction.

Table 5.6: Peak widths and kinetic energies for hydrogen in NH_4TaWO_6

Temperature/K	σ (Å^{-1})	Kinetic Energy (meV)	Kinetic Energy (cm^{-1})
4.4	4.5416±0.1183	128.29±6.68	1379.6±71.9
150	4.6292±0.1759	133.28±10.13	1433.3±108.9
298	4.6429±0.0933	134.07±5.39	1441.8±57.9

No evidence of tunnelling can be found from eVS data for the hydrogen kinetic energy. The material ND_4TaWO_6 shows better proton hopping capabilities than $DTaWO_6$[204]; initially it would therefore be expected that hydrogen in the analogue $HTaWO_6$ would have a higher kinetic energy than in NH_4TaWO_6 in accordance with it being in a more tightly bound state. The reverse trend (though only showing a marginal difference) is observed. This does not contradict conductivity measurements in the two defect pyrochlores, as the increased conductivity in the ammonium pyrochlore could originate from the reduced proton hopping distance between two neighbouring ammonium molecules of 2.280Å relative to their hopping distance of 2.653Å in $DTaWO_6$. It does imply that the different site potentials of the protons is not a determining factor in the proton jumping ability in these materials.

The measured kinetic energy of hydrogen in the ammonium pyrochlore contains two essentially independent components. The first is due to the energy of the N-H vibration in a reference frame where the nitrogen atom is stationary. The second originates from the motion of the nitrogen atom to which the hydrogen is attached. The latter contributes an energy of approximately $M_H K_N / M_N$ where M_H and M_N are the respective masses of hydrogen and nitrogen atoms and K_N is the mean kinetic energy of the nitrogen atom. Using this expression, the kinetic energy associated with the N-H bond is given in Table 5.7 at each of the three temperatures. The nitrogen translational motion does not affect the trend in the kinetic energy of the hydrogen with temperature.

Table 5.7: Energy of the N-H vibration.

Temperature/K	**Kinetic energy contribution of nitrogen atom /meV**	**Kinetic energy associated with N-H bond/meV**
4.4K	6.97	121.32
150K	6.22	127.06
295K	5.04	129.03

Chapter Six

Discussion

One of the interests in incorporating organic molecules within inorganic hosts is the striking contrasts between the properties of the nanocomposite produced and those of the host structure. Furthermore, the behaviour of an organic molecule incorporated within a host solid may show significant differences compared with the isolated dispersed species or the corresponding species in its pure crystalline state. Issues related to these contrasts include the degrees of conformational and translational freedom experienced by the guests as well as the regularity of the packing of these species within the layers and the extent to which the host may be modified by or respond to the presence of the guest. These and related issues will be discussed in this chapter with respect to the synthesis and characterisation of intercalation compounds described in this thesis.

6.1 LITHIUM INTERCALATION INTO MoS_2

Evidence accumulated by a number of research groups leads to the conclusion that, when lithium is incorporated into MoS_2 with accompanying reduction of molybdenum within the host, there is a change in the co-ordination of the molybdenum atom from trigonal prismatic to octahedral. Py and Haering inserted lithium into MoS_2 electrochemically[206] and produced a crystalline material Li_xMoS_2 ($x \approx 1$), although the lithium content of this phase was not determined accurately. Using in-situ X-ray diffraction, they observed that the host underwent a first-order phase transition upon insertion of lithium. They compared the observed X-ray intensities with those of four possible structural models; each having a hexagonal layer structure with a unit cell restricted to either one or two layers. Closest agreement was obtained with a 1T model, with only one layer per unit cell and octahedral co-ordination for the metal atom. It has been suggested that such a structural change would involve a shear mechanism, based on partial dislocation along successive glide planes, in which adjacent Mo and S layers slide relative to each other. This has already been proposed[207] for the 1T→2H transition in TaS_2.

The insertion process was subsequently studied by Chrissafis and co-workers using transmission electron microscopy[148]. With initial intercalation, they observed the formation of defects, mainly dislocations, at the edges of the specimens. Further intercalation led to a phase transformation, completed in Li_xMoS_2 when $x \geq 1.3$.

A $2a_0 \times 2a_0$ superstructure accompanies this phase transformation. This has been tentatively linked to the 2H→1T transition proposed by Py and Haering. The driving force behind such a transformation requires a thermodynamic basis for explanation i.e. the total Gibbs free energy of Li_xMoS_2 as a function of x and for different atomic arrangements. However, it is known that ideal octahedral co-ordination symmetry has a lower Madelung energy than the ideal trismatic prismatic one[93] by ca. 20% and that the Coulomb repulsion energy factors for partially charged ligands also favour an octahedral arrangement.

For Group 16 dichalcogenides, trigonal prismatic co-ordination of the metal atoms is favoured on the basis of electronic energy considerations, because in the Group 16 dichalcogenides, trigonal prismatic co-ordination results in the low-lying dz^2 valence band being completely filled. However, this stabilisation of trigonal prismatic co-ordination is affected by the transfer of electrons from lithium into the conduction band of the host. Owing to the large band gap between the valence and conduction bands in 2H-MoS_2, the electronic energy of 2H-$Li_{1.0}MoS_2$ would be significantly higher than in 2H-MoS_2. In contrast, the increase in 1T-$Li_{1.0}MoS_2$ would be much smaller because of the lack of a band gap. Hence, upon lithium intercalation, the metal atom of a Group 16 dichalcogenide will tend to adopt the more stable octahedral co-ordination.

6.2 SINGLE LAYER MoS_2

The question of whether this octahedral co-ordination is carried through to the structure of single layer MoS_2 has been the focus of many investigations. Structural studies of single layer MoS_2 in aqueous suspension using EXAFS show that the single layers differ from those in 2H-MoS_2 by having two nearest neighbour Mo-Mo distances at 2.82Å and 3.82Å, substantially altered from the value of 3.16Å in the crystalline phase. The nearest neighbour Mo-S distance was found to be essentially unchanged from that of 2H-MoS_2; 2.40Å in single layer MoS_2 compared with 2.42Å in the latter[147].

An X-ray diffraction modelling study[150] has also been carried out on single layer MoS_2. Comparison of X-ray diffraction line shapes for the single layer material against those from models developed for octahedrally co-ordinated and trigonal prismatically co-ordinated molybdenum led to the conclusion that molybdenum is octahedrally co-ordinated. Raman scattering results supported this conclusion. It was found that in the Raman spectrum of single layered material, there was an absence of a mode which is Raman active when molybdenum is in a trigonal prismatic environment, but is solely infrared active in an octahedral environment. Whether this octahedral co-ordination of molybdenum is carried through to restacked material is yet to be established.

6.3 STRUCTURAL STUDIES OF RESTACKED MoS_2

A consensus on the structure of restacked MoS_2 has not yet been reached; not even to the point of establishing the local co-ordination of molybdenum that could become a building block for the MoS_2 layers. A variety of techniques have been employed to study the structure of restacked MoS_2. Dungey and Curtis have carried out EXAFS on $Li_{0.85}MoS_2$, restacked MoS_2 and MoS_2 intercalated with $Co(OH)_2$[149]. Table 6.1 shows the fitting parameters for Mo EXAFS of restacked MoS_2.

Table 6.1 Fitting parameters obtained by Dungey and Curtis.

Coordination Shell	N	R/Å	A/Å^2×10^3
Mo-S	4.28	2.42	4.1
Mo-Mo	0.49	2.77	1.6*
Mo-Mo	1.14	3.17	1.6*
Mo-Mo	0.29	3.77	1.6*

* fixed during fitting procedure

Although the co-ordination numbers differ from those obtained in this work, they are within the uncertainties expected for EXAFS refinement. The distances observed are in very good agreement with those reported in Chapter Three. These authors carried out an electron diffraction study which revealed a $2a_0 \times 2a_0$ superlattice. Using the distances calculated from the Mo K-edge EXAFS spectra and the a,b lattice parameters from the electron diffraction pattern, they proposed a structural model that is a heterogeneous phase mixture of 2H-MoS_2 and and a disordered structure described as "1T-MoS_2". The former with one Mo-Mo distance of 3.16Å and the latter with two distances at 2.77Å and 3.77Å, containing linked Mo_3 clusters and molybdenum in a distorted octahedral environment. A plot of the atomic positional parameters proposed, show that a molybdenum atom would on average have 3 neighbouring molybdenum atoms at a distance of 2.77Å (cf. 0.3Mo at 2.77Å from the EXAFS data in this thesis) and have 8 sulphur atoms in close proximity at 2.42Å.

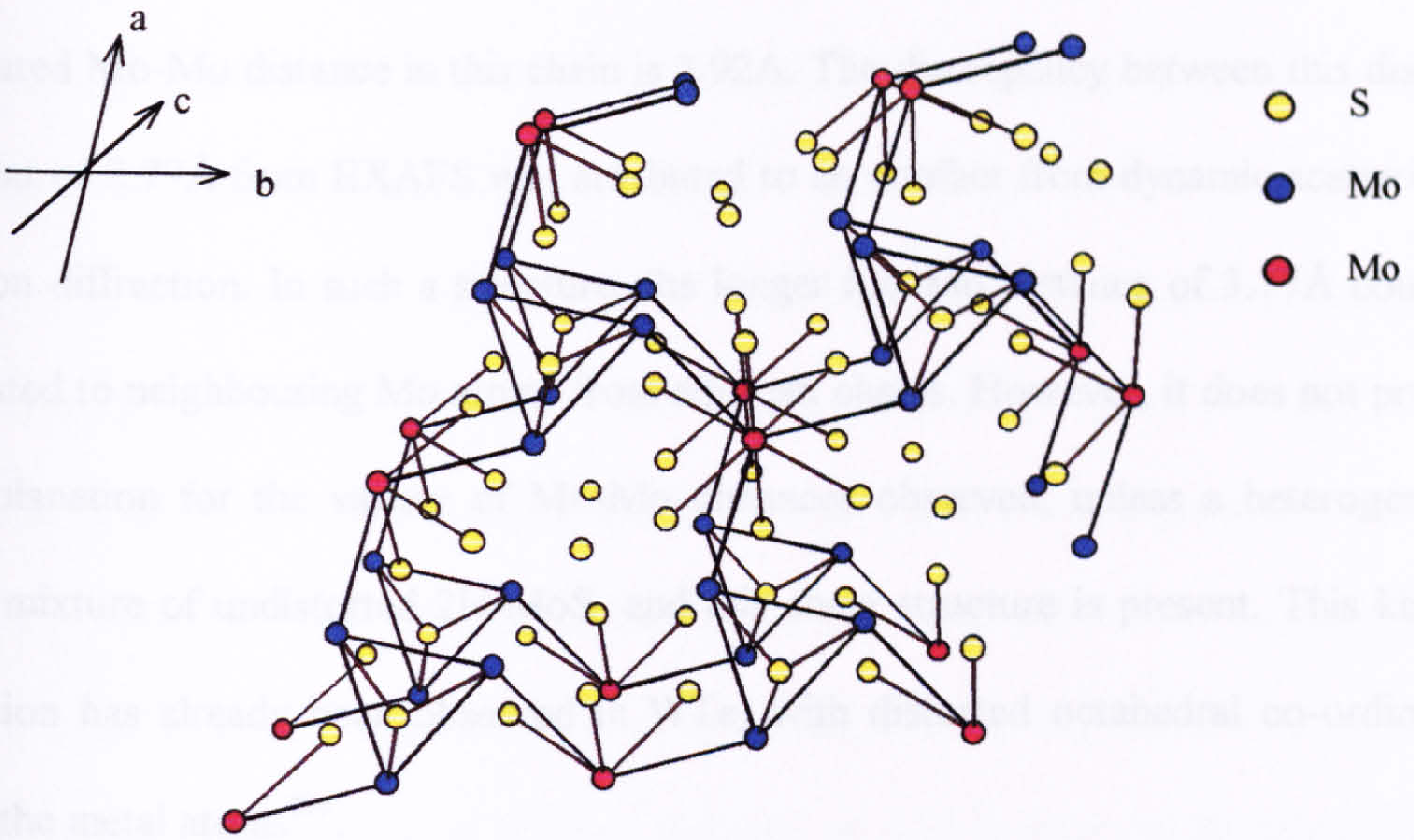

Figure 6.1: Structural model for restacked MoS_2 layers proposed by Dungey et al.

However, all Mo K edge EXAFS data obtained by Dungey and Curtis, by Yang et al and those reported in this work, lead to an average 1st co-ordination shell number of <6 for sulphur. Thus, a phase mixture, dominated by $2H-MoS_2$ would have to account for the large discrepancy in the co-ordination numbers from EXAFS and those for the proposed model of the distorted MoS_2 phase. Dungey and Curtis also found that upon intercalating various Co species into MoS_2, the Mo K-edge EXAFS of the intercalation compounds revealed that there was a similar distortion to the Mo co-ordination environment as in the restacked material. This has also been observed in this work for the intercalates of naphthalene and 2-methylnaphthalene.

Heising and Kanatzidis tried to elucidate the structure of restacked MoS_2, prepared via the exfoliation-reflocculation route, using electron diffraction[157]. They observed an $a_0 \times 2a_0$ (or $\sqrt{3}a_0 \times a_0$) superstructure. This correlates with the $a \times 2a_0$ superstructure observed in films of MoS_2 layers on graphite[208]. Patterson maps generated from the data show substantial displacement of the metal atoms from their ideal positions (in $2H-MoS_2$) generating two crystallographically inequivalent metal atom positions.

Formation of zig-zag chains of molybdenum atoms in the a-b plane was proposed. The calculated Mo-Mo distance in this chain is 2.92A. The discrepancy between this distance and that of 2.77Å from EXAFS was attributed to an artefact from dynamic scattering in electron diffraction. In such a structure, the longer Mo-Mo distance of 3.77Å could be attributed to neighbouring Mo atoms from adjacent chains. However, it does not provide an explanation for the variety of Mo-Mo distances observed, unless a heterogeneous phase mixture of undistorted 2H-MoS_2 and this chain structure is present. This kind of distortion has already been observed in WTe_2 with distorted octahedral co-ordination about the metal atoms[209].

All the work carried out on this restacked material by various authors clearly shows that the structure of the molybdenum sulphide layer is different from that in 2H-MoS_2; EXAFS has also demonstrated that it differs from that in $LiMoS_2$. When initial investigations were being carried out in this area, the view was taken that the distorted structure observed was the same as the 1T-MoS_2 modification, originally synthesised by Wypych and Schöllhorn in 1992. Structural work on the latter is limited and this premise seemed to arise from the observation of metallic conductivity for 1T-MoS_2 and also for intercalates comprising restacked MoS_2 layers. From the extensive studies which have subsequently been carried out on the restacked material it is becoming clear that restacked MoS_2 is not the same as 1T-MoS_2.

1T-MoS_2 can be prepared[97] by the oxidation of the intercalation compound $K_x(H_2O)_yMoS_2$. Distortions within the *ab* plane lead to an $\sqrt{3}a_0 \times \sqrt{3}a_0$ superstructure i.e different to that observed for restacked MoS_2. It was found using STM, that incomplete oxidation with $x<0.3$ leads to a product with a $a_0 \times 2a_0$ superstructure. This has been reported to resemble the $a_0 \times 2a_0$ superstructure observed in films of MoS_2 single layers on graphite[208]. Thus, evidence exists that partially reduced MoS_2 has an $a_0 \times 2a_0$

superstructure, and differs from that observed in the 1T-MoS_2 prepared by Schollhorn and Wypych, in which molybdenum is fully oxidised. The implication is that restacked MoS_2 may carry some residual negative charge.

With more expansive research in the whole field of exfoliation and reflocculation, the possibility of a poorly crystalline phase mixture comprising trigonal prismatically co-ordinated molybdenum and a partially reduced unstable phase, which gradually reverts to trigonal prismatically co-ordinated molybdenum, has been considered. Such a phase mixture with Mo in two different environments is reflected in the EXAFS data where 3 Mo-Mo distances are found. A Mo-Mo distance of 3.16Å observed in this work, by Liang *et al* and by Dungey *et al* implies trigonal prismatic co-ordinated molybdenum. A second phase could consist of MoS_2 layers which are still partially reduced and so lead to the formation of zig-zag chains, Mo_3 clusters or indeed another co-ordination environment. Linked Mo_3 clusters could also be possible, though with this proposed structure containing Mo-S distances of 2.2Å, it is difficult to understand why such distances were not observed with EXAFS. The coexistence of this disordered structure with that of 2H-MoS_2 as a heterogeneous phase would be difficult to distinguish from the alternative of regions of disorder contained within the dominant 2H modification.

From a synthetic perspective, it must be mentioned that under these reaction conditions, it is highly likely that this material would possess random defects in considerable quantities. Loss of sulphur by abstraction in acid would leave sulphur defects which may be compensated by Mo-Mo clustering. Equally, protons could attach themselves to the sulphide layers, compensating for the partially reduced regions in the layers. Such static disorder may contribute to the structural distortions.

The X-ray diffraction study of the drying and restacking process presented in Chapter Three and the EXAFS data of Liang et al, show that restacked MoS_2 changes structure with ageing. Raman spectra of single layer MoS_2, 2-hour and 2-month old restacked MoS_2 suggest that the molybdenum reverts to trigonal prismatic co-ordination upon restacking. In addition, it is known that 1T-MoS_2 is metastable and reverts to the hexagonal form after 3-4 days[97]. One important factor in comparing data obtained in different studies therefore, is that the structural features observed by the various groups will depend not only on the method of preparation but also on the age and thermal history of the sample. Hence , not only heat but age of sample can also result in a gradual reversion to 2H-MoS_2 and molybdenum to a trigonal prismatic environment.

Both the chain and cluster structures are predicted to be metallic. The semiconducting properties observed for the restacked material in this work suggest that this material contains predominantly Mo^{4+} and that a band gap is present. Since trigonal prismatic MoS_2 is close to the frontier between trigonal prismatic and octahedral domains for the transition metal dichalcogenides, partially reduced MoS_2 might be expected to have a number of similar structures of approximately equal energies.

Further work to elucidate the structural changes could include performing EXAFS on 1T-MoS_2, as prepared by Wypych. Comparison with the data for restacked MoS_2 would show whether there is any similarity in the environment of the molybdenum in the two MoS_2 phases. In addition, band structure and density of states calculations for the possible structures and degrees of reduction of the MoS_2 might determine whether several possible structures of similar energy can exist.

6.4 INTERCALATION OF ORGANIC GUEST SPECIES

The insertion of a variety of small organic species into MoS_2 has been described in earlier chapters. Compositions and interlayer expansions of the intercalated materials produced in this thesis are compared to those prepared by other workers in Table 6.2.

Table 6.2: Intercalated species in MoS_2 via exfoliation.

Guest	x in $(Guest)_xMoS_2$	Interlayer spacing	Δc/Å	Ref
Naphthalene	0.20	10.0	4.3	This work
2-Methylnaphthalene	0.19	10.5	4.3	This work
2-Ethylnaphthalene	0.09	9.7	3.5	This work
1,5-Dihydroxynaphthalene	0.40	11.9	5.7	210
1-Chloromethylnaphthalene	0.36	13.8	7.6	210
Pyridinium	0.15	9.6	3.4	This work
Benzofuran	0.17	11.0	4.8	This work
Tetrahydronaphthalene	Not reported	14.9	8.7	129
Decahydronaphthalene	Not reported	14.7	8.5	129
Hexamethylbenzene	Not reported	7.7	1.5	129
Toluene	Not reported	14.9	8.7	129
Biphenyl	0.17	12.0	5.8	This work
Crystal violet	0.07	10.2	4.00	This work

Examining the relationship between the structure of the guest species and the observed Δc, it can be seen firstly, that upon intercalation of 2-methylnaphthalene instead of naphthalene, the same degree of incorporation can be attained. It has been concluded that naphthalene and its alkylated derivatives are incorporated with the molecular plane parallel to the inorganic layers. Although addition of a methyl group does not affect the degree of incorporation, progression to an ethyl group appears to hinder uptake of this guest. Despite the extra bulk of the ethyl substitiuent, it causes a smaller increase in interlayer spacing. The presence of the ethyl group reduces the degree of planarity of the molecule and this may reduce the degree of interaction possible between the inorganic layers and the pπ electrons of the aromatic centre. Thus, intercalation would be disfavoured and the lower uptake represents an average of occupied and vacant van der Waals gaps.

Much larger increases are observed for the 1,5-dihydroxy- and 1-chloromethyl-derivatives, synthesised by McDowall[210]; the extent of insertion of both molecules is greater than the geometrically limiting value, for an orientation similar to that of naphthalene. For 1,5-dihydroxynaphthalene, a lattice expansion of 5.7Å is inconsistent with a parallel orientation of guest molecules. In plane dimensions of ca. 6.7 × 6.2Å, together with the large degree of insertion, suggest that the molecular plane is perpendicular to the layers. From molecular modelling studies, the –OH groups were not found to alter the thickness of the aromatic ring.

For 1-chloromethylnaphthalene, the $-CH_2Cl$ side chain increases the effective thickness of the aromatic ring to 5.4Å, but with such a large uptake and a Δc of 7.6Å, again the molecule is unlikely to be oriented with the molecular plane parallel to the dichalcogenide layers. Hence, when comparing intercalation of 2-methylnaphthalene vs. 1-chloromethylnaphathlene and 1,5-dihydroxynapahthlene vs. naphthalene, replacement of methyl by chloromethyl appears to instigate a change in the orientation of the guest species. Similarly, replacement of hydrogen atoms on naphthalene by hydroxyl groups on 1,5-dihydroxynaphthalene brings about the same effect. The implication is that these orientations are stabilised by a favourable interaction between the polar substituents and the dichalcogenide layers. Interestingly, the functionality on the pyridinium ion does not appear to produce the same effect. This molecular ion is inserted with the molecular plane parallel to the disulphide layers.

Tagaya and co-workers[129] had intercalated a variety of non-electron donors into MoS_2 including tetrahydronaphthalene and decahydronaphthalene, for which they observed increases in the repeat distances of 8.7Å and 8.5Å respectively. This suggests that the guest species is oriented with the ring plane perpendicular to the host layers in both cases. It is interesting to note that partial hydrogenation results in this change of orientation. The driving force for this is not clear; no polarity exists as with the chlorinated or hydroxyl derivatives. Possibly it is the removal of aromaticity which promotes this change; with reduced or no interaction between the pπ electrons and the sulphide layers, interaction between aromatic hydrogen atoms and sulphide layers becomes the most favourable contact between guest and host.

The powder X-ray diffraction pattern of the benzofuran intercalate does not produce an unambiguous identification of the orientation of this molecule. For a planar species with its molecular plane parallel to the layers, the value of Δc is unusually high. For the degree of insertion observed, a Δc of between 4.0-4.2Å would be expected, assuming the aromatic ring thickness is equivalent to that of naphthalene. The alternative is that the molecule is perpendicular to the layers; with such an orientation, with occupancy of every van der Waals gap, a Δc of 5.4-5.8Å would be anticipated (referring to the dimensions of Figure 4.4). Thus, having observed a Δc of only 4.8Å, such an orientation would have to be accompanied by some van der Waals gaps remaining empty. To elucidate the orientation of this guest, INS would be an appropriate technique with which to examine the vibrations of the trapped species relative to those of the gas phase molecule and so identify if vibrations of particular symmetry were being suppressed.

The biphenyl molecule has been inserted and the Δc observed is consistent with its orientation being similar to that of 1,5-dihydroxynaphthalene and 1-chloromethylnaphthalene intercalates. However, the degree of intercalation by biphenyl is less than half of these polar molecules. The Δc is consistent with the biphenyl molecule oriented as shown in Figure 6.3, with the C_2 axis through the aromatic rings parallel to the *ab* plane. If the molecule rotates about this axis, it would sweep out a volume such that the degree of uptake would be limited by the geometrical restrictions in the *ab* plane;

ca. 0.20 mole of biphenyl per mole of MoS_2. At the same time, rotation would cause a separation of the inorganic layers such that a $\Delta c > 3.7Å$ would be observed.

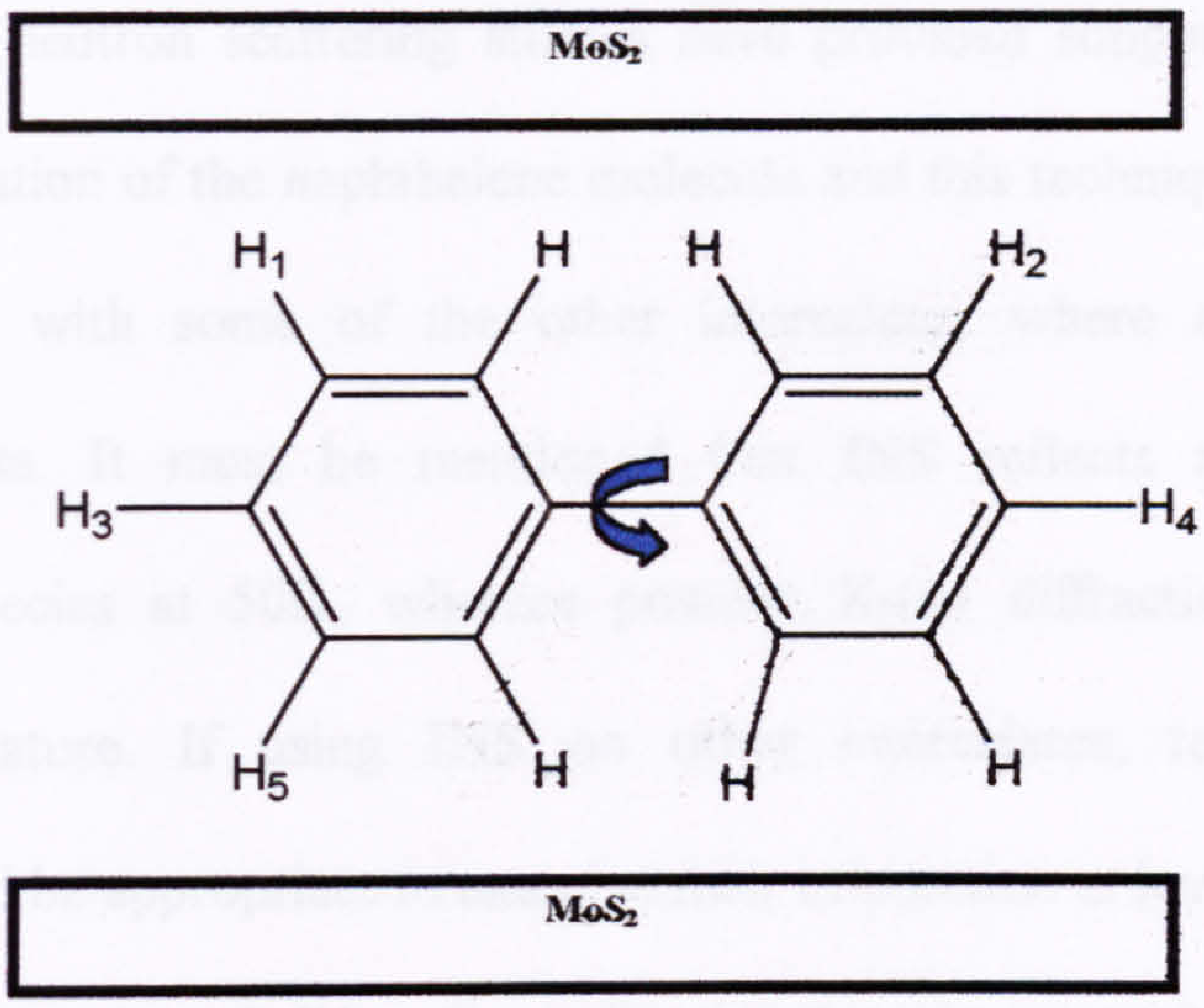

Figure 6.3: Possible orientation of the biphenyl molecule.

This rotation could either be a dynamic motion where the molecular species is undergoing rigid body rotation or a static rotation where one benzene ring rotates relative to the other so that a non-coplanar geometry is generated. The alternative is that there is a mixture of biphenyl molecules occupying the van der Waals gap as in Figure 6.3 and those with the aromatic plane parallel to the sulphide layers. ^2H NMR is one possible technique which would allow motions of this guest to be investigated although with a powder sample, the broadness of the line shape would be a severe problem to overcome.

An uptake of crystal violet comparable to that of 2-ethylnaphthalene was observed. The two molecules are similar in that both are non-planar. The fan blade structure in the former is responsible for its non-planarity whereas in the latter, it is the ethyl group. The shear bulk of the crystal violet molecule could be expected to prevent a large degree of incorporation. Interestingly, the Δc observed suggests that the molecule has been forced to lose it's fan blade structure and become planar or, that the Δc corresponds to an average of occupied and unoccupied van der Waals gaps.

Inelastic neutron scattering studies have provided supporting evidence for the proposed orientation of the naphthalene molecule and this technique could be used even more profitably with some of the other intercalates where ambiguity about their orientation exists. It must be mentioned that INS reflects the behaviour of the hydrogenous species at 50K, whereas powder X-ray diffraction was performed at ambient temperature. If using INS on other intercalates, temperature dependent diffraction would be appropriate to examine their orientation at lower temperatures.

The suppression of all but these vibrational modes, provides strong evidence that the molecule is oriented with the molecular plane parallel to the inorganic layers. For the three surviving bands of intercalated naphthalene; the one centred at 1154cm^{-1} in solid naphthalene is virtually unchanged in the intercalate while the 982cm^{-1} band drops to 959cm^{-1} and the 473cm^{-1} band falls to 461cm^{-1} in the naphthalene intercalate. The frequency reductions for these bending motions may indicate that the molecule is experiencing a softer potential than in solid naphthalene.

At the same time as indicating clearly that the molecular vibrations are suppressed and hence the naphthalene molecule itself, the extent of suppression means that little indication of the bonding picture or direction of electron transfer can be ascertained from these data. Similar experiments performed on the intercalates of 1,5-dihydroxynaphthalene or biphenyl where the molecule would be expected to be less restricted in its vibrations would hopefully show greater detail in the INS spectrum. Such spectra might reveal a shift in the vibrational energies of the molecule in its intercalated form which aid in determining the direction of any electron transfer between guest and host. Clearly, such a spectrum would not be enough to ascertain definitively the interaction between the intercalate and the inorganic host, but such data are valuable in understanding these materials.

6.5 ELECTRONIC CONDUCTION PROCESSES

In this thesis, one of the most striking contrasts between the host and the intercalation compounds lies in the electronic conduction properties of each. 2H-MoS_2 itself is a semiconductor with an activation energy of 0.235eV below 790K. This behaviour has been shown to continue after subjecting MoS_2 to lithiation, exfoliation and flocculation in the absence of a guest species, although the semiconducting behaviour is no longer of the Arrhenius type. The four probe conductivity data collected for all the intercalation compounds indicate their transport properties. The magnitude of the conductivity displayed by each intercalate over the temperature range 5-300K remains considerably lower than would be expected for a metal and yet, semiconductor to metal transitions are observed upon cooling.

The conductivity of restacked MoS_2 is an order of magnitude lower than in the crystalline material. This may be attributed to a combination of structural disorder within the layers comprising defects, stacking disorder and grain boundary effects owing to the inability to sinter the material. However, the intercalation compounds which also have structural disorder within the layers and have not been sintered, show conductivity similar in magnitude to the pristine material.

It has been shown that there is structural change within the MoS_2 layers after the process of exfoliation and flocculation; EXAFS has demonstrated that this structural alteration occurs whether an organic species is occupying the van der Waals gap or not. Yet, occupation of the van der Waals gap with an accompanying perturbation to the interlayer spacing is sufficient to produce dramatic changes in the electronic properties with temperature relative to that observed for restacked MoS_2. It is known that in crystalline MoS_2 the conductivity parallel to the layer is approximately 200 times that perpendicular to the layers[87]. Although insertion of an organic guest species must alter the van der Waals interactions between the layers, it would only have a very slight effect on the electronic band structure.

Since the accurate in-plane structure of the material is not yet established, it is difficult to account for the electronic conductivity data on the basis of a qualitative electronic band picture. However, some similarities in behaviour in each of the intercalates has been identified. Over certain temperature ranges, shown in Table 6.3, the $\ln(\sigma)$ exhibits $T^{-1/4}$ dependence, indicating that the dominant conduction mechanism in the region is variable range hopping. This mechanism is usually associated with materials in which the electrons experience short range order. A randomly varying potential of the lattice gives rise to localised states near the band edges and with the Fermi level lying inbetween the extended and localised states, metal-insulator transitions can be observed. With variable range hopping, electrons hop from one localised state to another similar in energy, by phonon assisted tunnelling. The presence of localised states may arise from the disordered nature of the molybdenum disulphide layers, since for restacked MoS_2, this hopping behaviour is exhibited over a large temperature range. This mechanism can be overtaken by thermally assisted hopping as the temperature is increased, at which point the $\ln(\sigma)$ has $1/T$ dependence. Interestingly, the conductivity data of the intercalates do not follow a $1/T$ dependence over any range of temperatures unlike 2H-MoS_2, which does for 5-300K.

Table 6.3: Temperature ranges over which variable range hopping is exhibited.

Guest Species	**Temperature /K**
Naphthalene	100-220
2-Methylnaphthalene	78-300
2-Ethylnaphthalene	80-195
Crystal violet	Non shown
Benzofuran	82-230
Pyridinium	10-80
Biphenyl	80-300
Restacked MoS_2	66-300
2H-MoS_2	77-94

Examining the $\sigma(T)$ data, it can be seen that for the intercalates of naphthalene, 2-methyl- and 2-ethyl- derivatives, there is a change in sign of $d\sigma/dT$ at 100K, 21-33K and 22K respectively. The benzofuran intercalate exhibits a semiconductor to metallic transition at 250K that is the reverse of the transition observed for the naphthalene intercalate and those of its derivatives. Alteration to the band structure is implied by such a change and one possibility is the onset of a charge density wave (CDW). A CDW is formed by electron-phonon interaction and its formation is determined by a number of competing energy factors. They have been much mentioned in the literature, sparked by their appearance in polytypes of TaS_2 and various intercalates of such structures[211]. A tight binding electronic band structure[212] calculation has been carried out for several d^2 ML_2 layers and factors controlling the charge density wave formation were evaluated. A charge density wave pattern of zig-zag chains is observed for 1T-ML_2 layers containing d^2 ions; β-$MoTe_2$[209], WTe_2[209] and α-ZrI_2[213]. Distortion of layered octahedral ML_2 d^2 systems to form such chains by a charge density wave, has been predicted by Rovira and Whangbo to lower the total electronic energy of the system.

The d^2 ML_2 systems 1T-MoS_2 and $LiVO_2$ do not exhibit this zig-zag clustering; a structure comprising weak $\sqrt{3}a_0 \times \sqrt{3}a_0$ superstructure has observed. Goodenough[214] has proposed a weak trimerisation of the metal atoms for the $\sqrt{3}a_0 \times \sqrt{3}a_0$ superstructure in $LiVO_2$. The nature of the CDW formed was found to depend on several competing energy terms[212] but two crucial factors were the M-M bonding interaction and the degree of lattice strain. Calculations showed that the trimerisation model for $LiVO_2$ and for 1T-MoS_2 lowers the total energy and opens a band gap for a very small displacement of the metal atoms, thereby supporting the CDW model for the $\sqrt{3}a_0 \times \sqrt{3}a_0$ superstructure observed in $LiVO_2$ and 1T-MoS_2.

There has been a great deal of research activity into the intercalation of conducting polymers into MoS_2 hosts as the intercalates so formed often show higher electrical conductivities than the parent hosts. Similar anomalous behaviour to that observed in this work has been measured in MoS_2 intercalated with conducting polymers; CDW's have been proposed as an explanation for this.

Common properties of the polymer intercalates may be identified[131, 132, 215];

- All show weak thermally activated behaviour between 50-300K.
- The intercalates of PEO and PANI show abrupt transitions between 14-15K and 8-9K respectively, the conductivity decreasing by six and three orders of magnitude respectively.
- Thermoelectric power measurements indicate that the dominant charge carriers are holes.
- Magnetic susceptibility measurements indicate Pauli paramagnetism; Curie-Weiss paramagnetism below 12K was observed for the PANI intercalate.

P-type conduction has been observed in all intercalates of electron rich conducting polymers. The presence of mixed valent molybdenum in the host could be one explanation for this. This is assuming that the band structure is similar to that of 2H-MoS_2.

If a CDW is present in the intercalated phases prepared here, it seems that the presence of the guest species is sufficient to favour of CDW formation whereas for restacked MoS_2, which is devoid of guest, no such unusual behaviour is observed. Stabilisation of a CDW could possibly be connected to the degree of charge transfer between the guest and host, favouring one band structure over another at these transition temperatures.

The intercalation compounds of pyridinium and crystal violet also show unusual temperature dependent conductivity behaviour. The pyridinium shows two transitions fairly close in temperature. Below 80K there is rapid excitation of charge carriers and variable range hopping is exhibited. The change in sign of $d\sigma/dT$ at 80K could be attributed to the dominance of scattering by phonons, except the transition is unusually sharp. Another possibility is an alteration to the orientation of the pyridinium ion. The second change in sign at 125K suggests that there is a delicate balance of competing factors which are influencing the conductivity behaviour with temperature for this intercalate. If localised states are present which result in the initial rapid increase in conductivity at low temperatures, thermal scattering effects could dominate at higher temperatures as such localised states are depleted. Hence the conductivity then begins to plateau and there is a slow change in sign of $d\sigma/dT$ between 125K and 300K.

The intercalate containing crystal violet as a guest does not exhibit variable range hopping over the temperature range measured. However, there are two stepwise increases in conductivity between 5-300K. For this material, these stepwise increases in conductivity suggest that excitation of the charge carriers into the conduction band, from either donor or acceptor states, is occurring at two discrete temperatures; 50K and

100K. Above 100K, the carrier concentration becomes constant as the donor/acceptor levels become depleted and the conductivity reaches a plateau.

With these conductivity data alone, it is not possible definitively to describe the conduction mechanisms without accompanying structural information. However, it has been previously mentioned that when MoS_2 is partially reduced, there may be a range of similar structures which are close in energy. Equally, the orientation of the molecule within the layer may be delicately balanced and its preferred orientation highly temperature dependent. Thus, conductivity behaviour is highly sensitive to temperature and is reflecting the nature of the interaction between guest and host.

6.6 ELECTRON VOLT SPECTROSCOPY

Having carried out the study of the applicability of eVS to the investigation of the dynamics of ions incorporated into complex chemical environments, it can be concluded that the presence of a complex environment does not preclude study of the atom or ion. The key factor in acquiring good data is separation of the recoil peak of the mass under investigation from those of the other masses present. Following this, the quality of the data will be determined by the atom%, the total neutron scattering cross-section of the atom and its neutron absorption cross-section, which, as was discovered, virtually excluded lithium from satisfactory data analysis. Insufficient detectors lead to problems in obtaining data of sufficient quality for satisfactory analysis to be carried out.

At low masses, there is greater separation of recoil peaks and as the masses increase, separation becomes virtually impossible. Currently, eVS is unique in the information it can provide for hydrogen within complex chemical environments. EVS provides information on protons, either by comparison of proton kinetic energy in two different environments or comparison of the data obtained with that proposed by a theoretical model for the potential well of the proton. Measurement of the kinetic energy provides insight into the nature of the potential well, whether it is harmonic or anharmonic and by using single crystals, can specifically pin-point the various anisotropies of motion for hydrogen in complex systems. Temperature dependent studies of proton motion cannot be carried out on eVS as, owing to the physics of the system, ΔRT is insufficient to excite a proton above its zero point motion..

However, for many other elements, the technique is still limited to the study of relatively simple systems such as binary compounds where separation of the recoil peak is satisfactory. A great deal of interest in the kinetic energy of atoms and ions lies in the temperature dependence of their motion. As was observed for lithium in $LiTiS_2$, it is possible to explore this avenue, but the errors on the data in that experiment precluded detailed analysis using standard eVS routines. Studies of lithium are prohibited by the low total neutron scattering cross-section and high neutron absorption cross-section of this element. The second problem could be overcome in future work by using ^7Li alone which has an absorption cross-section of only 0.05 barns compared to the 940 barns of ^6Li. Most importantly EVS would benefit greatly from a large increase in the number of detectors available to help overcome the problem of low atom%, a factor which is unavoidable for many materials of interest, especially within intercalation chemistry. At the time of writing, funding for upgrading of the instrument had been secured. This will involve installation of a filter cooling device at back scattering angles to improve the resolution by a factor of 2 and installation of a new back scattering bank to improve the count rate by a factor of 4.

Background subtraction using the host structure to provide a background was successful to a certain extent. It was demonstrated that in the case of the ammonium pyrochlore this technique allowed extraction of a recoil peak of interest from a complex spectrum, but in retrospect, insufficient neutron counting time was allocated to this experiment to compensate for the increased complexity of data analysis. This method has considerable potential for analysis of complex systems.

At a time when the instrument set-up is to be developed further, as are the analysis routines, the information presented here demonstrates what the instrument is capable of within its current state. These pilot experiments provided information not only on the atoms and ions under investigation but have also provided information on the approach needed to study complex compounds on eVS.

6.7 FURTHER WORK

These initial measurements of electronic conductivity of the intercalation compounds need more extensive investigations to be understood. Firstly, given the lack of capacity to sinter these materials, conduction behaviour under a.c current should be measured in order to eliminate grain boundary effects when measuring the resistivity. Thermopower measurements would show whether charge transport is via holes, as observed for MoS_2 intercalated with conducting polymers, or via electrons. The question of the oxidation state of molybdenum could be addressed by ESR measurements to see whether molybdenum is existing in a mixed valence state.

Further measurements need to be made to study the structural and physical properties as a function of temperature. Given that these are poorly crystalline materials with disorder in the sulphide layers, a number of techniques would be required:-

- low temperature EXAFS to examine the co-ordination environment of molybdenum.
- low temperature electron microscopy to determine whether there are molybdenum atomic displacements on reducing the temperature below the semiconductor/metal transition.

- total neutron scattering over 10-300K would show gross structural alterations with temperature;
- changes in the vibrational spectra of the intercalated guest using INS would show alterations in electron density, but these need to be made over a temperature range to correlate with structural data.
- temperature dependent powder X-ray diffraction would show a change in the interlayer spacing which would be expected if the guest changes its orientation relative to the layers with temperature.
- solid state temperature dependent NMR might be an appropriate technique to study the motion of the organic guest.

Although intercalation is a versatile technique for preparing new materials with tailored properties, certain limitations have been reached e.g. size of channels in the host, stability of host structures when intercalated with a guest and also the nature of the guests that can be incorporated using the known synthetic approaches. Techniques using "chimie douce" have exploded in recent years, opening up routes to new materials which were previously unobtainable. An offshoot of this new approach to materials synthesis has been the exfoliation-reflocculation technique as applied to layered materials. This synthetic route is one technique which has pushed back some limitations of intercalation encountered in the more usual synthetic approaches. This thesis has demonstrated that host structures previously limited in their ability to intercalate materials can be persuaded to accommodate an unusual complement of guest species. In addition, exfoliation provides access to new materials by expanding the range of guest species able to be incorporated into the more well established hosts such as TaS_2.

Chapter Seven

Conclusions

7.1 SYNTHESIS OF NOVEL INTERCALATES OF MoS_2

This thesis describes the synthesis, via the technique of exfoliation, of single-layered MoS_2, the nature of its restacking to a poorly crystalline phase and the insertion of small organic species in between the layers of MoS_2 via flocculation of these single layers.

With respect to the restacked MoS_2 layers, powder X-ray diffraction and EXAFS have been used to show that:-

- the material is poorly crystalline with particle size < 150Å.
- changes in the powder X-ray diffraction pattern were observed with ageing of the material.
- the structure of this material is different to that of crystalline 2H-MoS_2 and cannot be described as 1T-MoS_2.
- no co-ordination environment of the molybdenum atom could be developed from EXAFS data, which might lead to a structural model for this material.

Four probe conductivity measurements demonstrate that this material is semi-conducting, indicative that molybdenum does not possess octahedral co-ordination, contrary to previous suggestions. Variable range hopping is exhibited, consistent with defects being present within the layers.

A synthetic method has been developed for the incorporation of small organic molecules that are electron-rich and unfunctionalised. The primary evidence for successful insertion is the increase in the repeat distance of the MoS_2 layers, observed by powder X-ray diffraction. Powder diffraction data for the products are similar in appearance, consisting of one or more moderately intense 00*l* reflections and Warren broadened lines at higher diffraction angles. The 00*l* reflections are shifted towards lower angles, indicating an expansion of the lattice in the direction perpendicular to the MoS_2 layers. Given that the pπ orbitals give aromatic rings an effective thickness of ca. 3.7Å, the observed Δc's suggest that for the majority of products, the molecules are oriented with the molecular plane parallel to the MoS_2 layers. Certainly this is the case for the intercalation compounds containing naphthalene, 2-methylnaphthalene and 2-ethylnaphthalene. The information obtained from the powder X-ray diffraction data is limited by the small particle size which results in broad reflections. No information about the structure of the layers could be gleaned, but from EXAFS data, a similar co-ordination environment of molybdenum is observable in intercalated material to that in restacked material.

Properties which have been observed for the intercalates synthesised in this thesis include:-

- Semiconducting behaviour in the temperature range 10-300K.
- Sharp transitions between semiconducting and metallic behaviour at critical temperatures where σ changes by less than an order of magnitude.
- Variable range hopping is exhibited by many intercalates between 10-300K, suggesting the presence of defects within the MoS_2 layers.
- Pauli paramagnetism between 5-300K with a weak upturn below 50K.

7.2 THE TECHNIQUE OF EVS

Studies using Electron Volt Spectroscopy to look at the kinetic energies of intercalated species, have shown that the presence of a complex environment does not preclude study of the atom or ion. When assessing the quality of data that will be obtained, consideration needs to be given to the atom% present in the material, its neutron absorption cross-section and its total neutron scattering cross section.

- The kinetic energy of lithium in $LiTiS_2$ was found to increase with temperature between 13-298K. The value at 70K was in agreement with that of elemental lithium at 70K, suggesting that zero point motion is dominant at this temperature.
- The kinetic energies of the hydrogen atoms in $H_{0.30}MoO_3$ and $H_{1.57}MoO_3$ at 4.3K can be concluded to be different, being 4.54 ± 0.06 Å^{-1} and 4.26 ± 0.03 Å^{-1} respectively. However, at 295K their values are statistically the same. No change of kinetic energy with temperature could be measured for either intercalate.
- The lithium kinetic energies in $Li_{0.45}MoO_3$ and LiV_2O_5 could not be measured using the current configuration of the instrument. The small lithium recoil peak could not be satisfactorily isolated from the dominating recoil peak of oxygen.
- The proton kinetic energies in $HTaWO_6$ and NH_4TaWO_6 were both found to be independent of temperature in the range 4.5K to 298K.
- The technique of background subtraction using the NCS profile of the host as background is a potential route to isolating poorly resolved peaks, but this needs further development of eVS analysis routines.

Appendix A

Table 5.1: RMS momenta values for $H_{0.30}MoO_3$

Scattering Angle θ	**σ_{unsym} Å^{-1} 295K**	**σ_{sym} Å^{-1} 295K**	**σ_{unsym} Å^{-1} 4.3K**	**σ_{sym} Å^{-1} 4.3K**
34.04	4.417±0.09	4.052±0.14	5.595±0.38	5.678±0.26
35.76	4.404±0.09	4.173±0.09	4.128±0.23	4.125±0.15
36.65	4.359±0.08	4.309±0.09	4.189±0.23	4.186±0.15
38.33	4.264±0.12	4.655±0.08	2.894±3.03	4.273±0.14
39.22	4.370±0.10	4.488±0.08	4.584±0.21	4.611±0.13
40.97	4.451±0.10	4.474±0.07	4.813±0.19	4.802±0.13
41.77	4.422±0.12	4.418±0.06	4.773±0.16	4.827±0.11
43.58	4.627±0.13	4.489±0.06	4.427±0.15	4.477±0.10
67.56	4.400±0.34	4.354±0.06	3.109±3.25	4.598±0.10
69.96	3.895±0.44	4.252±0.08	4.558±0.20	4.550±0.13
70.27	4.472±0.36	4.400±0.06	4.565±0.17	4.561±0.12
72.45	3.331±0.42	4.531±0.09	4.830±0.25	4.814±0.16
72.82	3.275±0.38	4.579±0.08	4.676±0.19	4.666±0.14
74.97	2.226±0.35	4.304±0.09	4.595±0.24	4.553±0.15
77.40	4.921±1.55	4.615±0.11	4.639±0.39	4.408±0.24

Table 5.2: RMS momenta values for $H_{1.57}MoO_3$

Scattering Angle θ	σ_{unsym} Å^{-1} at 295K	σ_{sym} Å^{-1} at 295K	σ_{unsym} Å^{-1}at 4.3K	σ_{sym} Å^{-1} at 4.3K
34.04	4.302±0.17	4.217±0.11	4.104±0.12	4.060±0.08
35.76	4.115±0.10	4.069±0.07	4.285±0.08	4.215±0.05
36.65	4.340±0.11	4.280±0.07	4.218±0.08	4.149±0.05
38.33	4.373±0.10	4.335±0.07	4.332±0.07	4.310±0.05
39.22	4.471±0.09	4.469±0.06	4.238±0.06	4.233±0.04
40.97	4.321±0.08	4.350±0.06	4.312±0.06	4.327±0.04
41.77	4.455±0.07	4.489±0.05	4.264±0.05	4.305±0.04
43.58	4.134±0.07	4.181±0.05	4.224±0.05	4.274±0.04
67.56	4.371±0.07	4.416±0.05	4.206±0.05	4.274±0.03
69.96	4.229±0.10	4.240±0.07	4.505±0.07	4.501±0.05
70.27	4.471±0.08	4.448±0.06	4.379±0.06	4.368±0.04
72.45	4.619±0.11	4.587±0.07	4.500±0.07	4.448±0.06
72.82	4.442±0.09	4.385±0.06	4.254±0.07	4.215±0.04
74.97	4.416±0.10	4.352±0.07	4.135±0.07	4.069±0.05
75.45	3.893±0.12	3.869±0.08	4.234±0.08	4.148±0.06
77.40	4.327±0.11	4.188±0.07	4.184±0.09	4.046±0.06

References

1 H. Selig, L. Ebert, Adv. Inorg. Radiochem., **23**, 281, 1980.

2 I.F. Cheng, B.L. Gilbert, T.I. Sun, J. Electrochem., Soc. **122**, 955, 1975.

3 M.S. Whittingham, Prog. Solid State Chem., **12**, 41, 1978.

4 A.M. Chippindale, P.G. Dickens, A.V. Powell, Prog. Solid State Chem., **21**, 3, 1991.

5 D. O'Hare, "Inorganic Materials," Chapter Four, Ed. D. Bruce, D. O'Hare, 1991, John Wiley & Sons Ltd.

6 R. Schöllhorn, Comments Inorg. Chem., **2**(6), 271, 1983.

7 R. Schöllhorn, R. Kuhlmann, J.C. Besenhard, Mater. Res. Bull., **11**, 83, 1976.

8 P.G. Dickens, S.J. French, A.T. Hight, M.F. Pye, Mater. Res. Bull., **14**, 1259, 1979.

9 D.W. Murphy, P.A. Christian, F.J. DiSalvo, J.V. Waszczak, Inorg. Chem., **18**, 2800, 1979.

10 R. Bruce, Solid State Ionics, **22**, 3, 1986.

11 J. Rouxel, P. Palvadeau, Rev. Chim. Miner., **19**, 317, 1982.

12 A. Clearfield, Comments Inorg. Chem., **10**, 89, 1990.

13 R. Schöllhorn, H.D. Zagefka, Angew. Chem. Int. Ed. Engl., **16**, 199, 1977.

14 M. Ohashi, K.U. Yeoka, S. Samanoka, M. Hattori, Chem. Lett., 93, 1990.

15 A. Weiss, Angew. Chem., **73**, 413, 1960.

16 J.M. Adams, J. Chem. Soc. Daltons Trans., 2286, 1974.

17 R. Schöllhorn "Inclusion Compounds," Vol. 1, Chapter 7, Academic Press, London.

18 M. Patel, R. Chevrel, M. Sergent, Acta. Cryst. B, **36**, 1545, 1980.

19 A. Herold "Intercalated Layer Materials" in "Physics and Chemistry of Materials with Layered Structures," Vol. VI, Ed. F. Lévy, Dordrecht, The Netherlands.

20 J.M. Thomas, G.R. Millwood, R.F. Schögl, H.P. Boechm, Mater. Res. Bull., **15**, 671, 1980.

21 B. Schlsche, R. Schöllhorn, Rev. Chim. Miner., **19**, 534, 1982.

22 P.G. Dickens, S. Crouch-Baker, M.T. Weller, Solid State Ionics, **18**, 89, 1986.

23 J.A. Maguire, J.J. Banawicz, Mater. Res. Bull., **19**, 1573, 1984.

24 R. Schöllhorn, , Mater. Res. Bull., **9**, 1237, 1974.

25 A.J. Jacobson, J.W. Johnson, J.F. Brody, J.C. Scanlon, J.T. Lewandowski, Inorg. Chem., **24**, 1782, 1985.

26 G. Lagaly, Solid State Ionics, **22**, 43, 1986.

27 T.J. Pinnevaia, R. Raythata, J.G.S. Lee, J. Am. Chem. Soc., **101**, 6891, 1979.

28 C. Riekel, H.G. Reznik, R. Schöllhorn, J. Solid State Chem., 253, 1989.

29 J.O. Besenhard, I. Kain, H.F. Klein, H. Witty, Mater. Res. Soc. Symp. Proc., **20**, 221, 1983.

30 L.F. Nazar, A.J. Jacobson, J. Mater. Chem., 4(9), 1419, 1994.

31 P.J.S. Foot, N.G. Shaker, Mat. Res. Bull., **18**, 173, 1983.

32 J.W. Johnson, A.J. Jacobson, S.M. Rich, J.F. Brody, J. Am. Chem. Soc., **103**, 5246, 1981.

33 S.M. Kauzlarich, J. F. Ellena, P.D. Stupik, W.M. Ruff, B.A. Averill, J. Am. Chem. Soc., **109**, 4561, 1987.

34 P. Bowen, W. Jones, J.M. Thomsa, R. Schlogi, J. Chem. Soc. Chem. Commun., 677, 1981.

35 O. Berkoos, E. Herman, Mat. Res. Bull., **5**, 173, 1970.

36 D. O'Hare, J.S.O. Evans, P.A. Turner, S.M. Stephen, J. Heyes, J. Greenwood, J. Mater. Chem., **5**, 1383, 1995.

37 L. Hérnan, J. Morales, L. Sánchez, J.L. Tirado, Chem. Mater., **7**, 1576, 1995.

38 J.O. Besenhard, H. Mohwald, J.J. Nickl, Synth. Metals, **3**, 187, 1981.

39 A. Herold p. 321 in"Intercalated Layer Materials" in "Physics and Chemistry of Materials with Layered Structures," Vol. VI, Ed. F. Lévy, Dordrecht, The Netherlands.

40 D. Vaknin, D. Davidov, H. Selig, J. Fluor. Chem., **32**, 345, 1986.

41 A. Payer, R. Schöllhorn, C. Ritter, W. Paulus, J. Alloys and Compounds, **37**, 191, 1993.

42 F. Viola, R. Schöllhorn, J. Chem. Soc. Chem. Commun., 907, 1992.

43 G.C. Wu, D.C. De Groot et al, J. Am. Chem. Soc., **117**, 9229, 1995.

44 R. Schöllhorn "Inclusion Compounds," ed. J.L. Atwood, J.E.D. Davies, D.D. MacNicol, Academic Press, London, 1984. Vol 1, p. 249.

45 R. Schöllhorn, H. D. Zagefka, T. Butz, A. Lerf, Mater. Res. Bull., **14**, 369, 1979.

46 A. Wold, W. Kunnemann, R.J. Arnott, A. Ferfetti, Inorg. Chem., **3**, 545, 1964.

47 S. Hibble, P.G. Dickens, J.C. Evison, J. Chem. Soc. Chem. Commun., 1809, 1985.

48 J.B. Goodenough, Prog. Solid State. Chem., **5**, 145, 1971.

49 P.G. Bruce, F. Krok, P. Lightfoot, J. Nowinski, V.C. Gibson, Solid State Ionics, **53-56**, 351, 1992.

50 P. Lacroix, J.P. Audière, R. Clement, J. Chem. Soc. Chem. Commun., 536, 1989.

51 R.P.Clement, W.B. Davies, K.A.Ford, M.L.H. Green, A.J. Jacobson, Inorg. Chem., **17**, 2754, 1978.

52 M.S. Whittingham, J. Chem. Soc. Chem. Commun., 328, 1974.

53 V. Cajipe, P. Molinie, P. Colombet, Solid State Ionics, **44**, 139, 1990.

54 M.B. Dines, Mater. Res. Bull., **10**, 287, 1975.

55 M.G. Kanatzidis, T.J. Marks, Inorg. Chem., **26**, 783, 1987.

56 P.G. Dickens, P.J. Wiseman, M.T.P. Int. Rev. Sci.: Inorg. Chem., Ser. Two, **10**, 211, 1975.

57 P.G. Bruce, F. Krok, J. Nowinski, V.C. Gibson, K. Tavakkoli, J. Mater. Chem., **1**, 705, 1991.

58 D.W. Murphy, P.A. Christian, Science, **205**, 651, 1979.

59 P. Hagenmuller, Prog. Solid State Chem., **5**, 71, 1971.

60 R. Clement, J. Am. Chem. Soc., **103**, 6998, 1981.

61 M.S. Whittingham, Prog. In Solid State Chem., **12**, 41-99, 1978.

62 S.K. Deb, Appl. Opt. Suppl., **3**, 192, 1969.

63 B.W. Faughnan, R.S. Cranda, P.J. Heymann, R.C.A. Rev., **56**, 177, 1975.

64 G. Betz, H. Tributsch, Prog. in Solid State Chem., **16**(4), 1985.

65 O. Glemser, G. Lutz, Z. Anorg. Allg. Chem., **264**, 17, 1971.

66 J. Conard, H. Estrade, Mat. Sci. Eng., **31**, 173, 1977.

67 K. Brodersen, G. Thiele, H. Breitbach, Z. Anorg. Chem., **357**, 162, 1968.

68 R.J. Cava, A. Santoro, D.W. Murphy, S.M. Zahurak, R.S. Roth, J. Solid State Chem., **50**, 121, 1983.

69 D.W. Murphy, M. Greenblatt, R.J. Cava, S.M. Zahurak, Solid State Ionics, **5**, 323, 1981.

70 R.J. Cava, A. Santoro, D.W. Murphy, S.M. Zahurak, R.S. Roth, J. Solid State Chem., **42**, 251, 1981.

71 R. Jellinek, G. Bauerand, H. Muller, Nature, **185**, 376, 1960.

72 P.J. Wiseman, P.G. Dickens, J. Solid State Chem., **17**, 91, 1976.

73 P.N. Iyer, A.J. Smith, Acta. Cryst., **23**, 740, 1967.

74 A. Nadiri, G. Le Flenn, C. Delmas, J. Solid State Chem., **73**, 338, 1988.

75 C.T. Kresge, M.E. Leonowicz, W.J. Roth, J.C. Vartuli, J.S. Beck, Nature, **359**, 710, 1992.

76 A. Monnier, F. Schüth et al, Science, **261**, 1299, 1993.

77 A. Magneli, Acta. Chem. Scand., **7**, 315, 1953.

78 B. Schlasche, R. Schöllhorn, Rev. Chim. Miner., **19**, 534, 1982.

79 D.W. Murphy, J.L. Dye, S.M. Zahurak, Inorg Chem., **22**, 3679, 1983.

80 M.F. Pye, Part II Thesis, University of Oxford, 1975.

81 "SERC Daresbury Laboratory EXCURV92 Program," N. Binsted, J.W. Campbell, S.J. Gurman, P.C. Stephenson, 1991.

82 J.C. Wildervanck and F. Jellinek, Zeit. Anorg. Allg. Chem., **328**, 309, 1964.

83 L.F. Mattheis, Phys. Rev. B, **8**, 3719, 1973.

84 R. Mansfield, S.A. Salem, Proc. Phys. Soc., **B66**, 377, 1953.

85 J.W. Johnson, A.J. Jacobson, J.F. Brody, S.M. Brody, Inorg. Chem., **21**, 3820, 1982.

86 B.G. Silbernagel, M.S. Whittingham, J. Chem. Phys., **64**, 3670, 1976.

87 B.L. Evans, P.A. Young, Proc. Roy. Soc., **A284**, 402, 1965.

88 P.G. Dickens, S.J. French, A.T. Hight, M.F. Pye, Mater. Res. Bull., **14**, 1295, 1979.

89 A. Souder, D.E. Brodie, Canad. J. Phys., **49**, 2565, 1971.

90 D. Tinet, M.H. Legay, L. Gatineau, J.J. Fripiat, J. Phys. Chem., **90**, 948, 1986.

91 W.M.R. Divigalpitaya, R.F. Frindt, S.R. Morrison, Science, **246**, 369, 1989.

92 F. Hulliger in "Structural Chemistry of Layer Type Phases" ed. F. Levy, D. Reidel, The Netherlands, 1976.

93 N.A. Johnson, C.A. Scholl, J. Phys. C., **17**, L73, 1984.

94 G.Y. Guo, W.Y. Liang, J. Phys. C., **20**, 4315, 1987.

95 S.H. El-Mahalawy, B.L. Evans, Phys. Stat. Sol. (B), **79**, 713, 1977.

96 A. Al-Hilli, B.L. Evans, J. Crystal Growth, **15**, 93, 1972.

97 R. Schöllhorn, F. Wypych, J. Chem. Soc. Chem. Commun., 1386, 1992.

98 M.S. Whittingham, J. Chem. Soc. Chem. Commun., 328, 1974.

99 A.H. Thompson, Physica B+C, 105B, 461.

100 M.B. Dines, Science, **188**, 1210, 1975

101 S.J. Heyes, N.J. Clayden, C.M. Dobson, M.L.H. Green, P.J. Wiseman, J. Chem. Soc. Chem. Commun., 1560, 1987.

102 F.R. Gamble, A.H. Thompson, Solid State Commun., **27**, 379, 1978.

103 D. O'Hara, W. Jaegermann, D.L. Williamson, F.S. Ohuchi, B.A. Parkinson, Inorg. Chem., **27**, 1537, 1988.

104 A. Weiss, A. Weiss, Angew. Chem., **72**, 413, 1960

105 F.R. Gamble, J.H. Osiecki, M. Cais, R. Pisharody, F.J. Di Salvo, T.H. Geballe, Science, **174**, 493, 1971.

106 F.R. Gamble, J.H. Osiecki, F.J. Di Salvo, J. Chem. Phys., **55**, 3525, 1971.

107 F.R. Gamble, B.G. Silbernagel, J. Chem. Phys., **63**, 2544, 1975.

108 M.J. McKelvy, W.S. Glausinger, Solid State Ionics, **25**, 287, 1987.

109 T. Butz, A. Vasquez, H. Saitovitch, R. Muhlberger, A. Lerf, Physica, **99B**, 69, 1980.

110 J. Cousseau, L. Trichet, J Rouxel, Bull. Soc. Chim. Fr., 872, 1973.

111 G.V. Subba Rao in "Intercalated Layered Materials"ed. F. Levy. P.99.

112 P.H. Nadeau, Applied Clay Sci., **2**, 83, 1987.

113 A. Lerf, R. Schöllhorn, Inorg. Chem., **16**, 2951, 1977.

114 M. Balkanski, Physica Scripta, **T39**, 9, 1991

115 L.F. Nazar, A.J. Jacobson, J. Mater. Chem., **4(9)**, 1419, 1994.

116 D.W. Murphy, G.W. Hull, J. Chem. Phys., **62(3)**, 967, 1975

117 L.F. Nazar, S.W. Liblong, X.T. Yin, J. Am. Chem. Soc., **113**, 5889, 1991.

118 K.S. Suslick, D.J. Casadante, M.L.H. Green, M.E. Thompson, Ultrasonics, **25**, 56.

119 K. Chatakandu, M.L.H. Green, M.E. Thompson, K.. Suslick, J. Chem. Soc. Chem. Commun., **900**, 1987.

120 J.F. Mansot, J. Rouxel, Mater. Res. Bull., **28**, 757, 1993.

121 G. Alberti, M. Casciola, U. Costantino, J. Colloid Interface Sci., **107**, 256, 1985.

122 S.M. Kauzlarich, J.F. Ellena, P.D. Stupik, W.M. Reiff, B.A. Averill, J. Am. Chem. Soc., **109**, 4561, 1987.

123 M.G. Kanatzidis, L.M. Tonge, T.J. Marks, H.O. Marcy, C.R. Kannewurf, J. Am. Chem. Soc., **109**, 3797, 1987.

124 B.A. Averill, T.E. Sutto, J. Fabre, J. Mol. Cryst. Liq. Cryst., **244**, 77, 1994.

125 R. Bissessur, J. Heising. W. Hirpo, M. Kanatzidis, J. Chem. Mater., **8**, 318, 1996.

126 A.S. Golub, I.B. Shumilova, Y.N. Novikov, J.L.Mansot, M. Danot, Solid State Ionics, **91**, 307, 1996.

127 A.S. Golub, G.A. G.A. Protzenko, I.M. Yanovskaya, O.L. Lependine, Y.N. Novikov, Mendeleev Commun., 199, 1993.

128 A.S. Golub, C. Payen, G.A. Protzenko, Y.N. Novikov, M. Danot, Solid State Commun., **102(5)**, 419, 1997.

129 H. Tagaya, T. Hashimoto, M. Karasu, Chem. Letts., 2113, 1991.

130 B.K. Miremadi, S.R. Morrison, J. Appl. Phys., **67(3)**, 1515, 1990.

131 R. Bissessur, M.G. Kanatzidis, J.L. Schindler, C.R. Kannewurf, J. Chem. Soc. Chem. Commun., 1582, 1993.

132 J.P. Lemmon, M.M. Lerner, Chem. Mater., **6**, 207, 1994.

133 M.M.J. Treacy, S.B. Rice, A.J. Jacobson, J.T. Lewandowski, Chem. Mater., **2**, 14, 1990.

134 C.T. Kresge, M.E. Leonowicz, W.J. Roth, J.C. Vartuli, J.S. Beck, Nature, **359**, 710, 1992.

135 J.M. Tarascon, F.J. DiSalvo, C.H. Chen, P.J. Carroll, M. Walsh, L. Rupp, J. Solid State Chem., **58**, 290, 1985.

136 P. Tayler, D.W. Shoesmith, Can. J. Chem., **56**, 2797, 1978.

137 J.M. Tarascon, F.J. DiSalvo, C.H. Chen, P.J. Carroll, M. Walsh, L. Rupp, J. Solid State Chem., 58, 290, 1985.

138 P. Joensen, R.F. Frindt, S.R. Morrison, Mater. Res. Bull., **21**, 457, 1986.

139 R.C.T. Slade, T.K. Halstead, P.G. Dickens, J. Solid State Chem., 34, 183, 1980

140 B.G. Silbernagel, Chem. Phys. Lett., 34, 298, 1975.

141 C. Riekel, C.O. Fischer, J. Solid State Chem., 29, 181, 1979

142 R. Schöllhorn, Angew. Chem. Int. Ed. Eng., 16, 199, 1977.

143 R. Schöllhorn, Mater. Res. Bull., 14, 369, 1979.

144 M. Danot, J.L. Mansot, A.S. Golub et al, Mat. Res. Bull., **29**(8), 833, 1994

145 A.S. Golub, I.B. Shumilova, Yu. N. Novikov, Solid State Ionics, **91**, 307, 1996.

146 K.S. Liang, R.R. Chianelli, F.Z. Chien, S.C. Moss, J. Non-Cryst. Solids, **79**, 251, 1986

147 P. Joensen, E.D. Crozier, N. Alberding, R.F. Frindt, J. Phys. C: Solid State Phys., **20**, 4043, 1987

148 K. Chrissafis, M. Zamani, K. Kambas, Mater. Sci. Eng., **B3**, 145, 1989

149 K.E. Dungey, M.D. Curtis, Chem. Mater., **10**, 2152, 1998.

150 D. Yang, S.J. Sandoval et al. Phys. Rev., B. **43**(14), 12053, 1991

151 X.R. Qin, D. Yang, R.F. Frindt, J. Irwin, Phys. Rev. B, **44**, 3490, 1991

152 B.E. Warren, Physical Rev., **59**(9), 693, 1941.

153 T. Shibahara, Adv. Inorg. Chem., **37**, 143, 1991

154 S.J. Hibble, D.A. Rice, D.M. Pickup, M.P. Beer, Inorg. Chem., **34**, 5109, 1995.

155 J.C. Muijsers, Th. Weber, J. Catal., **157**, 698, 1995

156 A. Leist, S. Stauf, S. Loken, J. Mater. Chem., **8**(1), 241, 1998

157 J. Heising, M. Kanatzidis, J. Amer. Chem. Soc., **121**, 638, 1999.

158 F. Wypych, Th. Weber, R. Prins, Chem. Mater., **10**, 723, 1998

159 "CS Chem 3D Pro", carried out by Dr. K. Morgan, Heriot-Watt University.

160 E. Mack, J. Phys. Chem., **41**, 221, 1937

161 C. Rovira, M-H Whangbo, Inorg. Chem., **32**, 4094, 1993

162 L.M. Sverdlov, M.A. Kovner, E.P. Krainov, "Vibrational Spectra of Polyatomic Molecules" John Wiley and Sons, New York, 1968, p.365.

163 F. Pauzat, D. Talbi, M.D. Miller, J. Phys. Chem., **96**, 7882, 1992.

164 P. Swiderek, G. Hohineicher, J. Chem. Phys., **98**(2), 974, 1993.

165 K. Ohno, J. Chem. Phys., **95**(8), 974, 1993.

166 G. Jas, K. Kuczera, Chem. Phys., **214**, 229, 1997.

167 A Davidson, B. Norden, Chem. Scripta., **11**, 68, 1977.

168 F. Fillaux, M.H. Baron, J. Mayers, J. Tomkinson, Chem. Phys. Lett., **240**, 114, 1995.

169 C. Andreani, A. Filabozzi, M. Nardone, F.P. Ricci, J. Mayers, Phys. Rev. B, **50**, 12744, 1994.

170 J. Mayers, Phys. Rev. Lett., **71**, 1553, 1993.

171 F.J. Berjerno, F.J. Mompean, J. Mayers, A.C. Evans, Phys. Lett., **A189**, 333, 1994.

172 J. Mayers, T.M. Burke, R.J. Newport, J. Phys. Condens. Matt., **6**, 641, 1994.

173 A.C. Evans, J. Mayers, D.N. Timms, J. Phys. Condens. Matt., **6**, 4197, 1994.

174 A.C.Evans, J. Mayers, D.N. Timms, Phys. Rev. B., **53**, 3023, 1995.

175 P.C.H. Mitchell, E. Payen, J. Grimblot, ISIS Ann. Rep. Rutherford Appleton Laboratory, RB5806, A282, 1995.

176 P.C. Hohenburg, P.M. Platzman, Phys. Rev., **152**, 198, 1966.

177 A.L. Fielding, D.N. Timms, A.C. Evans, J. Mayers, J. Phys. Condens. Matter, **8**, 7205, 1996.

178 V.F. Sears, Phys. Rev. B., **41**, 41, 1984.

179 J. Mayers, Rutherford Appleton Laboratory Report no. RAL-TR-96-067.

180 O. Glemser, G. Lutz, Z. Anorg. Allg. Chem., **264**, 17, 1951.

181 J.J. Birtill, P.G. Dickens, Mater. Res. Bull., **13**, 311, 1978.

182 P.G. Dickens, J.J. Birtill, C.J. Wright, J. Solid State Chem., **28**, 185, 1979.

183 K.A. Wilhelmi, Acta Chem. Scand., **23**, 419, 1969

184 A.C. Evans, D.N. Timms, S.M. Bennington, J. Mayers, Phys. Rev. B, **53**, 6, 3023.

185 J.O. Besenhard, R. Schöllhorn, J. Power Sources, **1**, 267, 176.

186 P. Postorino, F. Fillaux, J. Mayers, J. Tomkinson, R.S. Holt, J. Chem. Phys., **94**, 6, 4411, 1991.

187 A.V. Powell, RSC. Ann. Rep., Sect. C. **94**, 177, 1993.

188 P.G. Dickens, M.F. Pye in "Intercalation Chemistry," ed. M.S. Whittingham and A.J. Jacobson, Academic Press, New York, 1982, Chapter 16, p.539.

189 G.J. Reynolds D.Phil Thesis, Oxford University, 1975.

190 M.S. Whittingham, M.B. Dines, J. Electrochem., Soc. **124**, 1387, 1977.

191 K.H. Cheng, M.S. Whittingham, Solid State Ionics, **1**, 151, 1980.

192 A.V. Powell, P.G. Dickens, Appl. Phys., **A51**, 226, 1990.

193 M.A. Butler, R.M. Biefeld, Phys. Rev B., **19**, 11, 5455, 1979.

194 D. Groult, C. Michel, B. Raveau, J. Inorg. Nucl. Chem., **36**, 61, 1974.

195 P.G Dickens, A.T. Short, S. Crouch-Baker, Solid State Ionics, **28-30**, 1294, 1988.

196 A.V. Powell, M.J. Pointon, P.G. Dickens, J. Solid State Chem., **113**, 109-115, 1994.

197 C.I. Ritter, W. Muller-Warmuth, R. Schollhorn, J. Chem. Phys., **83**, 6130, 1985.

198 A. Cirillo, J.J. Fripiat, J. Phys., **39**, 247, 1978.

199 B.S. Schirato, K.W. Herwig, P.E. Sokol, Chem. Phys. Lett., **165**, 6, 453, 1990.

200 J. Mayers, T.M. Burke, R.J. Newport, J. Phys. Condens. Matt., **6**, 641-658, 1994.

201 J. Noreland, ISIS Ann. Rep. Rutherford Appleton Laboratory, 1996.

202 R. Slade, A. Ramanan, P. Hirst, H. Pressman, Mat. Res. Bull., **23**, 793-798, 1988.

203 M.A. Butler, R.M. Biefeld, Solid State Commun., **29**, 5, 1979.

204 M. Kuntz, G. Tomandl, Solid State Ionics, **25**, 121, 1987.

205 F.W. Paulsen, p.21 in "Solid State Protonic Conductors I for Fuel Cells and Sensors," eds. J. Jensen, M. Kleitz, Odense University Prense, 1982.

206 M.A. Py, R.R. Haering, Can. J. Phys., **61**, 76, 1983.

207 J. Van Landuyt, G. van Tendaloo, S. Amelinckk, Phys. Status. Solidi **A**, **26**, 585, 1974.

208 X.R. Qin, D. Yang, R.F. Frindt, J.C. Irwin, Ultramicroscopy, **42-44**, 630, 1992.

209 B.E. Braun, Acta. Cryst., **20**, 268, 1966.

210 A. McDowall, Final Year Project, Chemistry Dept. Heriot-Watt University, 1999.

211 J.A Wilson, F.J. DiSalvo, S. Mahajan, Adv. Phys., **24**, 117, 1975.

212 C. Rovira, M-H Whangbo, Inorg. Chem., **32**, 4094, 1993.

213 D.H. Guthrie, J.D. Corbett, J. Solid State Chem., **37**, 256, 1981.

214 J.B. Goodenough, G. Dutta, A. Manthiram, Phys. Rev. B., **43**, 10170, 1991.

215 L. Wang, J. Schindler, J.A. Thomas, C.R. Kannewurf, M.R. Kanatzidis, Chem. Mater., **7**, 1753, 1995.

216 G.W. O'Bannon, R.F. Marzke, W.S. Glausinger, Solid State Ionics, 26, 15, 1988.

217 V.G. Young, M.J. McKelvy, W.S. Glausinger, R.B. Von Dreele, Solid State Ionics, **26**, 47, 1988.

218 W.S. Glausinger, M.J. McKelvy, E.M. Larson, R.B. Von Dreele, J. Eckert, N.L. Ross, Solid State Ionics, **34**, 281, 1989.

Heriot-Watt University Department of Chemistry

Record of Postgraduate Training

This report provides a record of training and received by research students during their research degree. A copy of this report should be appended to your thesis and also submitted to the Director of Postgraduate Studies at the end of your period of study.

Full name of candidate Maria-Laura Starforth Kosidowski

Degree **MPhil** ☐ **PhD** ☒

Date of first registration 1st October 1995

Title of Research **The Preparation and Characterisation of Intercalation Compounds**

Supervisor(s) **Dr. A. V. Powell**

1. Postgraduate Lecture Courses Attended

Year	Member of Staff	Course
Year 1	JMG Cowie JE Parker	Selected Topics in Polymer Chemistry Reaction Dynamics
Year 2	P John	Laser Chemistry
Year 3	SA Macgregor PN Preston	Theory as a Tool in Inorganic Chemistry Organometallics in Organic Synthesis

2. Other Courses Attended

Date	Course
Jan 1996	A Practical Neutron Training Course: Rutherford Appleton Laboratory

3. Conferences Attended

Date	Conference and venue
23-05-96	RSC. Materials Chemistry Forum, Aberdeen
12-09-96	Universities of Scotland Inorganic Club Conference, St. Andrews
23-09-96	UK Neutron and Muon Users Meeting, Rutherford Appleton Laboratory, Oxon.
5-02-97	RSC. Scottish Dalton Meeting, Edinburgh
17-08-97	International Conference on Neutron Scattering, Toronto.
2-09-97	RSC. Autumn Meeting, Aberdeen
18-09-97	Universities of Scotland Inorganic Club Conference, Edinburgh.
24-09-97	UK Neutron and Muon Users Meeting, Rutherford Appleton Laboratory, Oxon
2-12-97	Intercalation Compounds:Structure and Dynamics, Rutherford Appleton Laboratory
27-03-98	Molecular Sciences User Meeting, Rutherford Appleton Laboratory.

4. Papers / Posters Presented

Date	Title, conference and venue
POSTER	"The Kinetic Energy of Lithium in $LiTiS_2$ as determined by Neutron Compton Scattering"
24-09-97	UK Neutron and Muon Users Meeting, Rutherford Appleton Laboratory, Oxon
12-09-96	Universities of Scotland Inorganic Club Conference, Edinburgh
17-08-97	International Conference on Neutron Scattering, Toronto
POSTER	"Exfoliation as a Route to Intercalation Compounds"
2-09-97	RSC. Autumn Meeting, Aberdeen
18-09-97	Universities of Scotland Inorganic Club Conference, Edinburgh
TALK	"Determination of the Kinetic Energy of Lithium Ions in Intercalation Compounds"
27-03-98	Molecular Sciences User Meeting, Rutherford Appleton Laboratory.

5. Internal Lectures / Presentations

Presentations in Inorganic Section Seminars, Final Year Presentation

6. Research Papers (submitted, in press or published)

"The Kinetic Energy of Lithium in $LiTiS_2$ as determined by Neutron Compton Scattering"
Physica B, 241-243, (1998), 335-337 [published]
"Naphthalene Intercalation into Molybdenum Disulphide" submitted to Chem. Comm.

7. Industrial Experience (eg CASE Students)

Dates
Company
Address

8. Miscellaneous (please add here any other items you consider to be relevant)

Signature of Student M.L. Konstanto Date 2-9-98
Signature of Supervisor A.V. Powell Date 2/9/98